NASA Technical Paper 2828

November 1988

Validation of a Pair of Computer Codes for Estimation and Optimization of Subsonic Aerodynamic Performance of Simple Hinged-Flap Systems for Thin Swept Wings

Harry W. Carlson
and Christine M. Darden

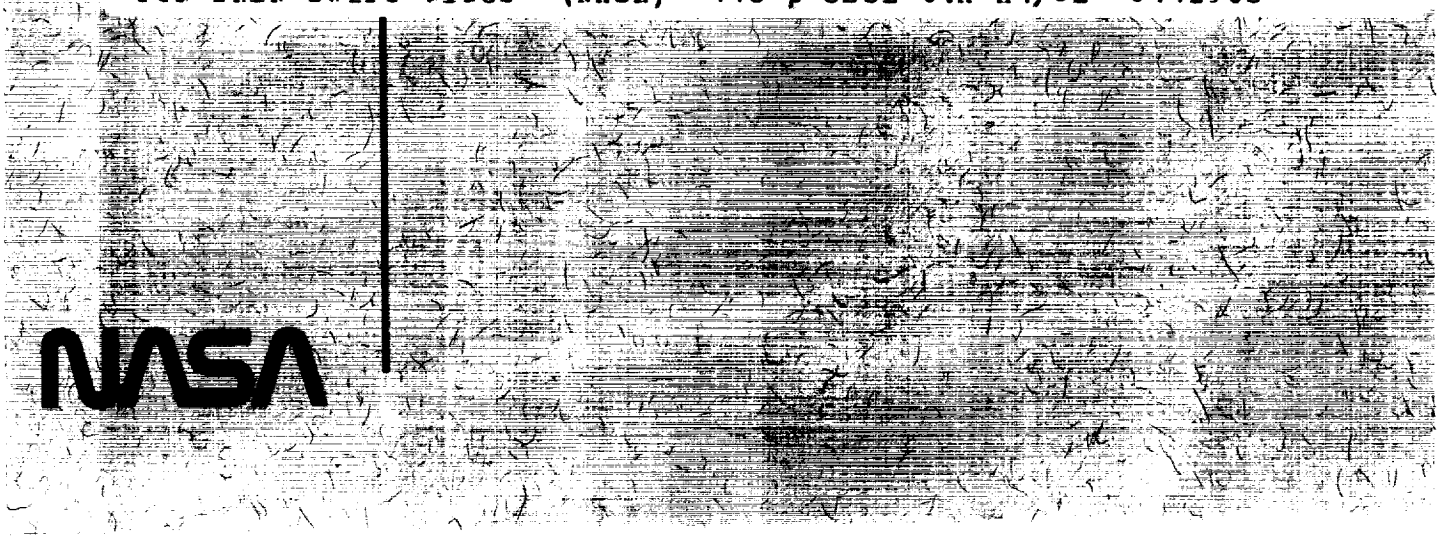

NASA Technical Paper 2828

1988

Validation of a Pair of Computer Codes for Estimation and Optimization of Subsonic Aerodynamic Performance of Simple Hinged-Flap Systems for Thin Swept Wings

Harry W. Carlson
PRC Systems Services
A Division of Planning Research Corporation
Hampton, Virginia

Christine M. Darden
Langley Research Center
Hampton, Virginia

National Aeronautics and Space Administration

Scientific and Technical Information Division

Summary

Extensive correlations of computer-code results with experimental data are employed to illustrate the use of linearized-theory, attached-flow methods for the estimation and optimization of the aerodynamic performance of simple hinged-flap systems. Use of attached-flow methods is based on the premise that high levels of aerodynamic efficiency require a flow that is as nearly attached as circumstances permit. This study covers a variety of swept-wing configurations ranging from fighters to supersonic transports, all with leading- and trailing-edge flaps for enhancement of subsonic aerodynamic efficiency. The results indicate that linearized-theory, attached-flow, computer-code methods (modified to include estimated attainable leading-edge thrust and an approximate representation of vortex forces) provide a rational basis for the estimation and optimization of flap-system aerodynamic performance at subsonic speeds. The analysis also indicates that "vortex-flap" design is not an opposing approach but is closely related to attached-flow design concepts. The successful vortex-flap design actually suppresses the formation of detached vortices to produce a small vortex which is restricted almost entirely to the leading-edge flap itself.

Introduction

This paper is intended to illustrate the use of two linearized-theory, attached-flow computer codes for the estimation and optimization of the subsonic aerodynamic performance of thin wings with simple hinged-flap systems. A previous study (ref. 1) provided an indication of the applicability of the computer methods for a few selected examples. Using the same two methods with some modifications for improved accuracy and increased capability, the present investigation treats a much broader spectrum of wing planforms, flap-system geometries, and test conditions to provide an extensive evaluation of the design and analysis concepts.

The application of linearized-theory, attached-flow methods to flap-system design and analysis is based on the premise that high levels of aerodynamic performance require a flow that is as nearly attached as circumstances allow. Simple hinged leading-edge flaps with sharp leading edges prevent the attainment of attached flow because of the separation that occurs at either the leading edge or the hinge line. However, the selection of flap geometry to provide a reasonable division of flow turning between that which occurs at the leading edge and that which occurs at the hinge line helps minimize the overall extent of flow separation. Also, the use of trailing-edge flap deflection to reduce the wing angle of attack for a given lift serves to reduce the necessary flow turning over the forward portion of the wing and further aids in the goal of providing an approach to attached flow.

Reference 2 illustrates how an attached-flow wing-design method (ref. 3) can be used in the selection of candidate flap systems to approximate attached-flow surfaces and loadings and how an attached-flow flap-system evaluation method (ref. 4) can be used to estimate achievable performance levels. In the present paper, extensive correlations of theoretical and experimental results are used to illustrate the good agreement for flap settings which result in good performance. The study also shows, in some detail, the variation of optimum leading-edge and trailing-edge flap deflections with lift coefficient as well as the ability of attached-flow methods to predict these settings and the resultant performance levels. Examples of the applicability of wing-design code results to the selection of efficient flap systems are also given where appropriate.

Symbols

AR	aspect ratio, b^2/S
b	span, in.
C_A	axial- or chord-force coefficient
C_D	drag coefficient
ΔC_D	drag coefficient due to lift, $C_D - C_{D,0}$
$C_{D,0}$	drag coefficient at $\alpha = 0^\circ$ for a wing with no camber or twist
C_L	lift coefficient
$C_{L,\text{des}}$	design lift coefficient
$C_{L,\alpha}$	lift curve slope at $\alpha = 0^\circ$, per deg
C_m	pitching-moment coefficient
$C_{m,\text{des}}$	design pitching-moment coefficient
C_N	normal-force coefficient
ΔC_p	lifting-pressure coefficient
c	local chord, in.
$\bar{c}$	mean aerodynamic chord, in.
c_L	chord of leading-edge flap or leading-edge design area, in.
c_r	root chord, chord at $y = 0$, in.

c_T	chord of trailing-edge flap or trailing-edge design area, in.
M	Mach number
R	Reynolds number based on mean aerodynamic chord
r	leading-edge radius, in.
S	reference area, in^2
S_s	suction parameter, $\frac{C_L \tan(C_L/C_{L,\alpha}) - \Delta C_D}{C_L \tan(C_L/C_{L,\alpha}) - C_L^2/(\pi \mathrm{AR})}$
t	section thickness, in.
x, y, z	Cartesian coordinates, positive aft, right, and up, respectively
x'	distance in x-direction measured from leading edge, in.
x_h	distance from wing leading edge to flap hinge line, in.
α	angle of attack, deg
α_{des}	angle of attack corresponding to design lift coefficient
α_{zt}	angle of attack for zero thrust
$\Delta\alpha_{ft}$	range of angle of attack for full thrust
β	$\sqrt{1 - M^2}$
$\delta_{L,n}$	leading-edge flap deflection angle measured normal to hinge line, positive with leading edge down (segmented flap deflection specified as inboard/outboard), deg
$\delta_{L,s}$	leading-edge flap streamwise deflection angle, positive with leading edge down (segmented flap deflection specified as inboard/outboard), deg
$\delta_{T,n}$	trailing-edge flap deflection angle measured normal to hinge line, positive with trailing edge down (segmented flap deflection specified as inboard/outboard), deg
$\delta_{T,s}$	trailing-edge flap streamwise deflection angle, positive with trailing edge down (segmented flap deflection specified as inboard/outboard), deg
η	location of section maximum thickness as a fraction of chord
$\Lambda_{h,L}$	leading-edge flap hinge-line sweep angle, deg
$\Lambda_{h,T}$	trailing-edge flap hinge-line sweep angle, deg

Fundamental Flap Performance Considerations

If it were possible for thin wings to achieve attached flow and develop the full theoretical leading-edge thrust, high levels of aerodynamic efficiency could be achieved without the use of flaps of any type. As depicted in sketch A, a thin flat wing could, if the flow remained attached to the surface, develop a lifting-pressure distribution with very high suction pressures in the vicinity of the leading edge (a singularity in the case of a flat section with no thickness). The high pressures acting on the nose of the wing section produce a leading-edge thrust which counteracts a large portion of the drag distributed over the remainder of the section. For two-dimensional flow, the counteraction is complete, and theoretically the drag disappears. Even for a flat section with no thickness, thrust is theoretically developed. In the limit, as the thickness approaches zero, the integral of the pressure acting on the projected frontal area tends to remain constant.

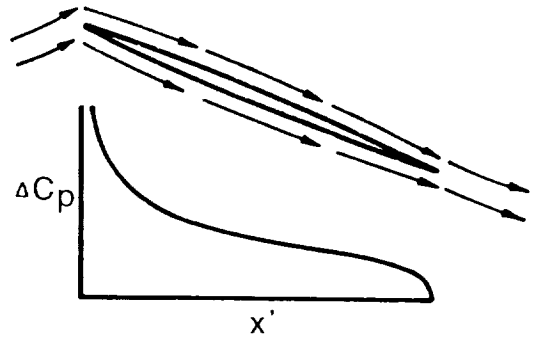

Sketch A

However, in the real flow there are severe limitations on the levels of suction pressures that can be achieved. Reference 5 presents a study of the factors limiting the achievement of full theoretical leading-edge thrust and provides a means of estimating attainable leading-edge thrust. When the high suction pressures associated with attached flow cannot be achieved, the flow tends to separate from the surface, and flow patterns and pressure distributions such as those shown in sketch B may result. The hatching

represents a separated-flow region with an embedded circulation. Although the actual leading-edge thrust may disappear, the force associated with the singularity is not lost, but according to the Polhamus analogy (ref. 6) is redistributed to appear as a normal force instead of a thrust force. Because the gain in normal force cannot compensate for the loss in thrust, the aerodynamic efficiency becomes much poorer.

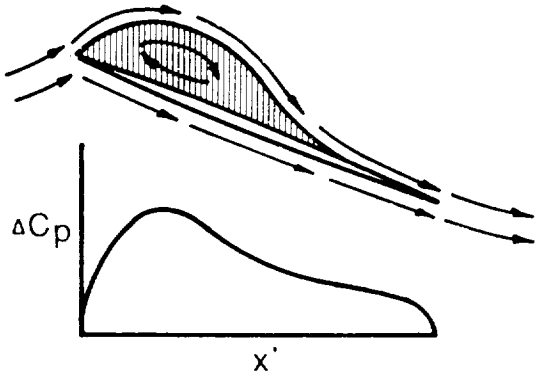

Sketch B

As shown in sketch C, use of a leading-edge flap can make the problem less severe. The theoretical attached-flow lifting pressures in the vicinity of the leading edge are much reduced. The one singularity at the leading edge is replaced by two singularities, one of lesser strength than the original at the leading edge and a second at the flap hinge line. Thus, a distributed thrust force replaces the concentrated leading-edge thrust of the flat wing. For the proper deflection angle, pressures in the vicinity of the two singularities can be made comparable. This distributed lifting pressure acting on the frontal projected area of the flap produces a theoretical thrust force approaching that of the concentrated leading-edge singularity of the flat wing. Because of the generally reduced pressures required to produce nearly the same level of theoretical thrust, that thrust is much more likely to be achieved or approached in the real flow. Within limits, the required pressure levels for the achievement of a distributed thrust nearly equivalent to that of the flat-wing singularity can be controlled by selection of the flap chords and deflections. Even with flow separation, the thrust force is preserved if reattachment takes place at or ahead of the hinge line and if no hinge-line separation occurs. This phenomenon is discussed in more detail in reference 1.

A trailing-edge flap can also be used to improve real-flow wing performance. As shown in sketch D, a deflected trailing-edge flap can increase the wing loading so that the required lift can be generated at

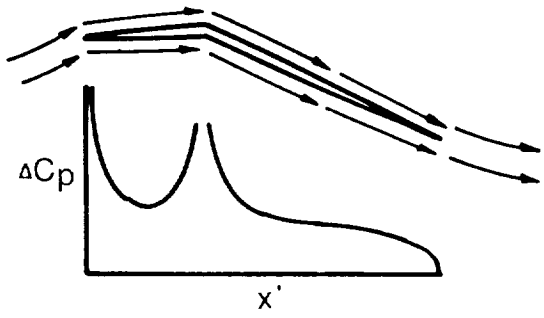

Sketch C

a lower angle of attack. This in turn reduces the required loading and singularity strength at the leading edge and thus decreases the chance of separation in the real flow. In a sense, the trailing-edge flap causes the remainder of the wing section to act as a large-chord leading-edge flap.

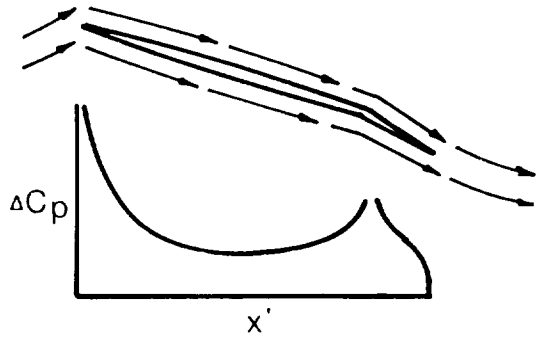

Sketch D

As shown in sketch E, the effects of leading-edge and trailing-edge flaps can be combined to further reduce the theoretical pressure peaks and decrease the chances for real-flow separation. Now there are three singularities associated with the turning of the flow, and, for properly selected deflection angles, pressures in the vicinity of singularities can be made to be of comparable strength. Possibilities for attached flow are further enhanced by a small leading-edge radius and an effective radius at the hinge lines (created in part by the boundary layer). As discussed previously, even with flow separation at the leading edge, good performance of the leading-edge flap may be retained if the separation is sufficiently localized. Such flow patterns are termed "predominantly attached" and are discussed in detail in references 1 and 2. As discussed in those references and subsequently in this paper, flow separation over the trailing-edge flap area only is not likely to be nearly as detrimental as separation at the wing leading edge.

An extension of the preceding arguments for the use of leading- and trailing-edge flaps would lead to

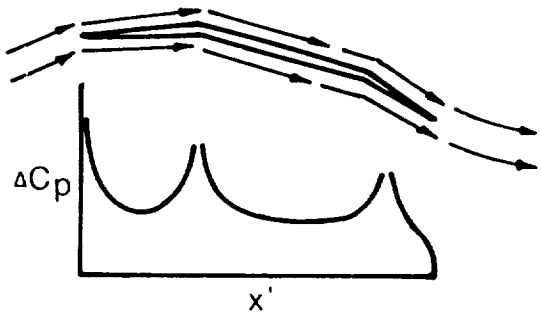

Sketch E

multisegmented flaps fore and aft and an approach to the continuously curved camber surface illustrated in sketch F. Such a surface, which may be derived from a wing-design method such as that discussed in reference 7, provides for the complete elimination of singularities and an approach to a uniform pressure distribution which should maximize the possibilities for a fully attached flow. Therefore, it is reasonable to use such a wing-design solution as a guide in the selection of flap chords and deflections to approximate that surface, its loading, and its aerodynamic performance. This approach is explored at some length in reference 2.

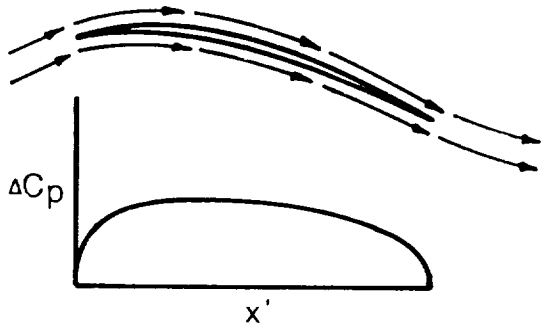

Sketch F

Analysis of Flap-System Performance

The comparisons of theory and experiment used in this paper to explore the applicability of linearized-theory, attached-flow methods to the analysis of flap-system data are restricted to force and pitching-moment data. This is believed to be sufficient because the simple nature of the surface slope distribution for most of the wings of this study and the analysis of the data through the use of axial- and normal-force coefficients allow a piece-by-piece study of the factors contributing to aerodynamic performance.

Data from a variety of experimental programs have been used in this analysis. Wing leading-edge sweep angles vary from 44° to 74°. Mach numbers from 0.3 to 0.8 are considered, and Reynolds numbers (based on $\bar{c}$) range from 1.9 to 4.8 $\times$ 10^6. The source of the data, the test conditions, and sketches of the wing-body planforms are given in each of the correlation figures.

The pair of computer codes used in this study provide a capability for the design of optimized wing-camber surfaces and the evaluation of the subsonic aerodynamic performance of wings which may employ leading- and trailing-edge flaps. These codes, which are described in detail in appendixes A and B, are improved versions of the codes used in the study of reference 1. As described in the appendixes, the modifications improve numerical accuracy and provide additional capabilities. Notes on application of the codes to the specific configurations and test conditions included in this study are given in appendix C. Sample code input data for the configurations studied are given in tables I and II.

Throughout the present report, an attached-flow computer-code solution that includes no leading-edge thrust forces and no separated leading-edge vortex forces is shown by the short-dash line. Code-estimated forces, which include attainable thrust and the effects of a separated vortex whose strength is determined by the Polhamus leading-edge suction analogy (ref. 6) and whose location is given by delta-wing empirical data (ref. 4), are shown by the long-dash–short-dash line. For reference, drag upper and lower bounds are also shown. The theoretical lower bound $[C_{D,0} + C_L^2/(\pi \mathrm{AR})]$ is the drag for a wing with an elliptical span load distribution. A theoretical upper bound shown on the figures $[C_{D,0} + C_L \tan(C_L/C_{L,\alpha})]$ is the drag for a flat wing with no leading-edge thrust and no vortex forces. The zero-lift drag for a flat wing $C_{D,0}$ was obtained from experimental data.

Cranked-Wing Fighter

Reference 8 provides subsonic maneuver performance data for a cranked-wing supersonic fighter configuration that is well suited to the purposes of this study. Data presented in figure 1 were obtained for a matrix of leading- and trailing-edge flap deflection angles so that maximum suction parameters and optimum flap settings can be ascertained and compared with theoretical predictions. The wind-tunnel tests were conducted in the Langley 7- by 10-Foot High-Speed Tunnel at Mach numbers of 0.3, 0.5, and 0.7. The experimental-theoretical correlations presented in the report are for data gathered at a Mach number of 0.5 and a Reynolds number of 2.9 $\times 10^6$.

Figure 1 provides data for the longitudinal aerodynamic characteristics of a flap system with

leading-edge flap deflections of 0°, 15°, and 30° and trailing-edge flap deflections of 0°, 10°, and 20° in all possible combinations. The data in figure 1(a) for undeflected flaps show the presence of a small amount of actual leading-edge thrust. This can be seen in the nonlinear behavior of the axial-force plot. In the complete absence of leading-edge thrust, the axial force for a flat wing (no twist or camber) such as this would be essentially constant over the angle-of-attack range. A small leading-edge radius, however, permits the achievement of some portion of the theoretical thrust, an amount well predicted by the code results. Sketch G helps to show the relative value of the thrust actually achieved, as predicted by the code, by comparing it with the full theoretical thrust (also given by the code). Up to an angle of about 3°, the full amount of theoretical thrust is achieved. Beyond this point, as the angle of attack is increased, decreasing percentages of the full theoretical thrust are realized. At the stated maneuver lift coefficient of 0.7, which for this flat wing corresponds to an angle of attack of about 14°, only a little more than 10 percent of theoretical leading-edge thrust is actually achieved. As predicted by the Polhamus analogy (ref. 6), which has been incorporated into the code, the remainder of the thrust is not lost, but

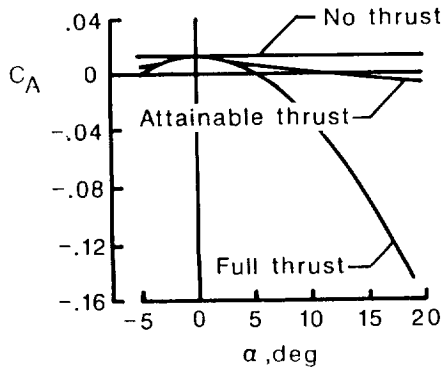

Sketch G

reappears as a normal rather than an axial force. As shown in the normal-force plot, the theoretical data with the estimated vortex-force increment included somewhat overestimate the measured normal force. The loss of most of the theoretical thrust and the substitution of the less efficient vortex-force result in a wing lifting efficiency only slightly better than that of a theoretical flat wing with no thrust and no vortex forces $[C_{D,0} + C_L \tan(C_L/C_{L,\alpha})]$, as shown in the lift-drag plot. The measured drag coefficients are somewhat larger than the theoretically predicted values (the curve with attainable thrust and vortex-force contributions) and are much larger than those of a wing with an elliptical span load distribution $[C_{D,0} + C_L^2/(\pi \mathrm{AR})]$. There is clearly a need for leading- and trailing-edge flaps to improve the wing performance.

Figures 1(a) to 1(c) form a series in which leading-edge flap deflection varies while the trailing-edge flap remains undeflected. The axial-force plots show the typical near-linear variation with angle of attack for flaps with thin sections and little or no leading-edge radius. Sketch H shows superimposed the theoretically predicted variation of C_A with α for three leading-edge flap deflections and an envelope curve for all possible deflections. This leading-edge flap

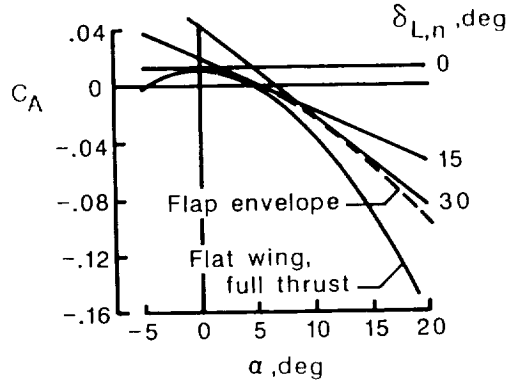

Sketch H

family, even though not optimized, provides a reasonable fraction of the full theoretical thrust benefits by substitution of a distributed thrust force for the concentrated full theoretical leading-edge force of the flat wing. As shown in these three figures, there is also a small reduction of normal force with increases in leading-edge flap deflection. However, this detrimental effect is far outweighed by the benefits of the reduction of axial force. Generally, the code provides a reasonable prediction of both axial and normal forces. There is, however, an indication of a more than moderate leading-edge flow separation (not confined to the flap itself) which prevents full achievement of code-indicated axial-force benefits beyond about $\alpha = 10°$ or $C_L = 0.5$ for the 15° deflection. For the 30° deflection, there may be a hinge-line separation beginning near $\alpha = 5°$, followed by a more general and extensive leading-edge separation at larger angles of attack. There is also evidence of a lower surface leading-edge flow separation in the low angle-of-attack region. The nature of these flow separations is discussed more fully in references 1 and 2. The code predicts the wing performance with deflected leading-edge flaps with good accuracy only up to lift coefficients of about 0.5. But as shown subsequently, optimum performance requires that

trailing-edge flap deflections accompany leading-edge deflections; for these conditions, improved correlations will be noted.

Figures 1(a), 1(d), and 1(g) form a series in which trailing-edge flap deflection varies while the leading-edge flap remains undeflected. As shown in these figures, the primary benefit of trailing-edge flap deflection is an increase in normal force at a given angle of attack. There is also an accompanying increase in axial force, but this increase does not outweigh the normal-force benefits. In effect, the wing ahead of the trailing-edge flap acts as a large-area leading-edge flap. In general, there is a good prediction of the lift-drag relationship for the deflected trailing-edge flap data, especially in the C_L range from about 0.2 to 0.6. This good prediction of drag occurs in spite of an underprediction of both axial and normal forces for the 20° flap deflection. Measured drag coefficients are lower than program predictions only for very small lift coefficients at the 20° deflection.

The behavior of the lift-drag data for this wing points out a difference in the effects on performance of separated flow in the leading-edge flap region and separated flow in the trailing-edge flap region. As discussed in reference 2, flow separation from the trailing-edge flap surface is much less likely to cause performance penalties than is flow separation from the leading-edge flap surface. This can be illustrated through the use of sketches. Sketch I shows the relationship between lift and drag changes on the wing as

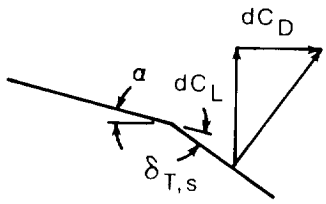

Sketch I

a whole as the result of a change in the trailing-edge flap loading. If changes in flow conditions such as those induced by changes in Reynolds number cause loading changes restricted to the flap itself, incremental changes in lift and drag are related according to the expression

$$\frac{dC_D}{dC_L} = \tan(\alpha + \delta_{T,s})$$

These considerations cause a loss in flap loading due to separation to bring about a loss in lift, which is accompanied by a decrease in drag. The net result is that the lift-drag ratio for an optimally deflected flap at a given lift coefficient is changed very little. An illustration of the effect of trailing-edge flap separation for the present configuration is given in sketch J. The arrows show the direction

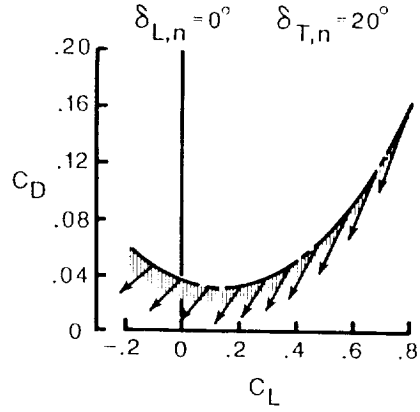

Sketch J

of the relative change in lift and drag caused by a loss in loading on the trailing-edge flap itself. The hatched area indicates the magnitude of the change if 50 percent of the theoretical loading is lost. As shown subsequently, with no leading-edge flap deflection, the 20° trailing-edge flap deflection is optimum for a C_L of about 0.8. At this condition, changes to lift and drag tend to occur along a tangent to the polar curve; thus, there is little or no performance penalty. Actually, penalties (drag increases) occur only for the lift coefficients in access of 0.8. For lift coefficients less than that at which the deflection is optimum, the separation brings about a decrease in drag, an effect noted in the experimental data. However, this drag reduction is relative to the excessive drag of a surface deflected beyond the optimum for that lift coefficient. Separation would not be expected to lead to a drag lower than that of an optimally deflected surface.

The relationship between lift and drag changes on the wing as a whole because of a change in leading-edge flap loading alone, which is illustrated in sketch K, may be expressed as

$$\frac{dC_D}{dC_L} = \tan(\alpha - \delta_{L,s})$$

Because of the negative sign, a loss in lift coefficient caused by a reduction of leading-edge flap loading is generally accompanied by an increase in drag. When applied to the present example, changes such as those shown in sketch L result. The arrows show the relative change in lift and drag caused by a loss in loading on the leading-edge flap itself, and

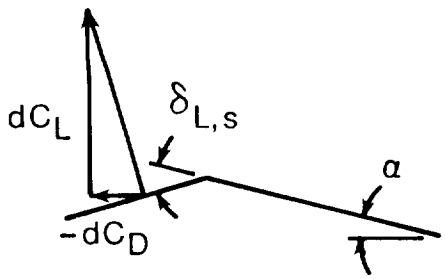

Sketch K

the hatched area indicates the magnitude of the change if 50 percent of the theoretical loading is lost. Obviously, there are severe penalties associated with the failure of the leading-edge flap to produce the anticipated loading.

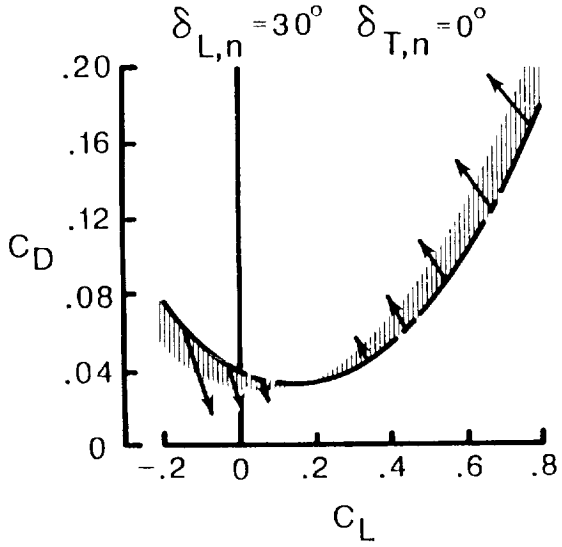

Sketch L

As discussed in reference 1, an appreciable loss in leading-edge flap loading occurs only if the flow fails to reattach ahead of or in the vicinity of the flap hinge line. When reattachment occurs aft of the hinge line, the leading-edge flap loading is reduced and the previously discussed penalties come into play. There are also additional penalties associated with leading-edge flow separation and the failure of the flow to reattach in the vicinity of the hinge line that are not covered by this simple analysis. These penalties can become particularly severe when reattachment to the wing surface does not occur at all.

The remaining parts of figure 1 cover combinations of leading- and trailing-edge flap deflections. In figure 1(e), for a moderate leading-edge flap deflection in combination with a moderate trailing-edge flap deflection, there is a good correlation of theory and experiment up to an angle of attack of about 12° and a lift coefficient of about 0.7. Above this point, the leading-edge flow separation region probably extends well beyond the hinge line and prevents the attainment of a predominantly attached flow. For the flap deflection combination with $\delta_{L,n} = 15°$ and $\delta_{T,n} = 20°$ (fig. 1(h)), there is a good correlation for the lift-drag polar in spite of evidence of trailing-edge flap separation. In view of the preceding discussion and the data for leading-edge and trailing-edge flaps alone, this might have been expected. For the combination with $\delta_{L,n} = 30°$ and $\delta_{T,n} = 10°$ (fig. 1(f)), the same discrepancies as for the 30° leading-edge flap deflection alone may be noted. However, there is still a moderate C_L region (0.3 to 0.5) in which the data appear to have predominantly attached-flow characteristics. For the extreme case of $\delta_{L,n} = 30°$ and $\delta_{T,n} = 20°$ (fig. 1(i)), there is evidence of extensive flow separation. There is still some degree of correlation for the lift-drag polar in the $C_L = 0.4$ to 0.6 region, even though it may be fortuitous.

Suction-parameter data for all the tested combinations of leading- and trailing-edge flap deflections are shown in figure 2. Experimental and program suction parameters are shown as a function of lift coefficient. The primary purpose of these data is their use in an exercise to determine as accurately as possible the maximum aerodynamic efficiency of the flap system and the flap deflections required. This information is helpful in assessing the applicability of linearized-theory attached-flow methods to the analysis (and presumably the design) of flap systems operating at or near maximum-efficiency conditions.

Experimental suction parameter as a function of leading-edge flap deflection angle for the three trailing-edge flap deflection angles and for four lift coefficients is shown at the top of figure 3. At the bottom of the figure, suction parameter is shown as a function of trailing-edge flap deflection for the three leading-edge flap deflection angles. The data represented by the symbols were obtained from fairings of the experimental data of figure 2. Fairing of these data points in figure 3 is intended to represent as accurately as possible the variation of suction parameter with deflection angles. An attempt was made to have each curve bear a family resemblance to each other and to display changes in a progressive manner.

The dashed curve in figure 3 represents an envelope, the maximum suction parameter obtainable with the optimum value of $\delta_{T,n}$ at the top of the figure, and the maximum suction parameter obtainable with the optimum value of $\delta_{L,n}$ at the bottom of the figure. The points to generate these curves were obtained by referring to both top and bottom plots for

a given lift coefficient. For example, the maximum value of suction parameter for a given leading-edge flap deflection from the bottom plot is entered in the top plot at the designated leading-edge flap deflection angle. This always gives a point equal to or greater than the points representing the faired experimental data from figure 2. An additional check on the generation of the optimum curves is that the maximum suction parameter of each of the pair of curves must be identical—there can be only one peak. The completed fairings provide data that describe the maximum suction parameter and the corresponding optimum leading- and trailing-edge deflection angles (the arrows) as a function of the lift coefficient.

Envelope data from the dashed curves of figure 3 and similar data from code results (not presented) are shown in figure 4. Optimum leading- and trailing-edge deflection angles and the maximum suction parameter are plotted as a function of the lift coefficient. The theoretical data with attainable thrust and vortex forces included provide a good estimate of the maximum suction parameter and the required deflection angles. The only really significant discrepancy is in the leading-edge deflection angle for $C_L = 0.8$. The theoretical data indicate that, for optimum deflection angles and maximum performance, the attainable thrust and vortex-force contributions are small. This is in accordance with the concept that maximization of flap-system aerodynamic performance requires a flow that is as nearly attached as circumstances allow. For the optimum flap deflection combinations, good aerodynamic performance is achieved. At low lift coefficients, suction parameters of about 0.9 are developed; even at $C_L = 0.8$, where there is some evidence of hinge-line separation, a parameter of about 0.75 was measured.

Vortex-Flap Wing-Body Configuration

Data for a wing with leading-edge vortex flaps and a 74° swept hinge line given in reference 9 are presented in figure 5. Three sets of leading-edge flap deflection angles were tested in combination with three sets of trailing-edge flap deflection angles, so that again it is possible to define maximum suction parameters and optimum flap angles. The tests were conducted in the Langley 7- by 10-Foot High-Speed Tunnel at a Mach number of 0.4 and a Reynolds number of 5.4×10^6.

Figure 5 shows the longitudinal aerodynamic characteristics for all possible combinations of 0°, 30°, and 45° leading-edge flap deflections and 0°, 10°, and 20° trailing-edge flap deflections. The data in figure 5(a) for undeflected flaps show the presence of a small amount of leading-edge thrust. The code estimate of attainable leading-edge thrust is based on an assumption of a constant leading-edge radius of 0.002 in. across the whole wing span of 27.24 in.; this radius is less than the thickness of a page of this report. There is, for this highly swept wing, a substantial contribution of the separated leading-edge vortex force to the normal force. The vortex force for this wing is much more powerful than that for the previous configuration. There is some failure of the code to predict the full magnitude of the normal force; consequently, there is a small overestimation of the drag.

Figures 5(a), 5(b), and 5(c), taken as a set, show the effects of leading-edge flap deflection for an undeflected trailing-edge flap. Within the range of the data presented, there is generally an excellent correlation of code data with experiment. There is a decreasing contribution of both the attainable leading-edge thrust and the vortex force for the flap-design lift coefficient of about 0.4 as the flap deflection angle is increased.

Figures 5(a), 5(d), and 5(g) show the effects of trailing-edge flap deflection for an undeflected leading-edge flap. As with the previous configuration, there is a good prediction of the lift-drag relationship in spite of an overestimation of the increase in axial and normal force caused by trailing-edge flap deflection. This good prediction again shows that flow separation from a trailing-edge flap does not necessarily degrade performance for flaps deflected beyond the optimum deflection for a given lift coefficient. As shown subsequently in this report, a trailing-edge flap deflection of 20° would be required for performance optimization only for lift coefficients in excess of 0.8.

Combinations of leading-edge and trailing-edge deflections are shown in the remaining parts of figure 5. Taken as a whole, the nine parts of figure 5 show a very good correlation of theory and experiment. There are appreciable discrepancies only at large lift coefficients for underdeflected flaps (where vortex force is underestimated) and at low lift coefficients for overdeflected flaps (where undersurface flow separation is the probable cause).

Suction-parameter data for all the flap deflection combinations covered in figure 5 are shown as a function of lift coefficient in figure 6. Figure 7 shows suction parameter as a function of leading- and trailing-edge flap deflection angles for each of four selected lift coefficients. This figure is similar to figure 3 for the cranked leading-edge fighter. The detailed description of the generation of the plots and their use given in the previous section are not repeated here. In reference 9, a leading-edge flap deflection of 40° was also tested. In fact, this was the selected deflection for the design lift coefficient of about 0.4. Data for

the 40° deflection have been added to the top set of plots in figure 7. As can be seen, the 40° leading-edge flap deflection in combination with a 10° trailing-edge flap deflection produced the best measured performance at $C_L = 0.4$.

Comparison of data for the vortex-flap wing-body configuration with data for the cranked leading-edge fighter shows that the performance of the vortex-flap wing-body configuration shown in figures 6 and 7 is much less sensitive to flap deflection angle than is the performance of the cranked leading-edge fighter shown in figures 2 and 3. A large part of this difference, according to the theoretical data, may be attributed to the stronger vortex for the highly swept wing with no leading-edge crank.

Envelope data from figure 7 and similar data from code results (not presented) are shown in figure 8. Optimum leading- and trailing-edge deflection angles and the maximum suction parameter are plotted as a function of the lift coefficient. The theoretical data with attainable thrust and vortex forces included provide a good estimate of the maximum suction parameter and the required deflection angles. The only significant discrepancy is in the leading-edge deflection angle for $C_L = 0.8$. The theoretical data indicate that, for optimum deflection angles and maximum performance, the attainable thrust and vortex-force contributions are small at the lower lift coefficients. At the higher lift coefficients, the vortex contribution becomes larger.

The analysis of this report indicates that the vortex-flap design and the attached-flow design are not opposing approaches, but are in fact closely related. The successful vortex-flap design actually suppresses the formation of detached vortices to produce a small vortex which is restricted almost entirely to the leading-edge flap itself.

44°-Swept Trapezoidal-Wing Fighter

Reference 10 provides the flap deflection data shown in figure 9 for a generic fighter configuration tested in the Langley 7- by 10-Foot High-Speed Tunnel at $M = 0.4$ ($R = 1.9 \times 10^6$) and $M = 0.8$ ($R = 3.1 \times 10^6$). Perhaps because of an emphasis on canard and horizontal tail effects, a full matrix of flap deflections was not covered. Nevertheless, there are sufficient data for specific leading- and trailing-edge flap deflection combinations to provide a test of program prediction capabilities.

Figure 9(a) shows data at $M = 0.4$ for undeflected flaps. Because of a code overestimation of the vortex force, correlation of theory and experiment is poor beyond $C_L \approx 0.5$. For an 8° deflection of both leading- and trailing-edge flaps shown in figure 9(b), there is good correlation up to $C_L \approx 0.8$. The 12° and 20° deflection data of figures 9(c) and 9(d) indicate good correlation of lift and drag up to C_L values approaching 1.0, again in spite of evidence of trailing-edge flap separation.

In reference 10, equal deflections of leading- and trailing-edge flaps (angles measured normal to the hinge line) were apparently considered to represent an optimum configuration. The contour map of figure 10 was prepared to determine what ratio of leading-edge to trailing-edge flap deflection the code would call for. The map was constructed for a lift coefficient of 0.8 using guidelines described in appendix B. The code indicates an optimum leading-edge flap deflection angle of 21.2°, which is about 1.4 times the optimum trailing-edge flap deflection angle of 14.9°. A similar map for $C_L = 0.4$ (not presented) gave smaller optimum deflection angles but about the same ratio. The code indicates, however, that equal deflections would result in only a small loss in efficiency. There is insufficient experimental data to identify a true optimum combination.

Figures 11(a) to 11(d) provide flap deflection data similar to that of figure 9, but for a Mach number of 0.8. Data for the code prediction without attainable thrust and vortex forces as well as the theoretical bounds are omitted, because the primary purpose here is to assess the effect of Mach number on the experimental-theoretical correlation. It is not surprising that the correlation of theory and experiment at this higher Mach number is considerably poorer. For undeflected flaps (fig. 11(a)), there is a breakaway in axial force for the experimental data (probably caused by shock development) at an angle of attack of only 8° or a lift coefficient of about 0.5. For deflections of 8° for both flaps shown in figure 11(b), the breakaway is delayed, and good correlation is shown up to $C_L \approx 0.8$. For 12° deflection (fig. 11(c)), good correlation is obtained up to $C_L \approx 0.7$. With the deflections increased to 20° (fig. 11(d)), there is evidence of trailing-edge flap flow separation as well as shock effects, and the overall correlation is poor.

60°-Swept Delta-Wing Fighter

Data for a companion to the preceding configuration are also reported in reference 10. The 60° delta-wing fighter was tested with both rounded and sharp leading-edge airfoil sections.

Data for a wing with a 64A00X (64A) section (6 percent thick at the root, 4 percent thick at the tip) are shown in figure 12. For undeflected flaps, figure 12(a) shows an underprediction of attainable thrust illustrated in the C_A plot and an overprediction of the vortex force illustrated in the C_N plot. These errors tend to compensate for one another, and there is a reasonably good prediction of

the lift-drag characteristics. Figures 12(b) to 12(d) form a series in which the trailing-edge flap deflection varies while the leading-edge flap deflection remains constant at 20°. The same discrepancies as noted for the undeflected case persist, but there is nonetheless a good prediction of lift-drag performance. Suction parameters for the three deflections as a function of lift coefficient are shown in figure 13. There is an improvement of suction parameters for the higher lift coefficients as the trailing-edge flap deflection increases. For $C_L \approx 0.6$, the optimum trailing-edge flap deflection (with $\delta_{L,n}$ fixed at 20°) appears to be only slightly less than 20°. For this condition, the code indicates a small contribution of attainable thrust and an even smaller vortex-force contribution.

Optimum leading-edge flap deflections for this configuration were considered to be between 1 and 2 times the trailing-edge flap deflections (ref. 10). The contour map of figure 14, generated from code data for $C_L = 0.6$, indicates that an optimum combination would be $\delta_{L,n} = 24.0°$ and $\delta_{T,n} = 17.6°$, a ratio close to 1.4.

Some sample data for the configuration tested with a sharp leading-edge wing section are shown in figure 15. The code data shown here are for an estimated constant leading-edge radius of 0.002 in. With the exception of a small decrease in leading-edge thrust, the data for the sharp leading edge are similar to those for the 64A section. Figure 16 shows suction-parameter data for a 20° deflection of both leading- and trailing-edge flaps as a function of lift coefficient. The suction parameter for the rounded leading-edge section is slightly better than that for the sharp section, because the rounded leading edge provides for a greater margin of error in achieving a proper leading-edge flow alignment to minimize flow separation.

Data for the wing with the rounded leading edge tested at $M = 0.8$ are given in figure 17. There is reasonably good prediction of the undeflected flap performance. Correlation is not good for the data where $\delta_{L,n} = 20°$ and $\delta_{T,n} = 20°$, but it is better than the corresponding correlation for the 44°-swept trapezoidal-wing fighter. The higher sweep angle should decrease the tendency for shock formation. Generally, however, it appears that the code cannot be relied on for transonic performance predictions.

Generic Arrow-Wing Supersonic Transport

Reference 11 provides the aerodynamic data for a highly swept, untwisted, and uncambered arrow-wing configuration with leading- and trailing-edge flaps shown in figure 18. The tests were performed in the Langley 4- by 7-Meter Tunnel at a Mach number of 0.25 and a Reynolds number of 4.8×10^6. The leading-edge flap is characterized by a long root chord and a large taper. The trailing-edge flap is segmented to fit between the fuselage and inboard nacelle and between the inboard nacelle and the outboard nacelle.

The flap deflection data of reference 11 are insufficient for determining optimum flap settings. There are, however, enough data to provide a test of the code and to illustrate some trends. A sample of data from this investigation is shown in figure 18. Figure 18(a) shows data for undeflected flaps. The correlation indicates attainable thrust somewhat larger than predicted and a somewhat better-than-predicted lift-drag performance. Figures 18(b) to 18(e) form a series in which the trailing-edge flap deflection varies while the leading-edge flap deflection remains constant at $\delta_{L,n} = 30°$. For all these data there is a good correlation of theory and experiment.

Figure 19 is composed of two parts. At the left of the figure, suction parameter with $\delta_{L,n} = 30°$ is shown as a function of C_L for each of the trailing-edge flap deflection angles. At the right, suction parameter is shown as a function of $\delta_{T,n}$ for three selected lift coefficients. The program data predict both the magnitude and trends of the experimental data quite well. The maximum suction parameter of 0.67 for $C_L = 0.6$, which represents takeoff or touchdown conditions for a typical supersonic transport ($\alpha \approx 12°$), is reasonably good, but is somewhat lower than might be expected of a well-designed system. The remainder of the discussion of this configuration and much of the discussion of the next configuration is devoted to the search for better performance at a representative C_L of 0.6.

In the section of this paper entitled "Fundamental Flap Performance Considerations," the concept of replacing a concentrated theoretical leading edge with a distributed force acting on a deflected flap was discussed. With that idea as a starting point, the code-calculated spanwise distribution of leading-edge thrust for the flat wing is shown in sketch M. The kink in the distribution near the $\frac{y}{b/2} = 0.2$ station is caused by the wing-body juncture. Otherwise, the curve is relatively smooth. For any given lift coefficient, 0.6 for example, the spanwise distribution of the leading-edge thrust would have the form of the curve of sketch M. This leads to the argument that inboard flap chords can be smaller rather than larger than outboard flap chords and still support the necessary distributed thrust loading. A process considerably more complicated than the simple idea expressed above (e.g., ref. 4) was used in derivation of reduced inboard chord flaps for the next configuration to be studied. The preceding argument,

however, is sufficient to justify the consideration of inverse-taper flaps for highly swept wings.

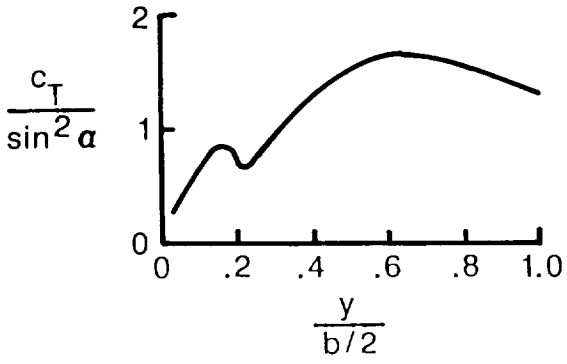

Sketch M

Advanced Arrow-Wing Supersonic Transport

An experimental program investigating flap systems for an advanced supersonic transport (SST) with a wing twisted and cambered for supersonic cruise is described in reference 12. Test data for deflections of two separate inverse-taper leading-edge flap planforms with a segmented trailing-edge flap are given in figure 20. In the discussion of these data it is important to note the difference in the measurement of deflection angle for the two flap systems. For flap system A, angles were measured normal to the hinge line; for flap system B, angles were measured in the streamwise direction. The data were obtained at a Mach number of 0.21 and a Reynolds number of 4.1×10^6 in a 7- by 10-foot wind tunnel at Texas A&M University.

Data for the undeflected flaps are shown in figure 20(a). These data are applicable to both leading-edge flap planform A (the larger inboard chord) and leading-edge flap planform B (the smaller inboard chord). The wing employed twist and camber designed for supersonic cruise, which is responsible for the slope of the axial-force curve and the positive value of C_N at $\alpha = 0°$. Again, there is evidence of the development of a small amount of leading-edge thrust. In general, the measured characteristics are predicted quite well.

Figure 20(b) shows data for trailing-edge flaps deflected to 20° with leading-edge flaps undeflected. These data are also applicable to both flap A and flap B. The correlation here is also considered good.

Figures 20(b), 20(c), and 20(d) form a series in which the leading-edge deflection of flap system A varies, while the trailing-edge flap deflection remains fixed at 20°. There is a better prediction of axial-force characteristics at $\delta_{L,n} = 40°$ than at $\delta_{L,n} = 30°$. This is puzzling. Nevertheless, there is a reasonably good prediction of lift-drag characteristics for both deflections.

Figures 20(b), 20(e), and 20(f) form a series in which the leading-edge deflection of flap system B varies with a fixed trailing-edge flap deflection. For flap system B, deflections are measured in the streamwise direction; thus, these deflections are much larger than those for flap system A. For example, the $\delta_{L,n} = 40°$ deflection of flap A produces streamwise angles of only 13.0° and 26.4° for the inboard and outboard panels, respectively. There is a good prediction of aerodynamic characteristics for the $\delta_{L,s} = 20°$ deflection. Correlation is poorer for the 40° deflection, but the correlation is best in the $C_L = 0.5$ to 0.7 range, where the effects of flow separation are apparently smaller.

Figure 21 shows suction parameter as a function of lift coefficient for the three leading-edge flap deflections of both flap systems. Using data from these plots, figure 22 shows suction parameter as a function of leading-edge flap deflection angle for three selected lift coefficients. From these derived data, it is shown that the two flap systems offer comparable performance. Flap system A offers a slight advantage at $C_L = 0.6$, and flap system B offers a slight advantage at $C_L = 0.8$. As expected, optimum deflections for flap system B, with its streamwise angle measurement, are smaller than those for flap system A.

At a representative lift coefficient of 0.6, flap system A of reference 12 offers a small increase in suction parameter ($S_s = 0.79$ experimentally; $S_s = 0.71$ given by the code in fig. 22) compared with the larger inboard chord flap system of reference 11 ($S_s = 0.67$ experimentally; $S_s = 0.67$ given by the code in fig. 19). In the following discussions, code data, both analysis and design, are used to explore possibilities for further improvements in aerodynamic efficiency by flap-system modifications.

Figure 23 shows calculations of the spanwise variation of the angle of attack for zero thrust α_{zt}, and the range of α for which full thrust is available. For the data shown here, the leading-edge deflection angle varies, but the trailing-edge flap deflection angle remains fixed at 20°. The quantity α_{zt} represents the angle of attack of the wing as a whole that is required to bring about an onset flow condition at a specified span station. With the wing at this angle, there is theoretically no leading-edge flow separation at the given station. The range of full thrust $\Delta\alpha_{ft}$ indicates the angular tolerance within which flow remains attached and full theoretical thrust is developed. This range, as determined by theoretical and empirical relationships discussed in reference 4,

depends on the wing-section geometric characteristics, the wing sweep angle, the Mach number, and the Reynolds number. Thus, for angles of attack within the range of full thrust ($\alpha_{zt} \pm \Delta\alpha_{ft}$), which is represented by the hatched area in figure 23, attached flow could be expected. The plots in the figure show how, according to the evaluation code, changes in the wing surface alter the range of full thrust and affect the possibilities for attached flow. According to these data, even for $\delta_{L,n} = 40°$, the angle of attack required for $C_L = 0.6$ (about 10°) is outside the range of full thrust, and flow separation would be expected. The amount of leading-edge separation at $\delta_{L,n} = 40°$ would, however, be relatively small, and the resultant vortex flow, if largely confined to the leading-edge flap itself, could counteract in part the loss in leading-edge thrust. The plot of suction parameter versus deflection angle at the bottom of the figure indicates that the optimum deflection for this example is close to 40°.

The wing-design code of reference 3 has been used as a guide in evaluating the maximum aerodynamic performance potential of the wing and describing the required wing-surface ordinates. The design conditions used in the code are $C_L = 0.6$ at a Mach number of 0.21 and a Reynolds number of 4.1×10^6. No restriction is placed on C_m. The wing-surface ordinates plotted in figure 24 theoretically give an optimized suction parameter of about 0.90. This design provides for a theoretical leading-edge onset flow that is tangent or nearly tangent to the leading-edge surface, as shown in sketch N. Because the range of full

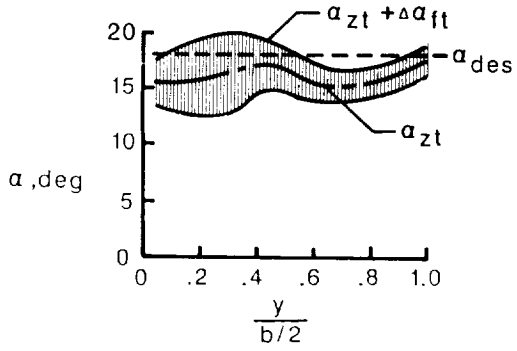

Sketch N

thrust (the hatched area) nearly covers the design angle of attack, only a mild-degree and limited-extent flow separation would be expected. Because this design surface differs from the supersonic cruise design over the whole of the wing planform, it is difficult to devise a simple flap system to replace the design surface and approach the performance benefits. Nevertheless, reference 2 offers guidelines for adapting the whole wing-design approach to the selection of flap geometry. Reference 2 also describes how the restricted-area design feature of the program may be employed in defining efficient flap surfaces. However, this latter procedure requires multiple runs to insure that proper consideration is given to trailing-edge flap contributions to the aerodynamic efficiency. Experience has shown that there is a better procedure; this procedure is described in the following paragraph.

A recommended procedure for using the wing-design program in the selection of flap geometry is as follows:

(1) Perform a whole-wing design for the entire wing planform at the design lift coefficient, Mach number, and Reynolds number conditions. Use no moment restraint if performance alone is the concern, but specify a design moment if trim conditions must also be considered. This design provides an indication of performance potential and aids in the selection of local flap chords within limitations imposed by wing structural restraints. Generally, flap chords should be as large as structural considerations allow; however, the whole-wing solution sometimes shows areas where leading-edge flap chords may be reduced or eliminated.

(2) Perform a restricted-area wing design for the same flight conditions and for a moment coefficient $C_{m,\text{des}}$ at the design lift coefficient as given by the whole-wing solution. Imposition of the design moment insures that adequate consideration is given to trailing-edge flap contributions to lifting efficiency. Use a restricted-area chord equal to the actual flap chord, and activate the flap-design (FLPDES) feature of the code to provide a spanwise flap deflection schedule.

(3) Examine the code output flap deflection schedule and modify it as necessary to meet design restraints such as those imposed by spanwise segmentation. Also, since the theoretically recommended deflections are only approximations, not true optimums, experience may be applied in modifying results, particularly in the reduction of large indicated angles. Application of the wing evaluation code to the selected flap system as was done for the preceding correlation examples will help in defining more accurately the optimum deflections.

An example of the application of the restricted-area design to the advanced SST is shown in figure 25. The design conditions are again $C_L = 0.6$ at a Mach number of 0.21 and a Reynolds number of 4.1×10^6. A C_m restraint of -0.05, as given by the whole-wing design at $C_L = 0.6$, is also imposed. The flap chord schedule of flap system A is retained. As

illustrated in sketch O, the design surface should allow only a mild degree and limited extent of leading-edge flow separation. Tick marks on the camber-surface curves indicate the location of the flap hinge line (long ticks) and the limit of the design area (short ticks). The code-calculated suction parameter for this restricted-area design is about 0.84 compared with 0.90 for the whole-wing design. The solid symbols in the plots of leading- and trailing-edge flap deflection angles indicate code-calculated values as described in appendix A. The solid line in these plots gives a modified schedule imposed by segmentation and, in the case of the trailing-edge flaps, by experience. The two small-span, trailing-edge flaps make it difficult to obtain a valid numerical solution with only eight spanwise elements.

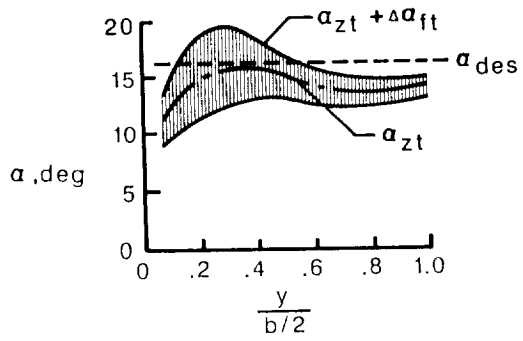

Sketch O

When the flap deflection schedules given in figure 25 are used in the wing evaluation program, the data generated may be used in the preparation of a performance map (fig. 26) according to procedures described in appendix B. This map shows contour lines of equal suction parameter at a lift coefficient of 0.6 with $\delta_{L,s}$ factor and $\delta_{T,s}$ factor as the independent variables. In previous performance maps, it was possible to use flap deflection angles as the independent variables, because in those cases the flap deflection angle and the hinge-line sweep angle had no spanwise variation. When this condition is not met, the use of input flap deflection multipliers (described in appendix B) to generate additional surfaces for code analysis no longer permits their representation by a single spanwise-invariant deflection angle. The only recourse is to use the multipliers or factors themselves. As shown in figure 26, the optimum leading-edge deflection factor is about 0.88 instead of the 1.00 value which corresponds to the input deflections of 22° for the inboard panel and 28° for the outboard panel. Thus, a more nearly optimum deflection for the leading-edge flap is 19.5°/25.0°. The trailing-edge flap deflection optimizes at about 16°. The maximum suction parameter for these designed flap deflections is about 0.73, which is only slightly better than the parameter of 0.71 obtained with the $\delta_{L,n} = 30°$ ($\delta_{L,s} = 9.0°/18.9°$) setting.

Figure 27 shows α for zero thrust and the range of full thrust as a function of span position for this new deflection schedule. The trailing-edge flap deflection is held constant at 20° as was the case for the original plots for $\delta_{L,n} = 20°$ and 40° in figure 23. For the design condition ($\delta_{L,s}$ factor = 1), the range of full thrust extends to the α for $C_L = 0.6$ line only at a station of about 0.25. The wing-body juncture makes it difficult for the code to give accurate values of α_{zt} in the region, inboard of the 0.20 station, and the assumption that the leading-edge radius is zero at $y = 0$ underestimates the range of full thrust inboard of the juncture. The real flow probably would be essentially attached inboard of the 0.25 station. Beyond that point, according to the theory, the leading-edge flow detaches and a separated vortex is formed. There is a loss of thrust, but it is made up for in part by the vortex-force contribution to the lift. As indicated by these theoretical results, attached flow over the outer portion of the wing cannot be achieved, even with a doubling of the $\delta_{L,s}$ factor. For such large deflection angles, there are nonlinear drag penalties, and, as indicated by the plot of suction parameter versus $\delta_{L,s}$ factor, these penalties bring about a severe deterioration in performance. A larger leading-edge flap chord for the outboard panel, particularly in the wingtip region, could improve performance by creating a surface more closely approximating the whole-wing design surface of figure 24.

Because the segmented small-span trailing-edge flaps may be responsible for some performance losses, a study of this configuration with full-span trailing-edge flaps was made. A restricted-area design for the same conditions as before, but with a full-span trailing-edge flap, is shown in figure 28. The suction parameter for this surface is promising at about 0.90, the same as that for the whole-wing design. However, when the flap deflections indicated in the plots of figure 28 were used in the wing evaluation program, the maximum suction parameter (fig. 29) was 0.77; this suction parameter was an improvement over the other flap systems but was far below the smooth-surface optimums.

The results of the steps that were taken to improve flap performance for a representative SST configuration are shown in figure 30. Theoretical suction parameters for specified surfaces and for optimum or near-optimum combinations of leading- and trailing-edge flap deflection angles are shown in the bar chart. For the flat-wing configuration at the top

of the figure, a suction parameter of about 0.32 is predicted. This prediction includes the effects of the estimated attainable thrust and vortex forces. The measured performance was actually somewhat better ($S_s = 0.45$) but still left much room for improvement. A flap system with a large-chord inboard leading-edge flap resulted in a predicted suction parameter of about 0.67 for a near-optimum combination of leading- and trailing-edge flap deflections. This condition produced results that were very close to the measured performance. A similar configuration with a much smaller inboard leading-edge flap had a predicted suction parameter of about 0.69 and a measured parameter of about 0.77. This improved performance was achieved with a leading-edge flap of about half the area of the original. This reduction was perhaps too extreme; the next flap configuration with smaller reduction in the inboard chord had a somewhat higher predicted suction parameter of about 0.71 and a measured value of about 0.79. When the wing-design code was used to devise a flap system with a better theoretical distributed thrust force, a slight improvement to a suction parameter of about 0.73 was predicted by the wing evaluation code. With the unrealistic assumption of full-span trailing-edge flaps, a suction parameter of about 0.77 is predicted. However, this prediction still falls far short of the predicted performance of a mission-adaptive or restricted-area camber-surface design. If the search for a more efficient flap system were to be continued, additional attention would need to be given to the outboard leading-edge flap; this is where the flat-wing theoretical leading-edge thrust is most pronounced and where the potential for the development of distributed thrust on a modified surface is greatest. Among the changes that might be considered are a larger flap chord and/or double-hinged flaps to more closely approximate a smooth-camber surface.

60°-Swept Trapezoidal-Wing Fighter

Subsonic flap configurations for the supersonic cruise fighter tested in reference 13 were selected by using an early version of the wing analysis code in a design-by-iteration mode. The tests were performed in the Langley 7- by 10-Foot High-Speed Tunnel at Mach numbers of 0.3, 0.5, and 0.7 with corresponding Reynolds numbers of 1.9×10^6, 2.9×10^6, and 3.3×10^6. Test data for a variety of combinations of leading- and trailing-edge flap deflection angles tested at a Mach number of 0.5 are shown in figure 31. Axial-force data for undeflected flaps presented in figure 31(a) show evidence of the mild twist and camber of the supersonic wing design and indicate the presence of an appreciable amount of attainable thrust. There is a good correlation of program and experimental data for all parts of figure 31. The greatest discrepancy occurs in figure 31(g) for the largest deflections tested. For low angles of attack, there apparently is a flow separation on the lower surface of the leading-edge flap which results in lower-than-predicted axial force and drag. At the higher lift coefficients, where the flow for these large deflections is more likely to be predominantly attached, there is again a good correlation. The segmented leading-edge flap data presented in figure 31(h) produced the lowest drag at the design C_L of 0.73 of all the deflection combinations tested. Selection of the $\delta_{L,s} = 15°/20°$ (inboard/outboard) schedule was based on an examination of code data for various candidate combinations.

Figure 32 shows suction parameter plotted versus lift coefficient for three leading-edge flap deflection angles and two trailing-edge flap deflection angles. For lift coefficients greater than about 0.4, there is generally a good prediction of the flap-system performance. The greatest discrepancy occurs at low lift coefficients for a trailing-edge flap that is deflected to an angle greater than that required for optimum performance. This behavior was noted and discussed in previous examples herein.

The tests of reference 13 included a leading-edge flap with a reduced-chord inboard segment. Figure 33 presents data to provide a comparison of the two leading-edge flap planforms. For both configurations, $\delta_{L,s}$ is 15° for the inboard segment and 20° for the outboard segment, and $\delta_{T,s}$ is 15° for the inboard segment and 12° for the outboard segment. This was the best of the combinations tested for the large-chord, inboard, leading-edge flap segment. Within the accuracy of the measurements, the two flaps may be considered to have equal performance. This is consistent with similar data for the SST configuration previously treated. Because of size and weight considerations, the smaller-chord version would again have the advantage.

For the best of the flap-deflection combinations tested, a suction parameter of about 0.84 was predicted and an experimental value of about 0.89 was obtained at the design C_L of 0.73. Application of the wing-design code to the problem is not likely to bring about any significant improvement. Nevertheless, it would be of interest to examine the concurrence between design-process results and those of the iterative approach. Figure 34 shows the camber surface for a whole-wing design with $C_{L,\text{des}} = 0.73$ at a Mach number of 0.5 and a Reynolds number of 2.9×10^6. This design gives a suction parameter of about 0.9. In accordance with a previously described flap-design

process and the assumption that no restraints need be placed on C_m, the C_m generated by the whole-wing design of -0.17 was used in a restricted-area design illustrated in figure 35. In the derivation of flap deflections from the program-listed recommendations, four segment flaps were assumed. When the flap deflection schedules indicated by the solid lines in the plots of figure 35 were used in the wing evaluation code, a suction parameter of about 0.83 was obtained. This suction parameter was slightly lower (about 1 percent) than the predicted suction parameter for the original two-segment flap system, which points out some precautions in the use of the wing-design code for flap deflection. First, the wing-design code listing of suggested flap deflection schedules is only an approximation based on a graphical fitting of straight-line segments to a continuous curve and does not necessarily represent a true optimum. Second, the wing evaluation code provides for a more accurate handling of discontinuous slopes and accounts for a nonlinear variation of pressures with surface slope. Thus, the evaluation code must be given the greater credence in any search for optimum flap systems. Nevertheless, the close correlation between design- and evaluation-code results helps to establish confidence in the suggested flap-design process.

Figure 36 shows data for the best of the tested leading- and trailing-edge flap deflection combinations at off-design Mach numbers of 0.3 and 0.7. In neither case is there any appreciable deterioration in the ability of the linearized-theory code to predict the measured characteristics. This good correlation is in contrast with higher Mach number data for other configurations treated in this study, notably the 44°-swept trapezoidal-wing fighter. It is likely that the linearized-theory methods are valid up to, but not beyond, the drag-rise Mach number.

Conclusions

An analysis of the subsonic aerodynamic performance of simple hinged-flap systems for a variety of thin, swept-wing, wing-body combinations has led to the following conclusions.

1. Linearized-theory, attached-flow, computer-code methods (with estimated attainable leading-edge thrust and an approximate representation of vortex forces) provide a rational basis for the estimation and optimization of flap-system aerodynamic performance at subsonic speeds below the drag-rise Mach number.
2. Optimization of flap-system aerodynamic performance requires specified deflections of both leading-edge and trailing-edge flaps which can be predicted with reasonable accuracy by the numerical methods. Near-maximum performance, however, can be achieved over a fairly broad range of deflection-angle combinations.
3. Generally, good prediction of aerodynamic performance as measured by the suction parameter can be expected for near-optimum combinations of leading- and trailing-edge flap deflection at a given lift coefficient; these conditions tend to produce a predominantly attached flow. Poor correlation of code results and experimental data may be experienced for undeflected flaps at high lift coefficients and for highly deflected flaps at low lift coefficients; these conditions tend to promote severe flow separation without reattachment.
4. Code prediction of the aerodynamic efficiency of flap systems is equally valid for sharp and rounded leading-edge wing sections.
5. This analysis indicates that vortex-flap design and attached-flow design are not opposing approaches, but are closely related. The successful vortex-flap design actually suppresses the formation of detached vortices to produce a small vortex which is restricted almost entirely to the leading-edge flap itself.

Performance degradation brought about by low Reynolds numbers and high Mach numbers was not investigated in this study. The conclusions are thus restricted to Mach numbers below the drag rise and Reynolds numbers sufficiently high to avoid drastic flow separation at or near design conditions.

NASA Langley Research Center
Hampton, VA 23665-5225
August 18, 1988

Appendix A

Description of Wing-Design Computer Code

The wing-design code introduced in reference 3 generates an optimized twisted and cambered lifting surface for a given wing planform operating at specified flight conditions, provides the corresponding lifting-pressure distribution, and gives wing force and moment data. The code provides an analysis of the designed surface and may be operated in an analysis-only mode. Supersonic and subsonic speeds can be handled, but it is not a transonic code. Because the solution is based on the use of candidate surfaces, it can provide a twisted and cambered surface restricted to specified wing regions (a mission-adaptive design) as well as a whole-wing design. This code has recently been modified to provide for the selection of spanwise flap deflection schedules which would approximate the surface and loadings of the optimized restricted-area design.

The numerical method is based on linearized-theory, potential-flow solutions for a zero-thickness lifting surface represented by an array of horseshoe vortices. A solution by iteration rather than by a matrix inversion is used. The code also provides for an estimate of attainable leading-edge thrust and of the forces caused by separated leading-edge vortices. Attainable leading-edge thrust considerations play a direct part in the design process, but vortex-force estimates do not, except for a reduction of design lift coefficient (and camber-surface severity) caused by the vortex-lift contribution.

The computer code

> WINGDES2—Wing-Design and Analysis Code

may be obtained for a fee from:

COSMIC
Computer Services Annex
University of Georgia
Athens, GA 30602
(404) 542-3265

Request the code by the designation LAR-13995. This code is written in FORTRAN V for use on the Control Data 6600 computer system and on the Control Data Cyber series.

The first record in the input is a code run identification that accepts up to 80 characters. The remainder of the input is placed in NAMELIST format under the name INPT1.

The wing-planform information is specified by a series of leading-edge and trailing-edge breakpoints for a right-hand wing panel. Up to 21 pairs of coordinates may be used to describe the leading edge and up to 21 pairs to describe the trailing edge. The planform input data in program terminology are as follows:

NLEY	number of leading-edge breakpoints (limit of 21)
TBLEY	table of leading-edge y-values; beginning at $y = 0$; increasing order of y from root to tip
TBLEX	table of leading-edge x-values that corresponds to TBLEY table
NTEY	number of trailing-edge breakpoints (limit of 21)
TBTEY	table of trailing-edge y-values; beginning at $y = 0$; increasing order of y from root to tip
TBTEX	table of trailing-edge x-values that correspond to TBTEY table
XMAX	largest x-ordinate anywhere on planform
SREF	wing reference area for use in aerodynamic force and moment coefficients
CBAR	wing reference chord for use in aerodynamic moment coefficients
XMC	x-location of moment reference center
ELAR	element aspect ratio

For flat and mildly cambered wings, an element aspect ratio approximately one-half the full-wing aspect ratio is recommended. For wings with small chord leading-edge or trailing-edge design areas it may be necessary to use a large element aspect ratio to place at least two elements within the chord. The number of elements in a given chord, c_L or c_T, may be approximated as

$$N = \frac{c_L}{b/2}(\text{JBYMAX})(\text{ELAR})$$

or

$$N = \frac{c_T}{b/2}(\text{JBYMAX})(\text{ELAR})$$

Because computational costs tend to increase as the fourth power of JBYMAX and the second power of ELAR, an increase in the element aspect ratio is the more efficient means of providing for improved definition. At supersonic speeds, where ELAR is set

to $1/\beta$, the only recourse is to increase JBYMAX. This parameter controls the size of the wing in code dimensions.

JBYMAX integer designating number of elements in spanwise direction (limit of 30)

The necessary scaling is done within the code by use of a scale factor 2(JBYMAX)/(SPAN (β)). The number of complete wing elements N corresponding to a given JBYMAX may be approximated as

$$N = 4(\text{JBYMAX}^2)\left(\frac{\text{ELAR}}{\text{AR}}\right)$$

The code has been written to accommodate 500 right-hand panel elements. Generally, the JBYMAX integer is less than the limit of 30. The normal range is 8 to 15 for subsonic speeds and 20 to 30 for supersonic speeds. Computational costs tend to increase as the square of the number of elements.

The wing mean-camber surface may be specified by a set of tabular entries. However, if a flat-wing analysis is to be performed or if a flat wing is to be used as the initial surface in a design process, these entries are not required. If a wing surface is input, the section mean-camber surface must be specified by exactly 26 chordwise ordinates at up to 32 span stations. When fewer than 26 camber coordinates are used to define the sections, the ordinate tables must be filled with enough zeros to complete the list of 26. The necessary section information is as follows:

NYC number of spanwise stations at which chordwise sections are used to define mean-camber surface (limit of 32)

TBYC table of y-values for chordwise camber-surface sections; beginning at $y = 0$; increasing order of y from root to tip

NPCTC number of chordwise stations used in definition of mean-camber surface (limit of 26)

TBPCTC table of chordwise stations, in percent chord, at which mean-camber-surface ordinates are defined; increasing order from leading edge to trailing edge

TZORDC table of mean-camber-surface z-ordinates that correspond to TBPCTC table; the full 26 values for root chord (including zeros for values in excess of NPCTC) are given first, followed by similar information for all spanwise stations in increasing order of y

TZSCALE multiplying factor applied to TZORDC table to change camber-surface ordinates

The TZORDC table may be multiplied by a scale factor TZSCALE. This factor may be useful if the original tabulated ordinates are nondimensionalized with respect to a single measurement (e.g., the wing root chord) or if it is necessary to evaluate the effect of change in camber-surface severity.

The following wing-section information is required for the calculation of attainable leading-edge thrust and leading-edge separation forces:

NYR number of spanwise stations at which information on airfoil sections is supplied (limit of 21)

TBYR table of y-values for airfoil section information; beginning at $y = 0$; increasing order of y-values from root to tip

TBTOC table of airfoil maximum thickness as a fraction of chord, t/c

TBETA table of section locations of maximum thickness as a fraction of chord, η

TBROC table of leading-edge radii as a fraction of chord, r/c

IVOROP vortex location option as follows:

- 0 full vortex force acts normal to wing reference plane at wing leading edge; does not contribute to axial force
- 1 vortex center given by empirical relationships derived from delta-wing experimental data (default)
- 2 vortex center given by method of Lan (ref. 14)

YAPEX spanwise location of vortex flow-field origin

For special planforms such as forward-swept wings or other wings with an apex away from the centerline, this input can help provide a better estimate of vortex-induced flow fields and forces. The default is YAPEX = 0.0.

The flight or test conditions are specified as follows:

XM	free-stream Mach number
RN	free-stream Reynolds number (based on $\bar{c}$) $\times 10^6$
NALPHA	number of angles of attack to be calculated (limit of 19)
TALPHA	table of angles of attack to be calculated, deg

The commonly accepted practice of performing subsonic calculations for a Mach number of 0.0 is not appropriate for this code. Realistic estimates of attainable thrust can be made only if both the Mach number and the Reynolds number correspond to actual conditions. In fact, the code stops and writes an error message when XM = 0.0 is input. A wide range of angle of attack is required in order to use the code in the design mode. This range must cover the angle of attack for $C_{L,\text{des}}$ of the original and all subsequent surfaces. An error message is written when the angle-of-attack range is too small.

To determine perturbation velocity distributions for the input camber surface, the flat-wing surface at 1° angle of attack, and the candidate camber surfaces used in the design mode, a maximum of 70 iterations are provided. If this number is reached without the convergence criteria being met, the results for the 70th iteration are printed with an appropriate message. The maximum number of iterations may be changed by the entry

ITRMAX	maximum number of perturbation velocity iterations (default 70)

The code convergence criteria are met when, for all wing surfaces, the average difference in perturbation velocity between successive iterations is less than half of one percent of the average velocity over the wing. If the average velocity for any of the wing surfaces is less than the average velocity for the flat surface at $\alpha = 1°$, the flat-wing surface value is used instead. In many instances, these criteria may be more stringent than necessary. If desired, the convergence criteria may be changed by the entry

CNVGTST	perturbation velocity convergence criteria (default 0.005)

The following entries control the solution for the optimized surface in the program design mode. For the analysis of a specified wing surface, omit these entries.

CLDES	design lift coefficient (if CLDES is not specified, the code defaults to CLDES = 0.0, which triggers an analysis-only solution)
CMDES	design pitching-moment coefficient (if CMDES is not specified, the code defaults to CMDES = 1000.0, which triggers an optimization solution without moment restraint)
IFLPDES	flap-design index (set this index to 1 if the code is to be used to define a spanwise distribution of leading- and trailing-edge flap deflections which approximate the designed camber surface; use this option only for a design in which leading- and trailing-edge modification surfaces are specified; code defaults to an index of 0, which bypasses the flap-design feature)

Use of the flap-design index, IFLPDES = 1, automates a graphical flap-fitting technique described in reference 2. The technique may be described with the aid of figure 37. When the flap-design feature is to be used, leading-edge and/or trailing-edge modification surfaces must be employed and NGCS must be set to zero. The chords of these surfaces should be input as the chords of the flaps themselves. The code then designs a restricted-area camber surface for leading- and trailing-edge areas whose chords are set to 1.5 times the flap chords. The original camber surface (a flat surface or a milder camber design such as for supersonic cruise) is then superimposed by rotation and translation on the new design. Differences in leading- and trailing-edge ordinates are then used to calculate flap deflections which approximate the designed camber surface. It must be emphasized that the flap deflections thus obtained are not necessarily optimum deflections, but only approximations. Iterative use of the companion evaluation code can help provide a better estimate of true optimum deflections.

In attempting to meet the convergence criteria for wing design, the code provides for a maximum of 20 iterations. If this number is reached without

the convergence criteria being met, the results for the 20th iteration are printed with a warning of the failure to meet the criteria. If desired, the maximum number of design iterations may be increased or decreased by the entry

ITRDESM maximum number of design iterations

The user has no control over the design convergence criteria.

The remainder of the design-mode entries are optional. These can be valuable for program user control of the design process but are covered by program defaults if the user chooses not to exercise the options.

The user may select the number of general camber surfaces to be used in the optimization process. These surfaces are described in reference 3.

NGCS number of general camber surfaces covering the entire wing (limit of 8, default 8)

In addition, the user may select exponents that control the shape of the various surfaces by use of the following entries:

EXPY1, EXPY2, EXPY3, EXPY4: exponents of y used in definition of general camber surfaces (defaults: EXPY1 = 0.0, EXPY2 = 1.0, EXPY3 = 2.0, and EXPY4 = 3.0)

EXPX1, EXPX2: exponents of x' used in definition of general camber surfaces (defaults: EXPX1 = 1.5, EXPX2 = 2.0)

To preserve the original surface between the leading-edge modification surfaces and the trailing-edge modification surfaces for a mission-adaptive design, NGSC may be set to zero. In this case, user options for both leading-edge and trailing-edge modifications must be employed.

The following entries control the region of the wing affected by the leading-edge modification surfaces. Because wing aerodynamic performance is critically dependent on the surface shape and pressure loading in the leading-edge region, these surfaces are essential to the optimization process. Program defaults provide candidate surfaces which generally provide a camber-surface design with good aerodynamic efficiency. The program user, however, may want to tailor a camber-surface solution more appropriate to the problem at hand and may want to search for solutions offering greater efficiency.

NLEC number of breakpoints used in definition of area of wing to be affected by leading-edge modification surfaces (limit of 21, default 2)

TBLECY table of y-values at breakpoints used in definition of area of wing to be affected by leading-edge modification surfaces; increasing order of y from wing root to wing tip (default 0.0, TBLEY (NLEY))

TBLEC table of c_L values corresponding to TBLECY table (default TBTEX(1) − TBLEX(1) for both entries); see note under ELAR entry regarding definition of leading-edge areas; it may be necessary to change ELAR or to place limits on non-zero c_L values

The following entries control the region of the wing affected by the trailing-edge modification surfaces and the streamwise section shape of these surfaces. The code defaults exclude these surfaces.

NTES number of trailing-edge modification surfaces (limit of 4)

NTEC number of breakpoints used in definition of area of wing affected by trailing-edge modification surfaces (limit of 21)

TBTECY table of y-values at breakpoints used in definition of area of wing affected by trailing-edge modification surfaces; increasing order of y from root to tip

TBTEC table of c_T values corresponding to the TBTECY table; see note under ELAR entry regarding definition of trailing-edge areas; it may be necessary to change ELAR or to place limits on nonzero c_T values

EXPXTE exponent of $(x' - (c - c_T))$ used in definition of trailing-edge modification surfaces (exponents of y are the same as those used in definition of general camber surfaces)

The following user option provides a degree of control over the smoothness of the camber-surface

solution. Code-determined weighting factors for the leading-edge modification surfaces are subject to numerical inaccuracies which may produce z-ordinates that do not have a smooth variation with respect to the y-dimension. See pages 19 to 23 of reference 3 for a discussion of the role of leading-edge modification surfaces in the design process and of the selection and use of leading-edge surface factors. By using this option, the user may substitute a smoothed set of leading-edge surface factors for the code-tabulated values. With the present program, two runs are required; the first finds the nonsmoothed values, and the second operates with the smoothed values.

IAFIX	smoothing-operation indicator; set IAFIX = 1 if smoothing is to be employed (default 0)
TAFIX	table of smoothed weighting factors replacing code-generated table in same order of increasing span stations

A modification to the computer code now permits the design of a wing lifting surface with flow fields of other airplane components, such as fuselage, nacelles, or canards, taken into account. This design may be accomplished by the addition of a table describing the interference pressure distribution on the wing surface generated by the other airplane components. This pressure field and the surface on which it acts, described by an existing input table, enter into the optimization process, but, unlike the other surfaces and loadings, remain unchanged throughout the design.

The interference pressure field must be supplied by the user. Normally, it is found by the use of some other aerodynamic analysis program capable of handling the desired airplane components. In most cases, two computer runs of this other program are required; one has all the airplane components represented, and one has only a mean-camber surface that matches as closely as possible the fixed input camber surface (surface 1) of the wing-design code. The wing-design code interference pressure field is then defined as the difference between these two loadings. By using the appropriate wing-design code options, the design surface may include only the wing outboard of the wing-fuselage juncture or may include the complete lifting surface, in which case a new fuselage camber surface is generated.

The following additional input data provide for a wing design with other airplane component-induced pressure fields taken into account. For normal program operation, simply omit these entries. If an interference pressure field is input, the distribution must be specified by exactly 26 chordwise positions at up to 32 span stations. When fewer than 26 chordwise positions are used to define the interference pressure field, the ΔC_p table must be filled with enough zeros to complete the list of 26.

ICP	other airplane component-induced pressure field indicator; set ICP = 1 if this option is used (default 0)
NYCP	number of spanwise stations at which chordwise sections are used to define interference pressure field (limit of 32)
TBYCP	table of y-values for interference pressure field chordwise sections; beginning at $y = 0$; increasing order of y from root to tip
NPCTCP	number of chordwise stations used in interference pressure field definition (limit of 26)
TBPCTCP	table of chordwise stations, in percent of chord, at which interference pressure field distributions are defined; increasing order from leading edge to trailing edge
TCP	table of interference pressure field coefficients corresponding to TBPCTCP table; full 26 values for root chord (including zeros for values in excess of NPCTCP) are given first, followed by similar information for spanwise stations in increasing order of y
YFUS	spanwise station of wing-fuselage juncture; this entry limits wing general camber surfaces to values of y greater than that specified; leading- and trailing-edge camber surfaces may be limited by existing options; use of these limitations yields a design lifting surface confined to wing outboard of fuselage (default 0.0)

The code is constructed so that successive runs may be made with a given code entry. To make additional runs, it is only necessary to add an identification record and namelist data that are to be changed from the previous run. An additional capability is provided by the entry NEWDES. When the code is run in the design mode and NEWDES is set to 1, a design camber surface is found, the input set

of camber-surface ordinates is replaced by camber-surface ordinates for the new design, and this new design is treated as an evaluation case. In the original code, the default for the entry NEWDES was 0, which provided for a design of the wing surface, but not for a subsequent evaluation. Now, however, because this feature has been found to be so useful, the default has been changed to NEWDES = 1. When the NEWDES option is used, successive runs may be employed to evaluate the new surface at off-design conditions.

The wing-design camber-surface ordinates are printed for a reference angle of attack defined by an entry of ALPZPR (reference angle of attack) or CLZPR (reference lift coefficient). The default is ALPZPR = 0.0. When CLZPR is specified, the code calculates the corresponding ALPZPR and uses it in the determination of ordinates.

If the code user desires, span load distribution data may be printed. If the index IPRSLD is set to 1, section aerodynamic characteristics, including the separate contributions of basic pressure loadings, attainable thrust, and vortex forces for each entry in the angle-of-attack table, are printed. These data are printed only for the evaluation mode or when the NEWDES option is used in the design mode.

The printed code results include the following:

1. An iteration-by-iteration history of the convergence parameters for the longitudinal perturbation velocity solution. In the design mode, data are given only for the most critical surface of up to 44 surfaces which may be used and for the flat surface at $\alpha = 1°$. For the supersonic solution in which iteration is not used, this printout is omitted.

2. A listing of the spanwise distribution of the leading-edge surface factor, the angle-of-attack range for full thrust, and the angle of attack for zero thrust. These data are given for the evaluation mode and for all iterations in the design mode from the first (input surface) to the last (optimized surface). For the evaluation mode, leading-edge surface factors are all zero.

3. A listing of overall wing aerodynamic characteristics as a function of angle of attack. These data are given for the evaluation mode and for all iterations in the design mode from the first (input surface) to the last (optimized surface).

4. A listing of the spanwise distribution of wing-section aerodynamic characteristics, including the separate contributions of basic pressure loadings, attainable thrust, and vortex forces. These data are given only for the evaluation mode (or when the NEWDES option is used in the design mode), and are given only if the print option IPRSLD is set to 1.

5. A listing of the wing-surface ordinates as a function of chord position for each of the span stations used in the program solution.

6. Listings of pressure distributions for the camber surface at $\alpha = 0°$ and for the flat surface at $\alpha = 1°$.

7. A listing of the leading-edge factors used in the design and a listing of suggested replacement values which may lead to improved performance when the NEWDES option is used. Generally, the need for this replacement arises only when it has not been possible to provide a sufficiently detailed numerical representation of the wing to give closely matched aerodynamic characteristics in the design and evaluation modes.

8. A listing of a suggested spanwise distribution of flap deflection angles to approximate the designed camber surface and to approach its aerodynamic performance when the IFLPDES option is used and flap chord information is supplied.

Appendix B

Description of Flap-System Analysis Code

The wing-analysis code described in reference 4 provides lifting-pressure distributions and wing forces and moments for a given camber surface. It provides only an analysis mode and is applicable only to subsonic speeds, but it provides for special handling of flap systems, including simplified flap-geometry input and computed results for various combinations of leading-edge and trailing-edge flap deflections in a single run. This code has recently been modified to provide for an improved accounting of the effect of hinge-line singularities in a manner similar to that for the leading-edge singularities which were handled in the original method.

The numerical method is based on linearized-theory, potential-flow solutions for a zero-thickness lifting surface represented by an array of horseshoe vortices. A solution by iteration rather than by a matrix inversion is used. The code also provides for an estimate of attainable leading-edge thrust and of the forces caused by separated leading-edge vortices.

The computer code

SUBAERF2—Wing and Flap-System Analysis Code

may be obtained for a fee from:

COSMIC
Computer Services Annex
University of Georgia
Athens, GA 30602
(404) 542-3265

Request the code by the designation LAR-13994. This code is written in FORTRAN V for use on the Control Data 6600 computer system and on the Control Data Cyber series.

The first record in the input is a code run identification that accepts up to 80 characters. The remainder of the input is placed in NAMELIST format under the name INPT1.

The wing-planform information is specified by a series of leading-edge and trailing-edge breakpoints for a right-hand wing panel. Up to 21 pairs of coordinates may be used to describe the leading edge and up to 21 pairs to describe the trailing edge. The planform input data in program terminology are as follows:

NLEY	number of leading-edge breakpoints (limit of 21)
TBLEY	table of leading-edge y-values; beginning at $y = 0$; increasing order of y from root to tip
TBLEX	table of leading-edge x-values that correspond to TBLEY table
NTEY	number of trailing-edge breakpoints (limit of 21)
TBTEY	table of trailing-edge y-values; beginning at $y = 0$; increasing order of y from root to tip
TBTEX	table of trailing-edge x-values that correspond to TBTEY table
XMAX	largest x-ordinate anywhere on planform
SREF	wing reference area for use in aerodynamic force and moment coefficients
CBAR	wing reference chord for use in aerodynamic moment coefficients
XMC	x-location of moment reference center
ELAR	element aspect ratio

For flat and mildly cambered wings, an element aspect ratio approximately one-half the full-wing aspect ratio is recommended. For small chord leading-edge or trailing-edge flaps it may be necessary to use a large element aspect ratio to place at least two elements within the chord. The number of elements in a given chord, c_L or c_T, may be approximated as

$$N = \frac{c_L}{b/2}(\text{JBYMAX})(\text{ELAR})$$

or

$$N = \frac{c_T}{b/2}(\text{JBYMAX})(\text{ELAR})$$

Because computational costs tend to increase as the fourth power of JBYMAX and the second power of ELAR, an increase in the element aspect ratio is the more efficient means of providing for improved definition.

The size of the wing in code dimensions is controlled by the entry:

JBYMAX	integer designating number of elements in spanwise direction (limit of 41)

The necessary scaling is done within the code by use of a scale factor 2(JBYMAX)/(SPAN(β)). The

number of complete wing elements N corresponding to a given JBYMAX may be approximated as

$$N = 4(\text{JBYMAX}^2)\left(\frac{\text{ELAR}}{\text{AR}}\right)$$

The code has been written to accommodate 2000 right-hand panel elements. Generally, the JBYMAX integer is much less than the limit of 41. The normal range is 8 to 20. Computational costs tend to increase as the square of the number of elements.

The wing mean-camber surface must be specified by exactly 26 chordwise ordinates at up to 21 span stations. When fewer than 26 camber coordinates are used to define the sections, the ordinate tables must be filled with enough zeros to complete the list of 26. The necessary section information is as follows:

NYC — number of spanwise stations at which chordwise sections are used to define mean-camber surface (limit of 21)

TBYC — table of y-values for chordwise camber-surface sections; beginning at $y = 0$; increasing order of y from root to tip

NPCTC — number of chordwise stations used in definition of mean-camber surface (limit of 26)

TBPCTC — table of chordwise stations, in percent chord, at which mean-camber-surface ordinates are defined; increasing order from leading edge to trailing edge

TZORDC — table of mean-camber-surface z-ordinates that correspond to TBPCTC table; the full 26 values for root chord (including zeros for values in excess of NPCTC) are given first, followed by similar information for all spanwise stations in increasing order of y

TZSCALE — multiplying factor applied to TZORDC table to change camber-surface ordinates

The TZORDC table may be multiplied by a scale factor TZSCALE. This may be useful if the original tabulated ordinates are nondimensionalized with respect to a single measurement (e.g., the wing root chord) or if it is necessary to evaluate the effect of change in camber-surface severity.

The following wing-section information is required for the calculation of attainable leading-edge thrust and leading-edge separation forces:

NYR — number of spanwise stations at which information on airfoil sections is supplied (limit of 21)

TBYR — table of y-values for airfoil section information; beginning at $y = 0$; increasing order of y-values from root to tip

TBTOC — table of airfoil maximum thickness as a fraction of chord, t/c

TBETA — table of section locations of maximum thickness as a fraction of chord, η

TBROC — table of leading-edge radii as a fraction of chord, r/c

IVOROP — vortex location option as follows:

- 0 full vortex force acts normal to wing reference plane at wing leading edge; does not contribute to axial force
- 1 vortex center given by empirical relationships derived from delta-wing experimental data (default)
- 2 vortex center given by method of Lan (ref. 14)

YAPEX — spanwise location of vortex flow-field origin

For special planforms such as forward-swept wings or other wings with an apex away from the centerline, this input can help provide a better estimate of vortex-induced flow fields and forces. The default is YAPEX = 0.0.

The flight or test conditions are specified as follows:

XM — free-stream Mach number

RN — free-stream Reynolds number (based on $\bar{c}$) $\times 10^6$

NALPHA — number of angles of attack to be calculated (limit of 19)

TALPHA — table of angles of attack to be calculated, deg

NADRN number of additional Reynolds numbers

TADRN table of additional Reynolds numbers (based on $\bar{c}$) $\times 10^6$ (limit of 3)

The commonly accepted practice of performing subsonic calculations for a Mach number of 0.0 is not appropriate for this code. Realistic estimates of attainable thrust can be made only if both the Mach number and the Reynolds number correspond to actual conditions. In fact, the code stops and writes an error message when XM = 0.0 is input.

The following information makes possible the calculation of loadings and forces on deflected leading-edge and trailing-edge flaps. If flap data are not desired, simply omit these entries.

NLEFY number of breakpoints in leading-edge flap chord distribution (limit of 20)

TBLEFY table of y-values at breakpoints in leading-edge flap chord distribution; beginning at $y = 0$; increasing order of y from root to tip

TBLEFC table of leading-edge flap chords corresponding to TBLEFY table

TBLEFD table of flap deflections in degrees (positive for leading edge down) corresponding to TBLEFY table

NADLEFD number of leading-edge flap deflection multipliers other than 1.0 (limit of 4)

TXMLEFD table of leading-edge flap deflection multipliers (applied as a multiplier of tangents of input flap deflections)

LEFTYPE type of leading-edge deflection

1 linear (default)

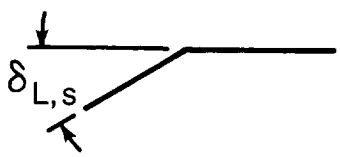

2 parabolic

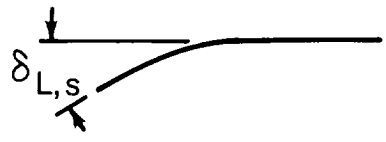

NTEFY number of breakpoints in trailing-edge flap chord distribution (limit of 20)

TBTEFY table of y-values at breakpoints in trailing-edge flap chord distribution; increasing order of y from root to tip

TBTEFC table of trailing-edge flap chords that correspond to TBTEFY table

TBTEFD table of flap deflections in degrees (positive for trailing edge down) that correspond to TBTEFY table

NADTEFD number of trailing-edge flap deflection multipliers other than 1.0 (limit of 4)

TXMTEFD table of trailing-edge flap deflection multipliers (applied as a multiplier to tangents of input flap deflections)

CLDES additional lift coefficient for which flap-system aerodynamic performance is to be specified; code aerodynamic characteristics are given only for angles of attack in input TALPHA table unless CLDES is specified

Spanwise tables must begin with $y = 0$ and extend to $y = b/2$ (with chords of 0 where there are no flaps). At spanwise positions where there are discontinuities in either flap chord or deflection, it is necessary to make closely spaced tabular entries inboard and outboard of the discontinuity.

The program requires flap-deflection angles measured in the x-z plane. Flap-deflection angles measured normal to the flap hinge line may be converted to code input angles by

$$\delta_{L,s} = \tan^{-1}(\cos \Lambda_{h,L} \ \tan \delta_{L,n})$$

$$\delta_{T,s} = \tan^{-1}(\cos \Lambda_{h,T} \ \tan \delta_{T,n})$$

The code provides solutions for wing surfaces composed of all possible combinations of leading-edge and trailing-edge flap settings provided by the original deflections (TBLEFD and TBTEFD) and by the flap-deflection multipliers (TXMLEFD and TXMTEFD). Up to 25 pairs of leading-edge and trailing-edge flap-deflection schedules may thus be treated simultaneously. Solutions obtained by using the multipliers (values other than 0 or 1) are determined by a perturbation process; thus, they are not

as accurate as solutions for the original or nominal input deflections. When increased accuracy is required, or when the change in performance with the change in deflection must be evaluated—as in the construction of suction-parameter contour maps—individual solutions without recourse to multipliers may be required. There is, however, a strategy that may be used to obtain a set of data nearly as accurate as the code is capable of providing with the use of only two code runs. The procedure is illustrated in figure 38. First, a code run is made for leading- and trailing-edge flap deflections near the middle of the range of interest with additional flap deflection multipliers of 0, 0.5, 1.5, and 2.0. A second run is then made for input deflections whose tangents are twice those of the original input deflections. For this run, the additional flap deflection multipliers are 0, 0.25, 0.50, and 0.75. Code data from these two runs may then be proportioned according to the factors shown on the two grids in figure 38. For example, for leading- and trailing-edge deflection angles, both of which have tangents that are 1.5 times the original deflection angles, the corrected suction parameter would be the sum of 0.72 times the first set of results for factors of 1.5 and 1.5 and 0.28 times the second set of results for factors of 0.75 and 0.75. These factors have been determined empirically from a fairly extensive exercise in graphical analysis. A single run provides four valid solutions (for factors of 0,0, 0,1, 1,0, and 1,1).

The revised code provides for an improved accounting of hinge-line singularities in determination of wing forces and moments. The technique used is illustrated in figure 39. In the original code (ref. 15), only wings with smooth camber surfaces were treated, and there was no provision for flaps. The solution for a wing at an angle of attack was composed of two parts, a flat-surface component and a camber-surface component. To provide an appropriate integration technique for the camber-surface component, the pressure distribution was divided into two parts—one with a leading-edge singularity and one with no singularity and a smooth variation from leading edge to trailing edge. As described in reference 15, a curve-fit and integration formula appropriate to each contribution was employed. The process works quite well for a smooth camber surface, even if the surface is inclined, to produce substantial leading-edge loading. When the program was expanded to cover leading- and trailing-edge flaps, two new surfaces were added, but the fairing and integration techniques were not changed. The flap-surface loadings were simply added to the existing camber-surface component. Thus, the fairing for a case with leading- and trailing-edge flaps and a $z = 0$ camber surface would appear as shown at the top of figure 39. As can be seen, the code fairing is not well suited to the character of the flap loadings. In spite of this handicap, acceptable results were obtained when a sufficient number of chordwise elements were used. However, there is a tendency for part of the singularity loading to be lost in the integration process.

To provide a partial remedy, the adjustment procedure illustrated in the middle portion of figure 39 is now used. The adjustment is made only to the leading- and trailing-edge flap-surface contributions to the camber-surface pressure distributions. A curve of the form

$$\Delta C_p = k_1 \sqrt{\frac{c}{x'} - 1} + \frac{k_2}{\sqrt{|x_h - x'|}}$$

is fitted to data for a given element and for the preceding and following elements. The integrated area under this curve is compared with the integrated area under a linear fairing, and the difference is represented as a ΔC_p adjustment extending over the given element. When this adjustment is made for all the chordwise elements, a revised distribution, as shown at the bottom of figure 39, is obtained. The original code integration procedures, when applied to the revised distribution, account for the lost singularity areas and provide for an improved integration of forces and moments.

To determine perturbation velocity distributions for the cambered wing, the flat wing, and the two flap surfaces, the code provides for a maximum of 70 iterations. If this number is reached without the convergence criteria being met, the results for the 70th iteration are printed with a warning of the failure to meet the criteria. The maximum number of iterations may be increased or decreased by the entry

ITRMAX	maximum number of perturbation velocity iterations (default 70)

The code convergence criteria are met when, for all four wing surfaces and for two successive iterations, the average difference in perturbation velocity between iterations is less than half of one percent of the average velocity over the wing. If the average velocity for the camber surface or either of the flap surfaces is less than the average velocity for the flat surface at $\alpha = 1°$, the flat-wing surface value is used instead. In many instances, these criteria may be more stringent than necessary. If desired, the convergence criteria may be changed by the entry

CNVGTST	perturbation velocity convergence criteria (default 0.005)

The printed code results include the following:

1. An iteration-by-iteration history of the convergence parameters.

2. A listing of theoretical pressure distributions for the camber surface at $\alpha = 0°$ and for the flat surface at $\alpha = 1°$. For each of the program spanwise stations (controlled by JBYMAX), interpolated or extrapolated pressure coefficients are given for a set of chordwise stations.

3. A listing of the spanwise distribution of section normal, axial, and pitching-moment coefficients for the cambered wing at $\alpha = 0°$ and for the flat wing at $\alpha = 1°$. The interference axial-force coefficient caused by the flat-surface loading acting on the camber surface and the theoretical thrust parameters $C_{t,F}$ and α_{zt} are also printed.

4. A listing of wing overall theoretical aerodynamic coefficients C_N, C_A, C_m, C_L, and C_D with no thrust and with full theoretical thrust as a function of angle of attack.

5. A listing of the spanwise distribution of the flat-wing angle-of-attack range for full theoretical leading-edge thrust.

6. A listing of wing overall estimated aerodynamic coefficients, including C_N, C_A, and C_m for the basic pressure loading, ΔC_N and ΔC_A for attainable thrust and vortex-force increments, and C_N, C_A, C_m, C_L, C_D, and S_s for the total loading.

Additional printed output data may be selected by using the following print options:

IPRCPD = 1	theoretical pressure distributions for each selected angle of attack
IPRSLDT = 1	theoretical span load distribution of C_N, C_A, C_m, C_L, and C_D with no thrust and with full theoretical thrust for each selected angle of attack
IPRSLDA = 1	estimated span load distribution of C_N, C_A, C_m, C_L, and C_D with attainable thrust and vortex-force effects for each selected angle of attack
IPRALL = 1	the preceding print control options apply only to the first set of flap deflections. Select this option if the three preceding options are to apply to all flap deflection combinations. Selection of this option could result in a very large volume of printed output

Appendix C

Notes on Computer-Code Application

Table I presents sample input data for the flap-system analysis code for each of the test configurations studied. The fuselage and the wing are represented in the planform submitted to the code. The camber ordinates, TZORDC, were determined from the mean ordinates of both the wing and fuselage.

As with any numerical solution of mathematical theory, the problem is to find a sufficiently detailed discretization which provides accurate answers without incurring prohibitive costs. To sufficiently represent the flap geometry of the study configurations, the number of semispan elements, JBYMAX, and the element aspect ratio, ELAR, were chosen so that, for the most part, two or more elements would be contained in any given flap chord. This resulted in element aspect ratios ranging from 2.0 to 4.0 and from 8 to 10 semispan elements. Generally, the whole-wing-body planform was represented by 500 to 600 elements.

To obtain estimates of attainable leading-edge thrust Reynolds number, RN $\times$ 10^6, and Mach number, XM, are both specified and the wing-section geometric characteristics of t/c, r/c, and η are entered in the appropriate tables. For evaluation of the estimated forces caused by leading-edge vortex separation, the vortex location option IVOROP = 1 was chosen. It has been found to be more accurate for the conventional swept wings of this study than the other two options.

The wing evaluation program has a feature which permits simultaneous solutions for a number of combinations of leading- and trailing-edge flap deflections by use of a perturbation process. This time-saving code option is sufficiently accurate for small deflection angles (streamwise angles of about 15° or less), but because of the large deflection angles often considered in this investigation and the need for a high degree of accuracy, this feature was not used to its full capacity. When required, individual computer runs were performed for each pair of leading- and trailing-edge deflections; however, it should be noted that a single computer run can be made to yield as accurate a prediction as the method is capable of for a set of four deflection-angle combinations which include zero deflections of leading-edge and trailing-edge flaps. The code input data of table I provide for flap deflection multipliers, TXMLEFD and TXMTEFD, of 0.0, which produces results for a leading-edge flap deflection with no trailing-edge flap deflection, a trailing-edge flap deflection with no leading-edge flap deflection, no leading-edge flap deflection with no trailing-edge flap deflection, and the leading-edge and trailing-edge flap deflections in combination. For the construction of performance maps, multiple deflection solutions using a strategy discussed in appendix B were employed.

Also, the input data of table I provide for a second computer run in which only the leading-edge deflection and/or the trailing-edge deflection are changed. It is unnecessary to repeat the other data.

Table II presents sample input data for the wing-design code for the two configurations of this study that were subjected to a design process. For each of these configurations, both a whole-wing area design and a restricted-area wing design are illustrated. The NEWDES = 1 option was used to provide an analysis of the designed surface. This is now the code default option. As for the flap-system analysis inputs, the IVOROP = 1 option was used. As explained in appendix A, the vortex-force estimates reduce the severity of the designed camber surface, because of the vortex-lift contribution, but play no other part in the design.

For the whole-wing design cases, the leading-edge modification surfaces were defined by the wing planform itself, rather than by the more conservative code default option, because of a small increase in performance. In reference 3 it is suggested that the user may wish to exercise control over the design by selection of candidate surfaces and may want to search for solutions offering greater efficiency.

For the restricted-area design cases, the IFLPDES = 1 option was used to provide an automated selection of flap deflection schedules as described in appendix A. In these examples, the chords of the leading-edge and trailing-edge modification surfaces, TBLEC and TBTEC, were input as the actual flap chords. The code automatically selects a larger design area to be used in the definition of flap surfaces. Also, an input camber surface, TZORDC, is supplied rather than deferring to the code default, which is a completely flat surface. This surface represents a supersonic cruise design. The code provides a design that preserves the input surface, except in the specified leading- and trailing-edge design areas. See appendix A for a more detailed description of the design of mission-adaptive surfaces and of the selection of flap deflections.

References

1. Carlson, Harry W.; and Darden, Christine M.: *Applicability of Linearized-Theory Attached-Flow Methods to Design and Analysis of Flap Systems at Low Speeds for Thin Swept Wings With Sharp Leading Edges.* NASA TP-2653, 1987.
2. Carlson, Harry W.: *The Design and Analysis of Simple Low Speed Flap Systems With the Aid of Linearized Theory Computer Programs.* NASA CR-3913, 1985.
3. Carlson, Harry W.; and Walkley, Kenneth B.: *Numerical Methods and a Computer Program for Subsonic and Supersonic Aerodynamic Design and Analysis of Wings With Attainable Thrust Considerations.* NASA CR-3808, 1984.
4. Carlson, Harry W.; and Walkley, Kenneth B.: *An Aerodynamic Analysis Computer Program and Design Notes for Low Speed Wing Flap Systems.* NASA CR-3675, 1983.
5. Carlson, Harry W.; Mack, Robert J.; and Barger, Raymond L.: *Estimation of Attainable Leading-Edge Thrust for Wings at Subsonic and Supersonic Speeds.* NASA TP-1500, 1979.
6. Polhamus, Edward C.: Predictions of Vortex-Lift Characteristics by a Leading-Edge Suction Analogy. *J. Aircr.*, vol. 8, no. 4, Apr. 1971, pp. 193–199.
7. Carlson, Harry W.; Shrout, Barrett L.; and Darden, Christine M.: Wing Design With Attainable Leading-Edge Thrust Considerations. *J. Aircr.*, vol. 22, no. 3, Mar. 1985, pp. 244–248.
8. Campbell, Bryan A.; Hom, Kam W.; and Huffman, Jarrett K.: *Investigation of Subsonic Maneuver Performance of a Supersonic Fighter Cranked Wing.* NASA TP-2687, 1987.
9. Frink, Neal T.: *Experimental Study of an Aspect-Ratio-1.955 Wing-Body Configuration Employing an Analytically Designed Vortex Flap at Mach 0.4.* NASA TP-2686, 1987.
10. Nicholas, W. U.; and Naville, G. L.: *An Evaluation of the Relative Merit of Wing-Canard, Wing-Tail, and Tailless Arrangements for Advanced Fighter Applications.* FZA-547, Fort Worth Div., General Dynamics, Apr. 19, 1984.
11. Coe, Paul L., Jr.; Kjelgaard, Scott O.; and Gentry, Garl L., Jr.: *Low-Speed Aerodynamic Characteristics of a Highly Swept, Untwisted, Uncambered Arrow Wing.* NASA TP-2176, 1983.
12. Scott, Samuel J.; Nicks, Oran W.; and Imbrie, P. K.: *Effects of Leading-Edge Devices on the Low-Speed Aerodynamic Characteristics of a Highly-Swept Arrow-Wing.* NASA CR-172531, 1985.
13. Riebe, Gregory D.; and Fox, Charles H., Jr.: *Subsonic Maneuver Capability of a Supersonic Cruise Fighter Wing Concept.* NASA TP-2642, 1987.
14. Lan, C. Edward; and Chang, Jen-Fu: *Calculation of Vortex Lift Effect for Cambered Wings by the Suction Analogy.* NASA CR-3449, 1981.
15. Carlson, Harry W.; and Walkley, Kenneth B.: *A Computer Program for Wing Subsonic Aerodynamic Performance Estimates Including Attainable Thrust and Vortex Lift Effects.* NASA CR-3515, 1982.

Table I. Sample Input Data for SUBAERF2 Code

(a) Cranked-wing leading-edge fighter

```
SUPERSONIC CRUISE FIGHTER - CAMPBELL,TP 2687 - DLN=15,DTN=10
$INPT1 XM=0.50,RN=2.9,JBYMAX=8,ELAR=4.0,IVOROP=1,IPRSLDA=1,
SREF=163.5,CBAR=12.4,XMC=20.64,XMAX=33.50,
NLEY=8,TBLEY=0.000,0.470,0.870,1.160,1.190,1.200,5.510,9.550,
       TBLEX=0.000,2.000,4.000,6.000,6.540,12.88,26.37,27.84,
NTEY=4,TBTEY=0.000,1.200,1.210,9.550,
       TBTEX=33.50,33.50,31.70,29.79,
NYC=2,TBYC=0.00,9.55,NPCTC=2,TBPCTC=0.00,100.0,TZORDC=52*0.0,
NYR=3,TBYR=0.00,1.20,9.55,
     TBTOC=.000,.040,.040,
     TBROC=.000,.001,.001,
     TBETA=.500,.500,.500,
NLEFY=5,TBLEFY=0.000,1.200,4.630,5.510,9.550,
        TBLEFC=0.000,0.000,3.310,1.080,.4870,
        TBLEFD=0.000,4.252,4.252,14.67,14.67,
NTEFY=4,TBTEFY=0.000,1.540,1.550,9.550,
        TBTEFC=0.000,0.000,1.658,.4870,
        TBTEFD=0.000,0.000,9.972,9.972,
NADLEFD=1,TXMLEFD=0.000,
NADTEFD=1,TXMTEFD=0.000,
NALPHA=14,TALPHA=-6.,-4.,-2.,0.0,2.,4.,6.,8.,10.,12.,14.,16.,
18.,20.,    $
SUPERSONIC CRUISE FIGHTER - CAMPBELL,TP 2687 - DLN=15,DTN=20
$INPT1 TBTEFD=0.000,0.000,19.94,19.94,    $
```

(b) Vortex-flap wing-body configuration

```
VORTEX FLAP MODEL - FRINK, TP 2686 - DLN=45,DTN=20
$INPT1 XM=0.40,RN=5.4,JBYMAX=8,ELAR=2.5,IVOROP=1,IPRSLDA=1,
SREF=550.32,CBAR=25.96,XMC=31.36,XMAX=47.58
NLEY=7,TBLEY=0.000,1.500,4.440,6.620,8.650,10.90,13.62,
       TBLEX=0.000,14.36,20.35,26.10,31.85,38.84,47.58,
NTEY=2,TBTEY=0.000,13.62,
       TBTEX=47.58,47.58,
NYC=2,TBYC=0.0,13.62,NPCTC=2,TBPCTC=0.0,100.0,TZORDC=52*0.0,
NYR=6,TBYR=0.0000,1.5000,4.4100,6.6200,8.6500,13.620,
     TBTOC=0.0000,.01880,.02290,.02910,.03970,.03970,
     TBROC=.00000,.00006,.00007,.00009,.00013,.00013,
     TBETA=0.5000,0.1800,0.4000,0.5800,0.8700,0.5000,
NLEFY=7,TBLEFY=0.000,1.500,4.440,6.620,8.650,10.90,13.62,
        TBLEFC=0.000,0.000,4.710,6.570,7.900,8.740,0.000,
        TBLEFD=0.000,15.41,15.41,15.41,15.41,15.41,15.41,
NTEFY=6,TBTEFY=0.000,1.490,1.500,8.770,8.780,13.62,
        TBTEFC=0.000,0.000,2.000,2.000,0.000,0.000,
        TBTEFD=0.000,0.000,20.00,20.00,0.000,0.000,
NADLEFD=1,TXMLEFD=0.0,
NADTEFD=1,TXMTEFD=0.0,
NALPHA=14,TALPHA=-6.,-4.,-2.,0.,2.,4.,6.,8.,10.,12.,14.,16.,
18.,20.,    $
VORTEX FLAP MODEL - FRINK, TP 2686 - DLN=45,DTN=10
$INPT1 TBTEFD=0.000,0.000,10.00,10.00,0.000,0.000,    $
```

Table I. Continued

(c) 44°-swept trapezoidal-wing fighter

```
44 DEG TRAPEZOIDAL WING FIGHTER - NICHOLAS, GD FZA 547 - DLN=20,DTN=20
$INPT1 XM=.40,RN=1.91,JBYMAX=10,ELAR=2.5,IVOROP=1,IPRSLDA=1,
SREF=160.0,CBAR=9.17,XMC=23.39,XMAX=38.03,
NLEY=4,TBLEY=0.000,1.400,1.500,10.00,
       TBLEX=0.000,4.250,18.78,27.00,
NTEY=4,TBTEY=0.000,1.400,1.500,10.00,
       TBTEX=38.03,38.03,30.51,29.66,
NYC=2,TBYC=0.0,10.0,NPCTC=2,TBPCTC=0.0,100.0,TZORDC=52*0.0,
NYR=3, TBYR=0.000,1.500,10.00,
      TBTOC=.0000,.0600,.0400,
      TBROC=.0000,.0025,.0011,
      TBETA=.4000,.4000,.4000,
NLEFY=4,TBLEFY=0.00,1.40,1.50,10.0,
        TBLEFC=0.00,0.00,1.80,1.80,
        TBLEFD=0.00,0.00,14.7,14.7,
NTEFY=6,TBTEFY=0.00,1.40,1.50,7.47,7.57,10.0,
        TBTEFC=0.00,0.00,2.32,1.04,0.00,0.00,
        TBTEFD=0.00,0.00,20.0,20.0,0.00,0.00,
NADLEFD=1,TXMLEFD=0.00,
NADTEFD=1,TXMTEFD=0.00,
NALPHA=15,TALPHA=-4.0,-2.0,0.0,2.0,4.0,6.0,8.0,10.0,12.0,14.0,16.0,
18.0,20.0,22.0,24.0,    $
44 DEG TRAPEZOIDAL WING FIGHTER - NICHOLAS, GD FZA 547 - DLN=12,DTN=12
$INPT1 TBLEFD=0.00,0.00,8.69,8.69,8.69,
       TBTEFD=0.00,0.00,12.0,12.0,0.00,0.00,    $
```

(d) 60°-swept delta-wing fighter

```
 60 DEG DELTA GENERIC FIGHTER - NICHOLAS, GD FZA 547 - DLN=20,DTN=20
$INPT1 XM=.40,RN=2.52,JBYMAX=10,ELAR=2.5,IVOROP=1,IPRSLDA=1,
SREF=181.94,CBAR=12.13,XMC=23.74,XMAX=41.63,
NLEY=4,TBLEY=0.000,1.400,1.500,10.00,
       TBLEX=0.000,4.250,17.53,32.25,
NTEY=4,TBTEY=0.000,1.400,1.500,10.00,
       TBTEX=41.63,41.63,33.00,32.25,
NYC=2,TBYC=0.0,10.0,NPCTC=2,TBPCTC=0.0,100.0,TZORDC=52*0.0,
NYR=4, TBYR=0.000,1.500,9.000,10.00,
      TBTOC=.0000,.0600,.0423,.0400,
      TBROC=.0000,.0025,.0013,.0032,
      TBETA=.4000,.4000,.4000,.4000,
NLEFY=5,TBLEFY=0.00,1.40,1.50,8.50,10.0,
        TBLEFC=0.00,0.00,1.37,2.62,0.00,
        TBLEFD=0.00,0.00,9.60,9.60,9.60,
NTEFY=6,TBTEFY=0.00,1.40,1.50,7.00,7.10,10.0,
        TBTEFC=0.00,0.00,1.69,1.21,0.00,0.00,
        TBTEFD=0.00,0.00,20.0,20.0,0.00,0.00,
NADLEFD=1,TXMLEFD=0.00,
NADTEFD=1,TXMTEFD=0.00,
NALPHA=15,TALPHA=-4.0,-2.0,0.0,2.0,4.0,6.0,8.0,10.0,12.0,14.0,16.0,
18.0,20.0,22.0,24.0,    $
60 DEG DELTA GENERIC FIGHTER - NICHOLAS, GD FZA 547 - DLN=10,DTN=10
$INPT1 TBLEFD=0.00,0.00,4.68,4.68,4.68,
       TBTEFD=0.00,0.00,10.0,10.0,0.00,0.00,    $
```

Table I. Continued

(e) Generic arrow-wing supersonic transport

```
 SUPERSONIC TRANSPORT  AST 200 - COE, TP 2176 - DLN=30,DTN=10
 $INPT1 XM=.25,RN=4.10,JBYMAX=10,ELAR=2.0,IVOROP=1,IPRSLDA=1,
 SREF=1291.9,CBAR=34.64,XMC=69.1,XMAX=97.94,
 NLEY=5,TBLEY=0.000,1.950,11.74,18.00,24.80,
        TBLEX=0.000,27.66,61.79,79.81,91.59,
 NTEY=4,TBTEY=0.000,8.280,13.61,24.80,
        TBTEX=86.77,86.59,88.05,97.94,
 NYC=2,TBYC=0.0,24.80,NPCTC=2,TBPCTC=0.0,100.0,TZORDC=52*0.0,
 NYR=9,
 TBYR =0.0000,1.9500,4.9600,8.2800,12.340,15.000,18.000,18.000,24.800,
 TBTOC=0.0000,.03030,.02770,.02570,.02570,.02770,.03000,.02000,.02000,
 TBROC=0.0000,.00064,.00054,.00046,.00046,.00054,.00063,.00030,.00030,
 TBETA=.40000,.40000,.40000,.40000,.40000,.40000,.40000,.50000,.50000,
 NLEFY=7,TBLEFY=0.00,1.85,1.95,11.7,16.7,18.0,24.8,
         TBLEFC=0.00,0.00,10.6,4.40,4.29,2.62,1.92,
         TBLEFD=0.00,0.00,10.8,10.8,10.8,16.1,16.1,
 NTEFY=10,TBTEFY=0.00,2.30,2.40,6.23,6.33,9.37,9.47,12.0,12.1,24.8,
          TBTEFC=0.00,0.00,4.75,4.65,0.00,0.00,4.95,5.60,0.00,0.00,
          TBTEFD=0.00,0.00,10.0,10.0,0.00,0.00,10.0,10.0,0.00,0.00,
 NADLEFD=4,TXMLEFD=0.00,
 NADTEFD=1,TXMTEFD=0.00,
 NALPHA=16,TALPHA=-8.0,-6.0,-4.0,-2.0,0.0,2.0,4.0,6.0,8.0,10.0,12.0,14.0,
 16.0,18.0,20.0,22.0,    $
 SUPERSONIC TRANSPORT  AST 200 - COE, TP 2176 - DLN=40,DTN=10
 $INPT1 TBLEFD=0.00,0.00,15.51,15.51,15.51,22.76,22.76,    $
```

(f) Advanced arrow-wing supersonic transport

```
SUPERSONIC TRANSPORT  AST 210 - SCOTT, CR 172531 - DLN=30,DTN=20
$INPT1 XM=.21, RN=4.1,JBYMAX=10,ELAR=2.0,IVOROP=1,IPRSLDA=1,
SREF=1338.2,CBAR=35.2,XMC=69.1,XMAX=97.94,
NLEY=4,TBLEY=0.000,1.950,18.00,24.80,
       TBLEX=0.000,27.24,79.81,91.59,
NTEY=4,TBTEY=0.000,8.280,13.61,24.80,
       TBTEX=86.77,86.59,88.05,97.94,
NYC=10,TBYC=0.00,2.40,3.72,4.96,8.28,12.34,15.00,18.00,22.32,24.80,
NPCTC=10,
TBPCTC=0.000,2.500,5.000,10.00,20.00,30.00,40.00,60.00,80.00,100.0,
TZORDC=0.000,0.000,0.000,0.000,0.000,-.300,-1.42,-4.07,-6.18,-7.43,16*0.0,
       0.000,-.023,-.082,-.296,-.893,-1.56,-2.22,-3.39,-4.38,-5.17,16*0.0,
       0.000,.0020,-.027,-.175,-.605,-1.09,-1.58,-2.49,-3.32,-4.05,16*0.0,
       0.000,.0230,.0140,-.069,-.362,-.707,-1.06,-1.77,-2.46,-3.14,16*0.0,
       0.000,.0430,.0770,.0900,.0350,-.071,-.210,-.563,-1.01,-1.51,16*0.0,
       0.000,.0340,.0670,.1170,.1490,.1290,.0790,-.091,-.336,-.626,16*0.0,
       0.000,.0250,.0500,.0940,.1230,.1170,.0880,-.023,-.179,-.359,16*0.0,
       0.000,.0050,.0090,.0190,.0210,.0110,-.010,-.065,-.129,-.188,16*0.0,
       0.000,-.009,-.018,-.037,-.062,-.079,-.094,-.114,-.118,-.110,16*0.0,
       0.000,-.005,-.010,-.018,-.037,-.055,-.066,-.078,-.079,-.078,16*0.0,
NYR=9,
TBYR =0.0000,1.9500,4.9600,8.2800,12.340,15.000,18.000,18.000,24.800,
TBTOC=0.0000,.03030,.02770,.02570,.02570,.02770,.03000,.02000,.02000,
TBROC=0.0000,.00064,.00054,.00046,.00046,.00054,.00063,.00030,.00030,
TBETA=.40000,.40000,.40000,.40000,.40000,.40000,.40000,.50000,.50000,
NLEFY=6,TBLEFY=0.00,1.85,1.95,15.5,18.0,24.8,
        TBLEFC=0.00,0.00,6.36,9.28,4.48,1.92,
        TBLEFD=0.00,0.00,9.03,9.03,18.9,18.9,
NTEFY=10,TBTEFY=0.00,2.30,2.40,7.07,7.17,9.44,9.54,12.3,12.4,24.8,
         TBTEFC=0.00,0.00,3.75,3.60,0.00,0.00,3.92,4.70,0.00,0.00,
         TBTEFD=0.00,0.00,20.0,20.0,0.00,0.00,20.0,20.0,0.00,0.00,
NADLEFD=1,TXMLEFD=0.00,
NADTEFD=1,TXMTEFD=0.00,
NALPHA=16,TALPHA=-8.0,-6.0,-4.0,-2.0,0.0,2.0,4.0,6.0,8.0,10.0,12.0,14.0,
                  16.0,18.0,20.0,22.0,    $
SUPERSONIC TRANSPORT  AST 210 - SCOTT, CR 172531 - DLN=40,DTN=20
$INPT1 TBLEFD=0.00,0.00,13.0,13.0,26.42,26.42,    $
```

Table I. Concluded

(g) 60°-swept trapezoidal-wing fighter

```
SUPERSONIC CRUISE FIGHTER - RIEBE, TP 2642 - FLAP A  DLS=15-20,DTS=15-12
$INPT1 XM=0.50,RN=2.9,JBYMAX=8,ELAR=4.00,IVOROP=1,IPRSLDA=1,
SREF=149.7,CBAR=9.78,XMC=20.64,XMAX=33.48,
CLDES=.73,
NLEY=7,TBLEY=0.000,0.470,.8700,1.160,1.190,1.200,9.200,
       TBLEX=0.000,2.000,4.000,6.000,6.540,14.44,28.29,
NTEY=5,TBTEY=0.000,1.190,1.200,5.200,9.200,
       TBTEX=33.48,33.48,27.56,28.16,30.29,
NYC=10,TBYC=0.00,1.20,2.20,3.20,4.20,5.20,6.20,7.20,8.20,9.20,
NPCTC=10,
TBPCTC=0.000,2.481,4.975,9.965,19.95,29.95,39.95,59.96,79.98,100.0,
TZORDC=0.000,0.000,0.000,0.000,0.000,0.000,0.000,0.000,0.000,0.000,16*0.0,
       0.000,-.012,-.023,-.039,-.061,-.081,-.100,-.116,-.080,-.019,16*0.0,
       0.000,.0030,.0020,.0010,-.003,-.007,-.007,.0020,.0230,.0460,16*0.0,
       0.000,.0090,.0150,.0260,.0410,.0430,.0460,.0630,.0850,.1090,16*0.0,
       0.000,.0090,.0160,.0290,.0490,.0560,.0610,.0830,.1060,.1310,16*0.0,
       0.000,.0060,.0120,.0230,.0390,.0520,.0650,.0890,.1120,.1370,16*0.0,
       0.000,.0060,.0100,.0200,.0350,.0490,.0610,.0850,.1070,.1320,16*0.0,
       0.000,.0050,.0090,.0170,.0300,.0420,.0530,.0740,.0950,.1150,16*0.0,
       0.000,.0030,.0060,.0120,.0240,.0330,.0430,.0600,.0770,.0950,16*0.0,
       0.000,.0010,.0030,.0060,.0140,.0240,.0330,.0520,.0720,.0910,16*0.0,
NYR=3, TBYR=0.000,1.200,9.200,
      TBTOC=0.000,0.040,0.040,
      TBROC=.0000,.0012,.0012,
      TBETA=0.400,0.400,0.400,
NLEFY=6,TBLEFY=0.000,1.190,1.200,5.190,5.200,9.200,
        TBLEFC=0.000,0.000,2.320,1.360,1.360,0.600,
        TBLEFD=0.000,0.000,15.00,15.00,20.00,20.00,
NTEFY=6,TBTEFY=0.000,1.190,1.200,5.190,5.200,9.200,
        TBTEFC=0.000,0.000,1.360,1.360,1.360,0.400,
        TBTEFD=0.000,0.000,15.00,15.00,12.00,12.00,
NADLEFD=1,TXMLEFD=0.00,
NADTEFD=1,TXMTEFD=0.00,
NALPHA=14,TALPHA=-6.,-4.,-2.,0.,2.,4.,6.,8.,10.,12.,14.,16.,
18.,20.,    $
```

Table II. Sample Input Data for WINGDES2 Code

(a) Advanced arrow-wing, supersonic-transport; whole-wing design

```
SUPERSONIC TRANSPORT  AST 210 - SCOTT, CR 172531 - WHOLE WING DESIGN
$INPT1 XM=.21, RN=4.1,JBYMAX=8,ELAR=2.0,IVOROP=1,IPRSLD=1,
CLDES=.60,
SREF=1338.2,CBAR=35.2,XMC=69.1,XMAX=97.94,
NLEY=4,TBLEY=0.000,1.950,18.00,24.80,
       TBLEX=0.000,27.24,79.81,91.59,
NTEY=4,TBTEY=0.000,8.280,13.61,24.80,
       TBTEX=86.77,86.59,88.05,97.94,
NYR=9,
TBYR =0.0000,1.9500,4.9600,8.2800,12.340,15.000,18.000,18.000,24.800,
TBTOC=0.0000,.03030,.02770,.02570,.02570,.02770,.03000,.02000,.02000,
TBROC=0.0000,.00064,.00054,.00046,.00046,.00054,.00063,.00030,.00030,
TBETA=.40000,.40000,.40000,.40000,.40000,.40000,.40000,.50000,.50000,
NLEC=4,TBLECY=0.000,1.950,18.00,24.80,
        TBLEC=86.76,59.53,12.12,6.350,
NEWDES=1,
NALPHA=16,TALPHA=-8.0,-6.0,-4.0,-2.0,0.0,2.0,4.0,6.0,8.0,10.0,12.0,14.0,
                    16.0,18.0,20.0,22.0,    $
```

(b) Advanced arrow-wing, supersonic-transport; restricted-area wing design

```
SUPERSONIC TRANSPORT  AST 210 - SCOTT, CR 172531 - RESTRICTED DESIGN
$INPT1 XM=.21, RN=4.1,JBYMAX=8,ELAR=2.0,IVOROP=1,IPRSLD=1,
CLDES=.60,CMDES=-.05,
IFLPDES=1,
SREF=1338.2,CBAR=35.2,XMC=69.1,XMAX=97.94,
NLEY=4,TBLEY=0.000,1.950,18.00,24.80,
       TBLEX=0.000,27.24,79.81,91.59,
NTEY=4,TBTEY=0.000,8.280,13.61,24.80,
       TBTEX=86.77,86.59,88.05,97.94,
NYC=10,TBYC=0.00,2.40,3.72,4.96,8.28,12.34,15.00,18.00,22.32,24.80,
NPCTC=10,
TBPCTC=0.000,2.500,5.000,10.00,20.00,30.00,40.00,60.00,80.00,100.0,
TZORDC=0.000,0.000,0.000,0.000,0.000,-.300,-1.42,-4.07,-6.18,-7.43,16*0.0,
       0.000,-.023,-.082,-.296,-.893,-1.56,-2.22,-3.39,-4.38,-5.17,16*0.0,
       0.000,.0020,-.027,-.175,-.605,-1.09,-1.58,-2.49,-3.32,-4.05,16*0.0,
       0.000,.0230,.0140,-.069,-.362,-.707,-1.06,-1.77,-2.46,-3.14,16*0.0,
       0.000,.0430,.0770,.0900,.0350,-.071,-.210,-.563,-1.01,-1.51,16*0.0,
       0.000,.0340,.0670,.1170,.1490,.1290,.0790,-.091,-.336,-.626,16*0.0,
       0.000,.0250,.0500,.0940,.1230,.1170,.0880,-.023,-.179,-.359,16*0.0,
       0.000,.0050,.0090,.0190,.0210,.0110,-.010,-.065,-.129,-.188,16*0.0,
       0.000,-.009,-.018,-.037,-.062,-.079,-.094,-.114,-.118,-.110,16*0.0,
       0.000,-.005,-.010,-.018,-.037,-.055,-.066,-.078,-.079,-.078,16*0.0,
NYR=9,
TBYR =0.0000,1.9500,4.9600,8.2800,12.340,15.000,18.000,18.000,24.800,
TBTOC=0.0000,.03030,.02770,.02570,.02570,.02770,.03000,.02000,.02000,
TBROC=0.0000,.00064,.00054,.00046,.00046,.00054,.00063,.00030,.00030,
TBETA=.40000,.40000,.40000,.40000,.40000,.40000,.40000,.50000,.50000,
NLEC=6,TBLECY=0.00,1.85,1.95,15.5,18.0,24.8,
       TBLEC=0.00,0.00,6.36,9.27,4.48,1.92,
NGCS=0,
NTES=2,
NTEC=10,TBTECY=0.00,2.30,2.40,7.07,7.17,9.44,9.54,12.3,12.4,24.8,
        TBTEC=0.00,0.00,3.75,3.60,0.00,0.00,3.92,4.70,0.00,0.00,
NEWDES=1,
NALPHA=16,TALPHA=-8.0,-6.0,-4.0,-2.0,0.0,2.0,4.0,6.0,8.0,10.0,12.0,14.0,
                   16.0,18.0,20.0,22.0,    $
```

Table II. Concluded

(c) 60°-swept trapezoidal-wing fighter; whole-wing design

```
SUPERSONIC CRUISE FIGHTER - RIEBE, TP 2642 - WHOLE WING DESIGN
$INPT1 XM=0.50,RN=2.9,JBYMAX=8,ELAR=2.00,IVOROP=1,IPRSLD=1,
CLDES=0.73,
NEWDES=1,
SREF=149.7,CBAR=9.78,XMC=20.64,XMAX=33.48,
NLEY=7,TBLEY=0.000,0.470,.8700,1.160,1.190,1.200,9.200,
       TBLEX=0.000,2.000,4.000,6.000,6.540,14.44,28.29,
NTEY=5,TBTEY=0.000,1.190,1.200,5.200,9.200,
       TBTEX=33.48,33.48,27.56,28.16,30.29,
NYR=3, TBYR=0.000,1.200,9.200,
      TBTOC=0.000,0.040,0.040,
      TBROC=0.000,.0012,.0012,
      TBETA=0.400,0.400,0.400,
NALPHA=14,TALPHA=-6.,-4.,-2.,0.,2.,4.,6.,8.,10.,12.,14.,16.,
18.,20.,    $
```

(d) 60°-swept trapezoidal-wing fighter; restricted-area wing design

```
SUPERSONIC CRUISE FIGHTER - RIEBE, TP 2642 - RESTRICTED DESIGN, FLAP A
$INPT1 XM=0.50,RN=2.9,JBYMAX=8,ELAR=2.00,IVOROP=1,IPRSLD=1,
CLDES=0.73,CMDES=-.17,
NEWDES=1,IFLPDES=1,
SREF=149.7,CBAR=9.78,XMC=20.64,XMAX=33.48,
NLEY=7,TBLEY=0.000,0.470,.8700,1.160,1.190,1.200,9.200,
       TBLEX=0.000,2.000,4.000,6.000,6.540,14.44,28.29,
NTEY=5,TBTEY=0.000,1.190,1.200,5.200,9.200,
       TBTEX=33.48,33.48,27.56,28.16,30.29,
NYC=10,TBYC=0.00,1.20,2.20,3.20,4.20,5.20,6.20,7.20,8.20,9.20,
NPCTC=10,
TBPCTC=0.000,2.481,4.975,9.965,19.95,29.95,39.95,59.96,79.98,100.0,
TZORDC=0.000,0.000,0.000,0.000,0.000,0.000,0.000,0.000,0.000,0.000,16*0.0,
       0.000,-.012,-.023,-.039,-.061,-.081,-.100,-.116,-.080,-.019,16*0.0,
       0.000,.0030,.0020,.0010,-.003,-.007,-.007,.0020,.0230,.0460,16*0.0,
       0.000,.0090,.0150,.0260,.0410,.0430,.0460,.0630,.0850,.1090,16*0.0,
       0.000,.0090,.0160,.0290,.0490,.0560,.0610,.0830,.1060,.1310,16*0.0,
       0.000,.0060,.0120,.0230,.0390,.0520,.0650,.0890,.1120,.1370,16*0.0,
       0.000,.0060,.0100,.0200,.0350,.0490,.0610,.0850,.1070,.1320,16*0.0,
       0.000,.0050,.0090,.0170,.0300,.0420,.0530,.0740,.0950,.1150,16*0.0,
       0.000,.0030,.0060,.0120,.0240,.0330,.0430,.0600,.0770,.0950,16*0.0,
       0.000,.0010,.0030,.0060,.0140,.0240,.0330,.0520,.0720,.0910,16*0.0,
NYR=3, TBYR=0.000,1.200,9.200,
      TBTOC=0.000,0.040,0.040,
      TBROC=0.000,.0012,.0012,
      TBETA=0.400,0.400,0.400,
NLEC=6,TBLECY=0.000,1.190,1.200,5.190,5.200,9.200,
       TBLEC=0.000,0.000,2.320,1.360,1.360,0.400,
NGCS=0,
NTES=2,
NTEC=6,TBTECY=0.000,1.190,1.200,5.190,5.200,9.200,
       TBTEC=0.000,0.000,1.360,1.360,1.360,0.400,
NALPHA=14,TALPHA=-6.,-4.,-2.,0.,2.,4.,6.,8.,10.,12.,14.,16.,
18.,20.,    $
```

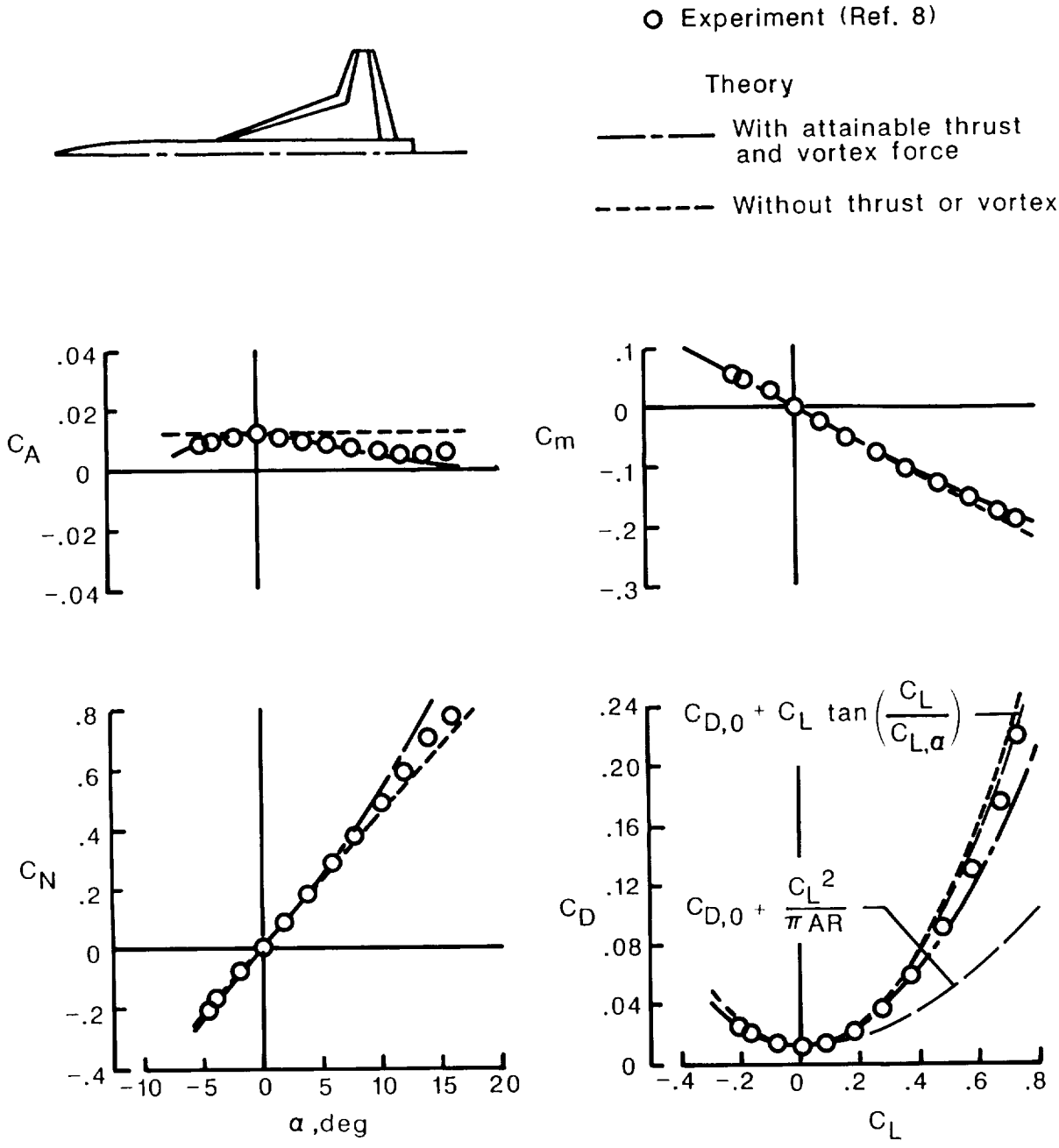

(a) $\delta_{L,n} = 0°$, $\delta_{T,n} = 0°$.

Figure 1. Theoretical and experimental data for cranked-wing leading-edge fighter. $M = 0.5$; $R = 2.9 \times 10^6$.

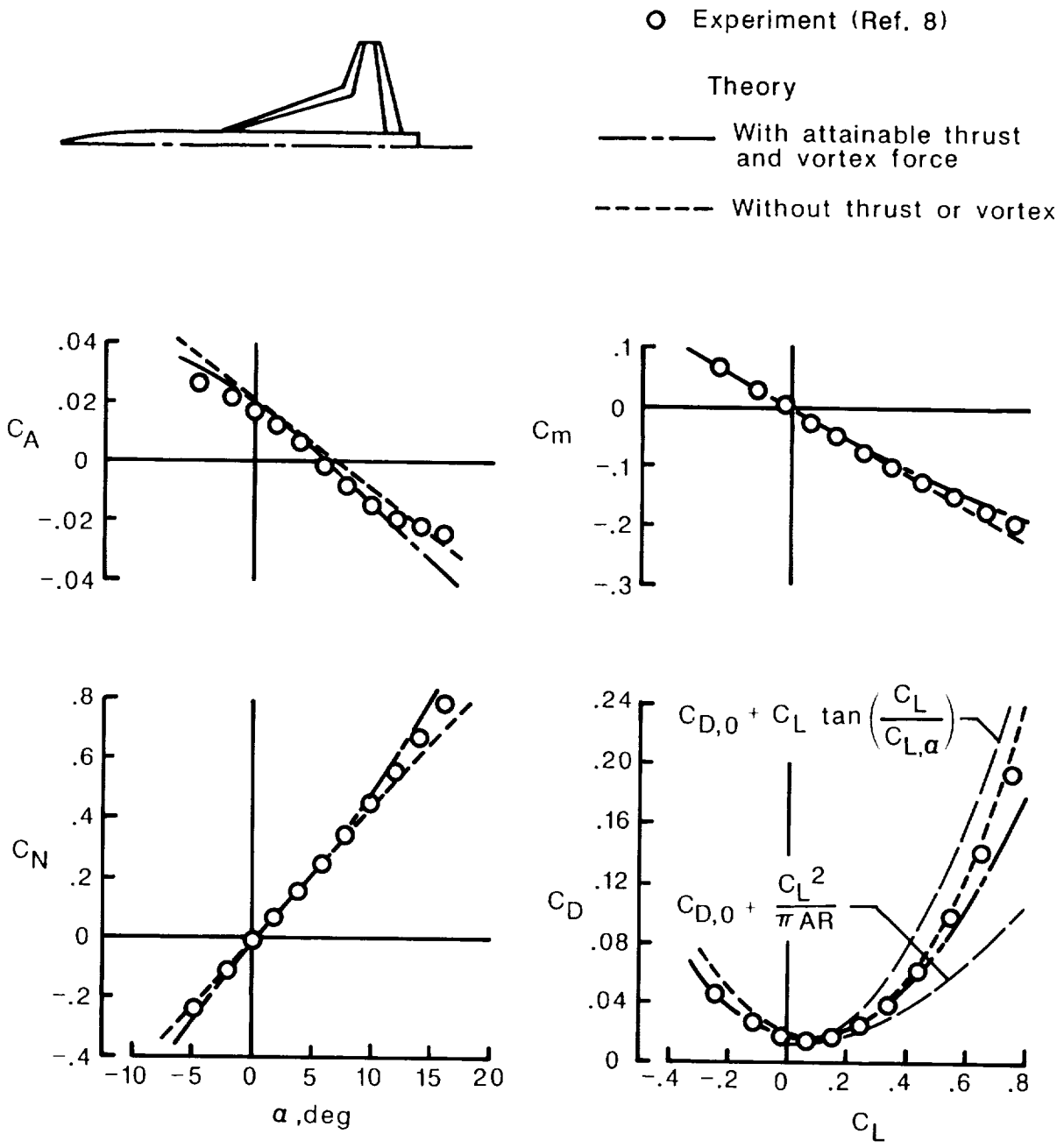

(b) $\delta_{L,n} = 15°$, $\delta_{T,n} = 0°$.

Figure 1. Continued.

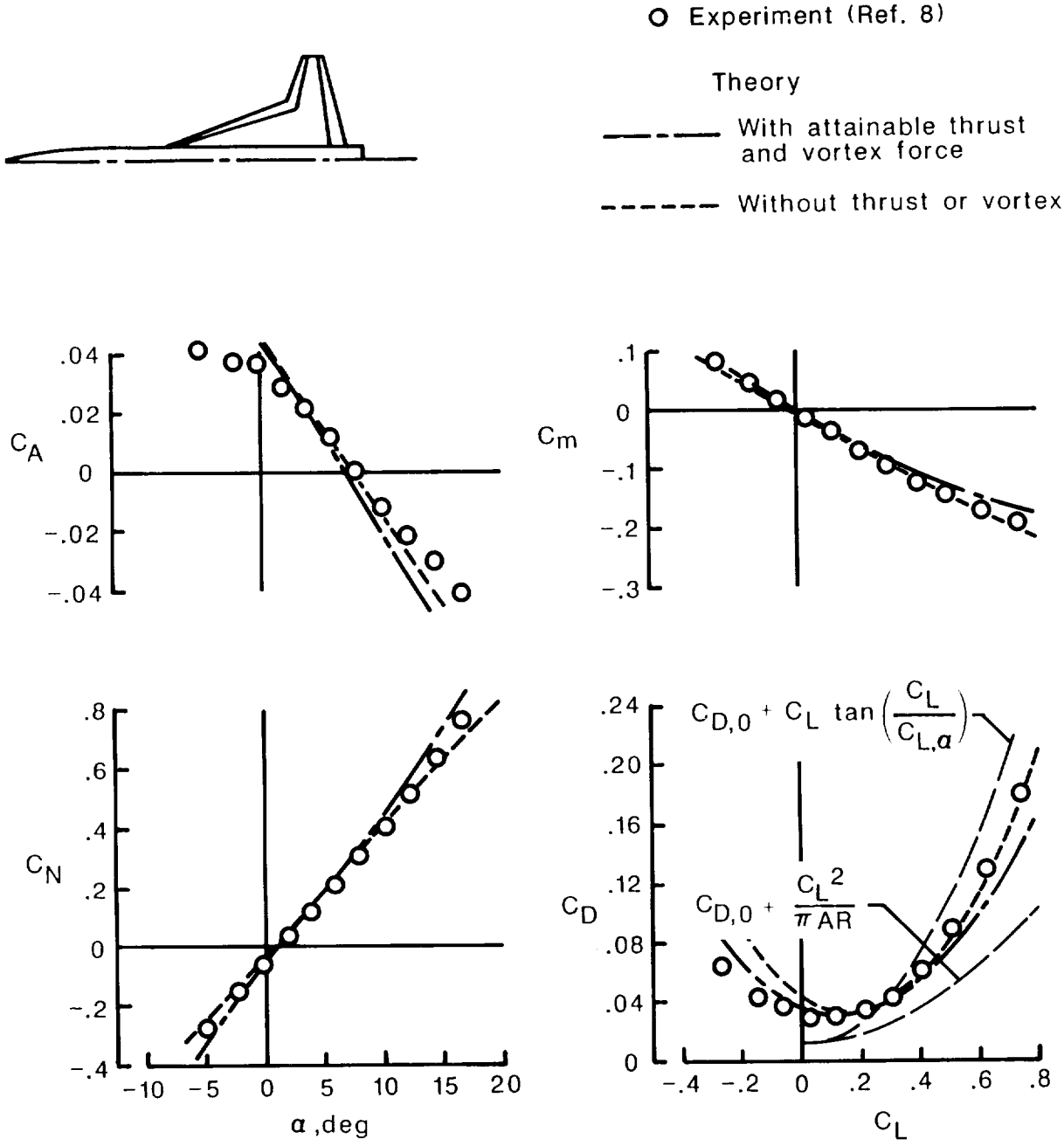

(c) $\delta_{L,n} = 30°$, $\delta_{T,n} = 0°$.

Figure 1. Continued.

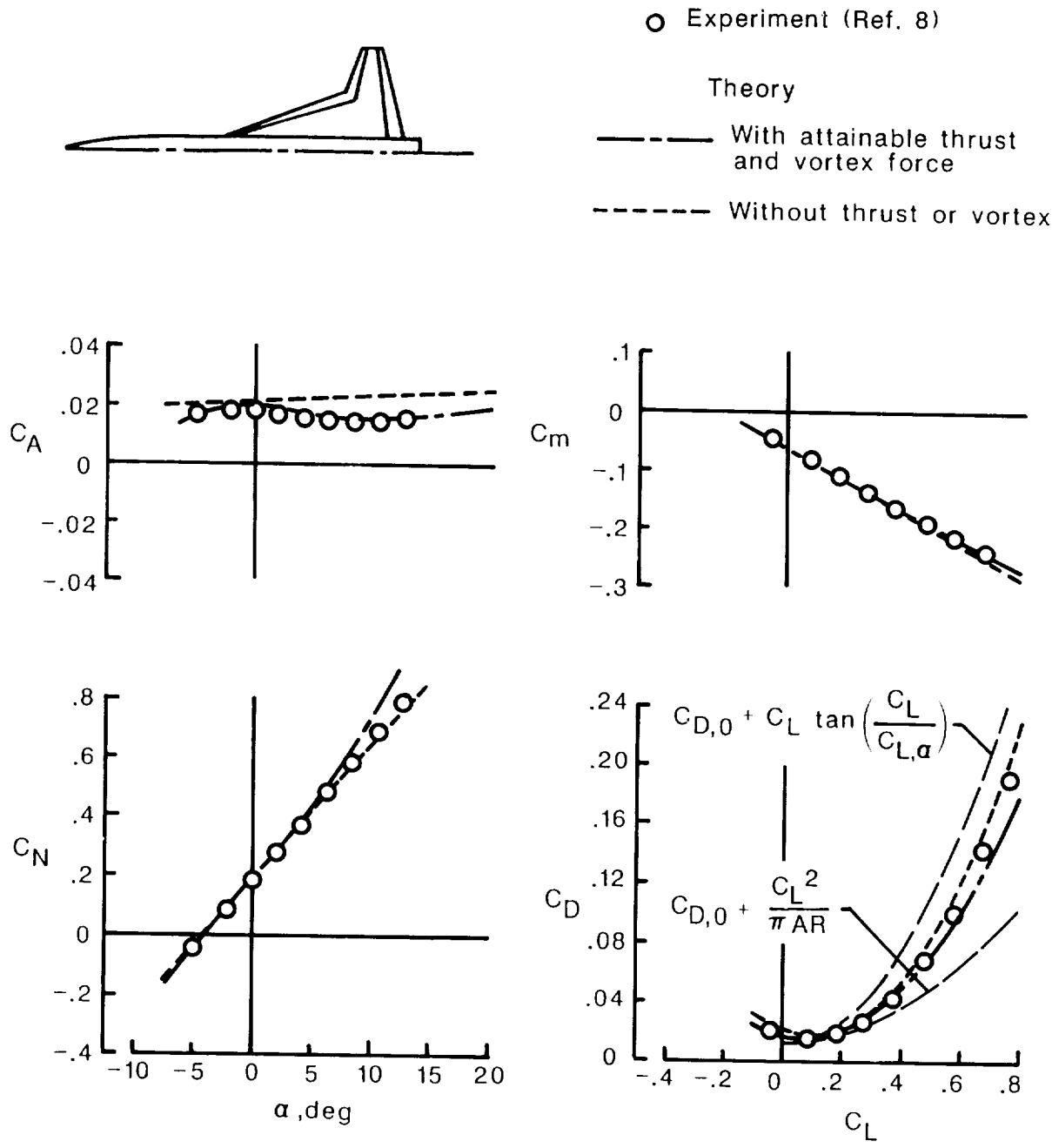

(d) $\delta_{L,n} = 0°$, $\delta_{T,n} = 10°$.

Figure 1. Continued.

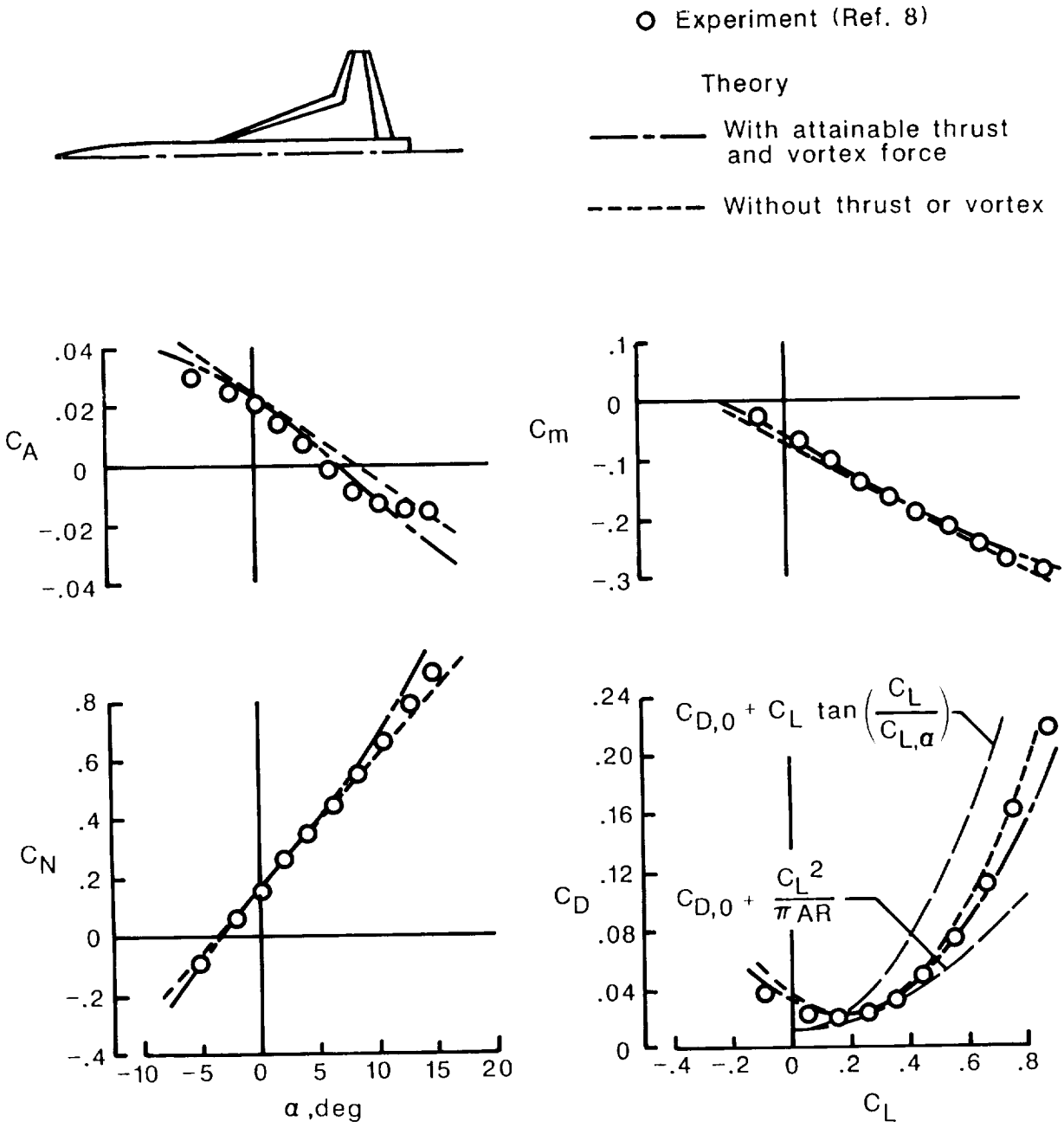

(e) $\delta_{L,n} = 15°$, $\delta_{T,n} = 10°$.

Figure 1. Continued.

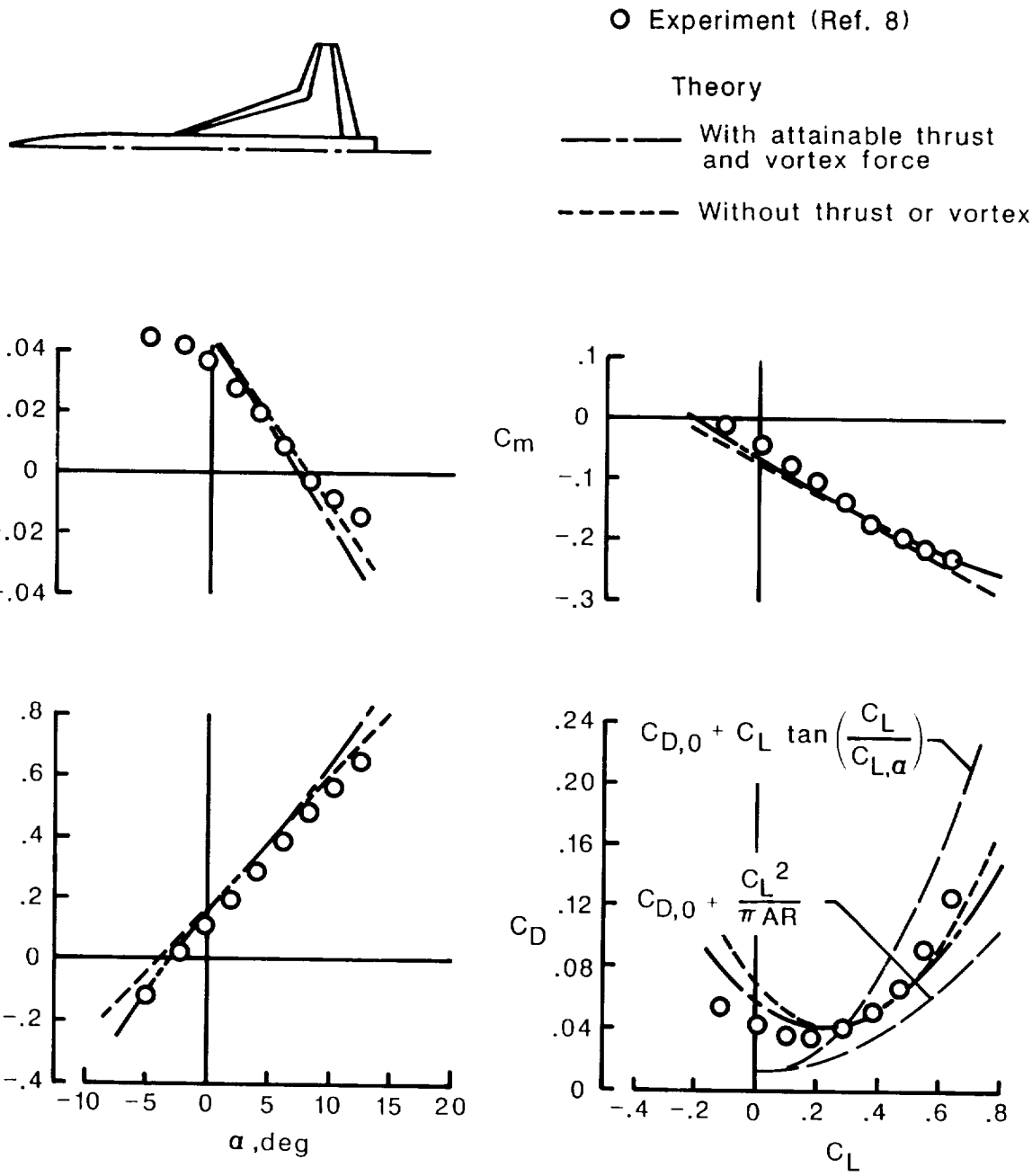

(f) $\delta_{L,n} = 30°$, $\delta_{T,n} = 10°$.

Figure 1. Continued.

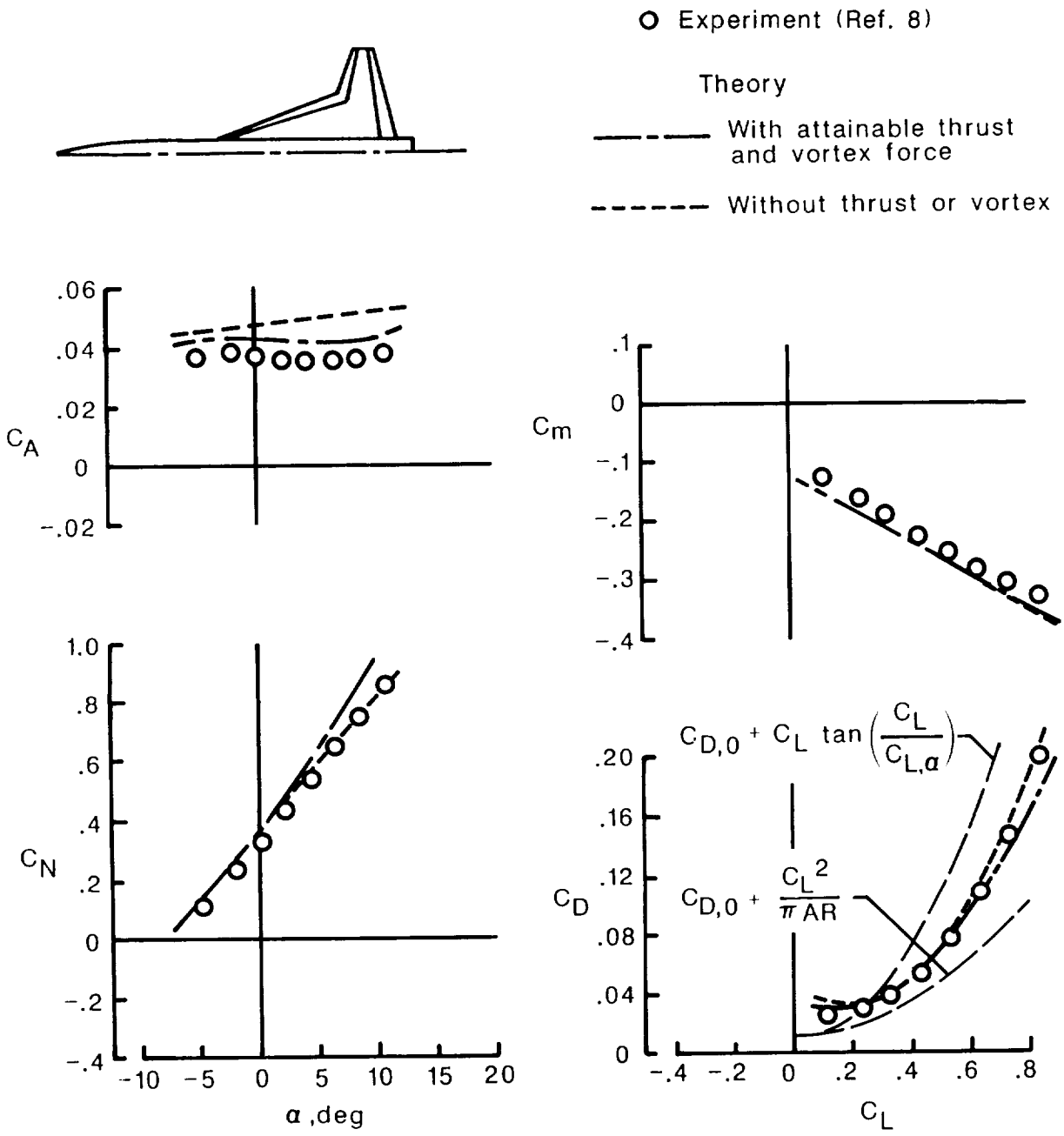

(g) $\delta_{L,n} = 0°$, $\delta_{T,n} = 20°$.

Figure 1. Continued.

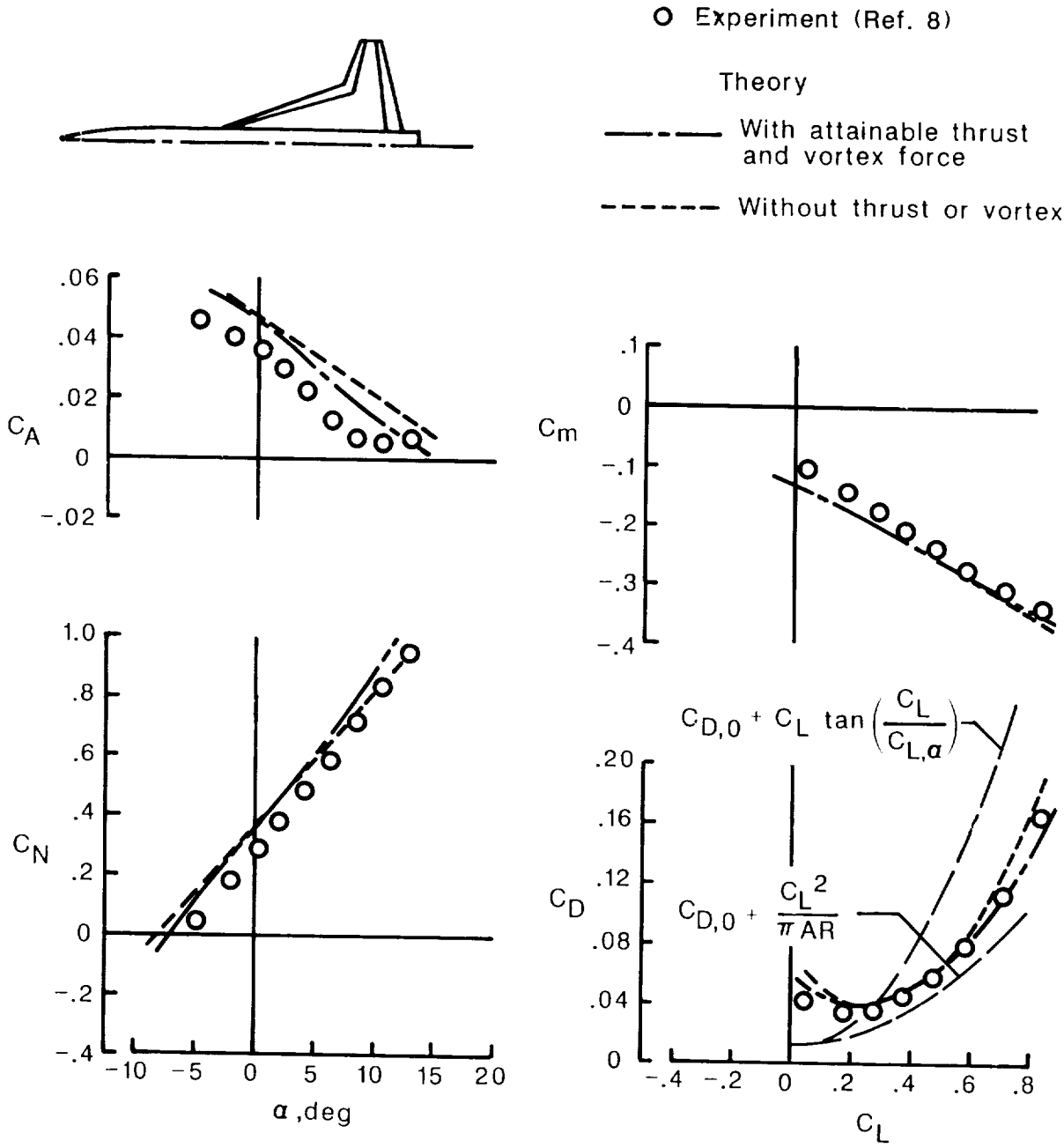

(h) $\delta_{L,n} = 15°$, $\delta_{T,n} = 20°$.

Figure 1. Continued.

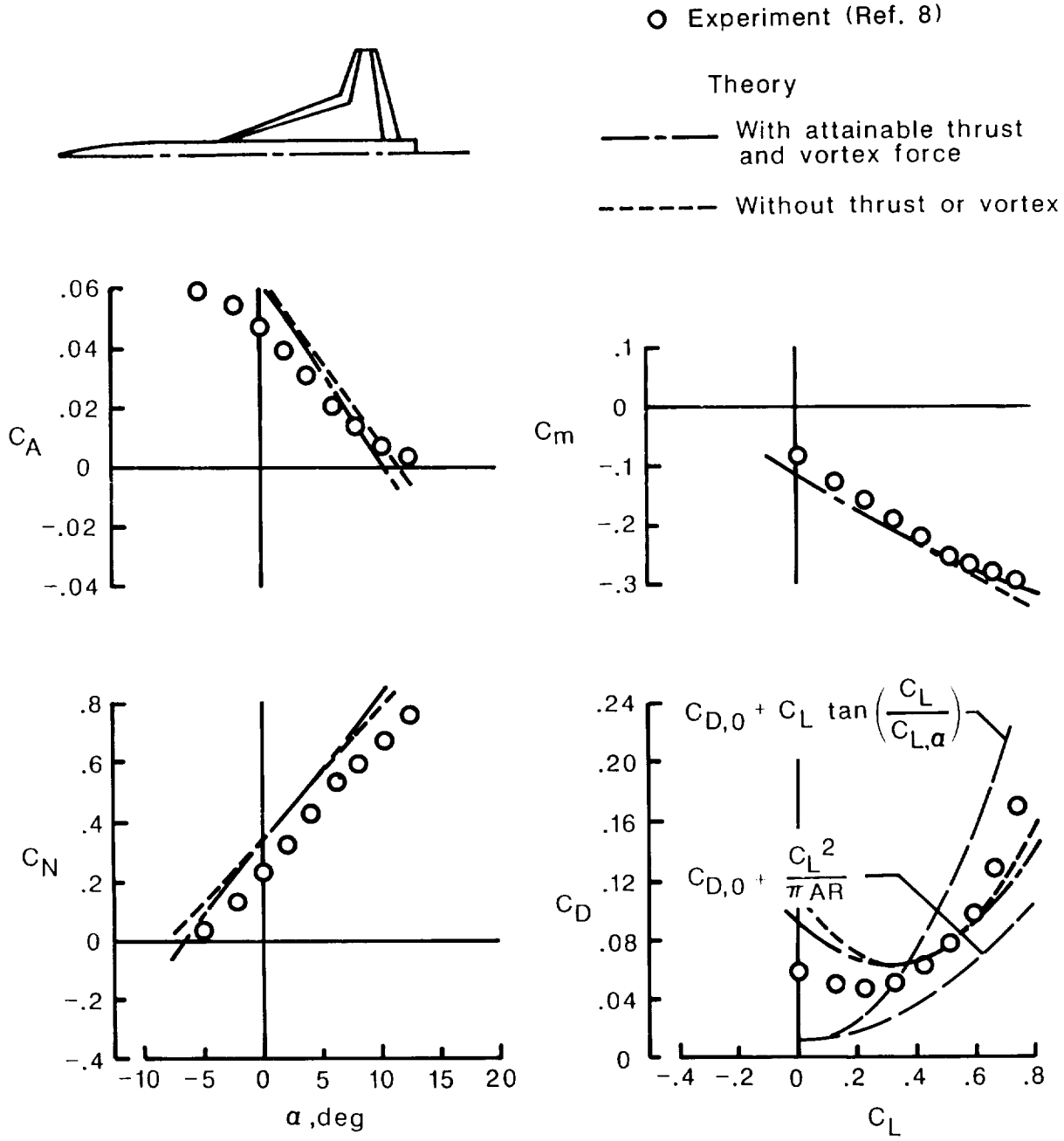

(i) $\delta_{L,n} = 30°$, $\delta_{T,n} = 20°$.

Figure 1. Concluded.

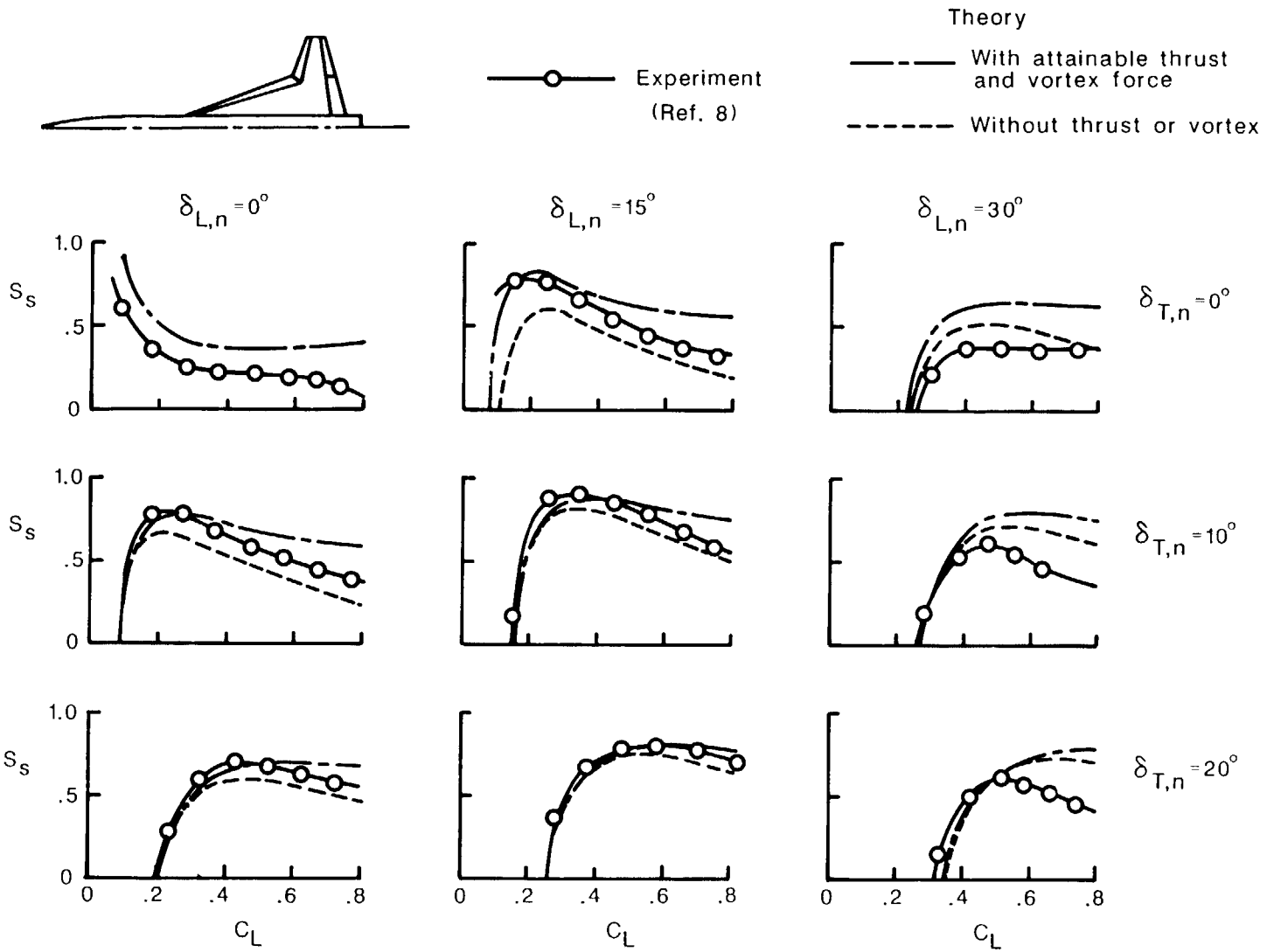

Figure 2. Suction-parameter variation with lift coefficient for various combinations of leading- and trailing-edge flap deflection angles for cranked-wing leading-edge fighter. $M = 0.5$; $R = 2.9 \times 10^6$.

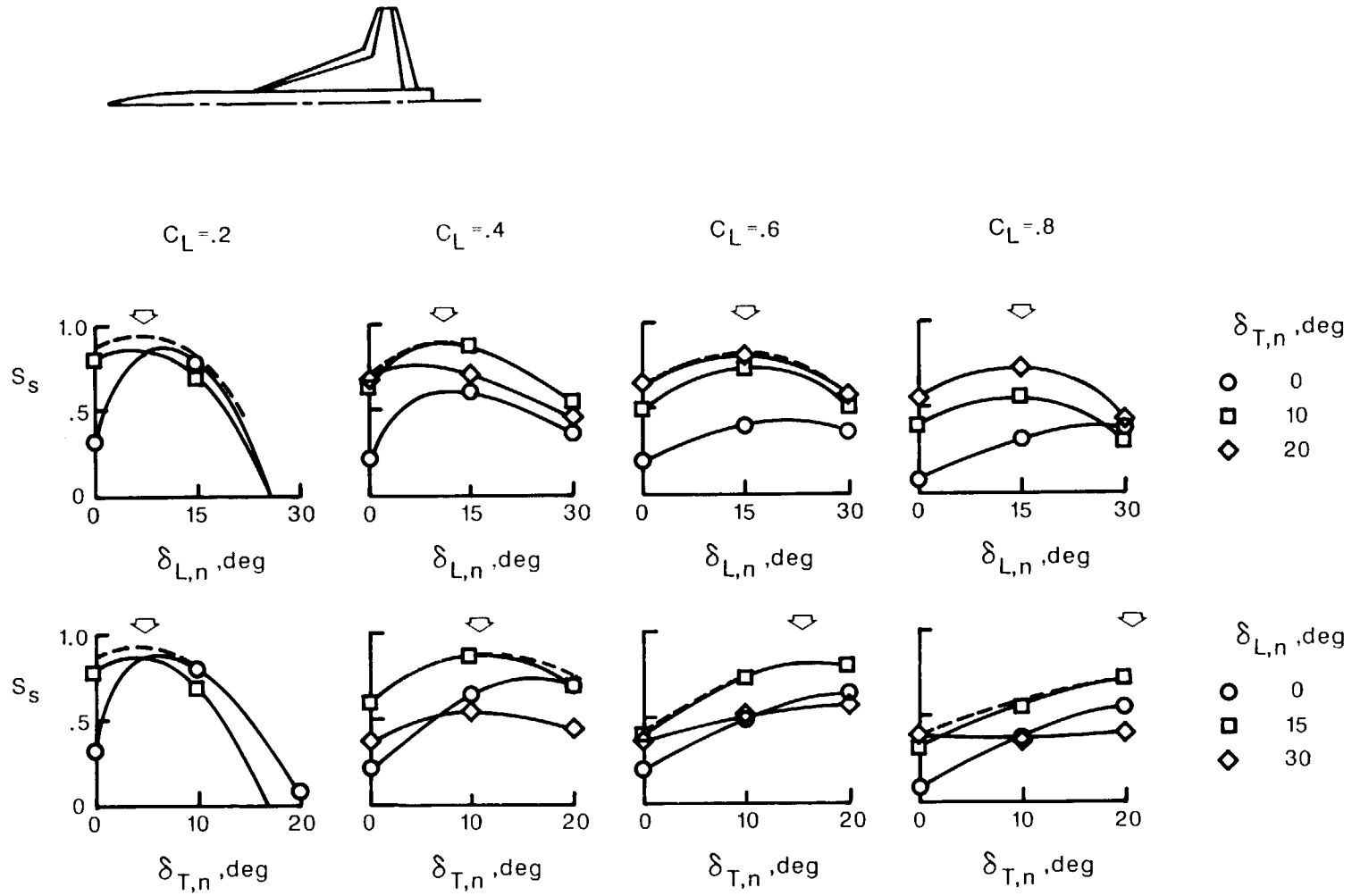

Figure 3. Suction-parameter variation with leading- and trailing-edge flap deflection angles for selected lift coefficients for cranked-wing leading-edge fighter. $M = 0.5$; $R = 2.9 \times 10^6$.

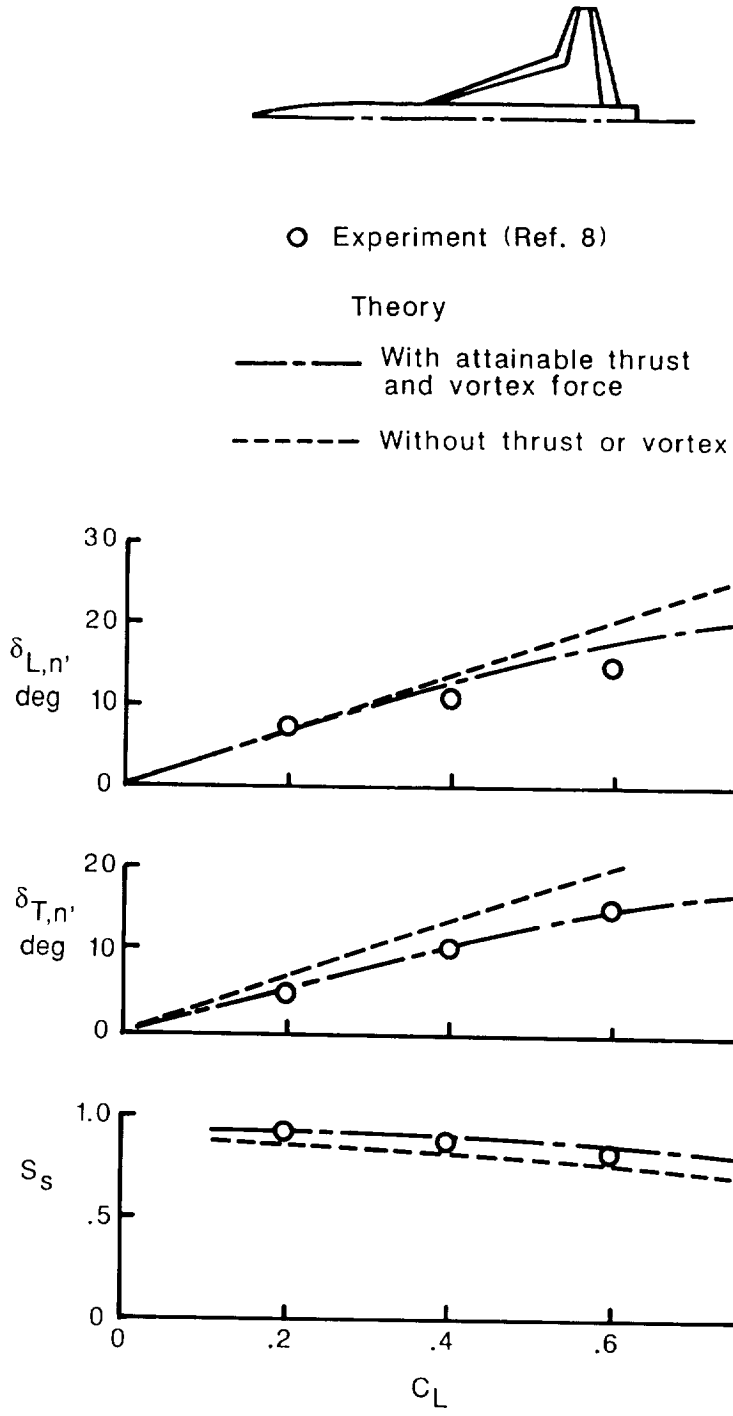

Figure 4. Optimum flap deflection and maximum suction-parameter variation with lift coefficient for cranked-wing leading-edge fighter. $M = 0.5$; $R = 2.9 \times 10^6$.

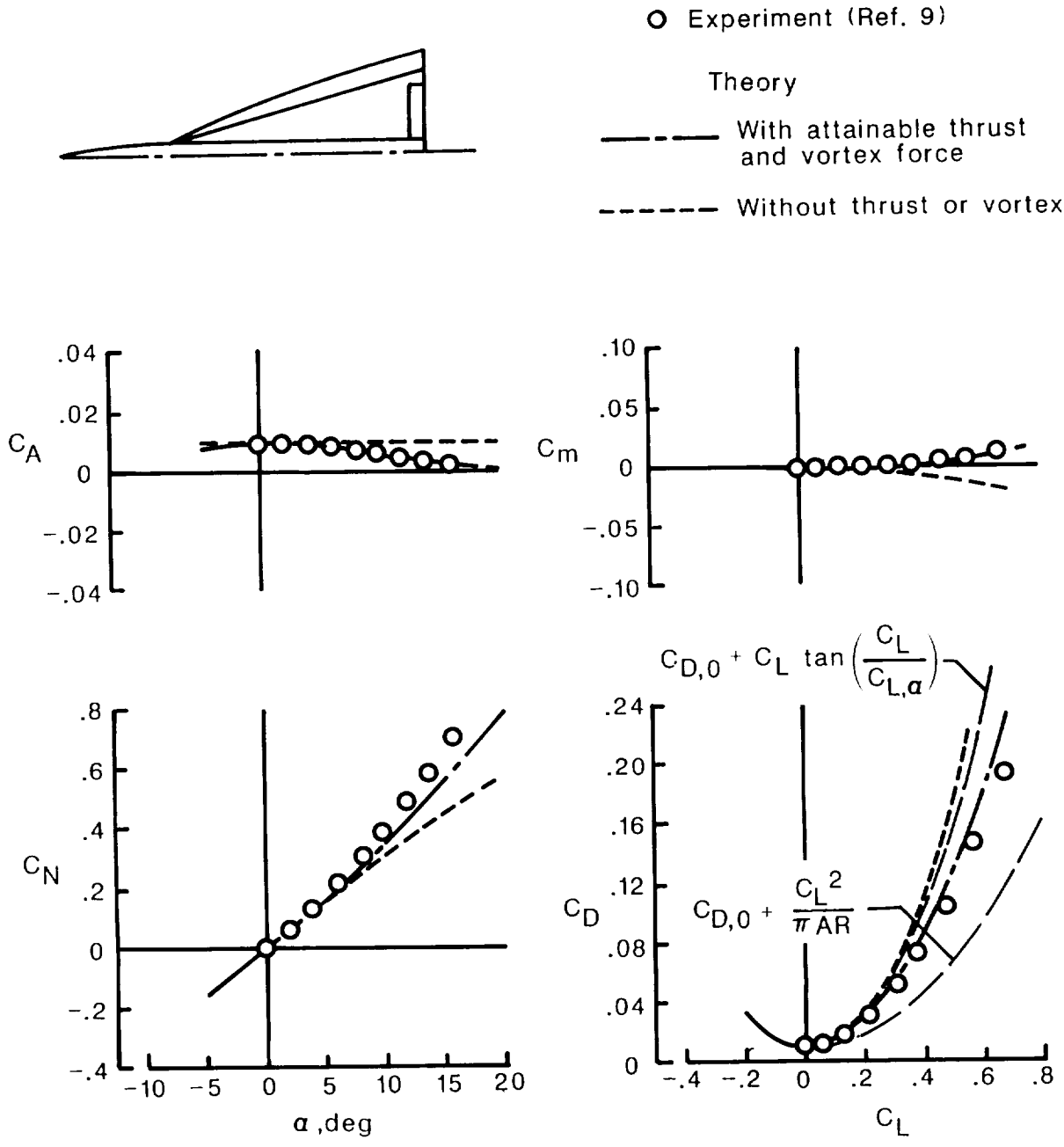

(a) $\delta_{L,n} = 0°$, $\delta_{T,n} = 0°$.

Figure 5. Theoretical and experimental data for vortex-flap wing-body configuration. $M = 0.4$; $R = 5.4 \times 10^6$.

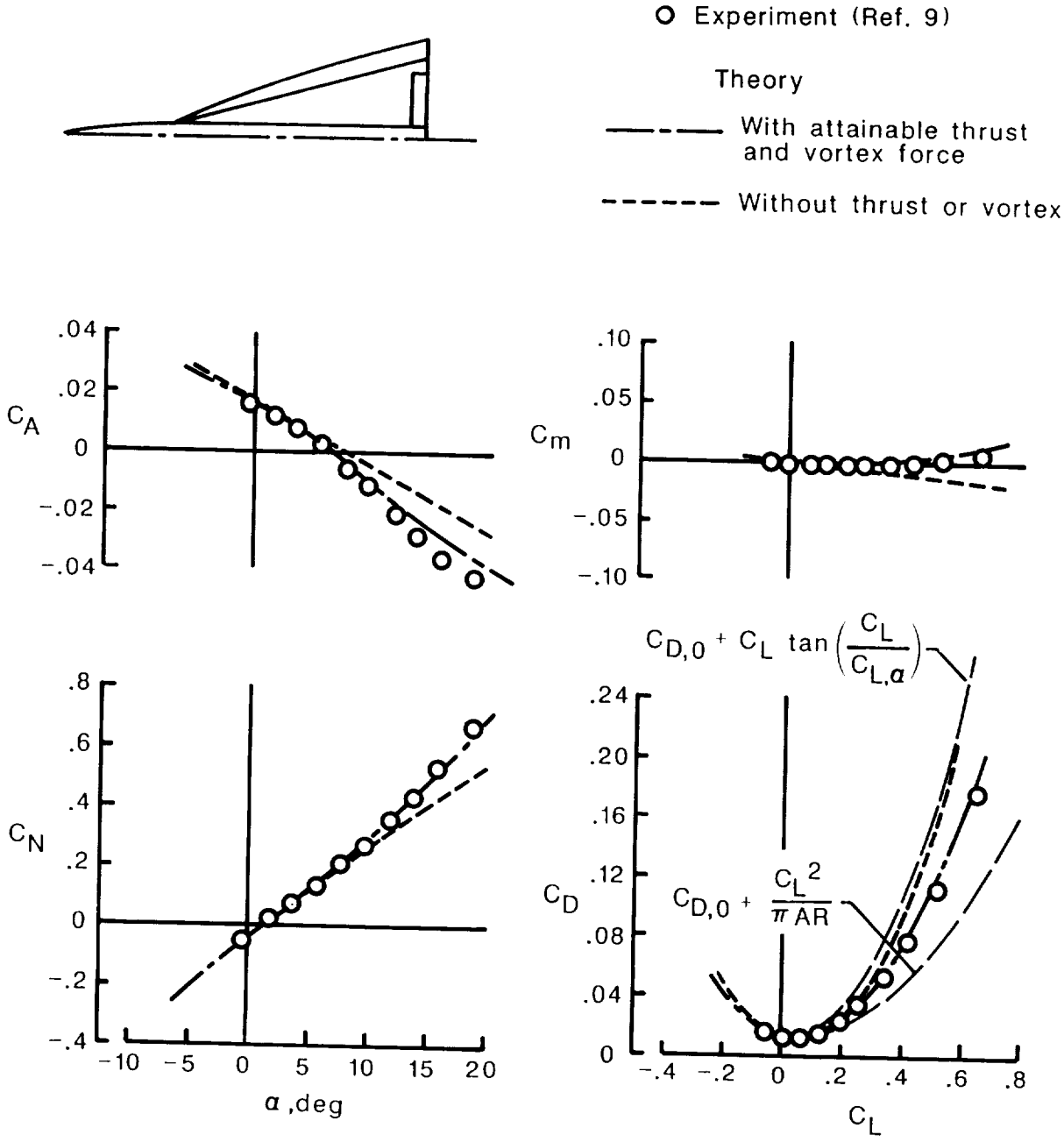

(b) $\delta_{L,n} = 30°$, $\delta_{T,n} = 0°$.

Figure 5. Continued.

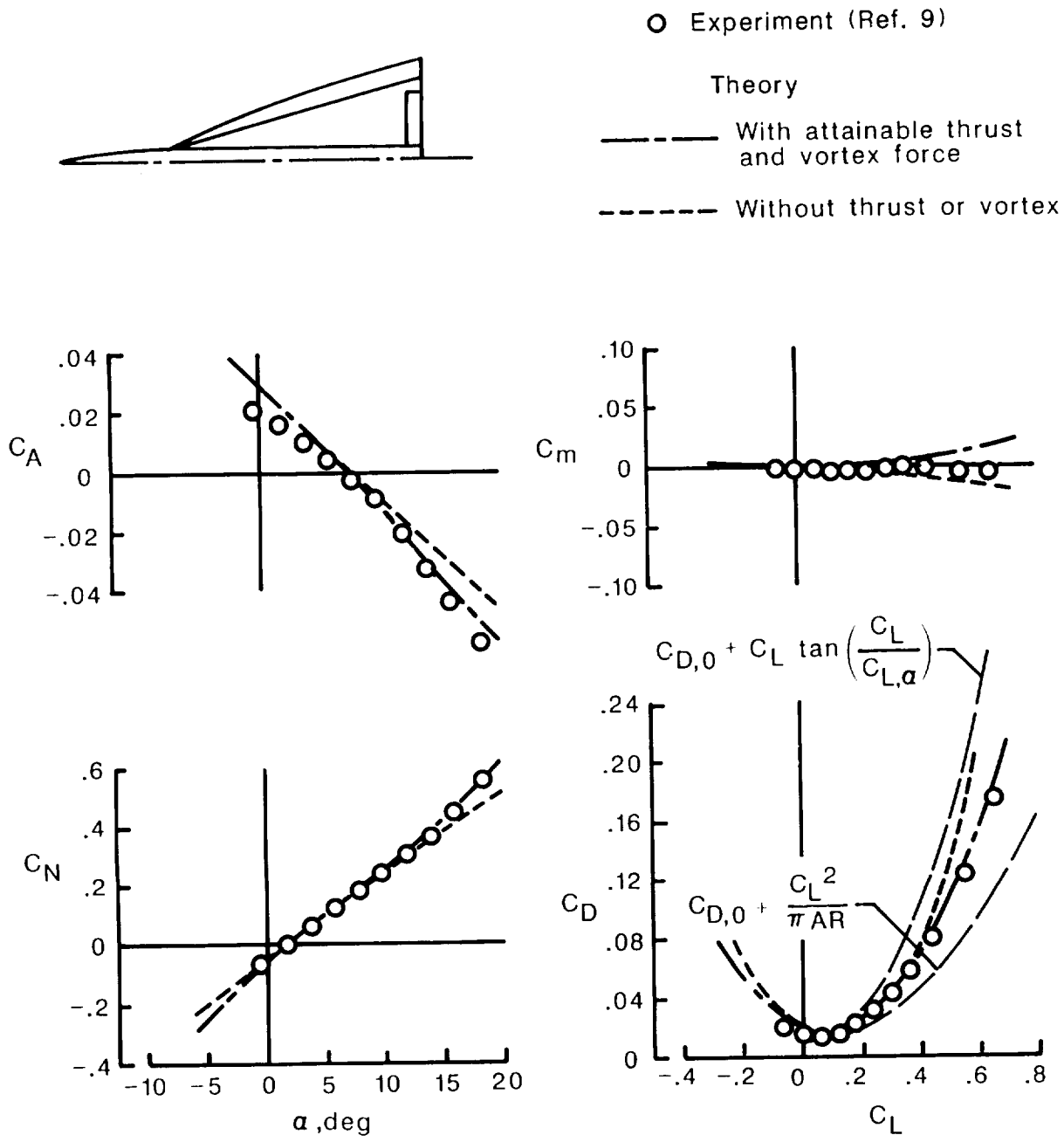

(c) $\delta_{L,n} = 45°$, $\delta_{T,n} = 0°$.

Figure 5. Continued.

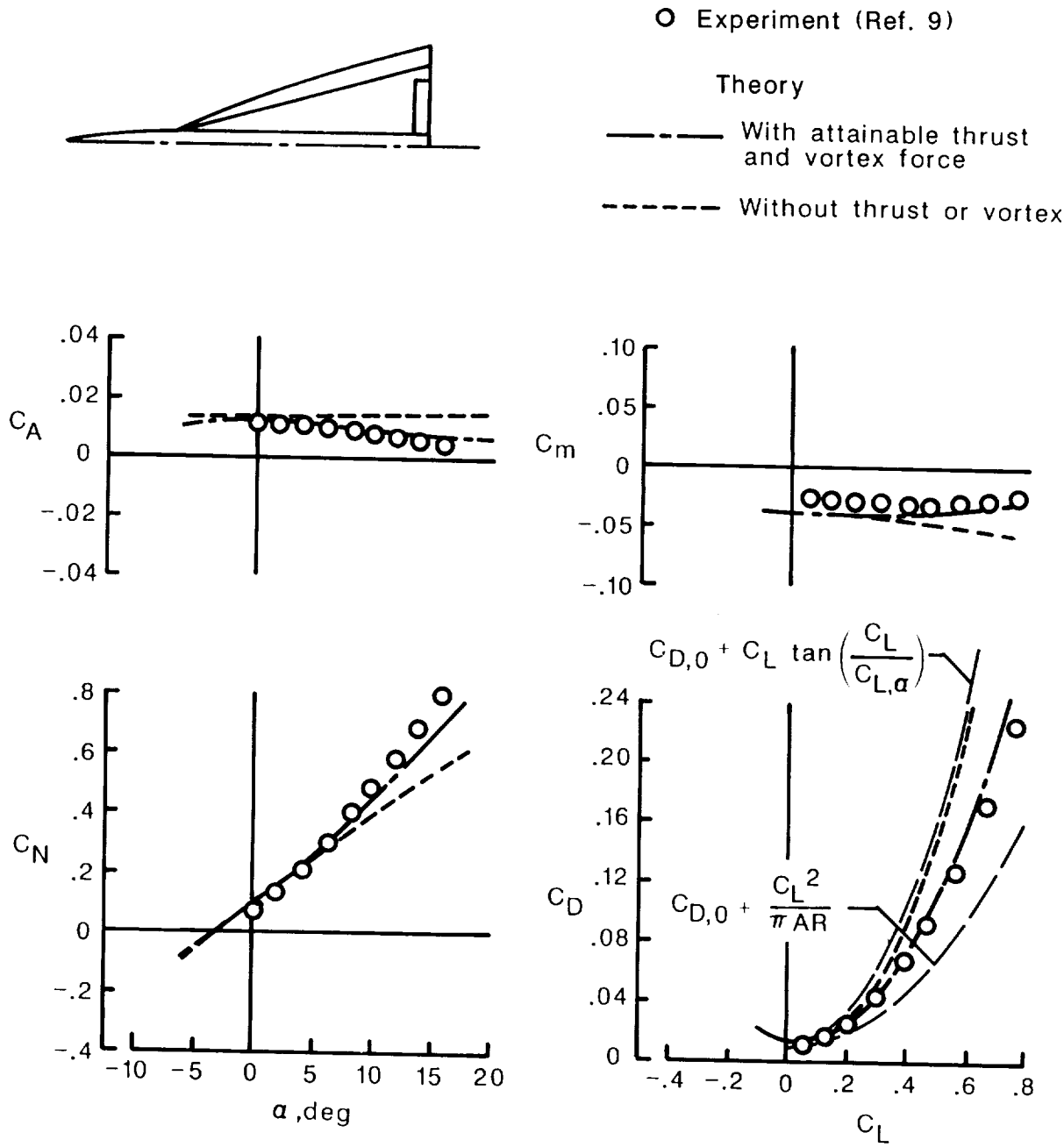

(d) $\delta_{L,n} = 0°$, $\delta_{T,n} = 10°$.

Figure 5. Continued.

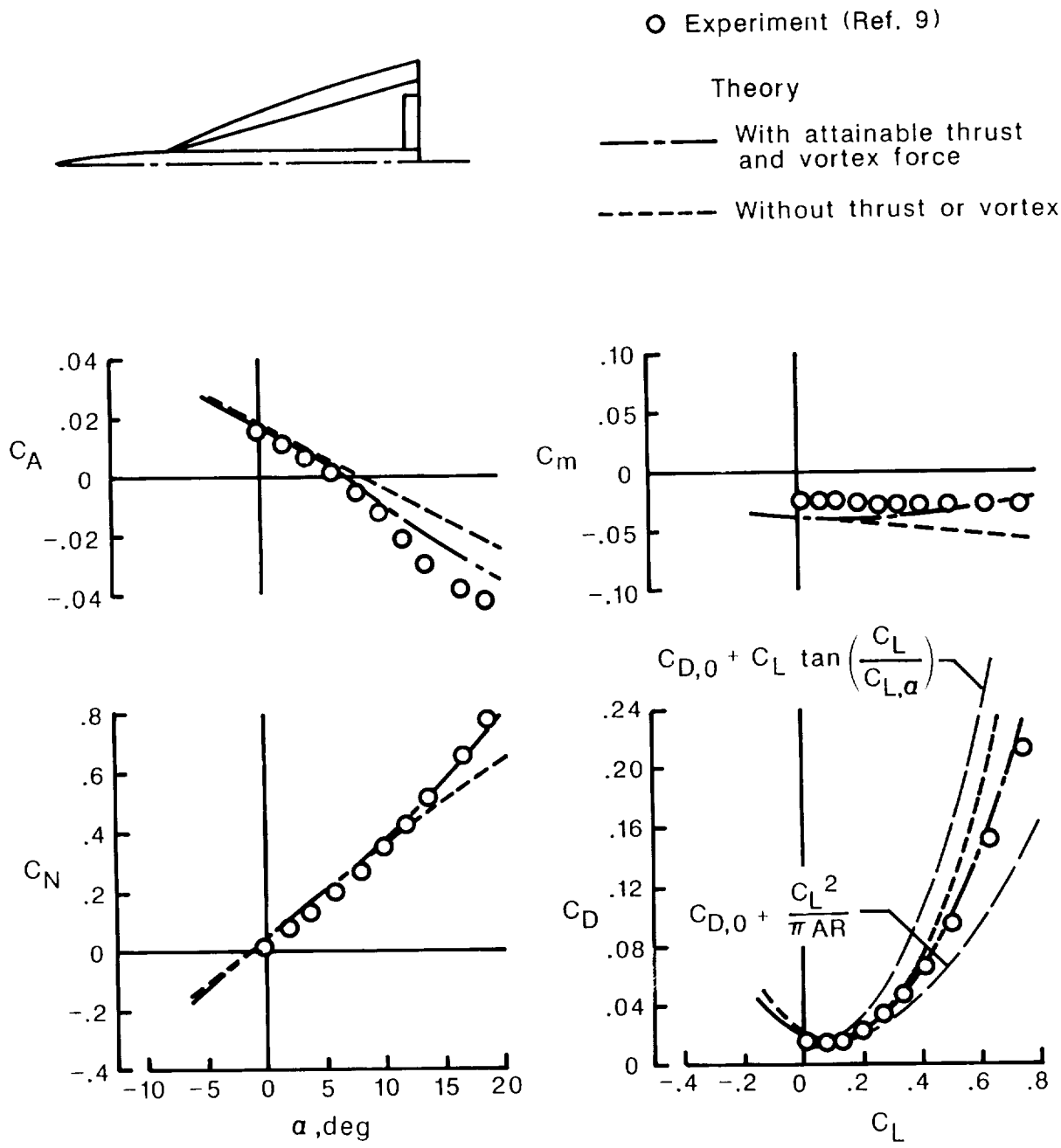

(e) $\delta_{L,n} = 30°$, $\delta_{T,n} = 10°$.

Figure 5. Continued.

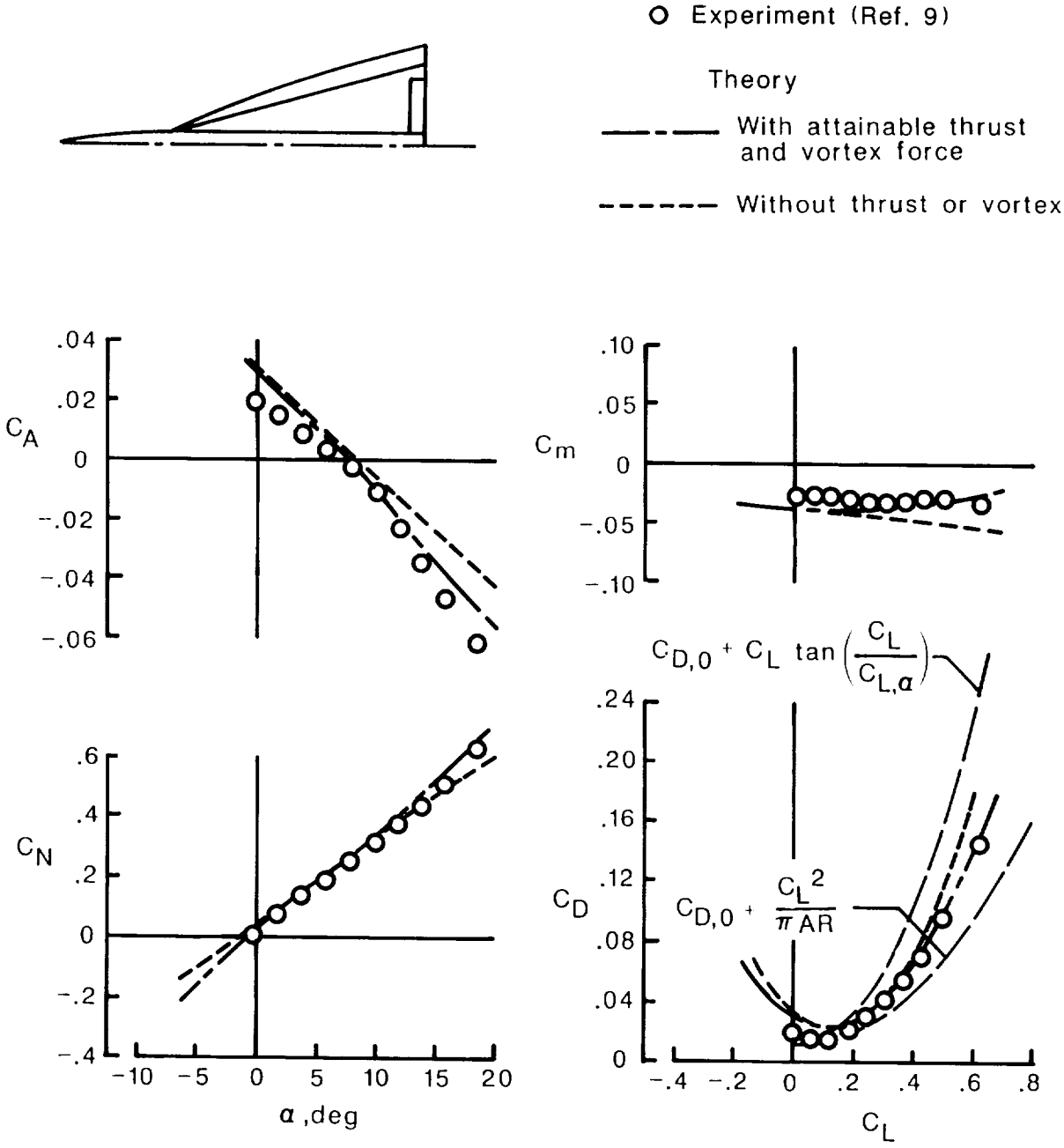

(f) $\delta_{L,n} = 45°$, $\delta_{T,n} = 10°$.

Figure 5. Continued.

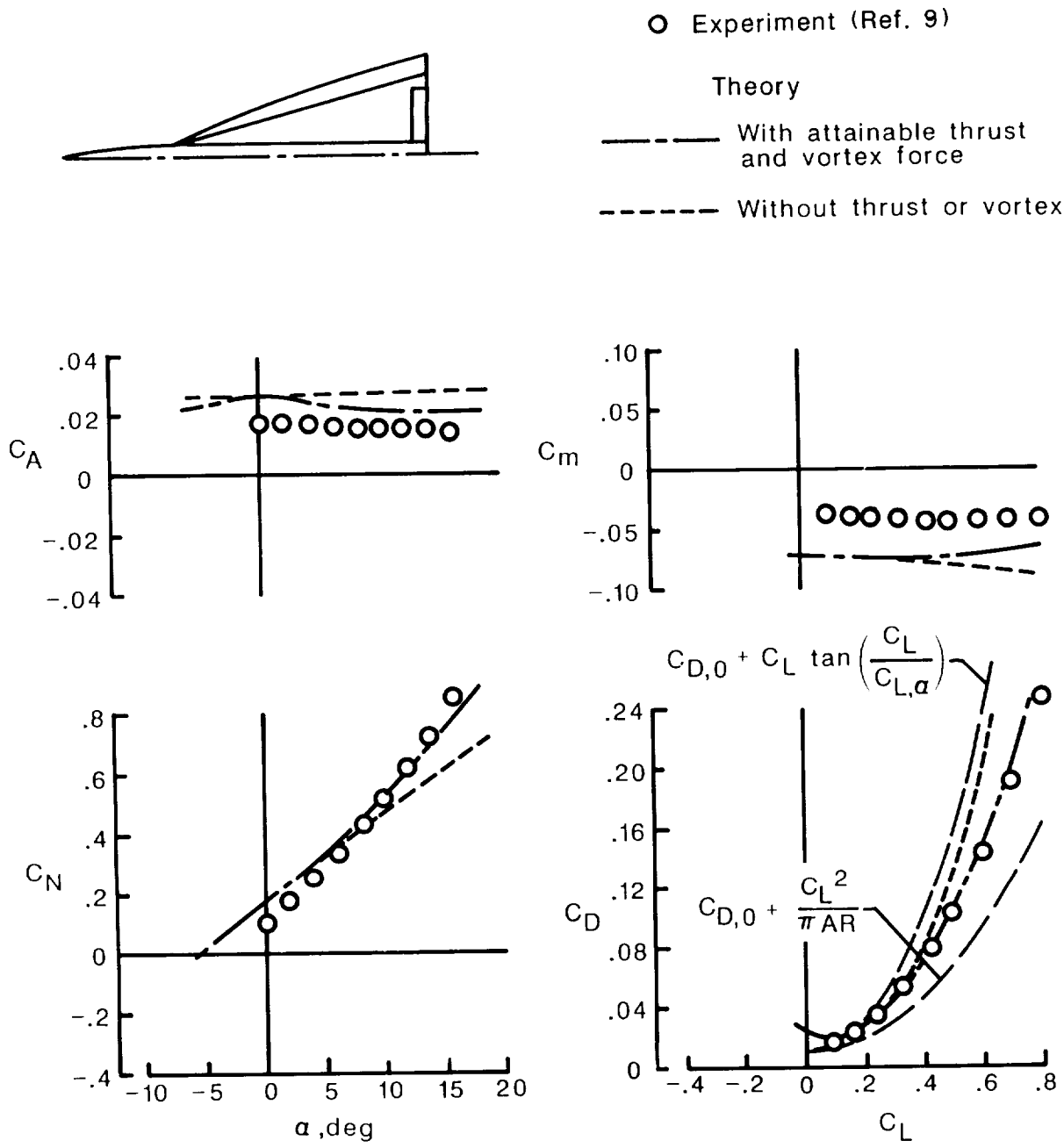

(g) $\delta_{L,n} = 0°$, $\delta_{T,n} = 20°$.

Figure 5. Continued.

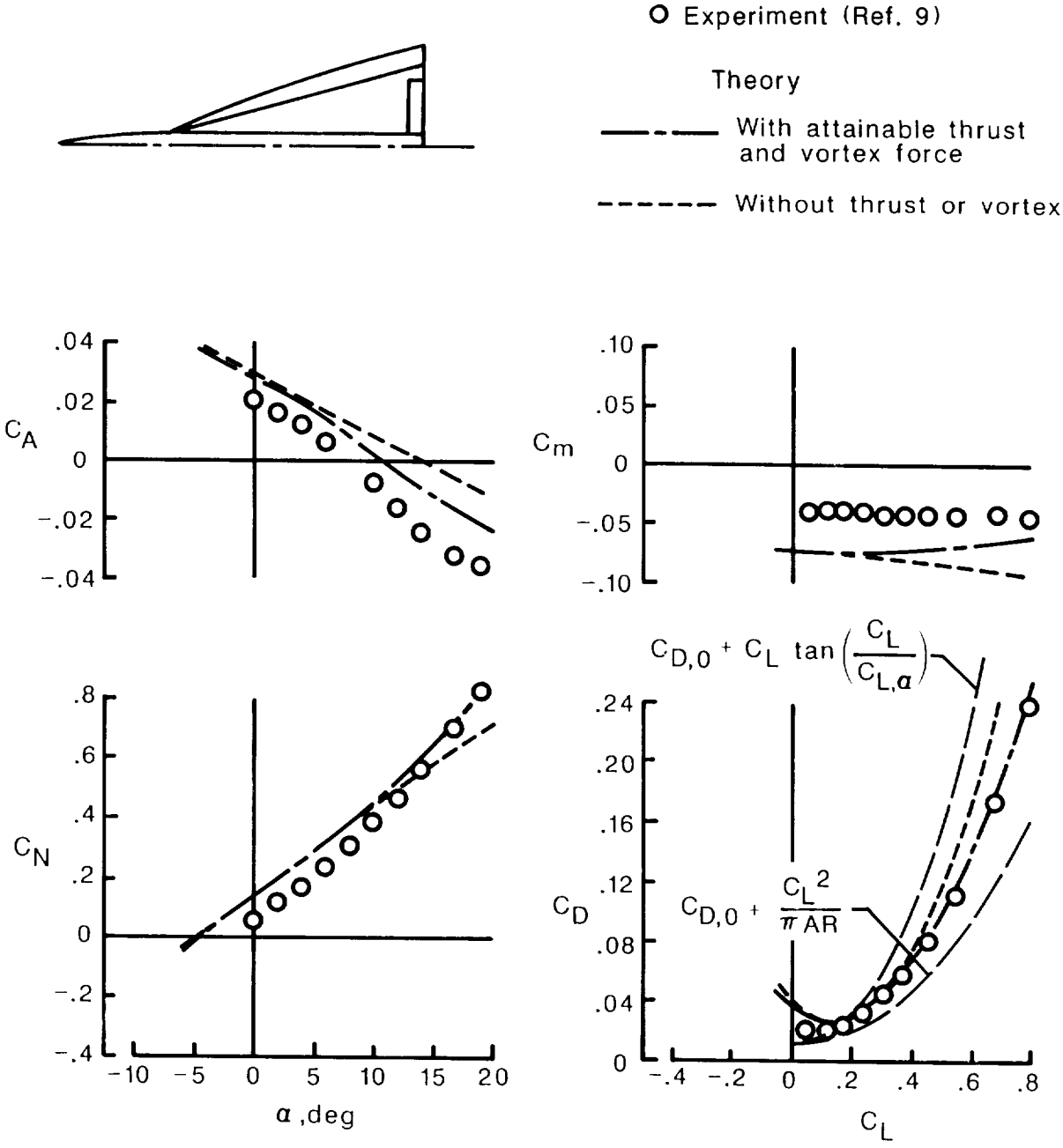

(h) $\delta_{L,n} = 30°$, $\delta_{T,n} = 20°$.

Figure 5. Continued.

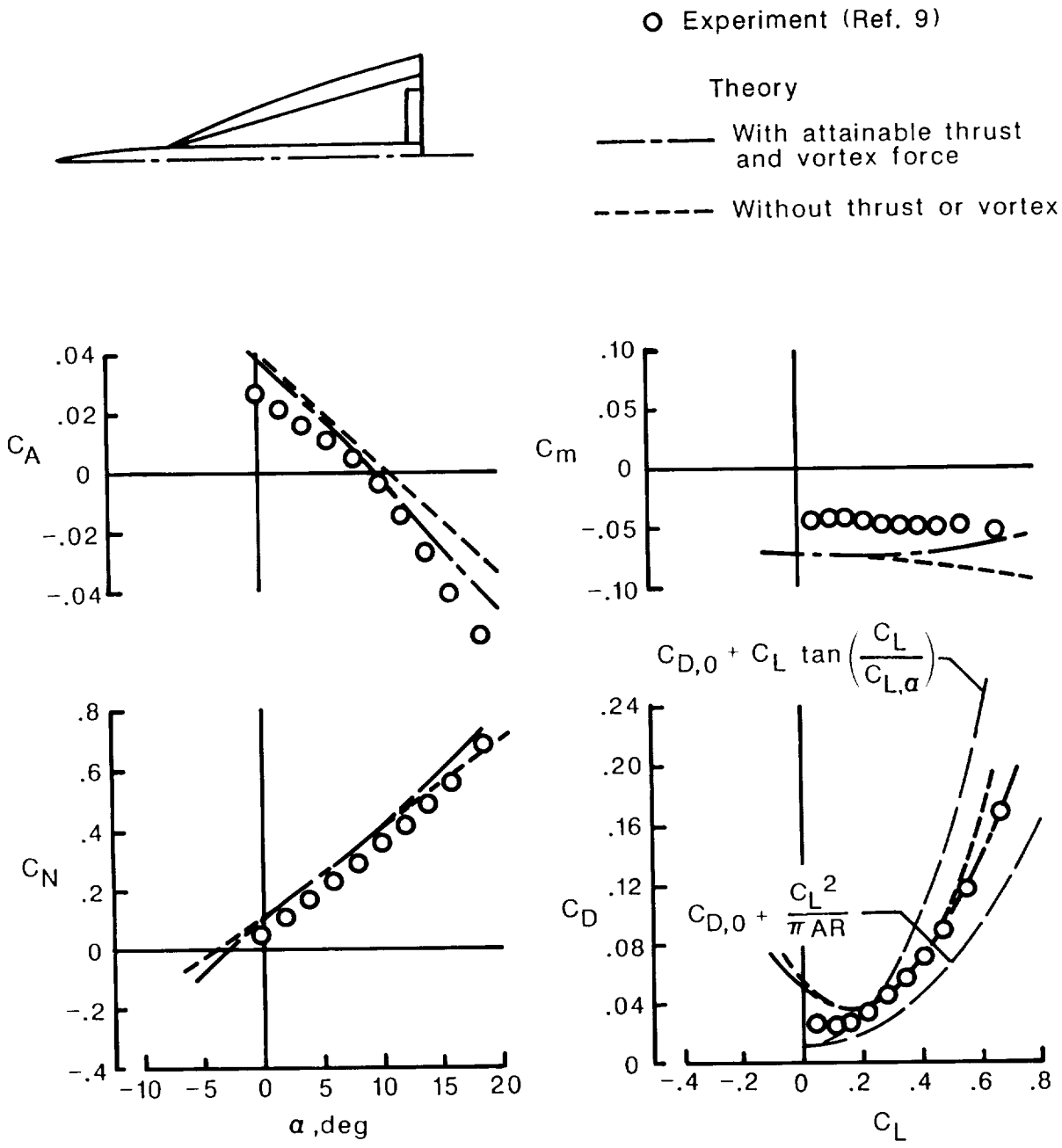

(i) $\delta_{L,n} = 45°$, $\delta_{T,n} = 20°$.

Figure 5. Concluded.

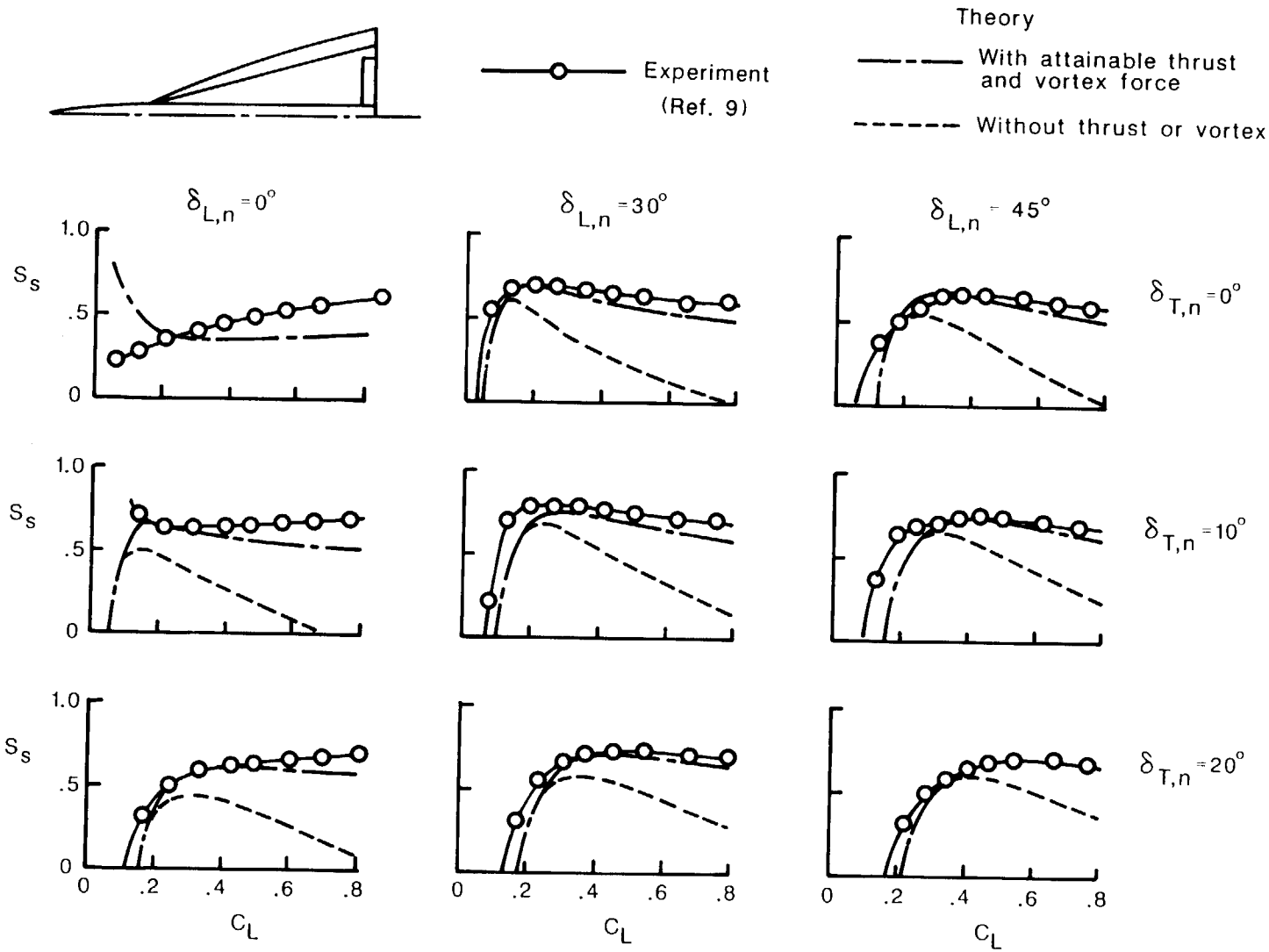

Figure 6. Suction-parameter variation with lift coefficient for various combinations of leading- and trailing-edge flap deflection angles for vortex-flap wing-body configuration. $M = 0.4$; $R = 5.4 \times 10^6$.

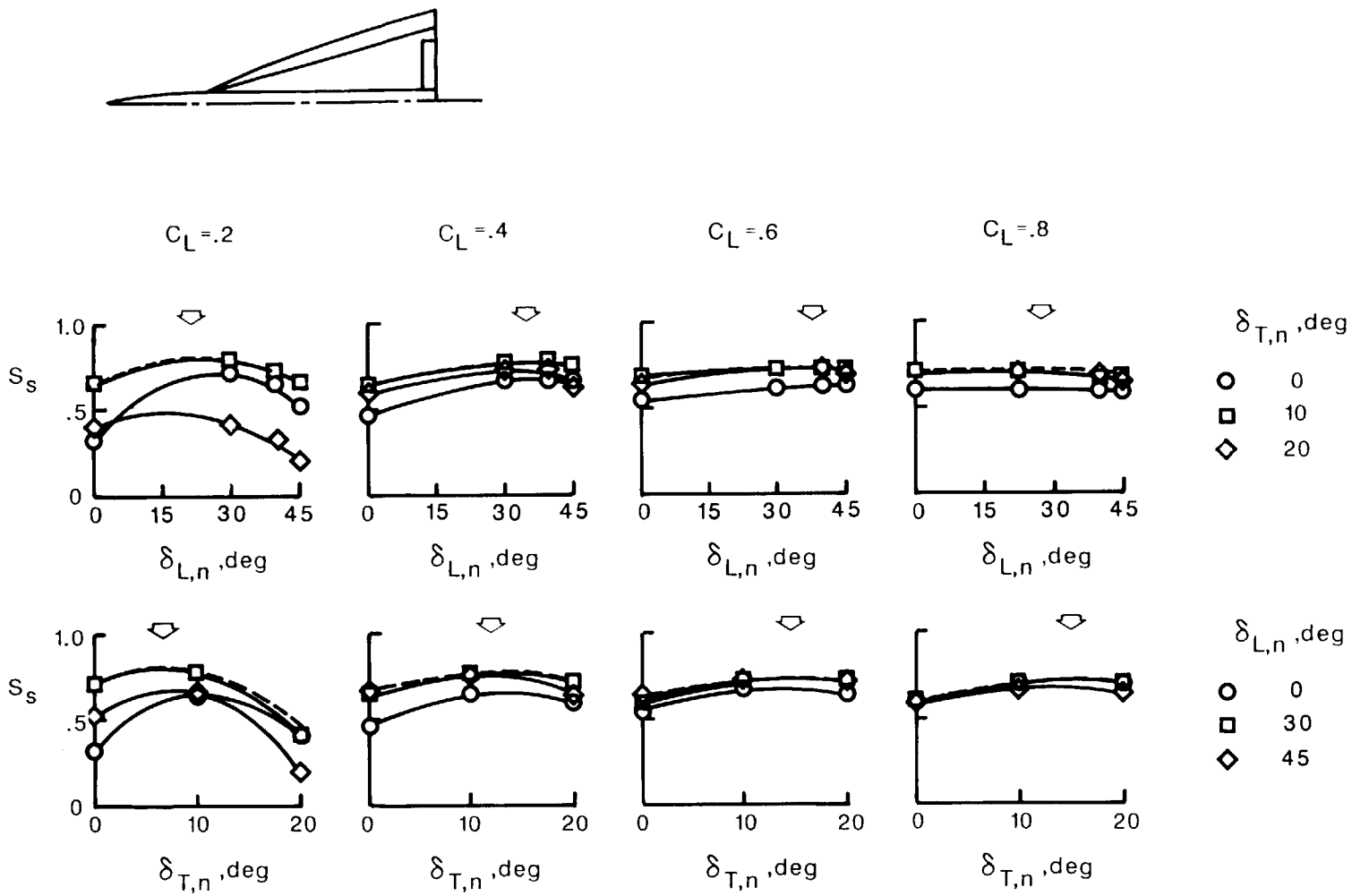

Figure 7. Suction-parameter variation with leading- and trailing-edge flap deflection angles for selected lift coefficients for vortex-flap wing-body configuration. $M = 0.4$; $R = 5.4 \times 10^6$.

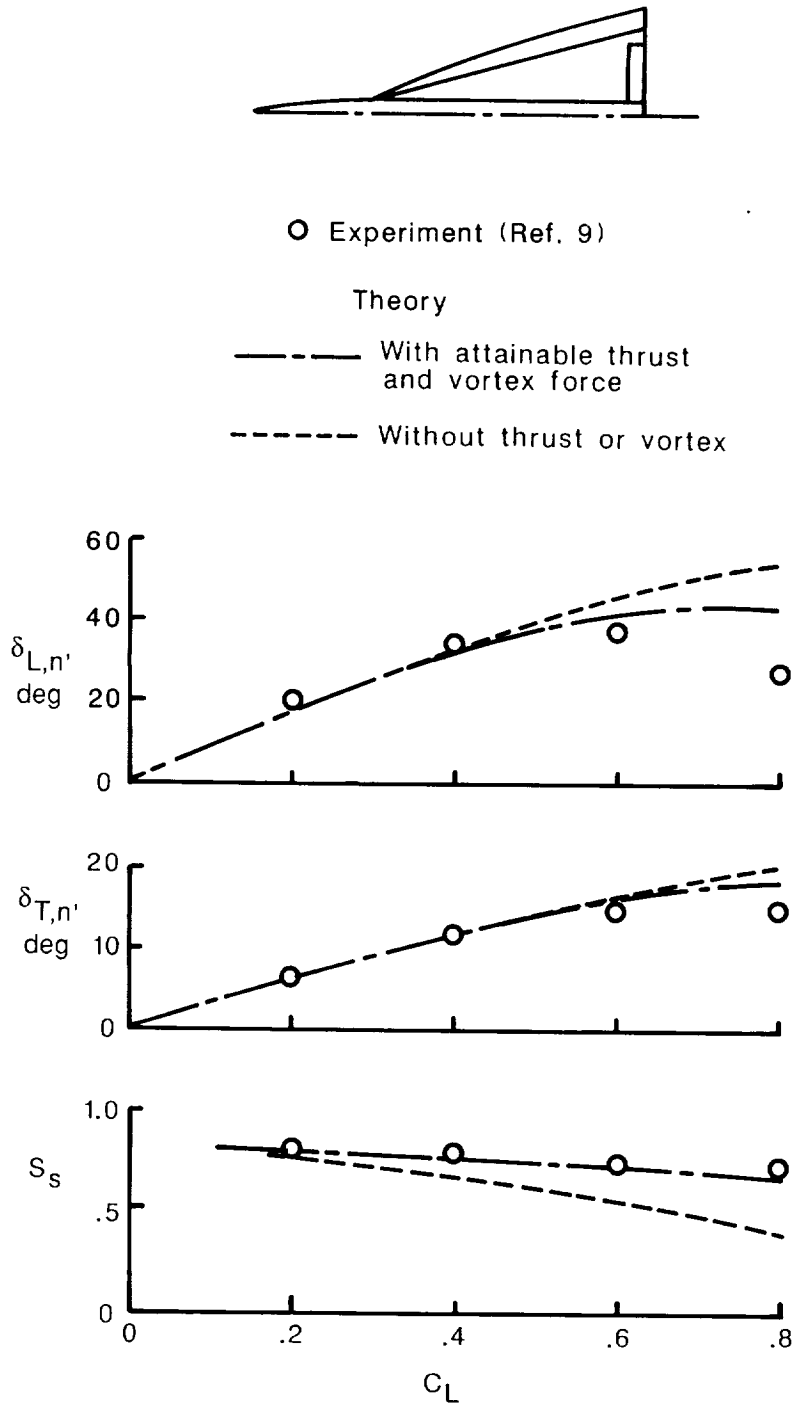

Figure 8. Optimum flap deflection and maximum suction-parameter variation with lift coefficient for vortex-flap wing-body configuration. $M = 0.4$; $R = 5.4 \times 10^6$.

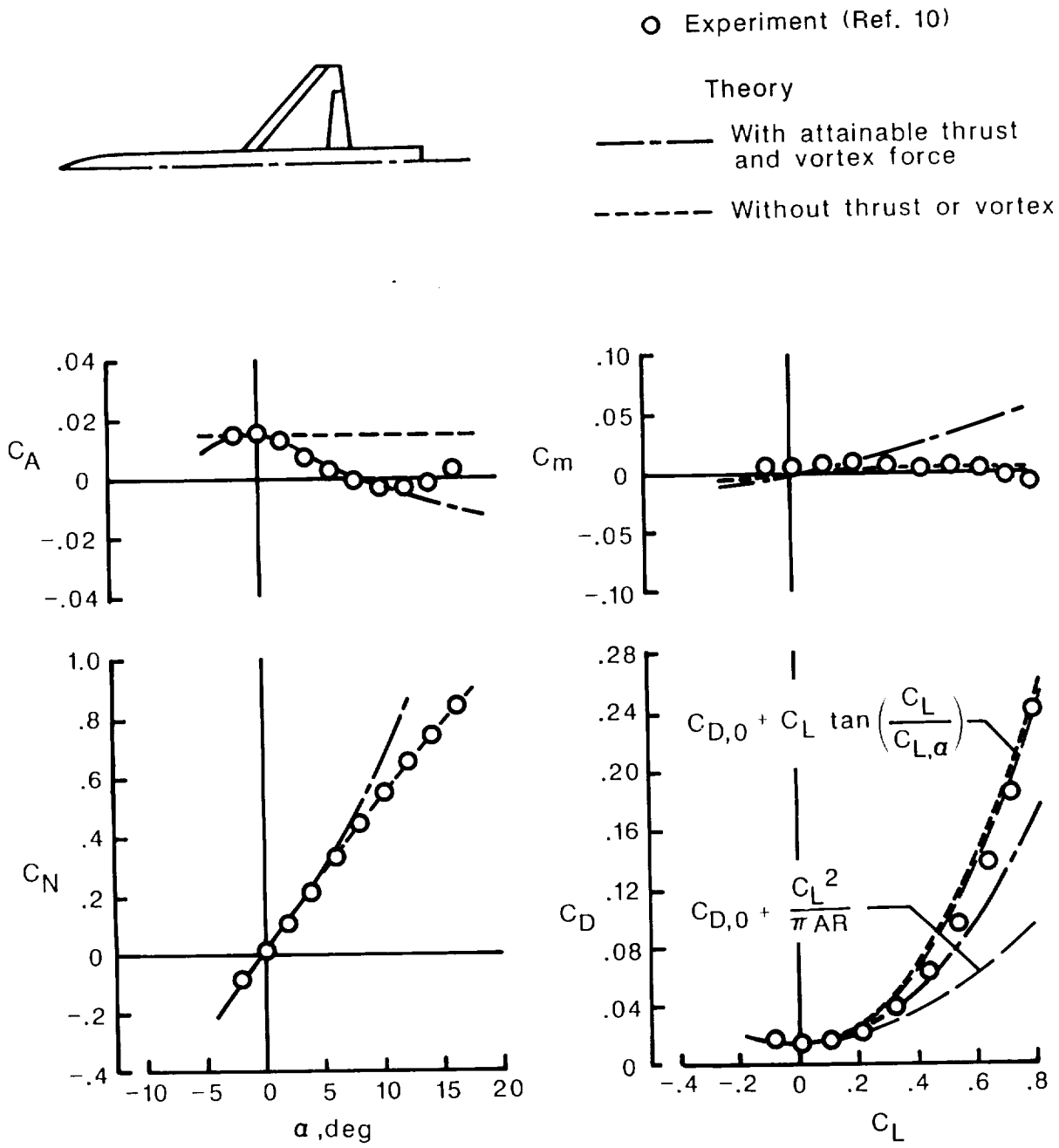

(a) $\delta_{L,n} = 0°$, $\delta_{T,n} = 0°$.

Figure 9. Theoretical and experimental data for 44°-swept trapezoidal-wing fighter. $M = 0.4$; $R = 1.9 \times 10^6$.

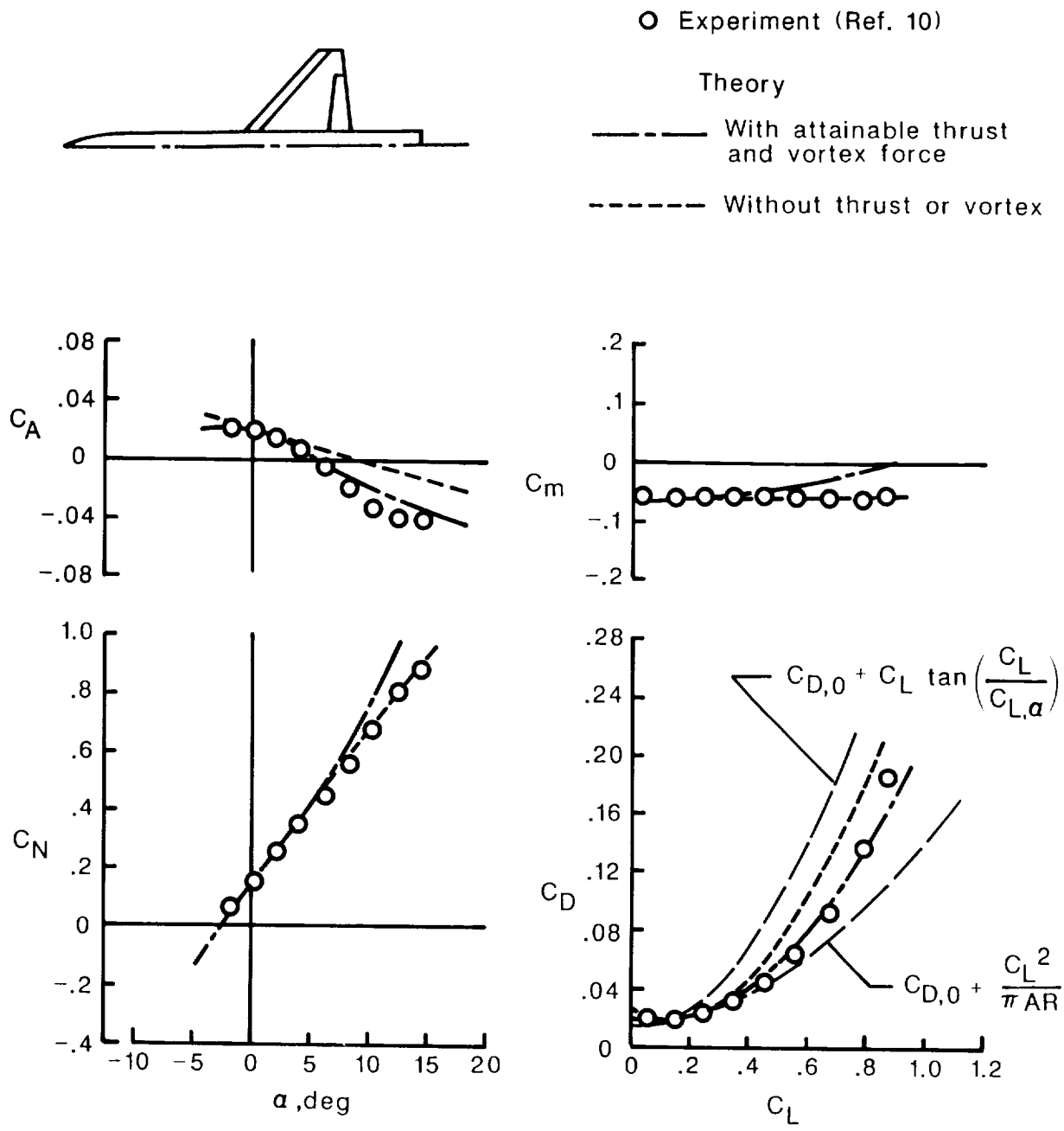

(b) $\delta_{L,n} = 8°$, $\delta_{T,n} = 8°$.

Figure 9. Continued.

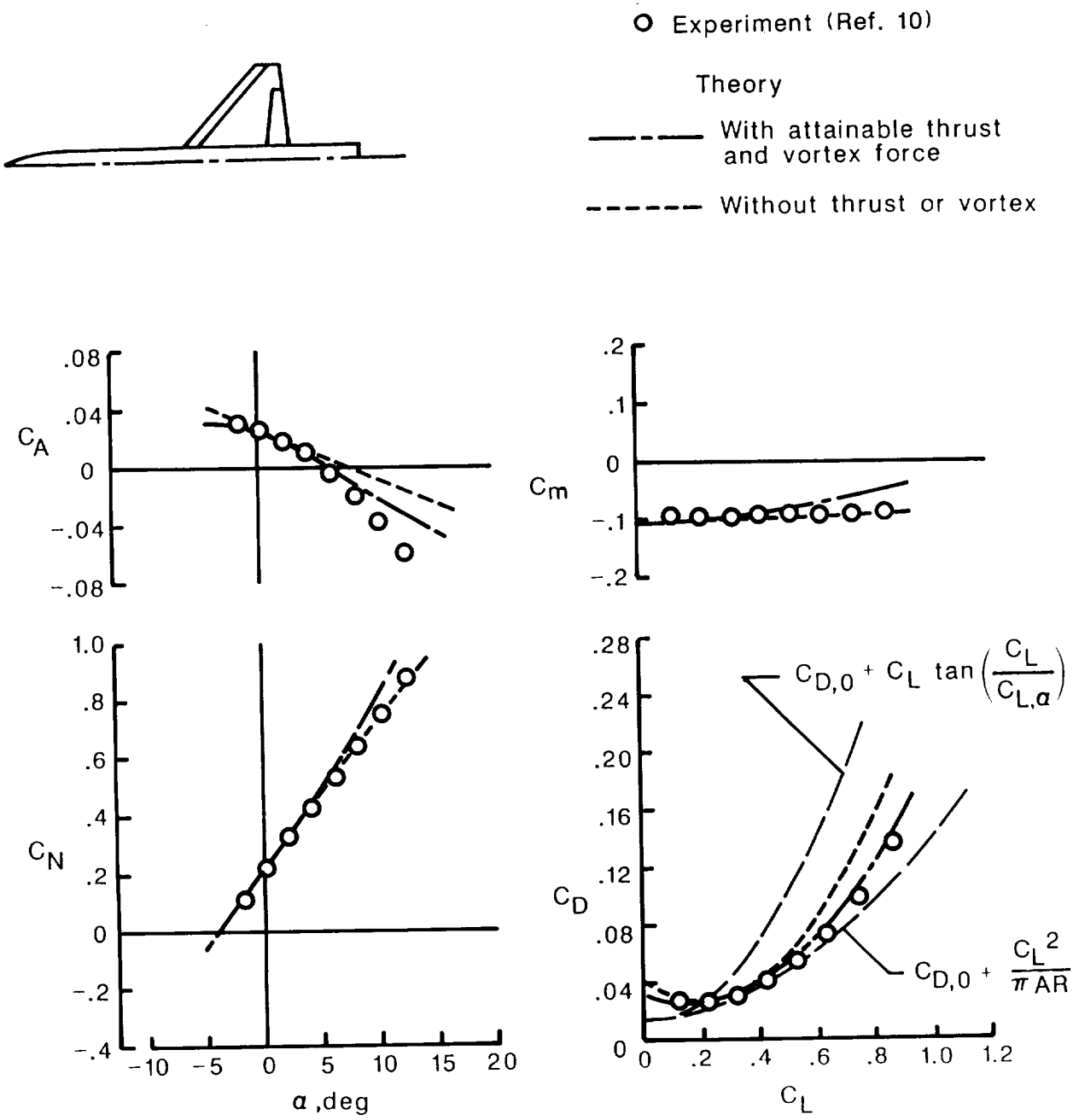

(c) $\delta_{L,n} = 12°$, $\delta_{T,n} = 12°$.

Figure 9. Continued.

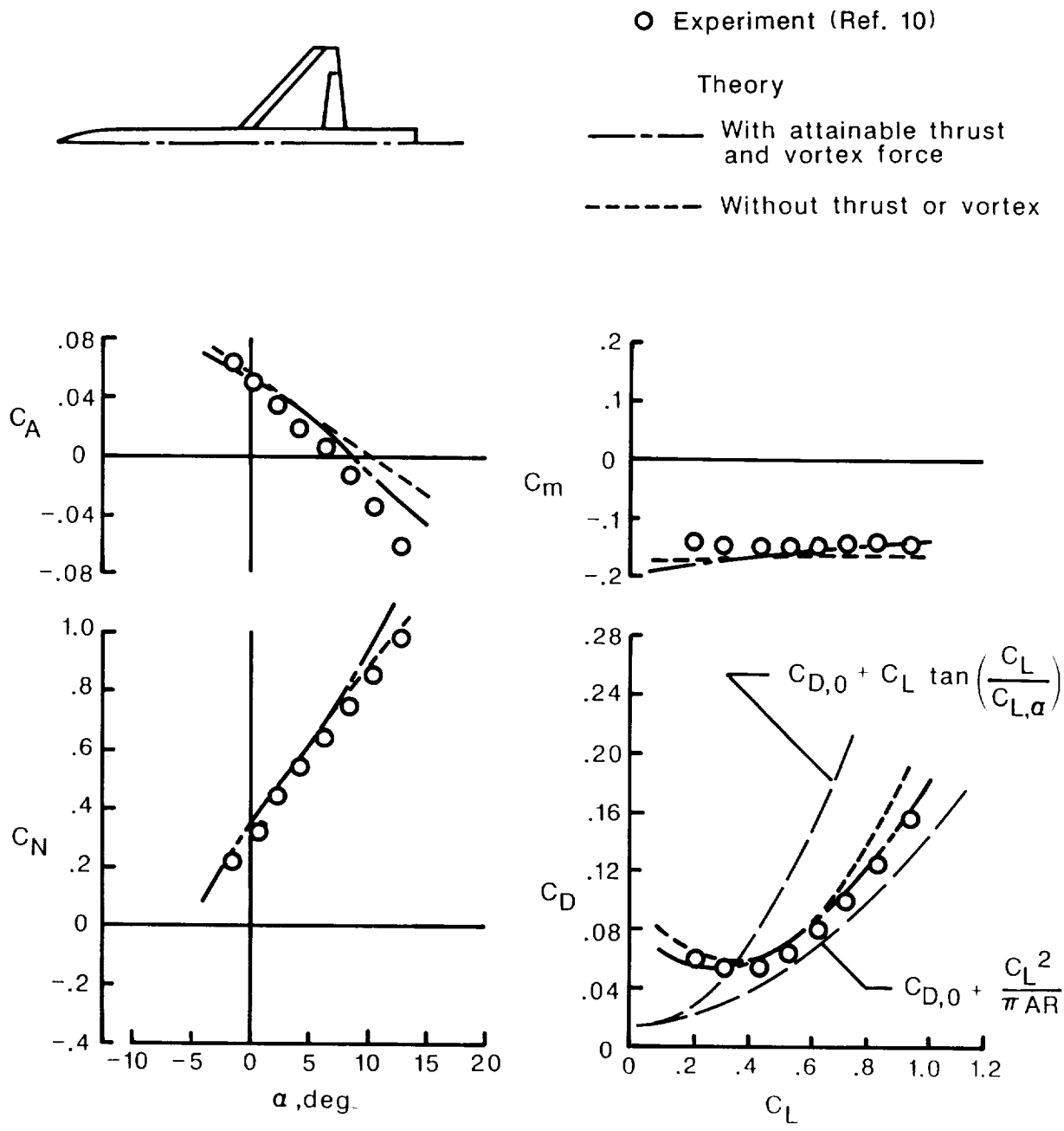

(d) $\delta_{L,n} = 20°$, $\delta_{T,n} = 20°$.

Figure 9. Concluded.

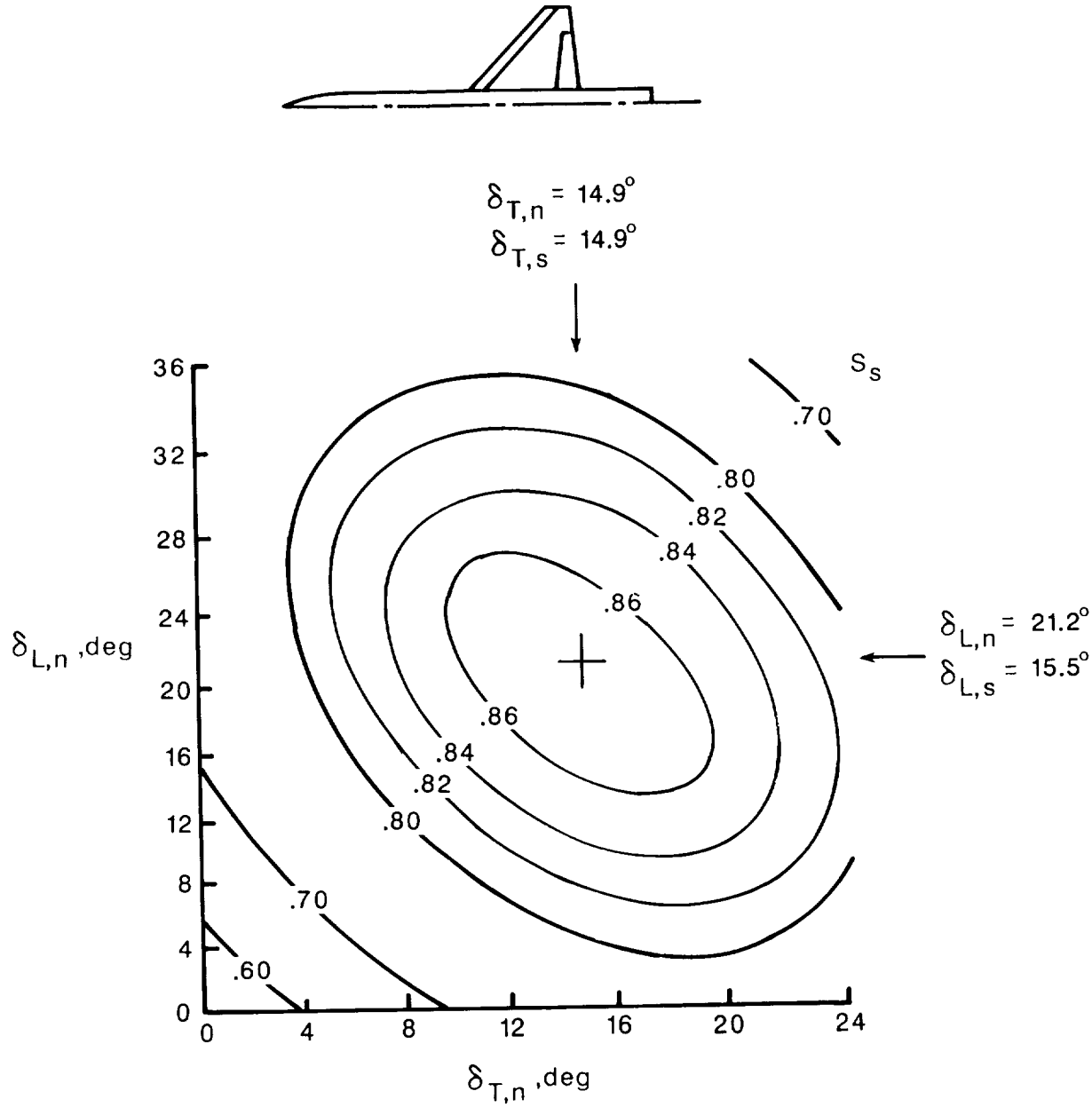

Figure 10. Suction-parameter contour map for 44°-swept trapezoidal-wing fighter. $C_L = 0.8$; $M = 0.4$; $R = 1.9 \times 10^6$.

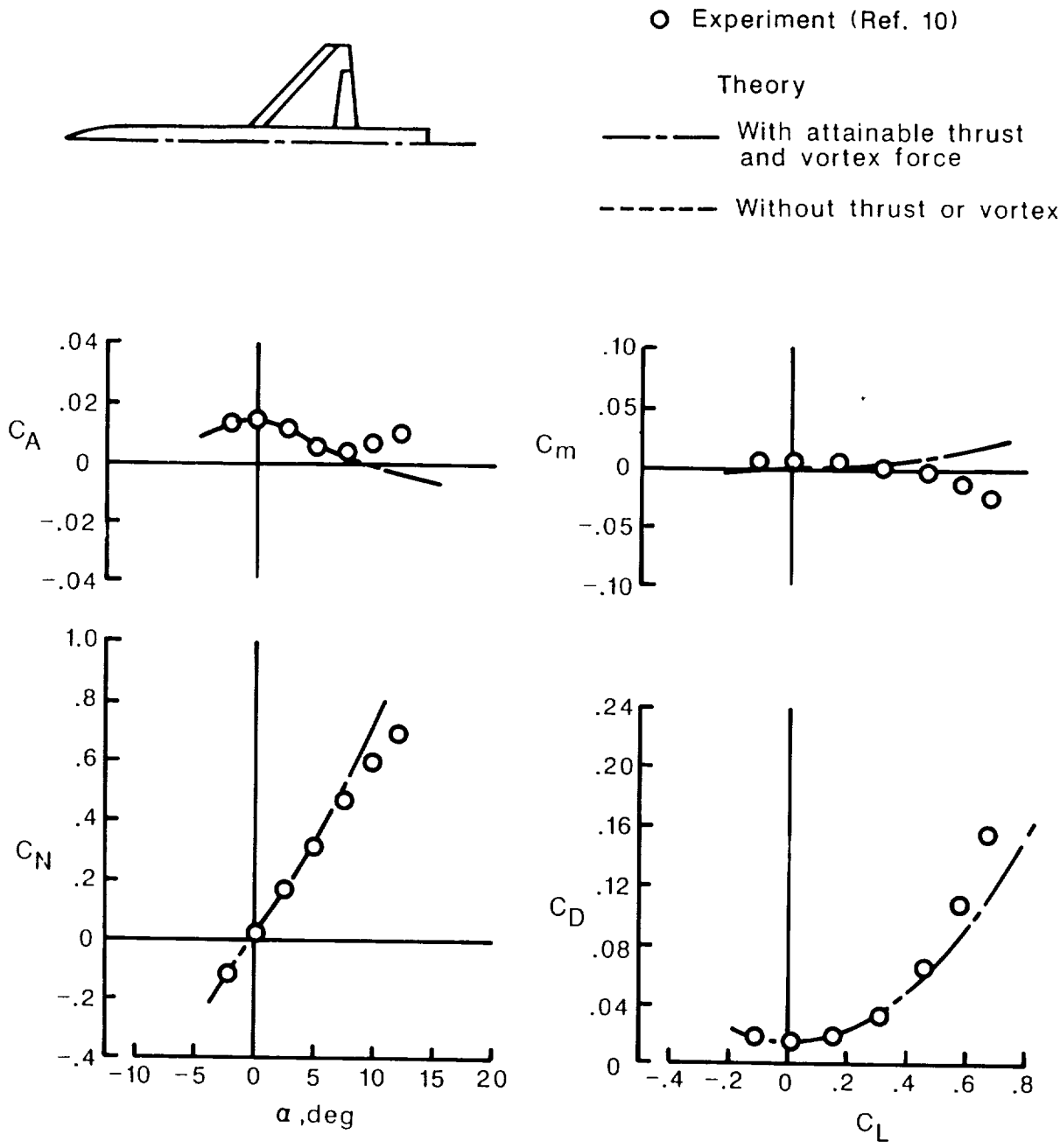

(a) $\delta_{L,n} = 0°$, $\delta_{T,n} = 0°$.

Figure 11. Theoretical and experimental data for 44°-swept trapezoidal-wing fighter. $M = 0.8$; $R = 3.1 \times 10^6$.

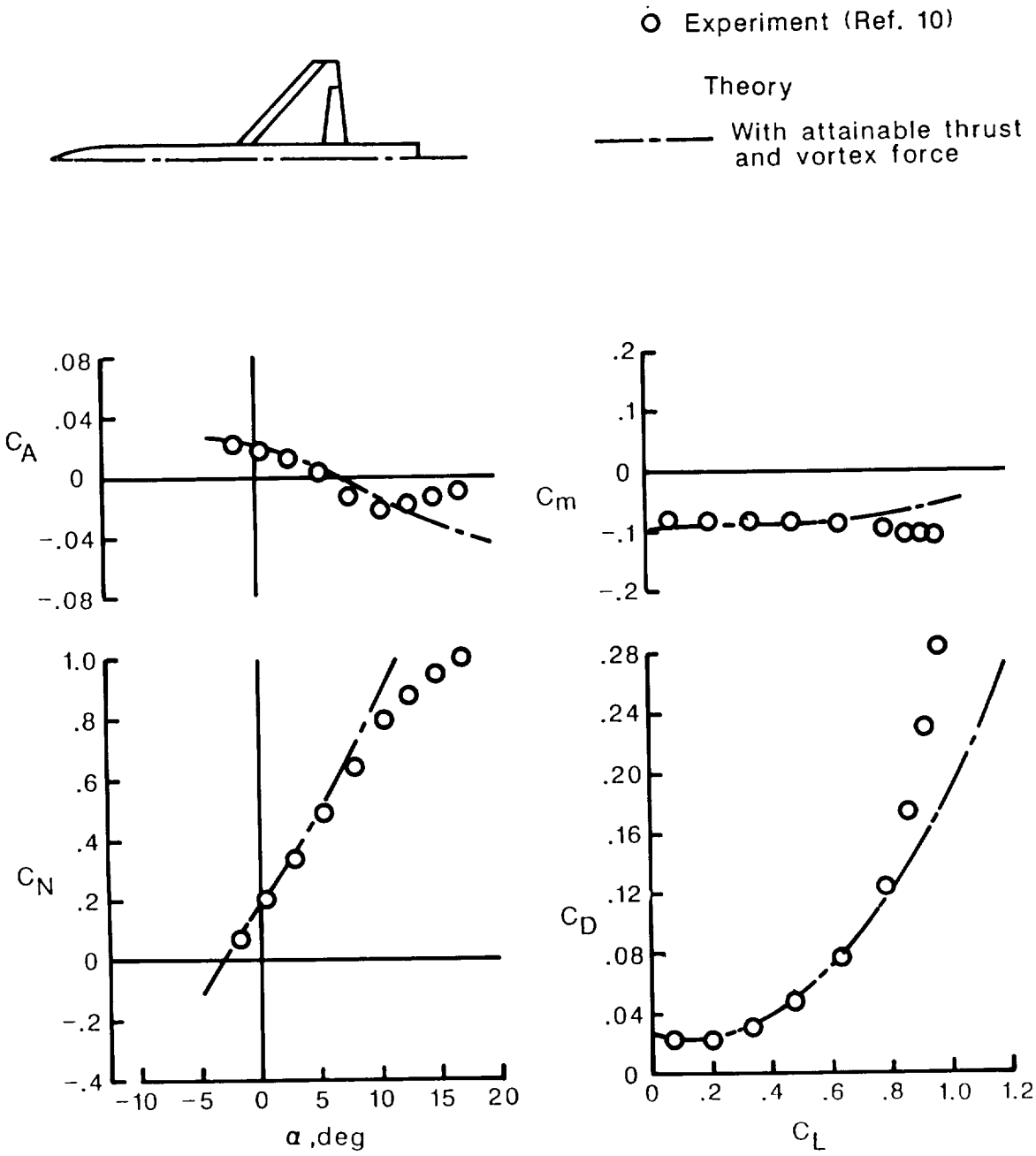

(b) $\delta_{L,n} = 8°$, $\delta_{T,n} = 8°$

Figure 11. Continued.

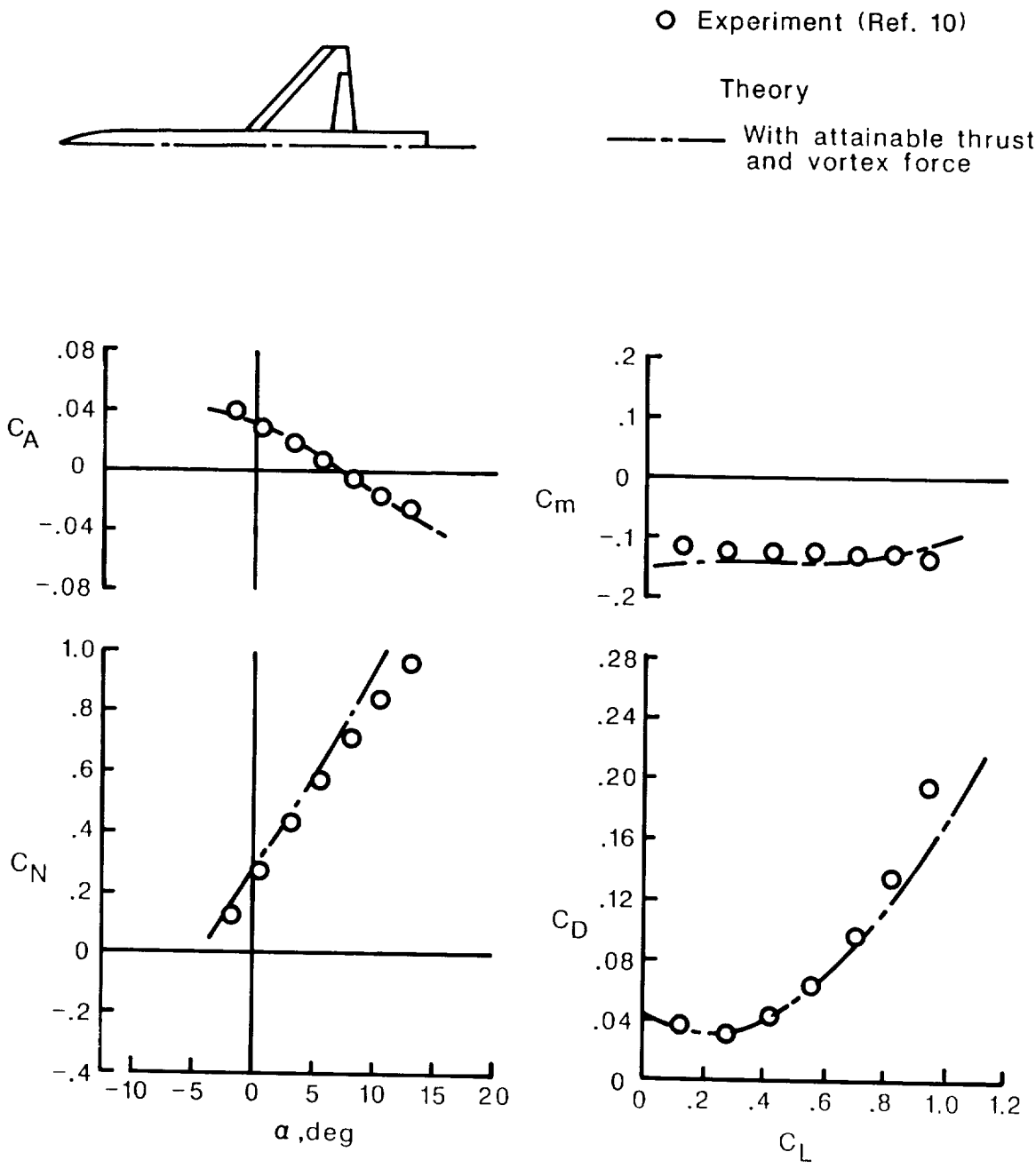

(c) $\delta_{L,n} = 12°$, $\delta_{T,n} = 12°$.

Figure 11. Continued.

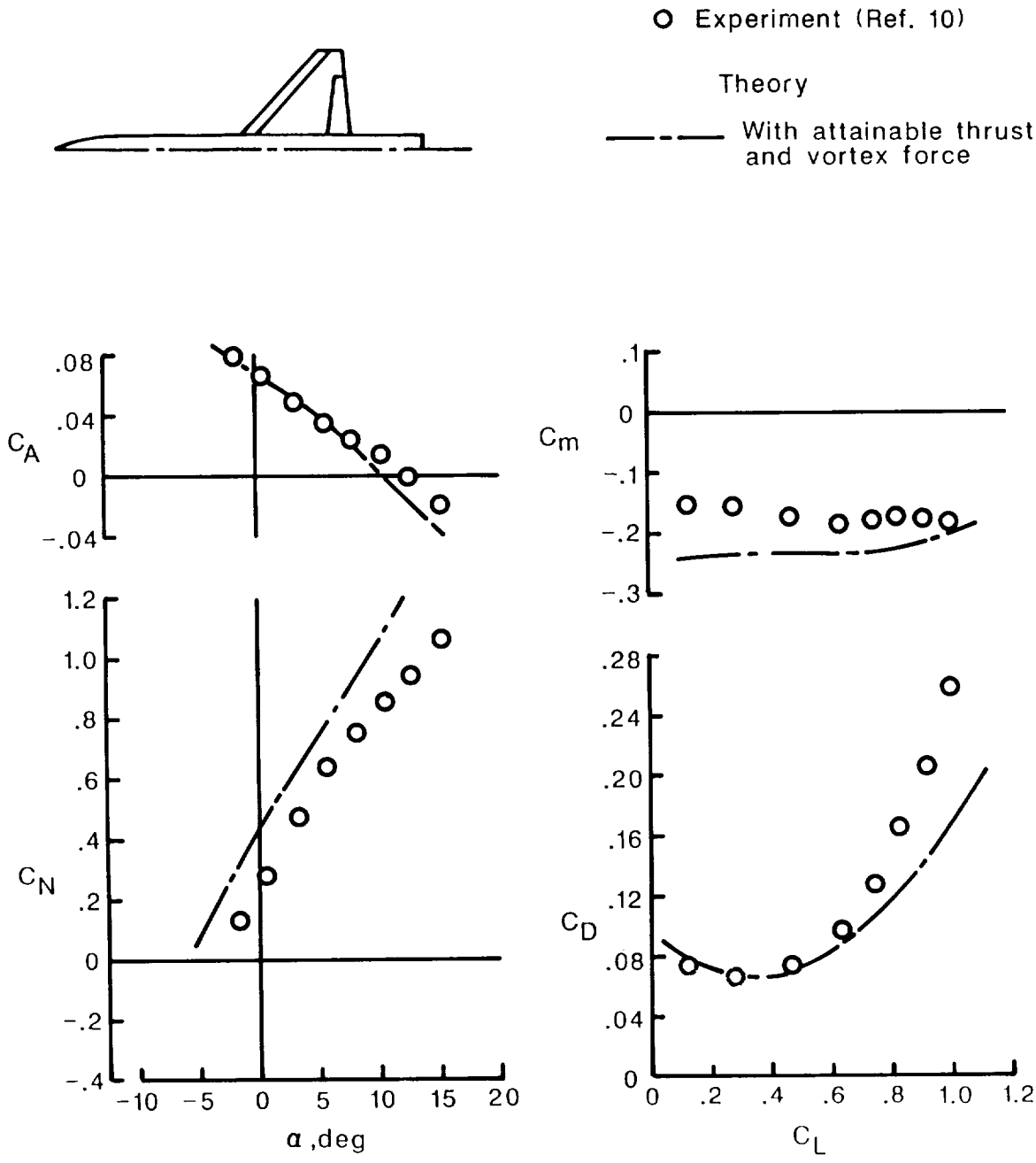

(d) $\delta_{L,n} = 20°$, $\delta_{T,n} = 20°$.

Figure 11. Concluded.

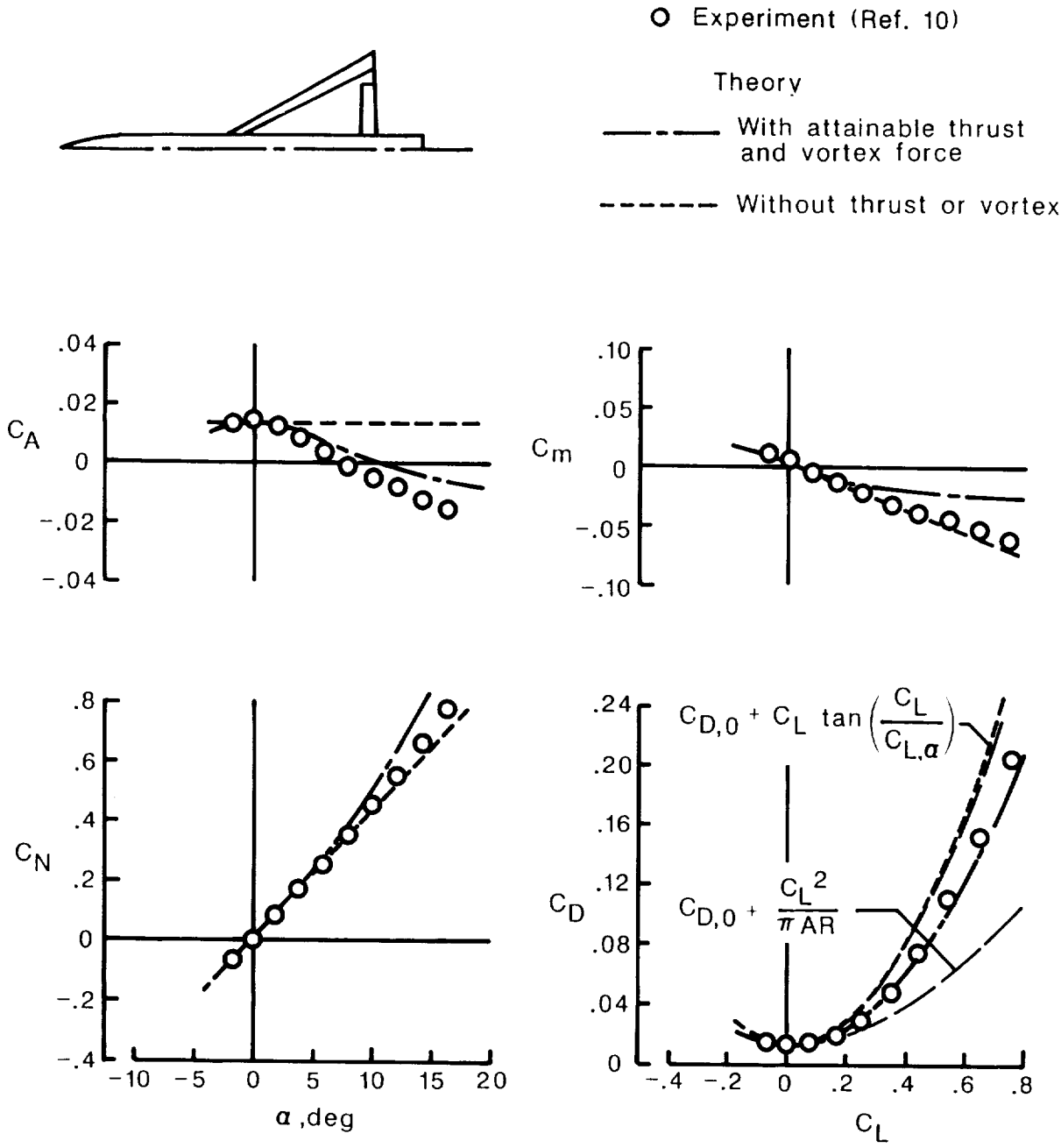

(a) $\delta_{L,n} = 0°$, $\delta_{T,n} = 0°$.

Figure 12. Theoretical and experimental data for 60°-swept delta-wing fighter with rounded leading-edge 64A00X airfoil. $M = 0.4$; $R = 2.5 \times 10^6$.

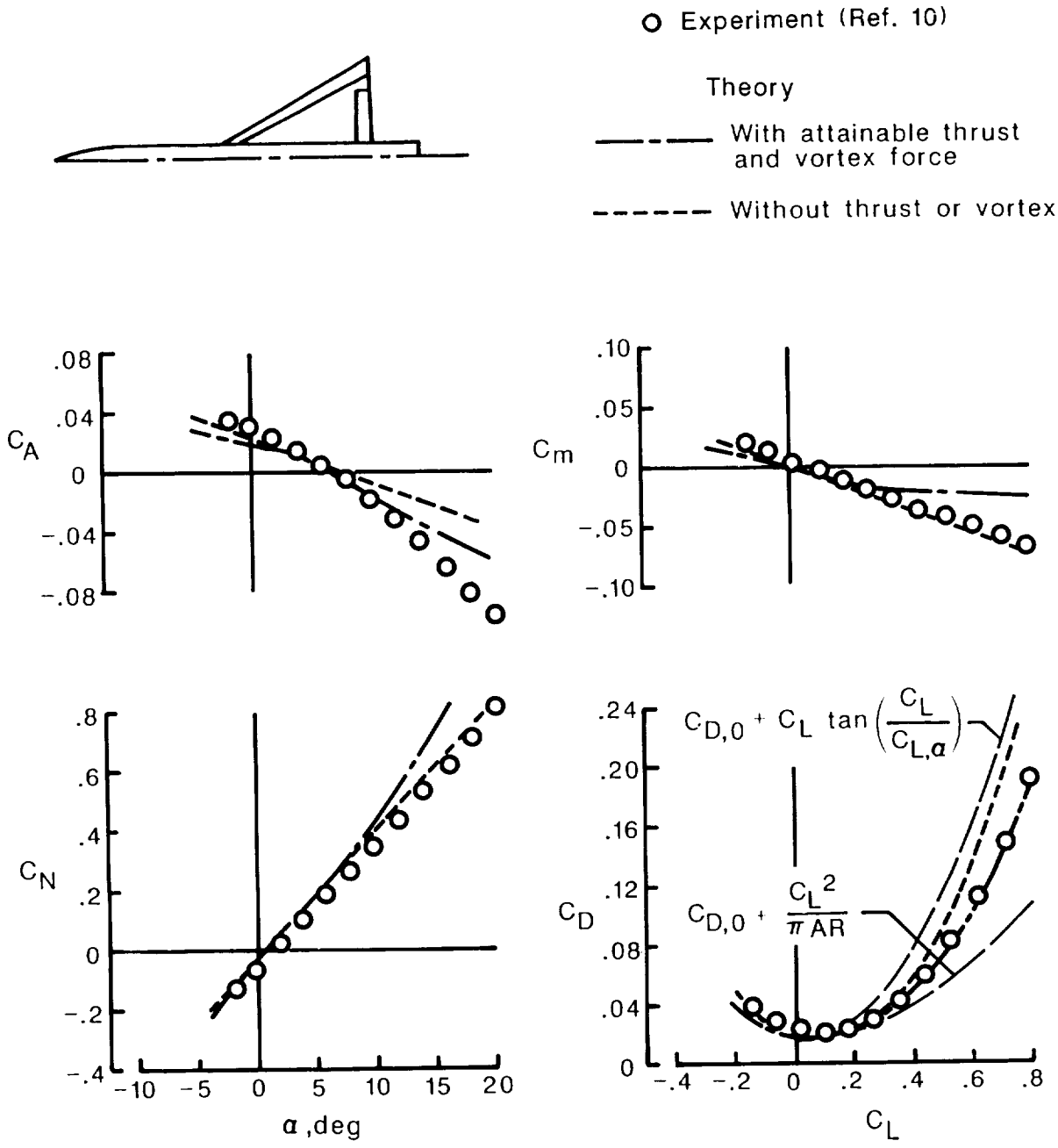

(b) $\delta_{L,n} = 20°$, $\delta_{T,n} = 0°$.

Figure 12. Continued.

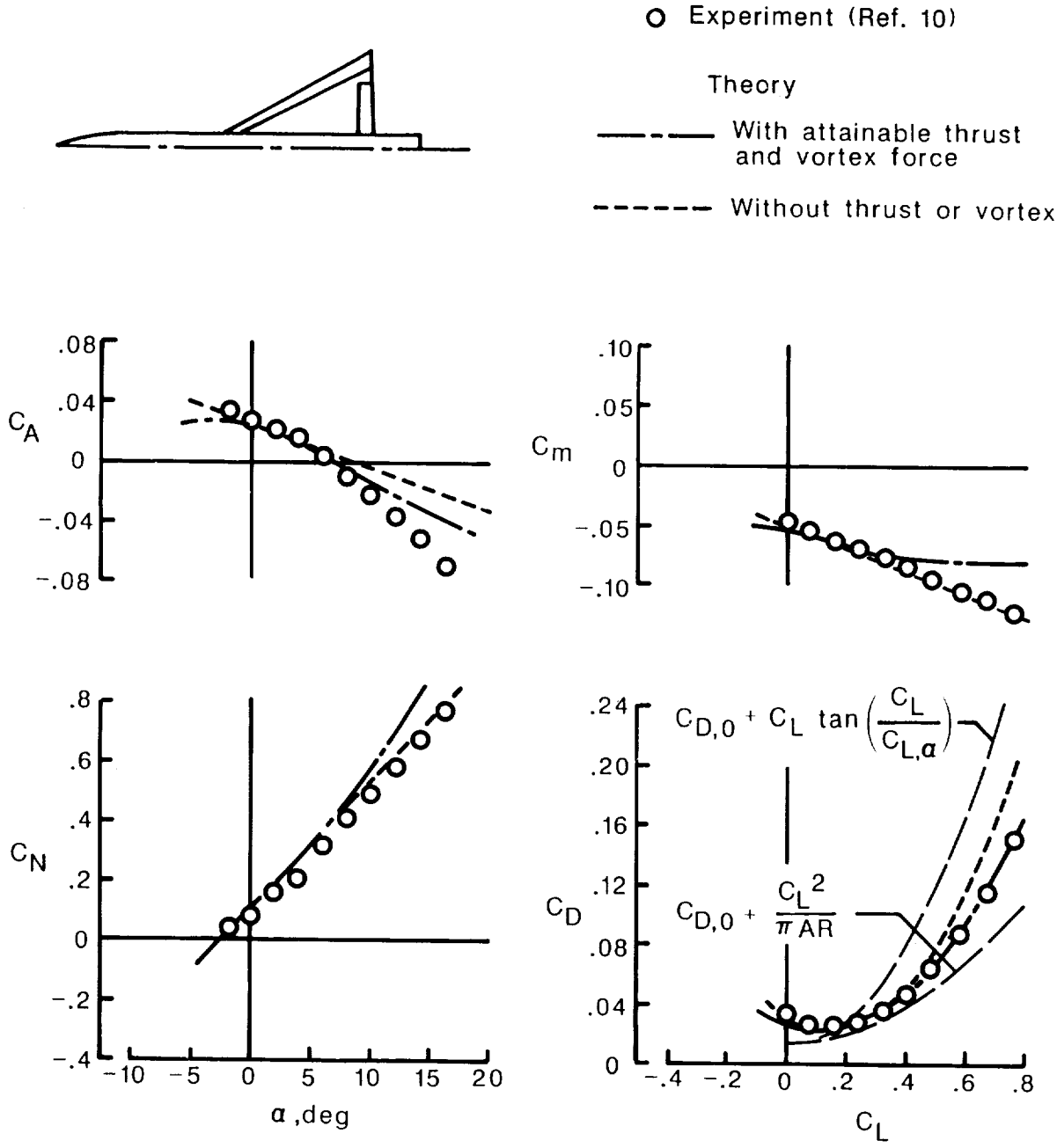

(c) $\delta_{L,n} = 20°$, $\delta_{T,n} = 10°$.

Figure 12. Continued.

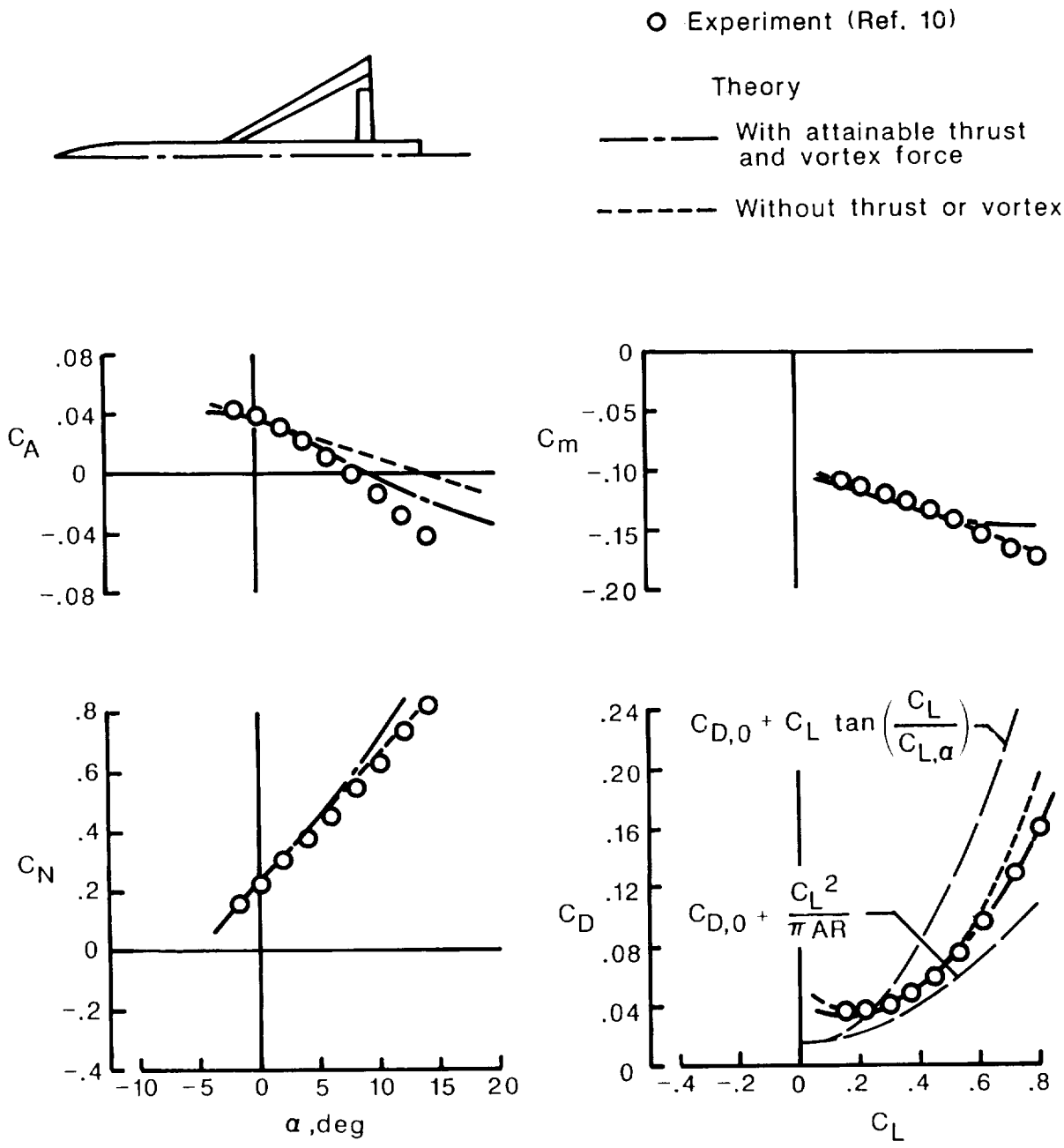

(d) $\delta_{L,n} = 20°$, $\delta_{T,n} = 20°$.

Figure 12. Concluded.

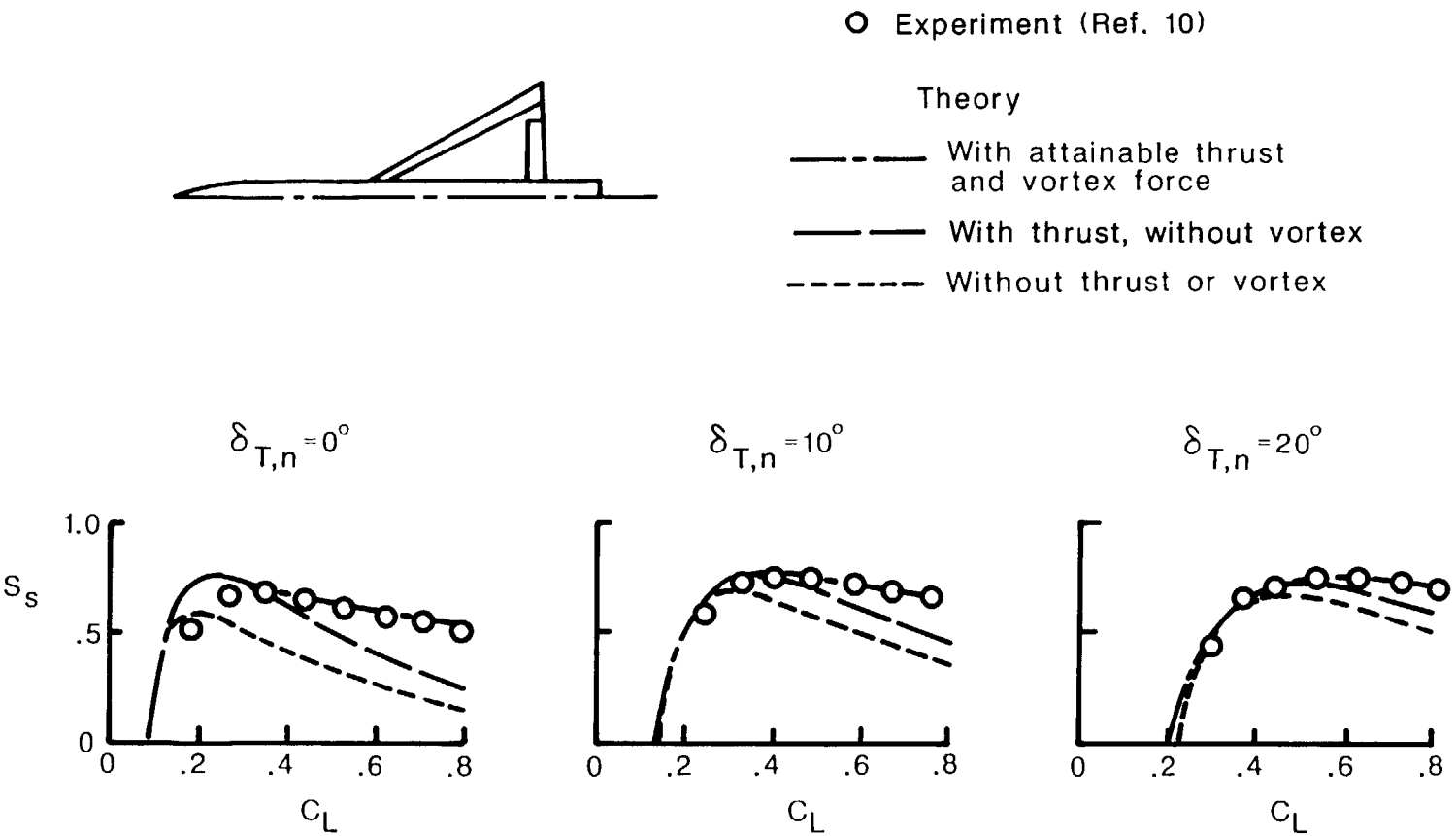

Figure 13. Suction-parameter variation with lift coefficient for various trailing-edge flap deflection angles. 60°-swept delta-wing fighter with rounded leading-edge 64A00X airfoil; $\delta_{L,n} = 20°$; $M = 0.4$; $R = 2.5 \times 10^6$.

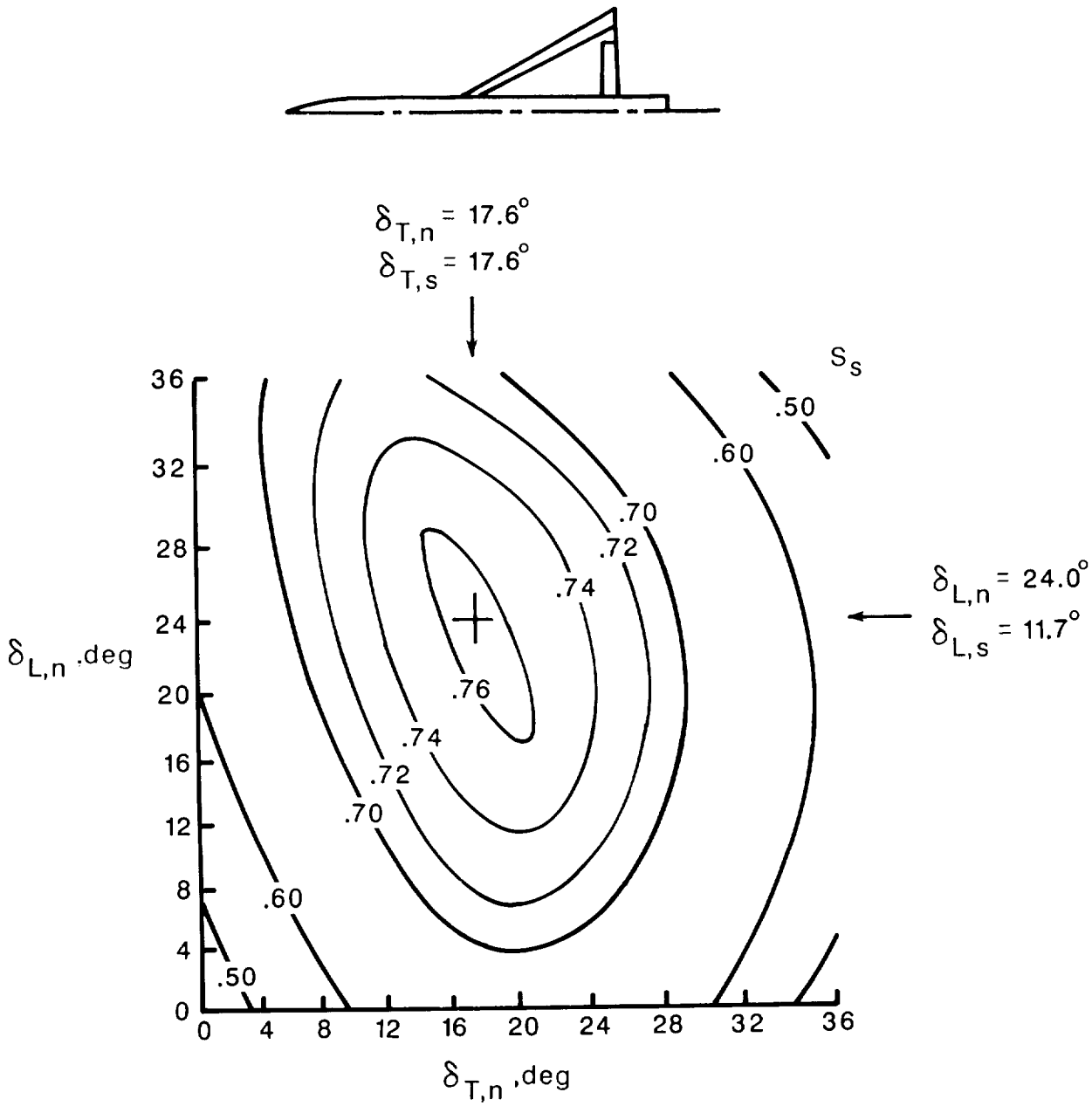

Figure 14. Suction-parameter contour map for 60°-swept delta-wing fighter with rounded leading-edge 64A00X airfoil. $C_L = 0.6$; $M = 0.4$; $R = 2.5 \times 10^6$.

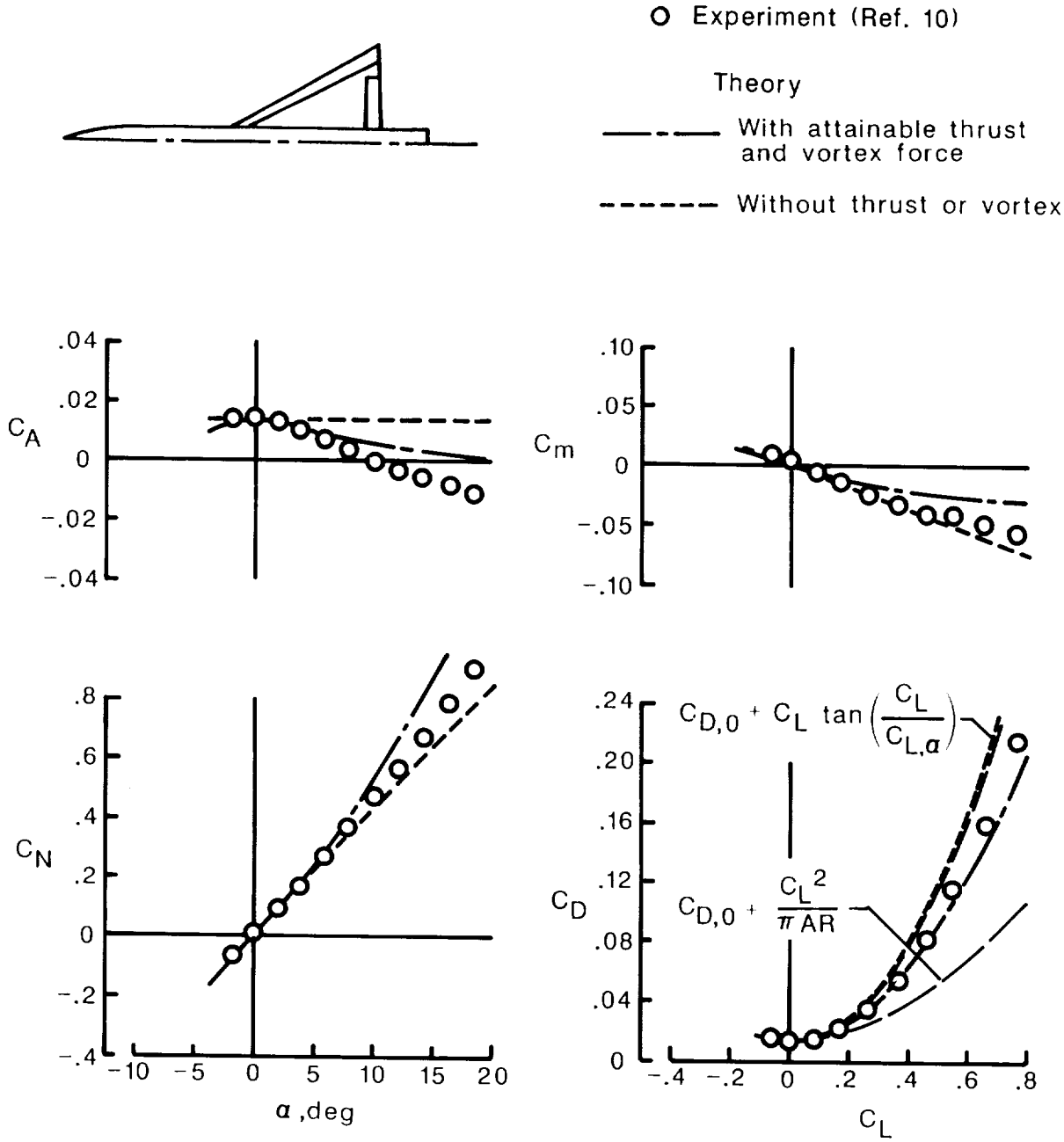

(a) $\delta_{L,n} = 0°$, $\delta_{T,n} = 0°$.

Figure 15. Theoretical and experimental data for 60°-swept delta-wing fighter with sharp leading-edge airfoil. $M = 0.4$; $R = 2.5 \times 10^6$.

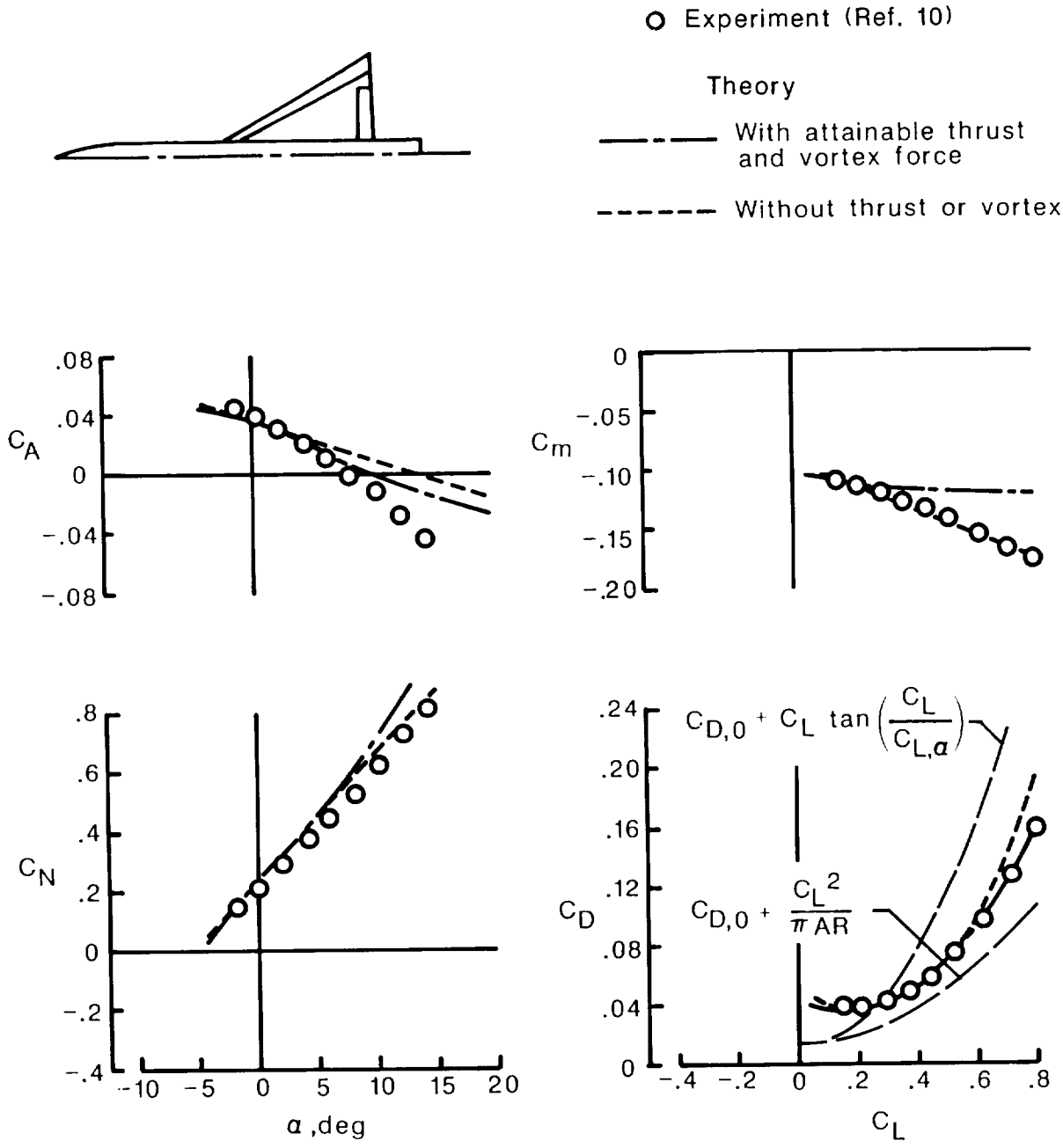

(b) $\delta_{L,n} = 20°$, $\delta_{T,n} = 20°$.

Figure 15. Concluded.

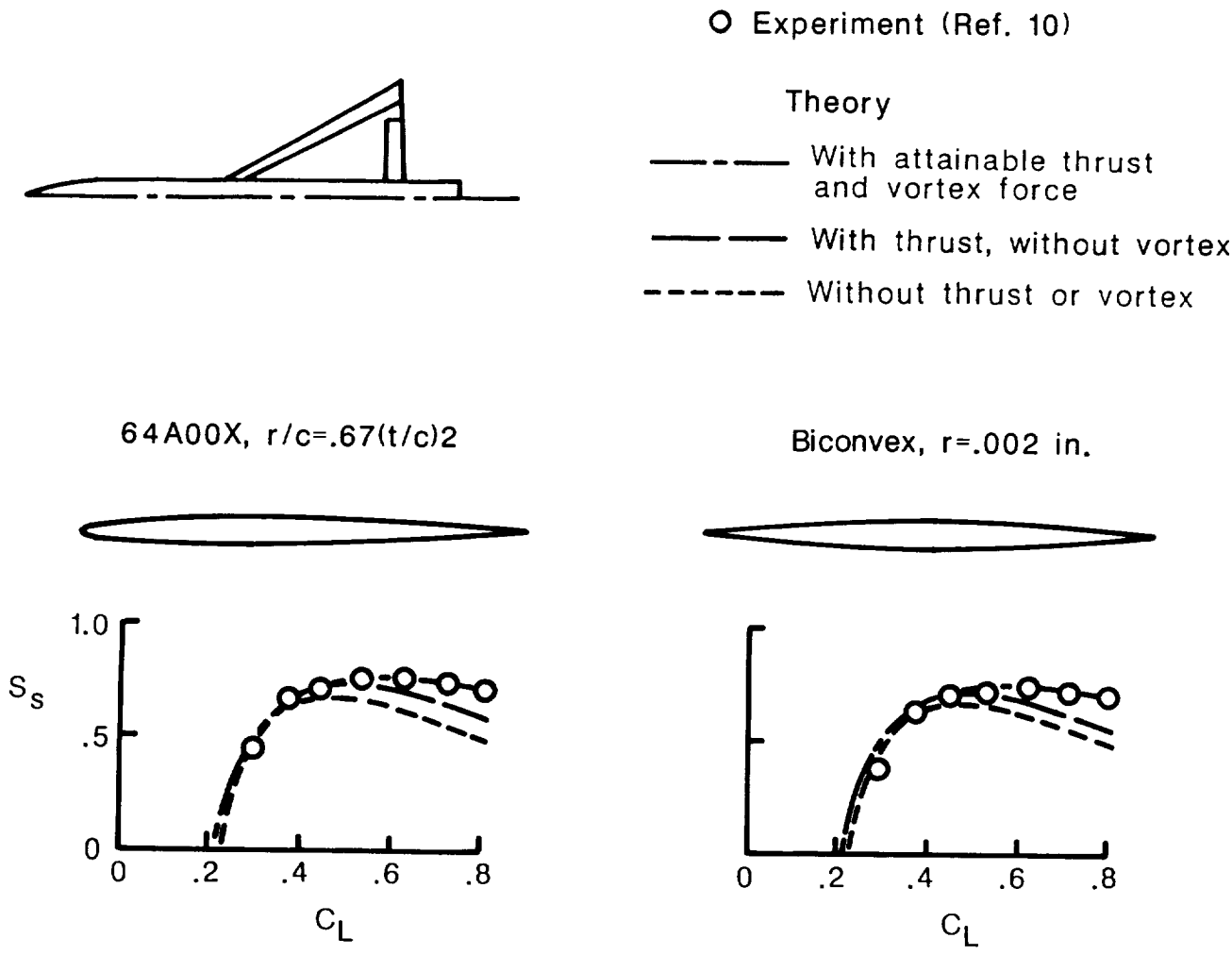

Figure 16. Suction-parameter data for rounded and sharp leading-edge airfoil sections. 60°-swept delta-wing fighter; $\delta_{L,n} = 20°$; $\delta_{T,n} = 20°$; $M = 0.4$; $R = 2.5 \times 10^6$.

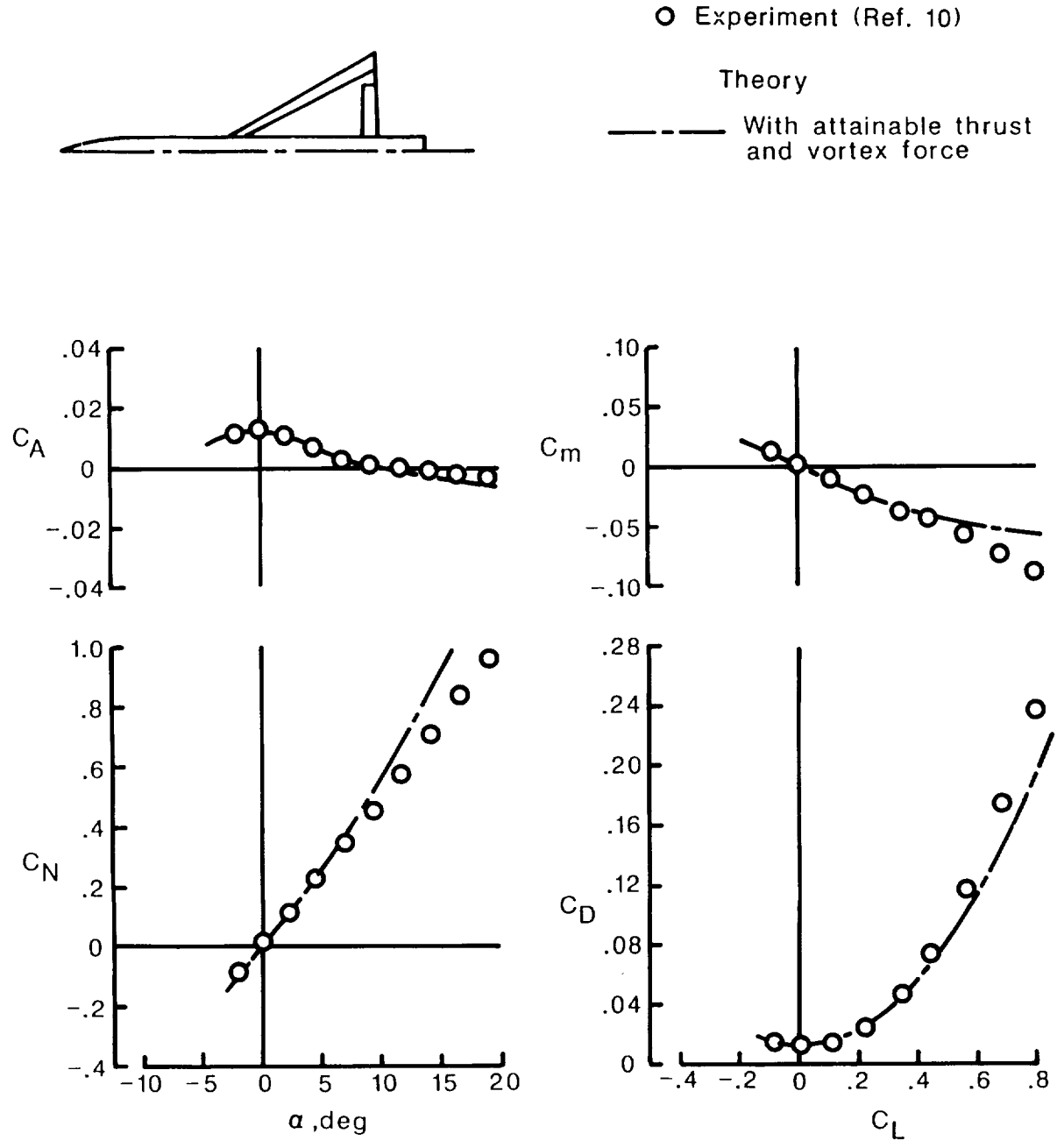

(a) $\delta_{L,n} = 0°$; $\delta_{T,n} = 0°$.

Figure 17. Theoretical and experimental data for 60°-swept delta-wing fighter with rounded leading-edge 64A00X airfoil. $M = 0.8$; $R = 4.1 \times 10^6$.

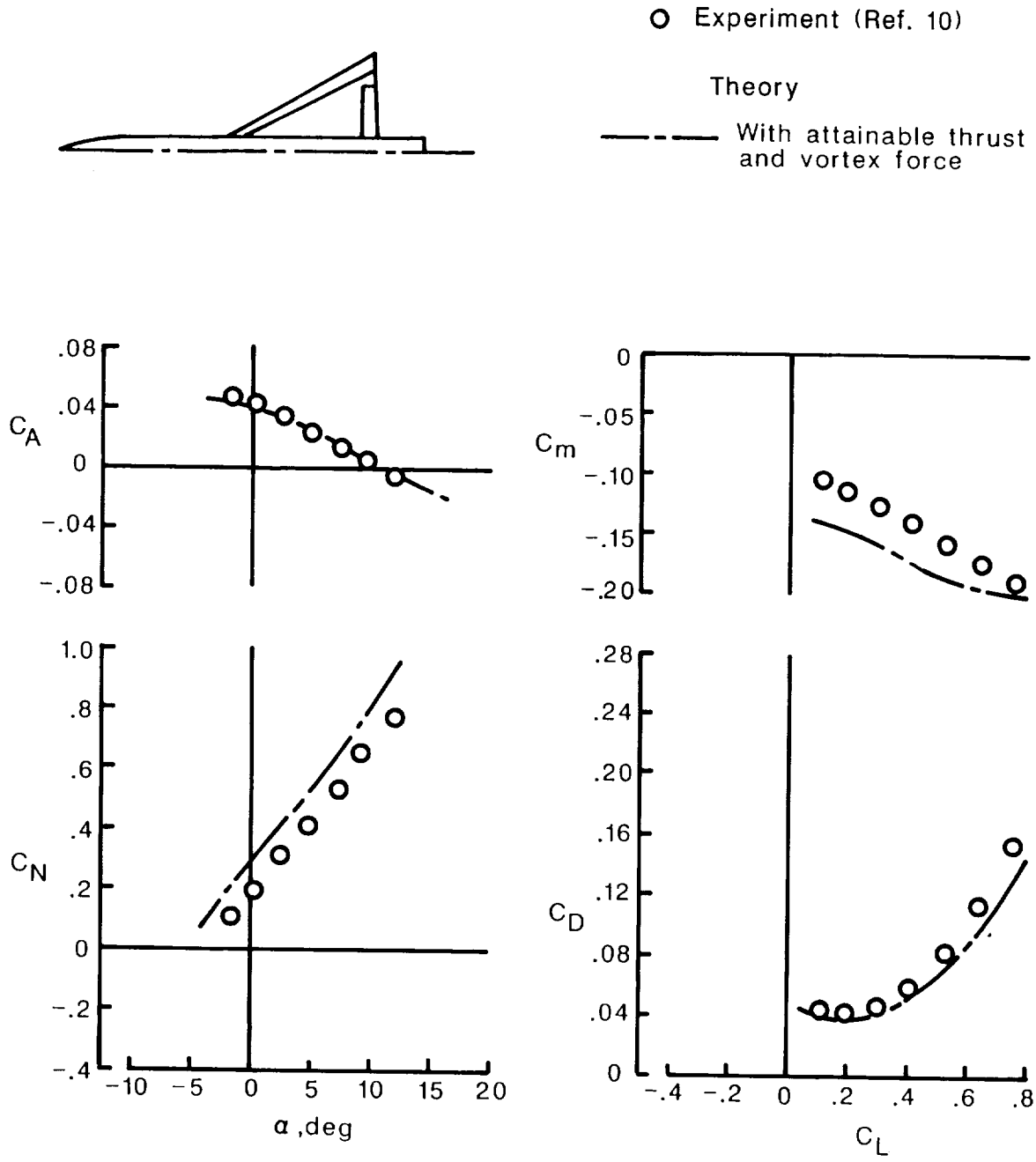

(b) $\delta_{L,n} = 20°$, $\delta_{T,n} = 20°$.

Figure 17. Concluded.

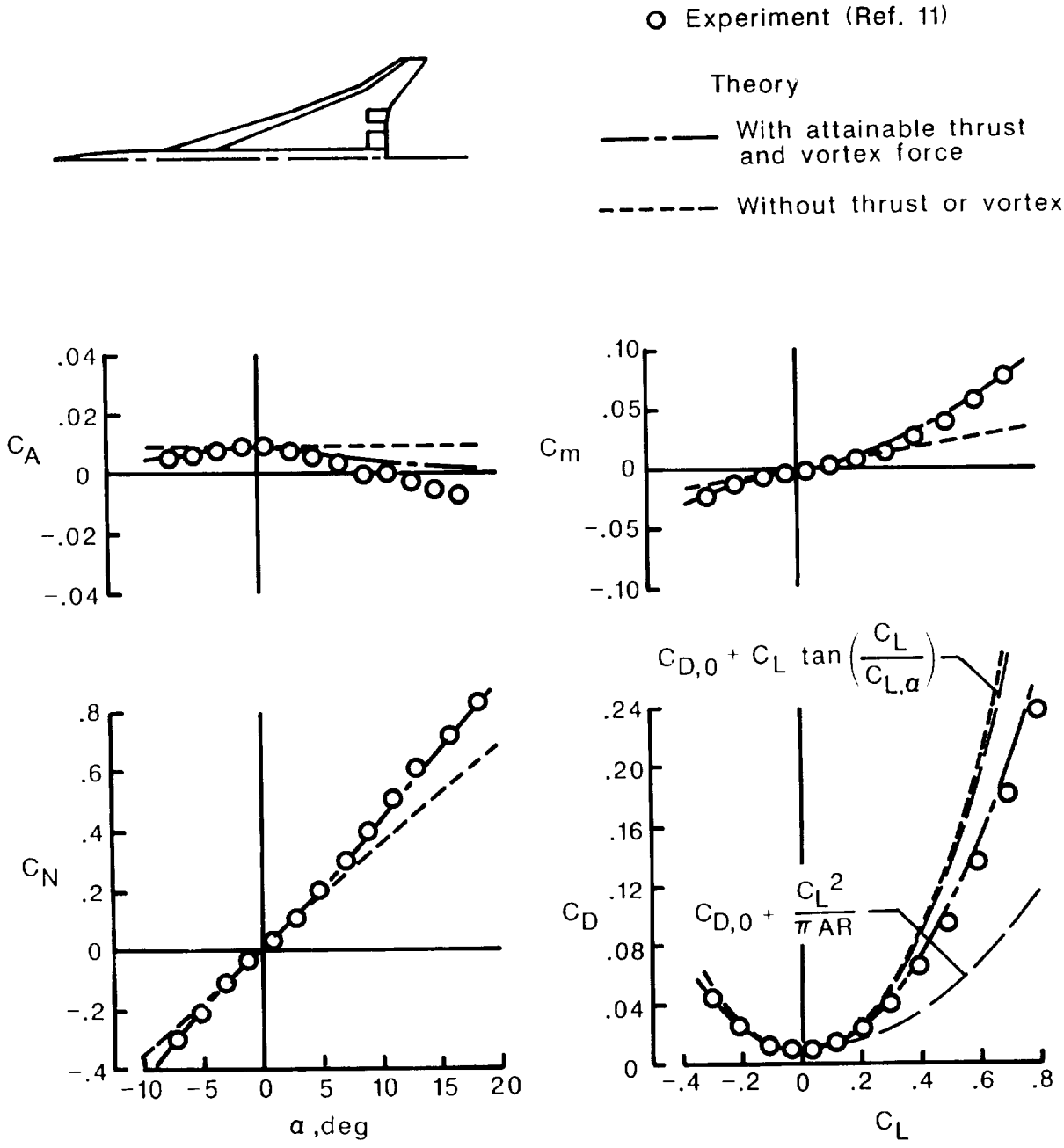

(a) $\delta_{L,n} = 0°$, $\delta_{T,n} = 0°$.

Figure 18. Theoretical and experimental data for generic arrow-wing supersonic transport. $M = 0.25$; $R = 4.8 \times 10^6$.

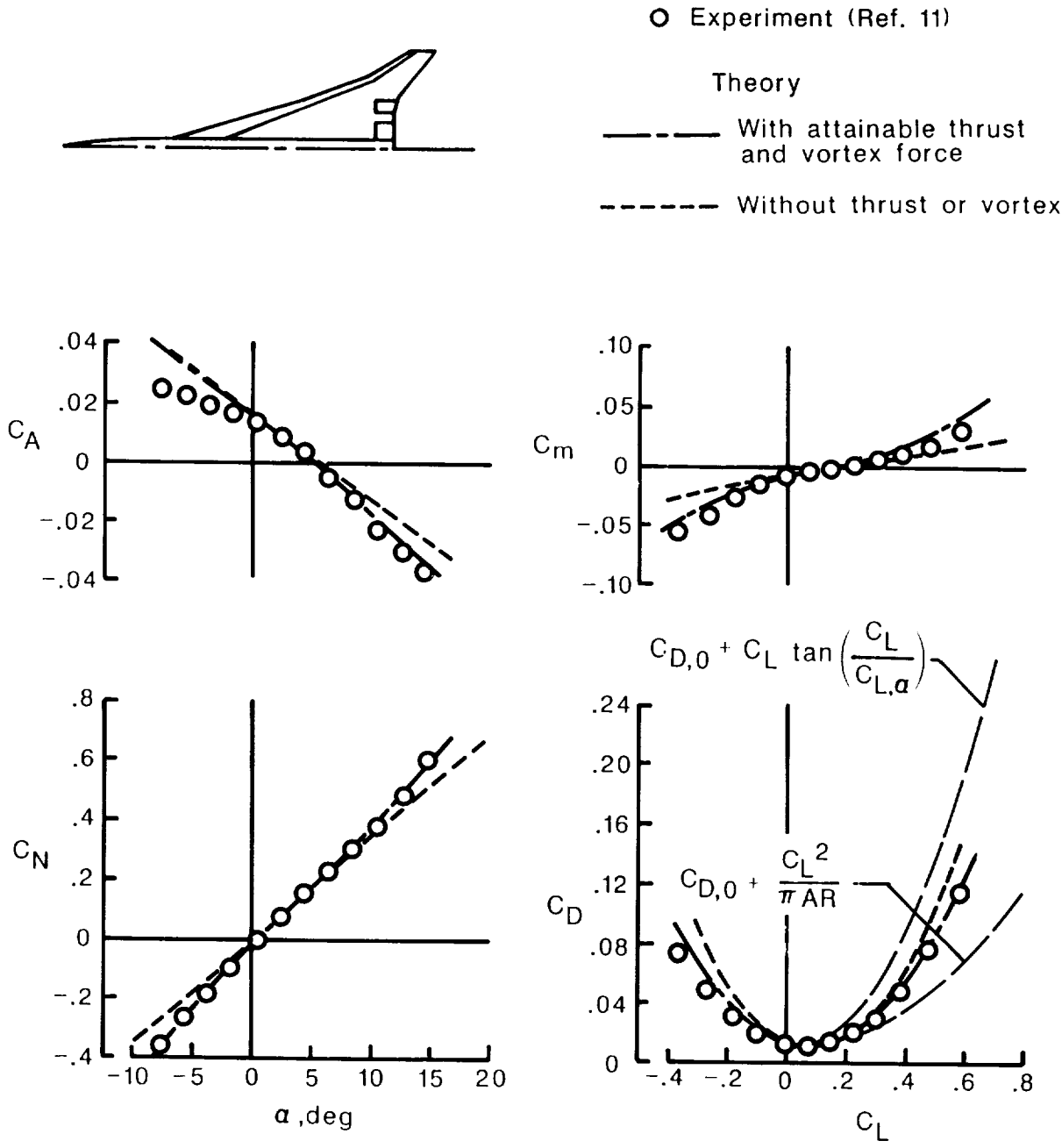

(b) $\delta_{L,n} = 30°$, $\delta_{T,n} = 0°$.

Figure 18. Continued.

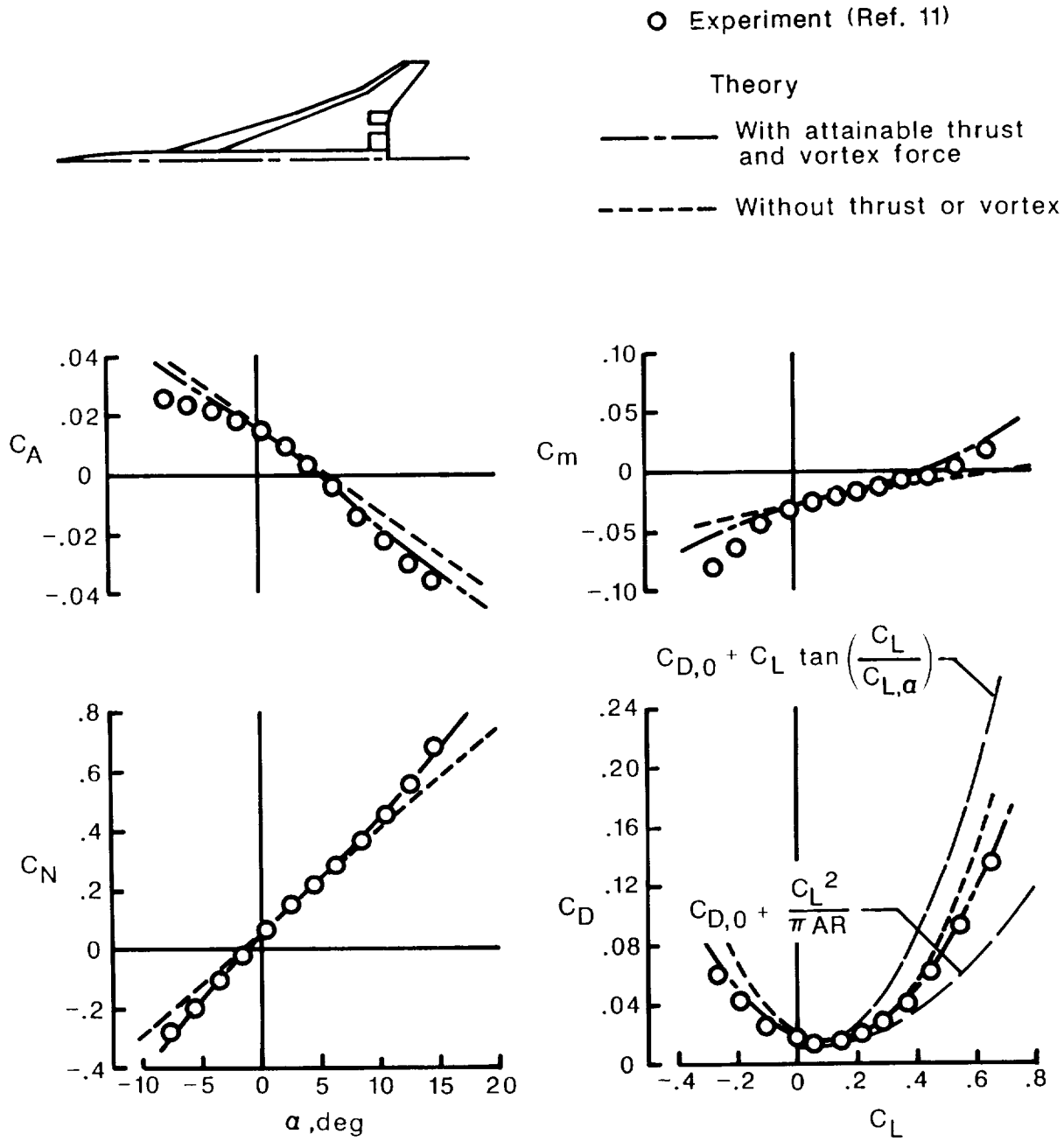

(c) $\delta_{L,n} = 30°$, $\delta_{T,n} = 10°$.

Figure 18. Continued.

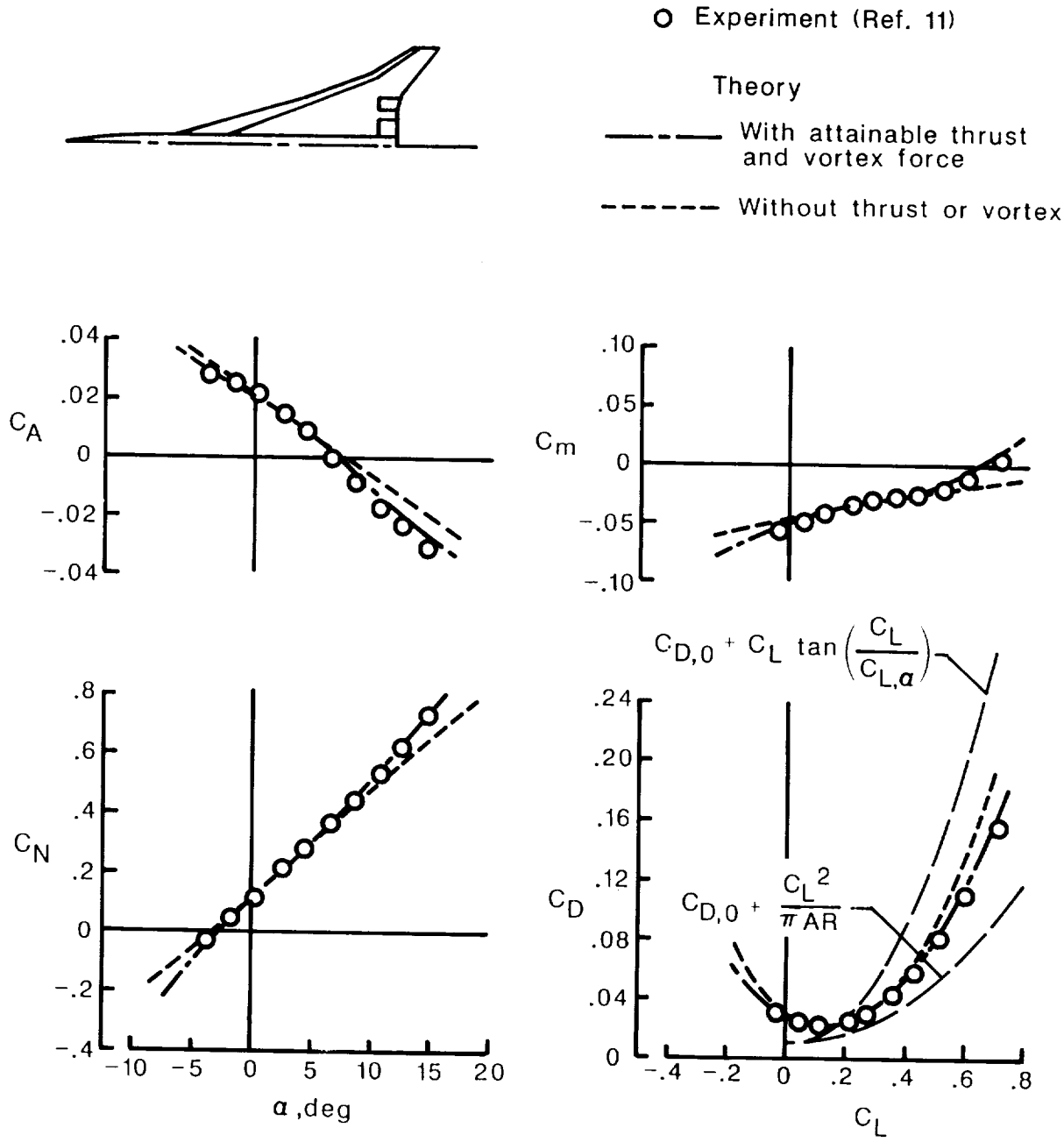

(d) $\delta_{L,n} = 30°$, $\delta_{T,n} = 20°$.

Figure 18. Continued.

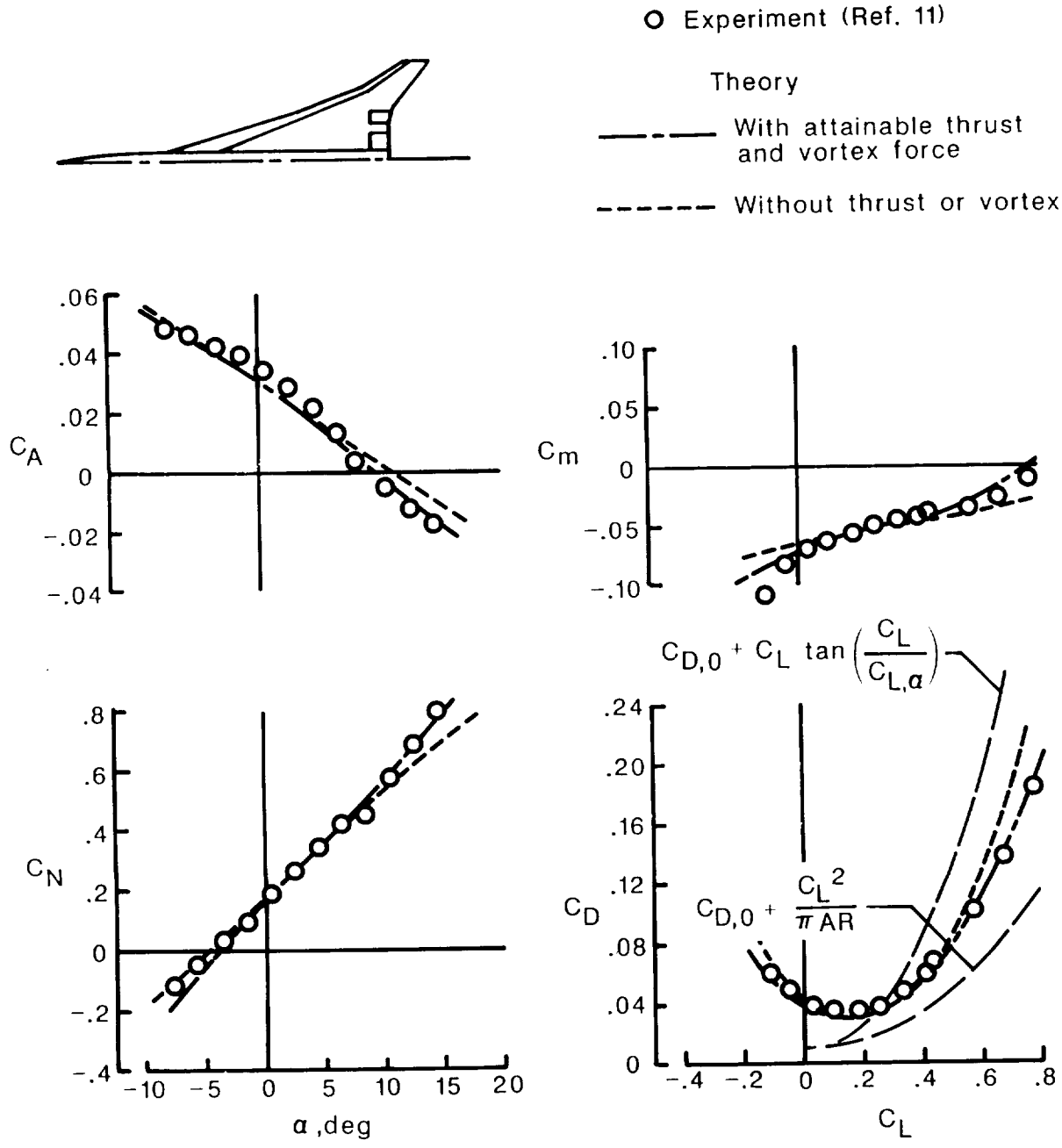

(e) $\delta_{L,n} = 30°$, $\delta_{T,n} = 30°$.

Figure 18. Concluded.

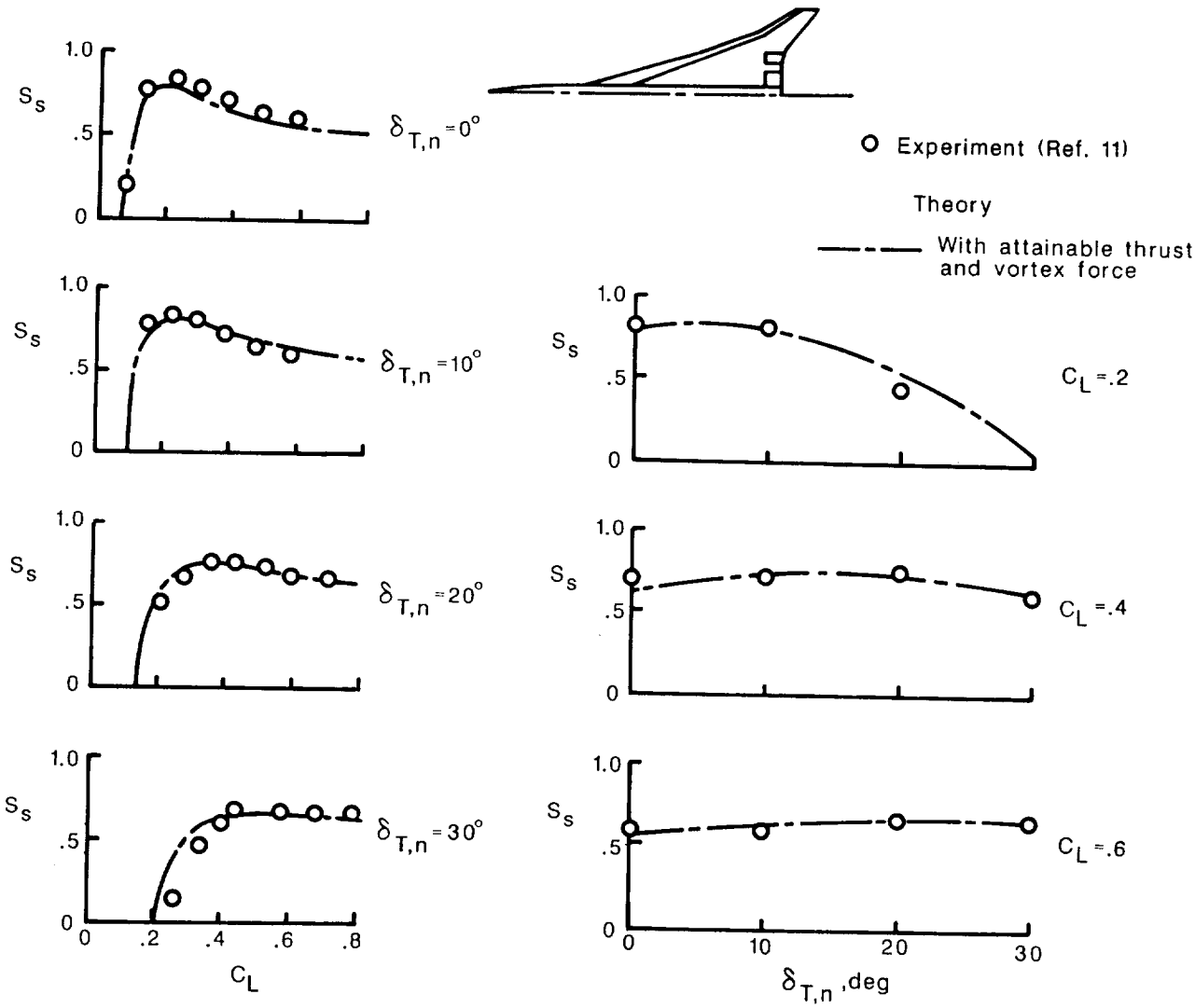

Figure 19. Suction-parameter variation with C_L for various trailing-edge flap deflection angles and suction-parameter-variation with trailing-edge flap deflection angle for selected lift coefficients. Generic arrow-wing supersonic transport; $\delta_{L,n} = 30°$; $M = 0.5$; $R = 4.8 \times 10^6$.

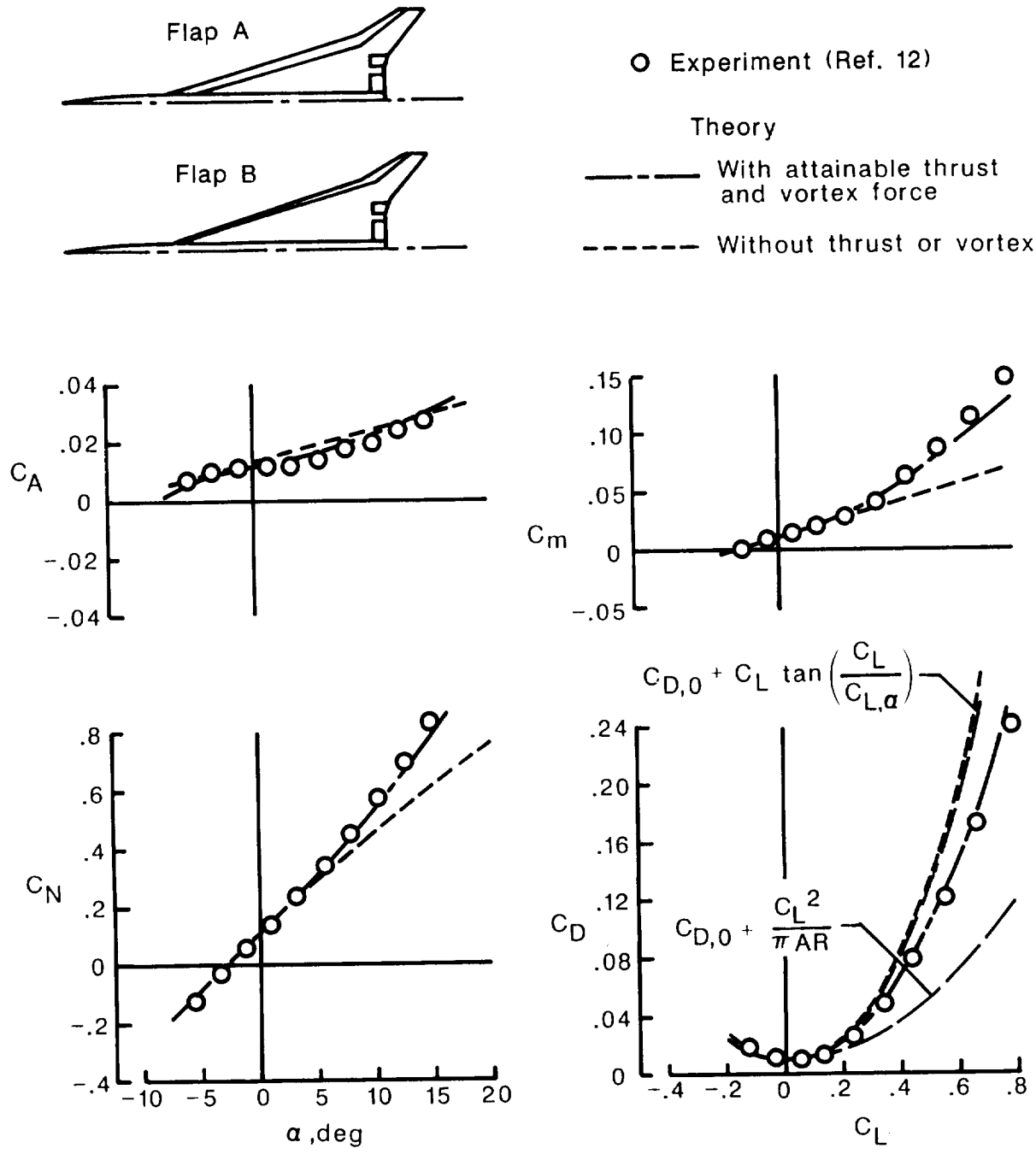

(a) Flap A or flap B; $\delta_{L,n} = 0°$, $\delta_{T,n} = 0°$.

Figure 20. Theoretical and experimental data for advanced arrow-wing supersonic transport. $M = 0.21$; $R = 4.1 \times 10^6$.

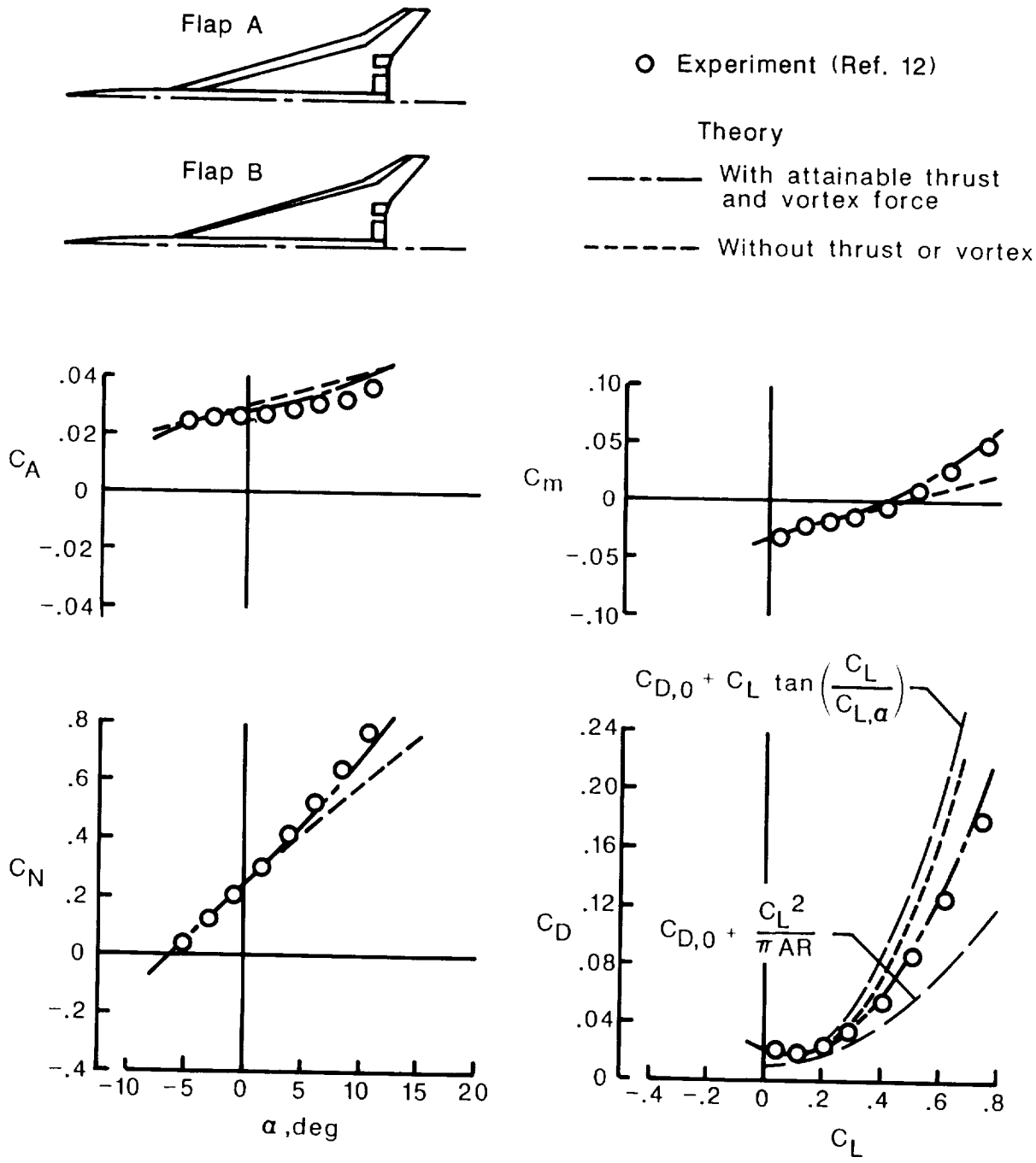

(b) Flap A or flap B; $\delta_{L,n} = 0°$, $\delta_{T,n} = 20°$.

Figure 20. Continued.

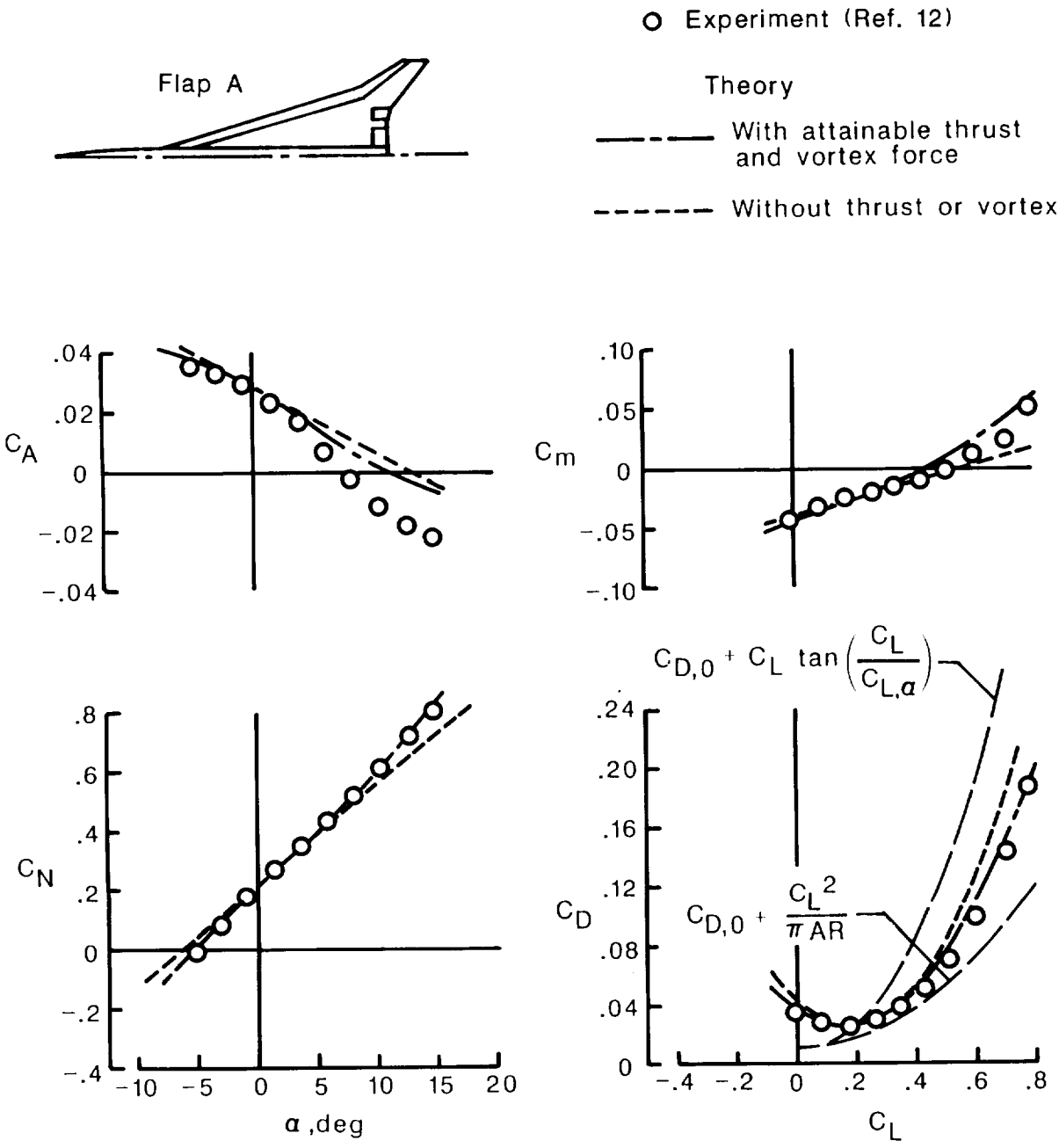

(c) Flap A; $\delta_{L,n} = 30°$, $\delta_{T,n} = 20°$.

Figure 20. Continued.

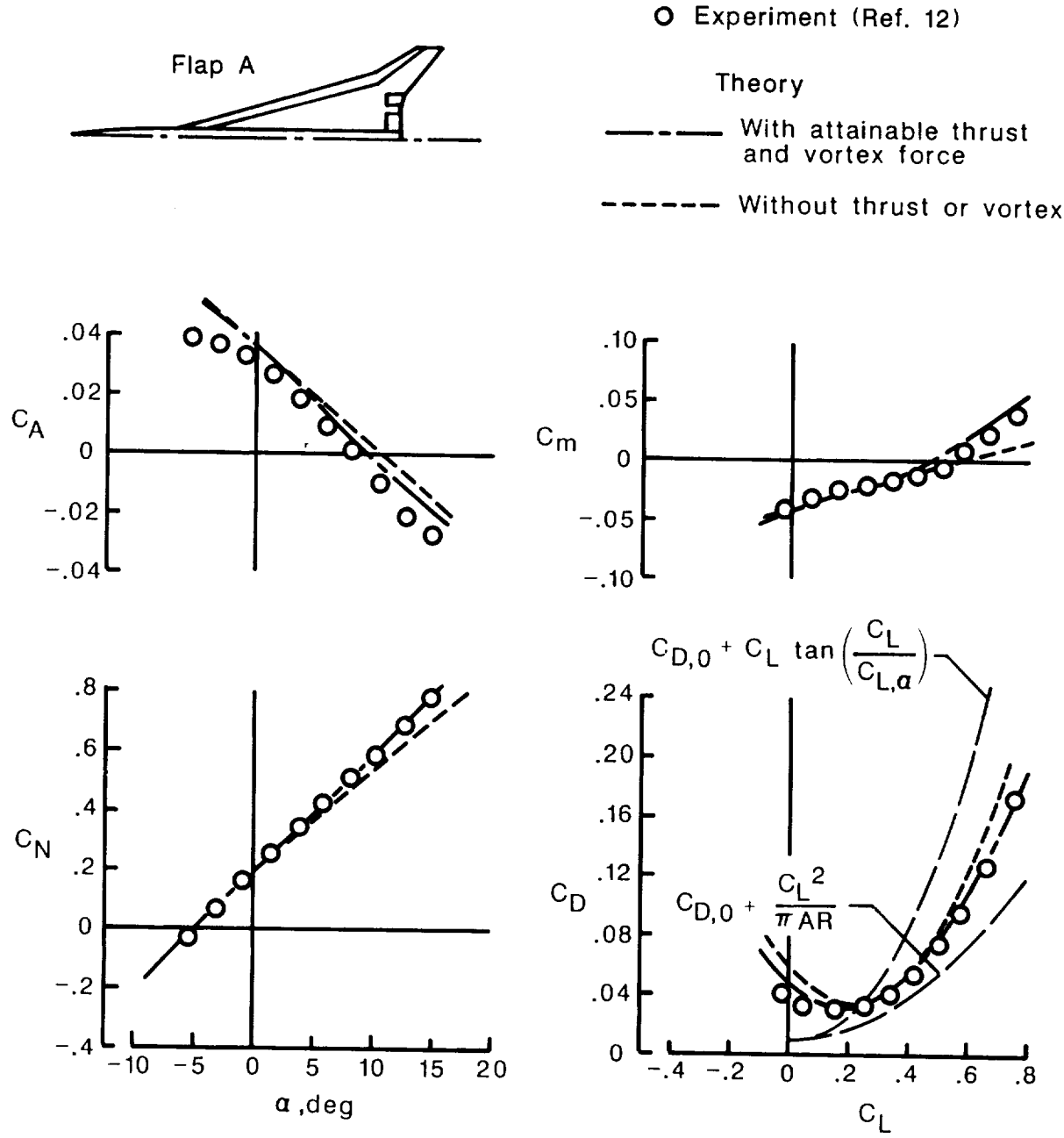

(d) Flap A; $\delta_{L,n} = 40°$, $\delta_{T,n} = 20°$.

Figure 20. Continued.

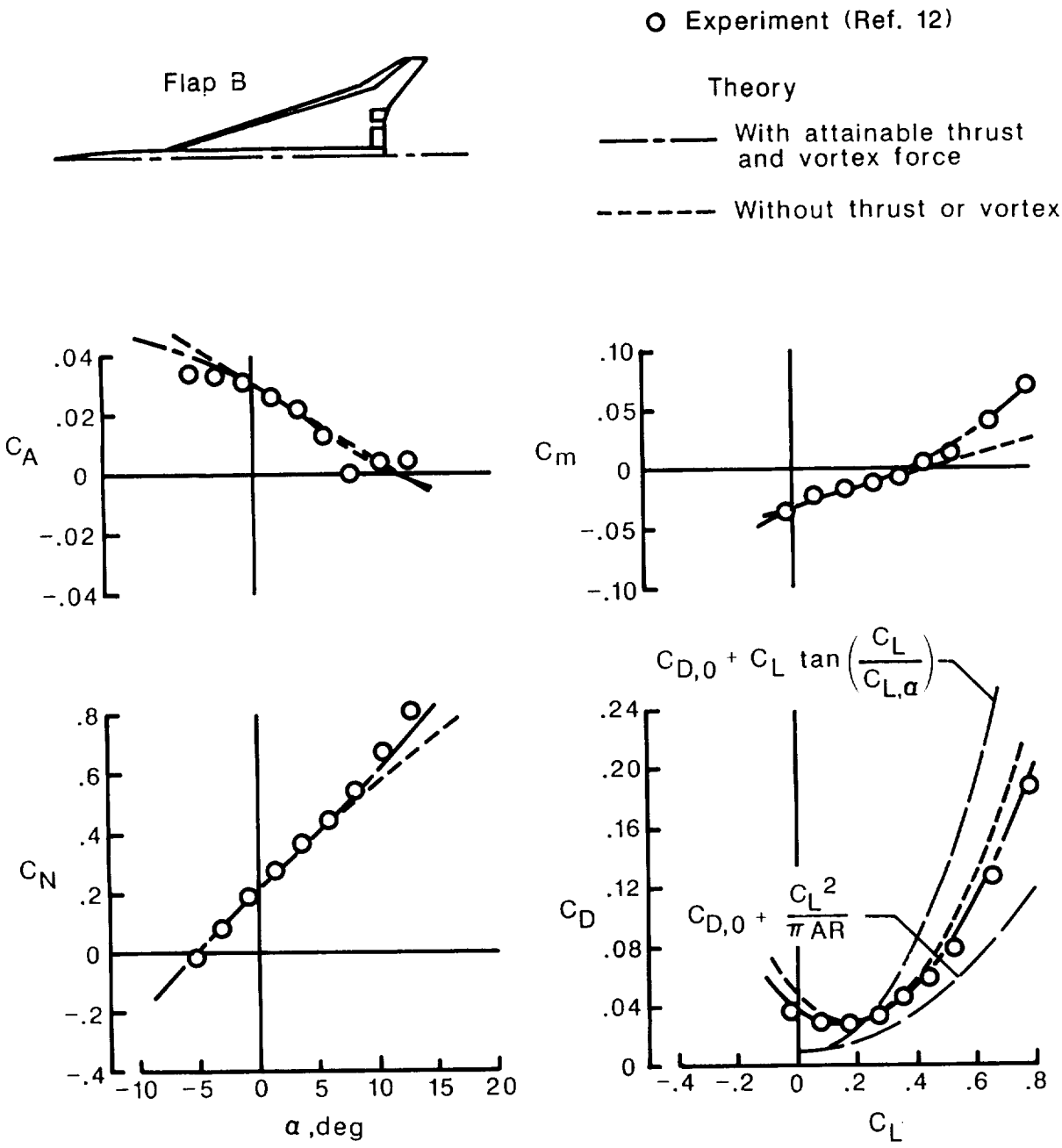

(e) Flap B; $\delta_{L,s} = 20°$, $\delta_{T,s} = 20°$.

Figure 20. Continued.

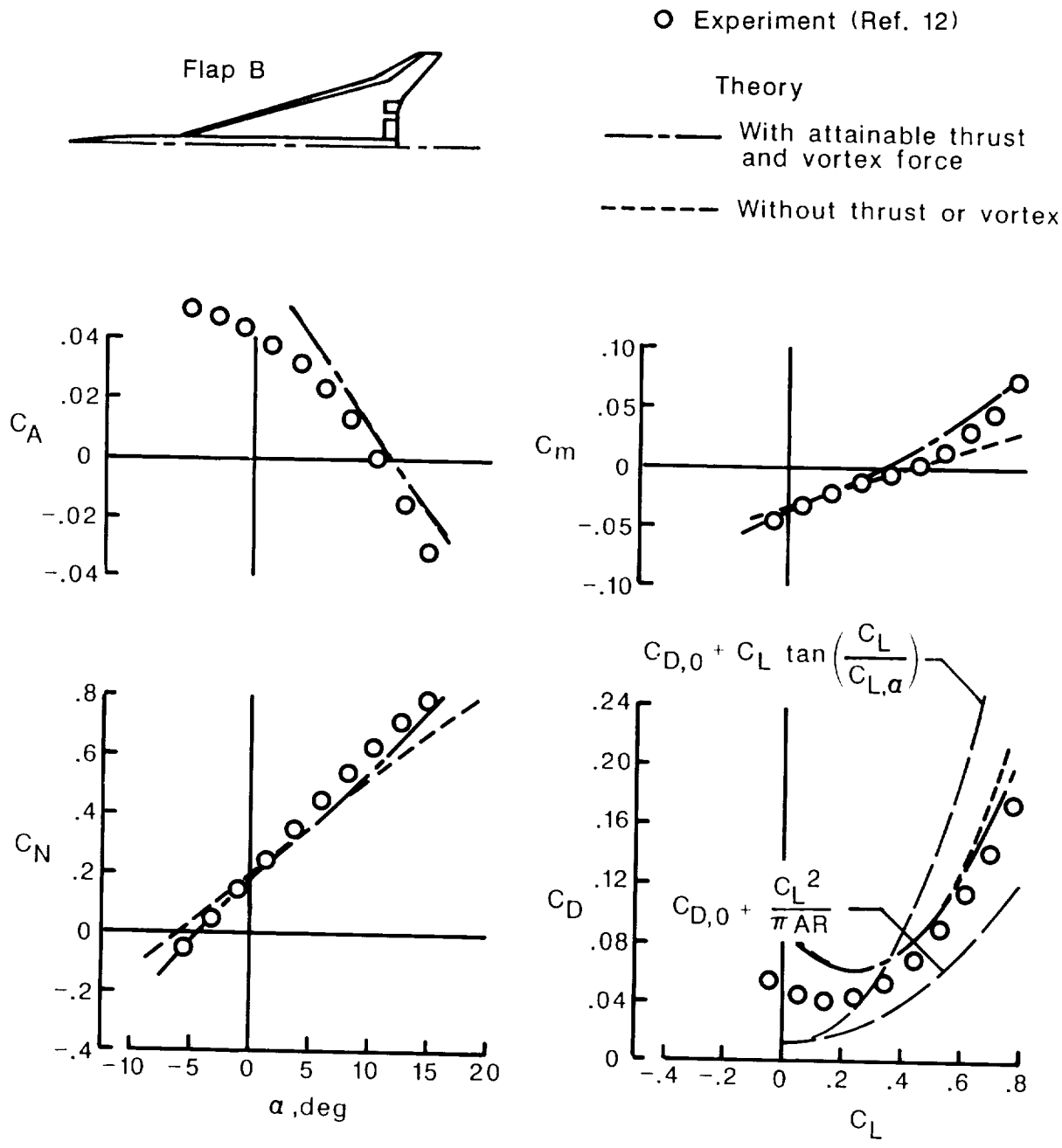

(f) Flap B; $\delta_{L,s} = 40°$, $\delta_{T,s} = 20°$.

Figure 20. Concluded.

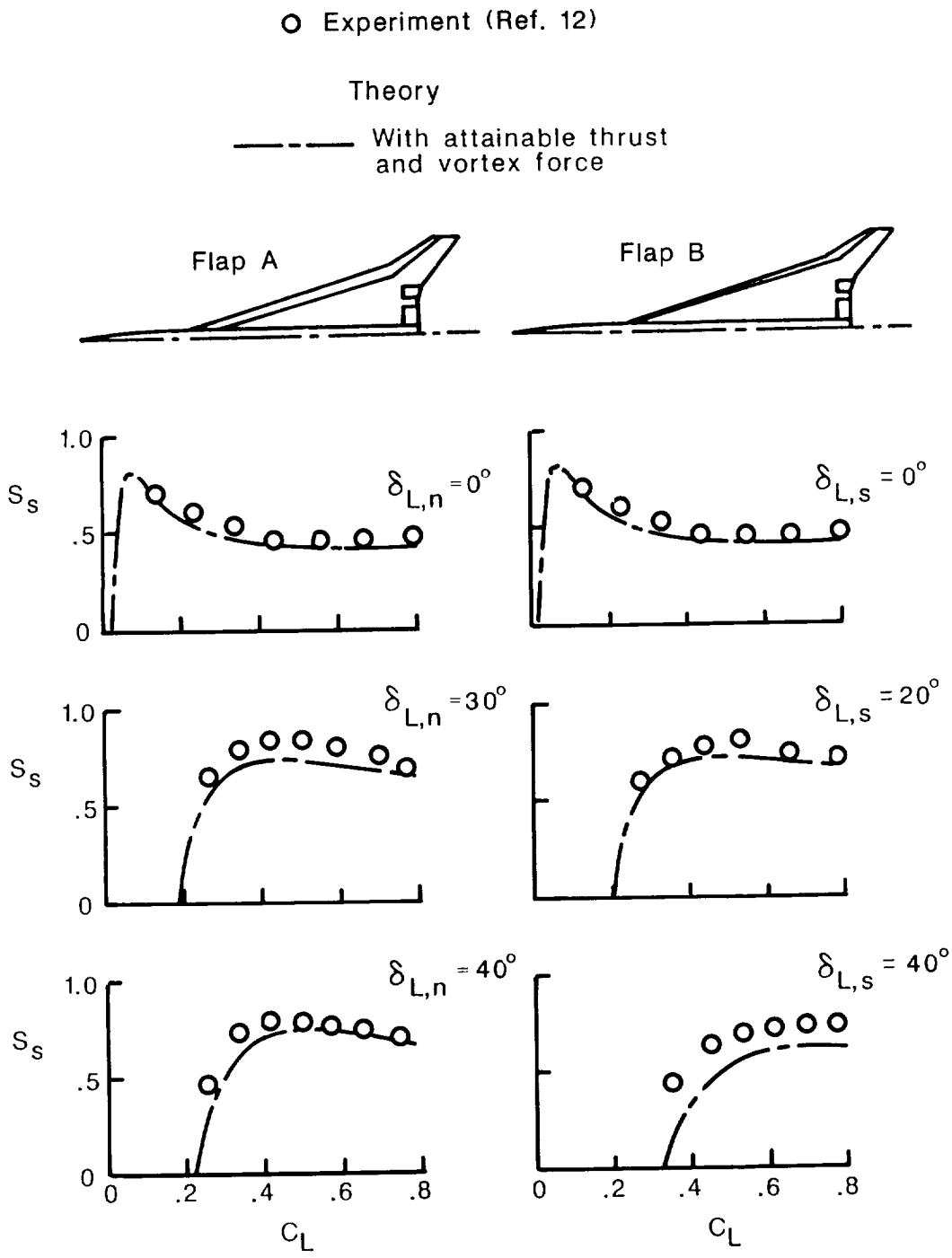

Figure 21. Suction-parameter variation with lift coefficient for various leading-edge flap deflections. Advanced arrow-wing supersonic transport; $\delta_{T,n} = \delta_{T,s} = 20°$; $M = 0.21$; $R = 4.1 \times 10^6$.

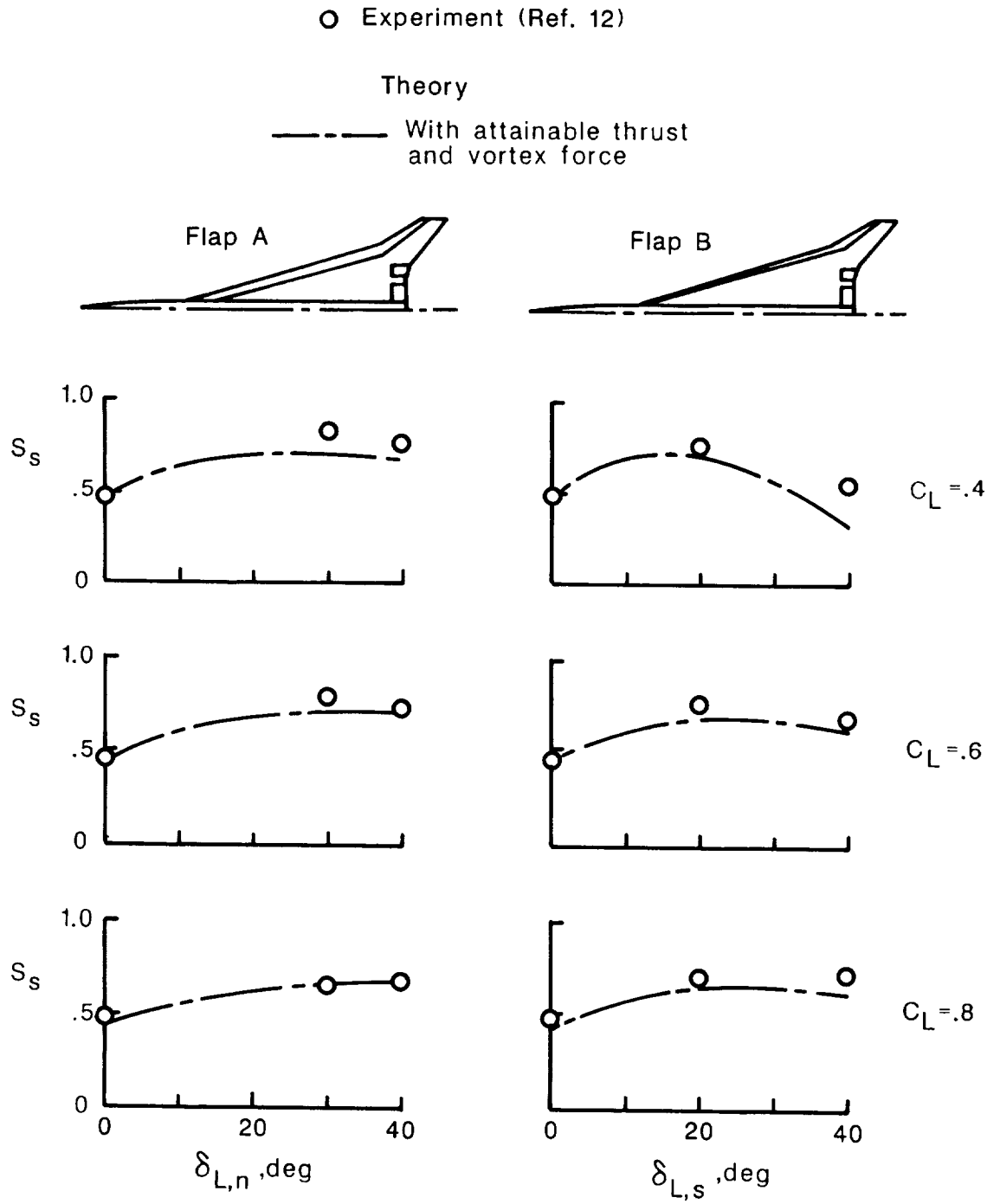

Figure 22. Suction-parameter variation with leading-edge flap deflection for selected lift coefficients. Advanced arrow-wing supersonic transport; $\delta_{L,n} = \delta_{T,s} = 20°$; $M = 0.21$; $R = 4.1 \times 10^6$.

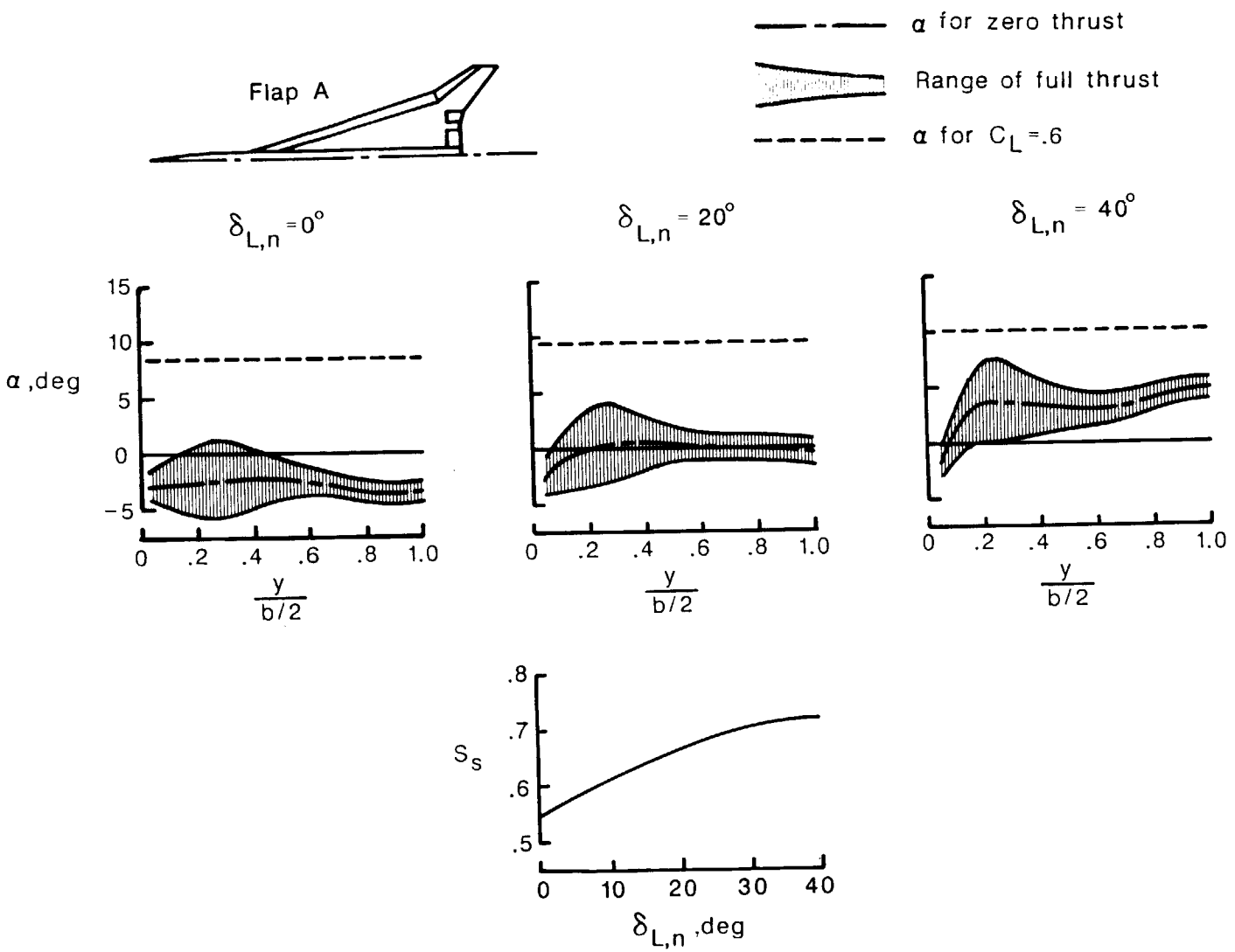

Figure 23. Variation of α for zero thrust and a range of full thrust with spanwise station for three leading-edge flap deflections. Advanced arrow-wing supersonic transport; $\delta_{T,n} = \delta_{T,s} = 20°$; $M = 0.21$; $R = 4.1 \times 10^6$.

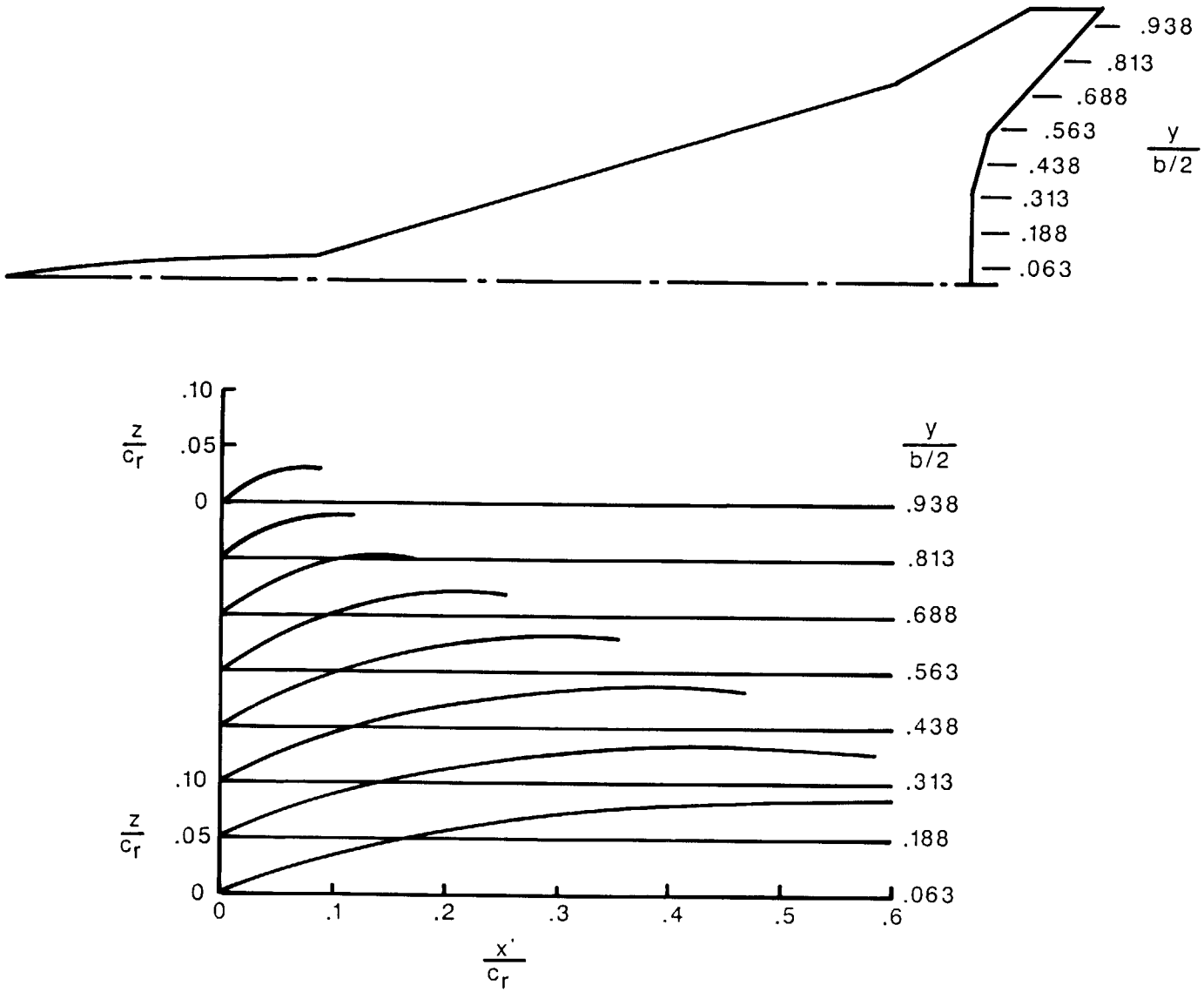

Figure 24. Whole-wing-design camber surface for advanced arrow-wing supersonic transport. $C_{L,\mathrm{des}} = 0.6$; $M = 0.21$; $R = 4.1 \times 10^6$.

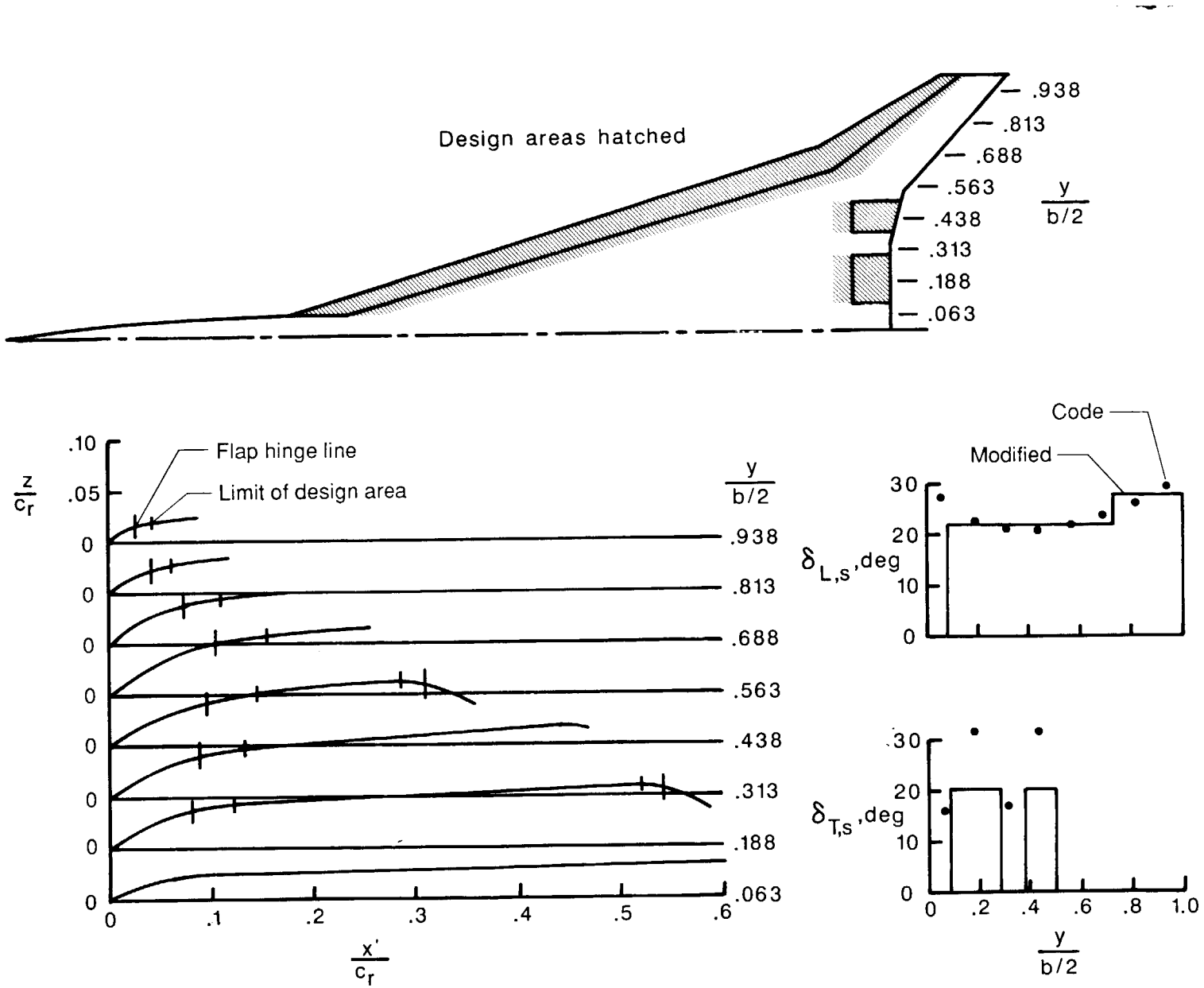

Figure 25. Restricted-area-design camber surface for advanced arrow-wing supersonic transport. $C_{L,\text{des}} = 0.6$; $C_{M,\text{des}} = -0.05$; $M = 0.21$; $R = 4.1 \times 10^6$.

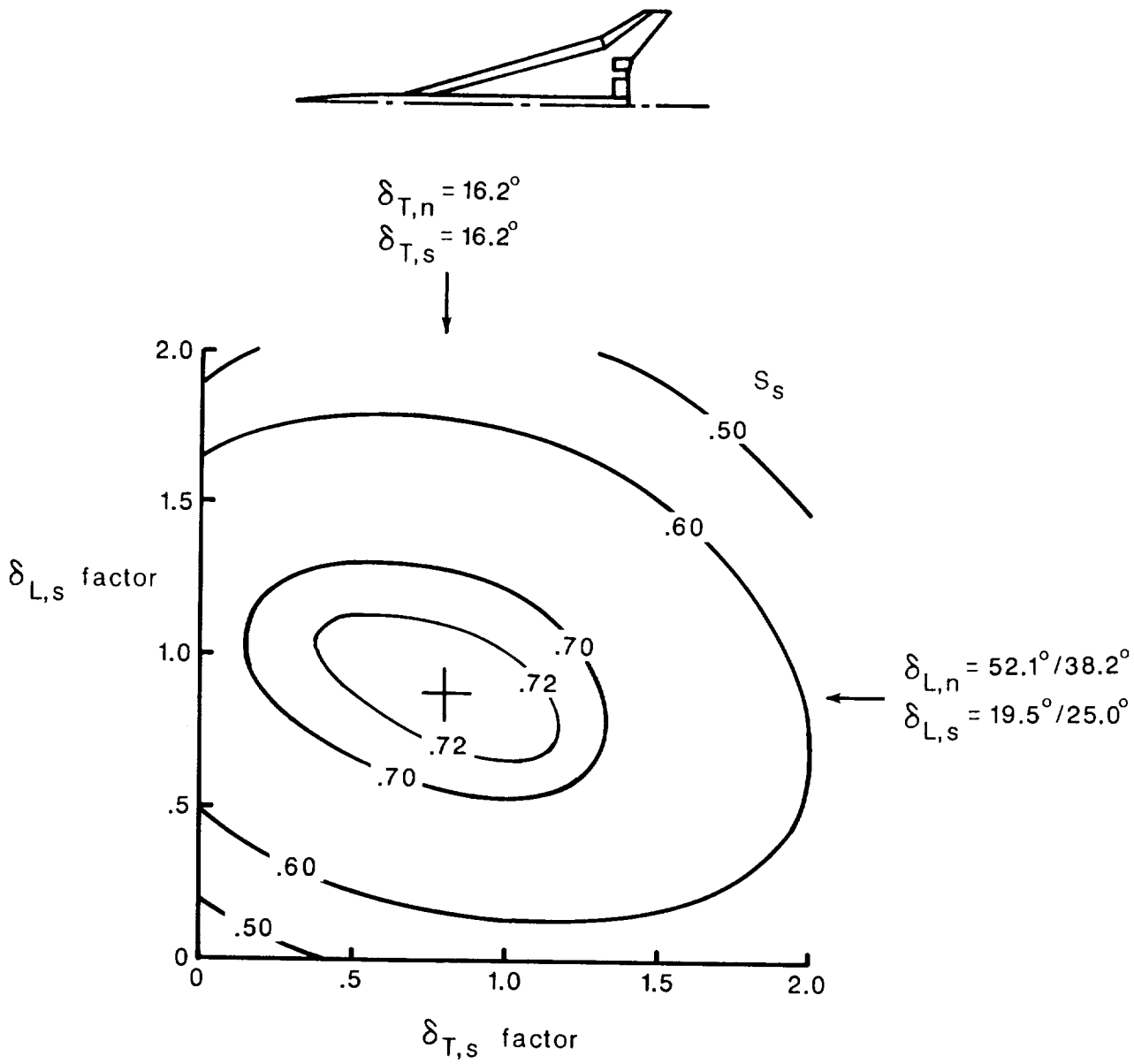

Figure 26. Suction-parameter contour map for advanced arrow-wing supersonic transport with revised leading-edge flap deflections. $C_L = 0.6$; $M = 0.21$; $R = 4.1 \times 10^6$.

C-2

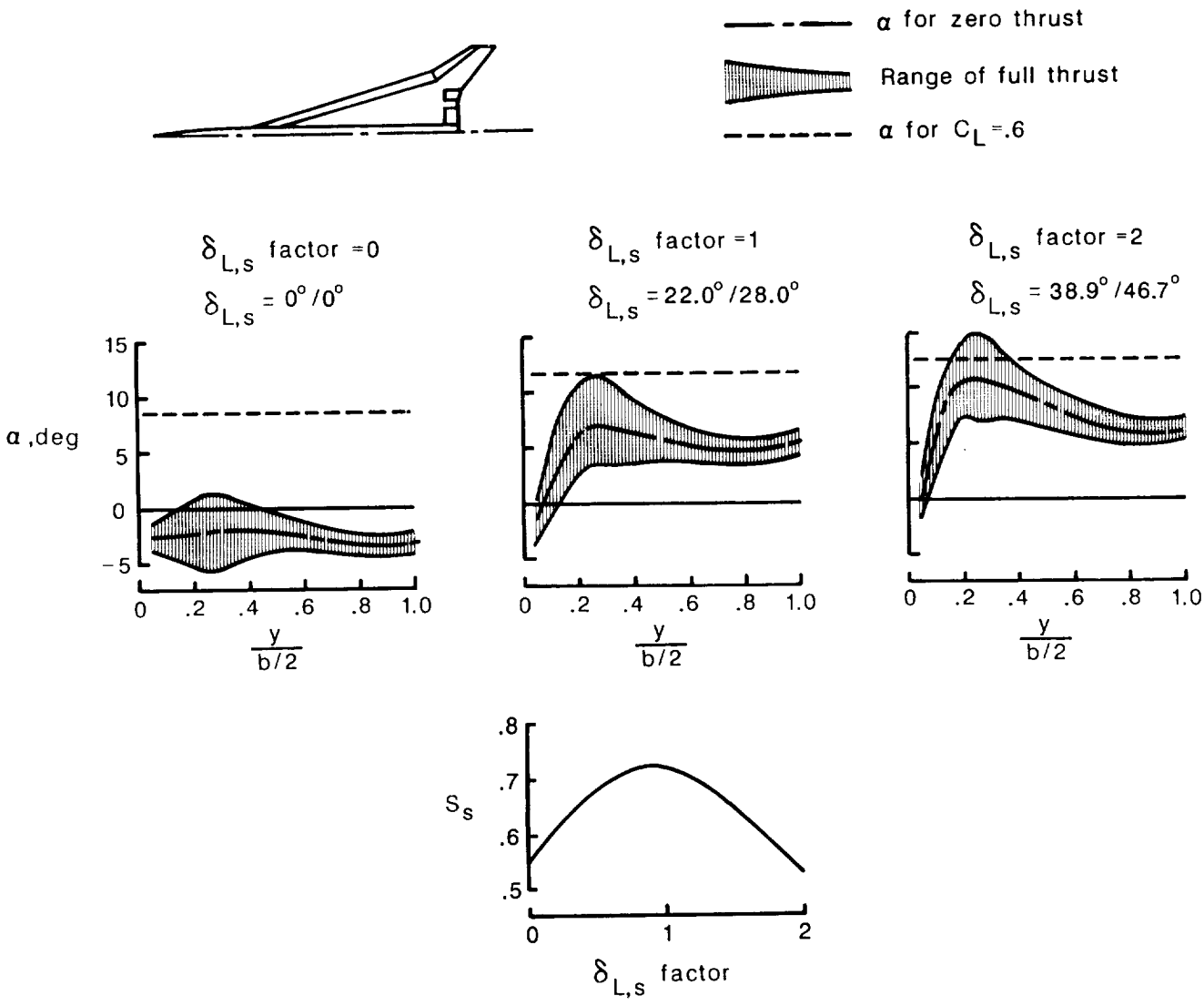

Figure 27. Variation of α for zero thrust and a range of full thrust with spanwise station for three leading-edge flap deflection factors. Advanced arrow-wing supersonic transport; $\delta_{T,n} = \delta_{T,s} = 20°$; $M = 0.21$; $R = 4.1 \times 10^6$.

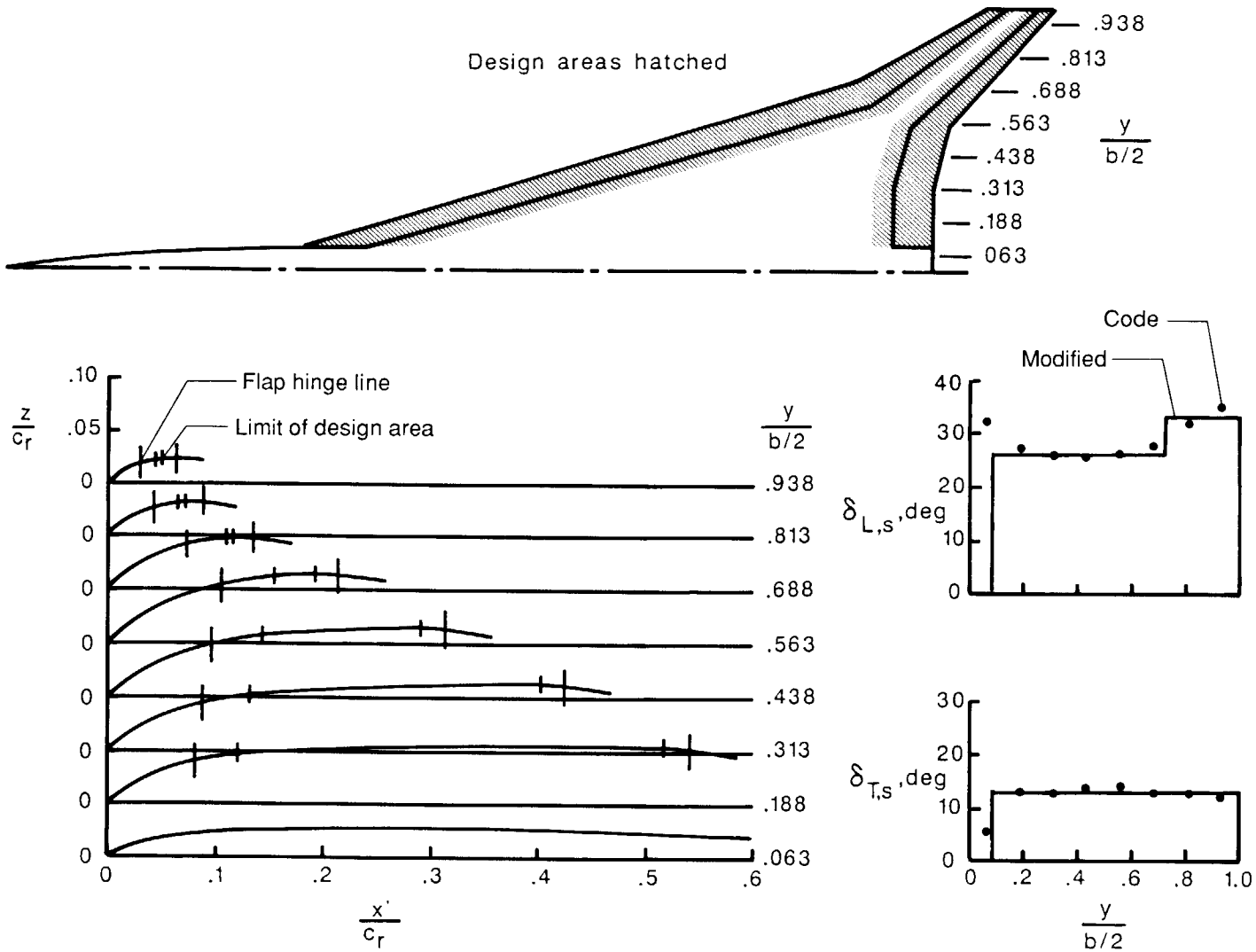

Figure 28. Restricted-area-design camber surface for advanced arrow-wing supersonic transport with full-span trailing-edge flaps. $C_{L,\mathrm{des}} = 0.6$; $C_{M,\mathrm{des}} = -0.05$; $M = 0.21$; $R = 4.1 \times 10^6$.

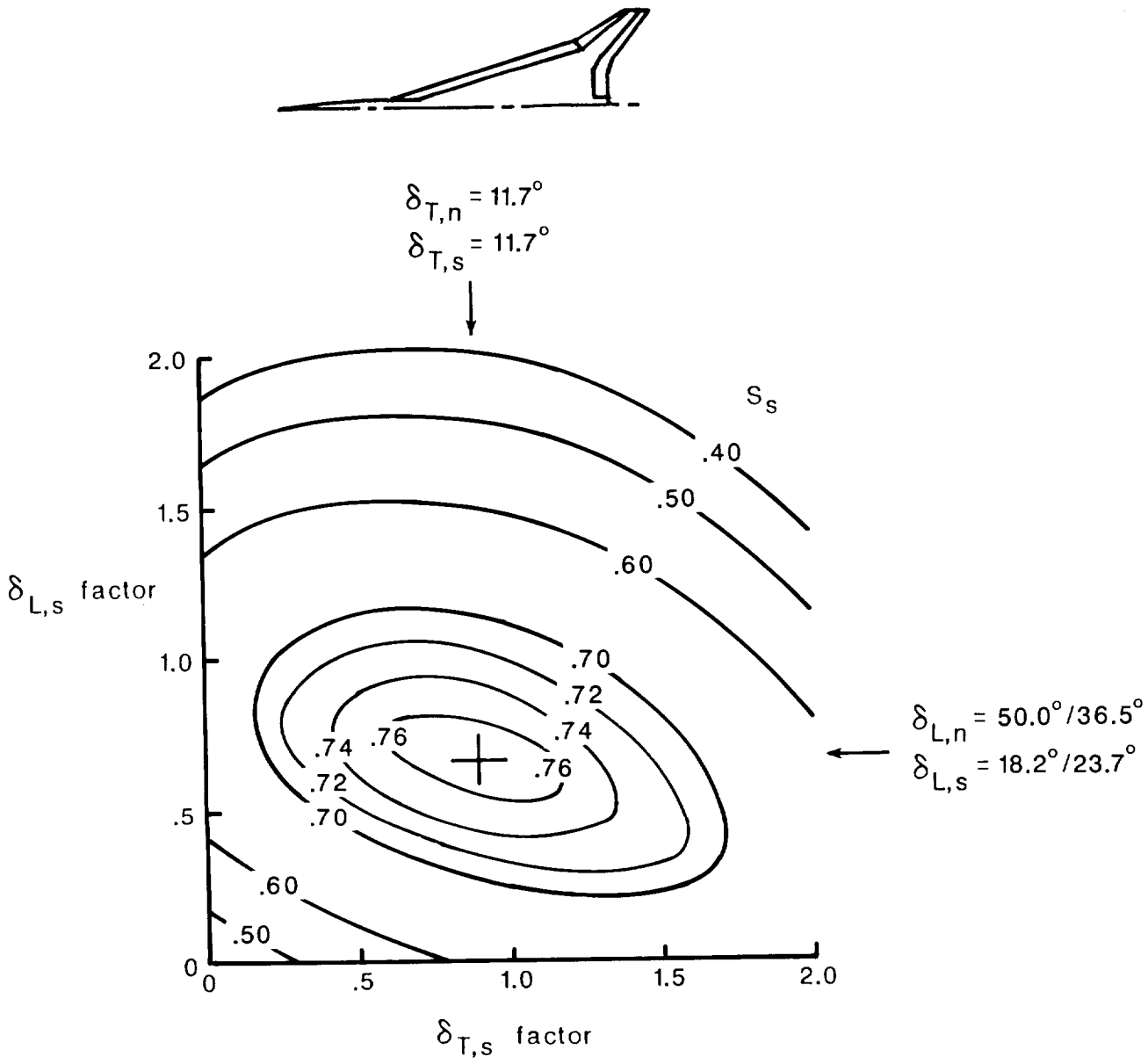

Figure 29. Suction-parameter contour map for advanced arrow-wing supersonic transport with revised leading-edge flap deflections and a full-span trailing-edge flap. $C_L = 0.5$; $M = 0.21$; $R = 4.1 \times 10^6$.

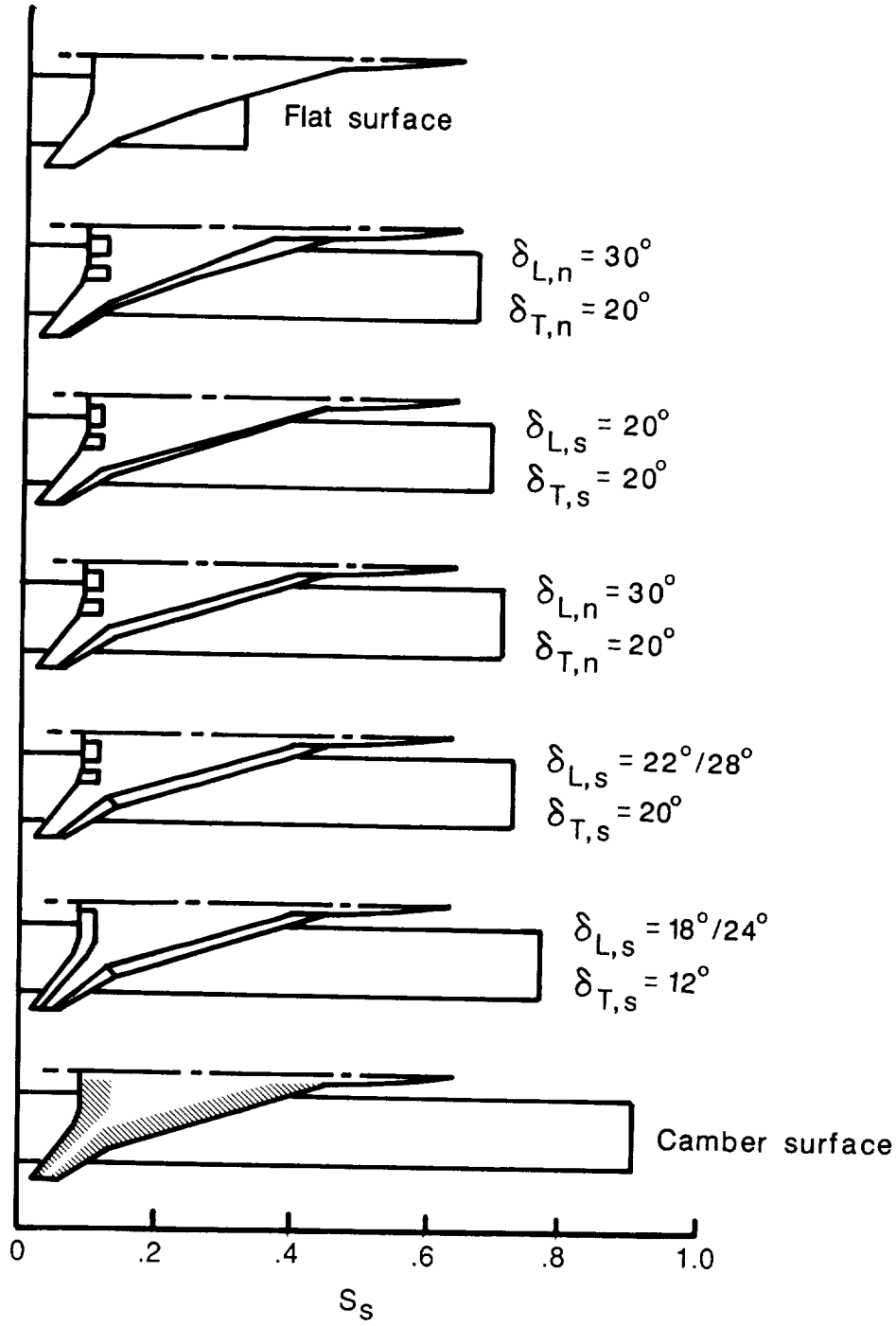

Figure 30. Summary of flap-design study for advanced arrow-wing supersonic transport. $C_L = 0.6$; $M = 0.21$; $R = 4.1 \times 10^6$.

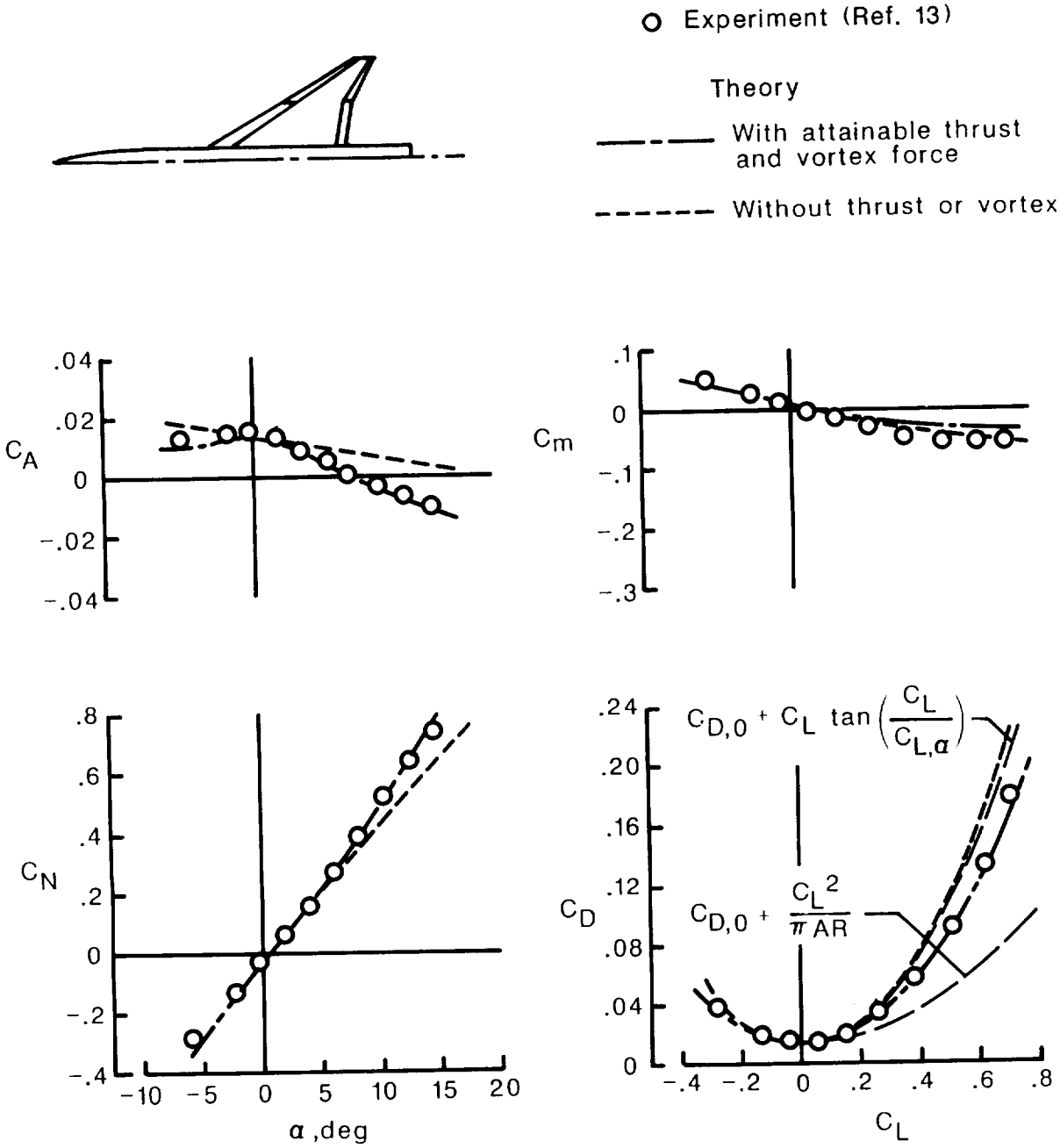

(a) $\delta_{L,s} = 0°$, $\delta_{T,s} = 0°$.

Figure 31. Theoretical and experimental data for 60°-swept trapezoidal-wing fighter. $M = 0.5$; $R = 2.9 \times 10^6$.

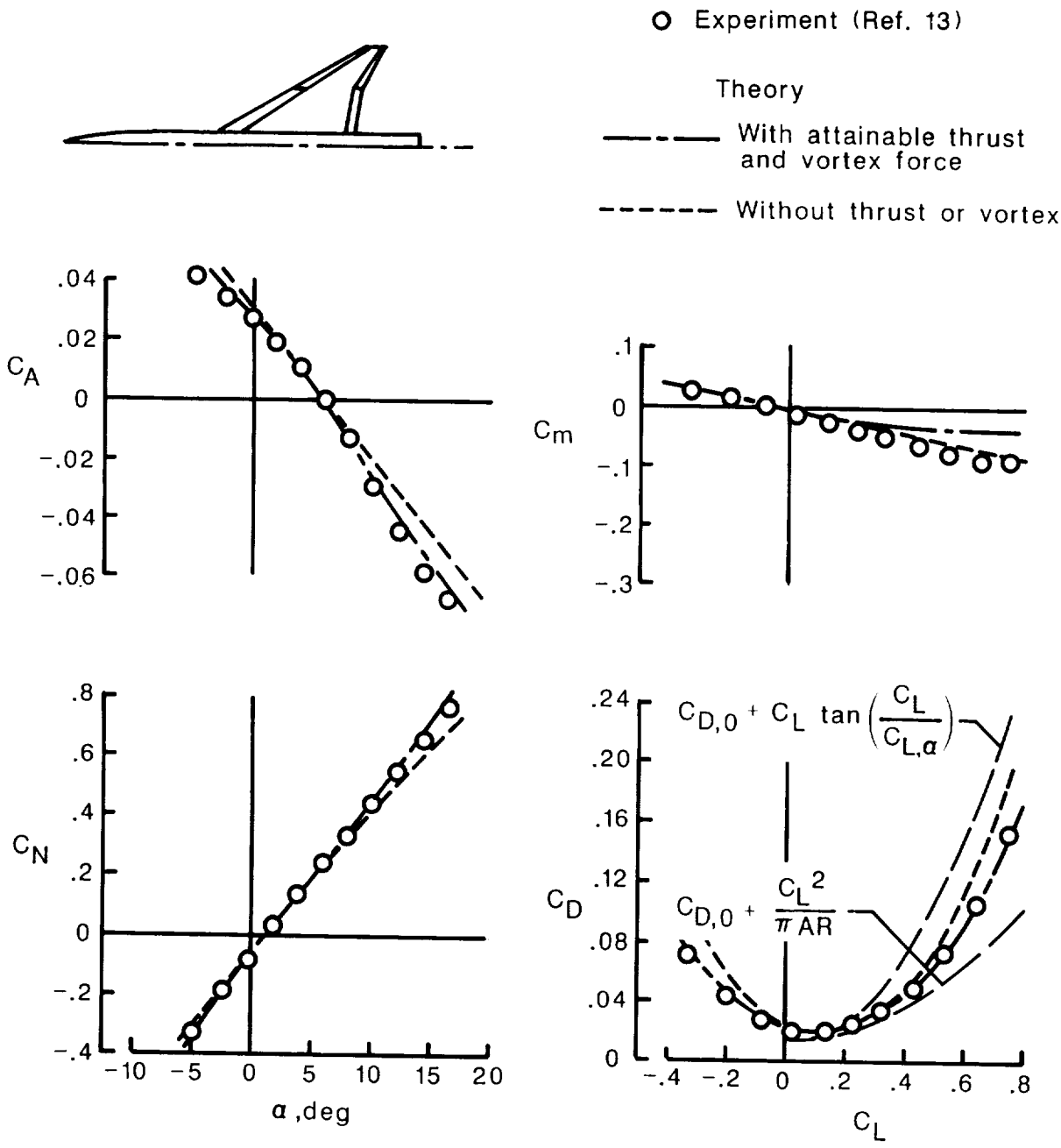

(b) $\delta_{L,s} = 15°/15°$, $\delta_{T,s} = 0°$.

Figure 31. Continued.

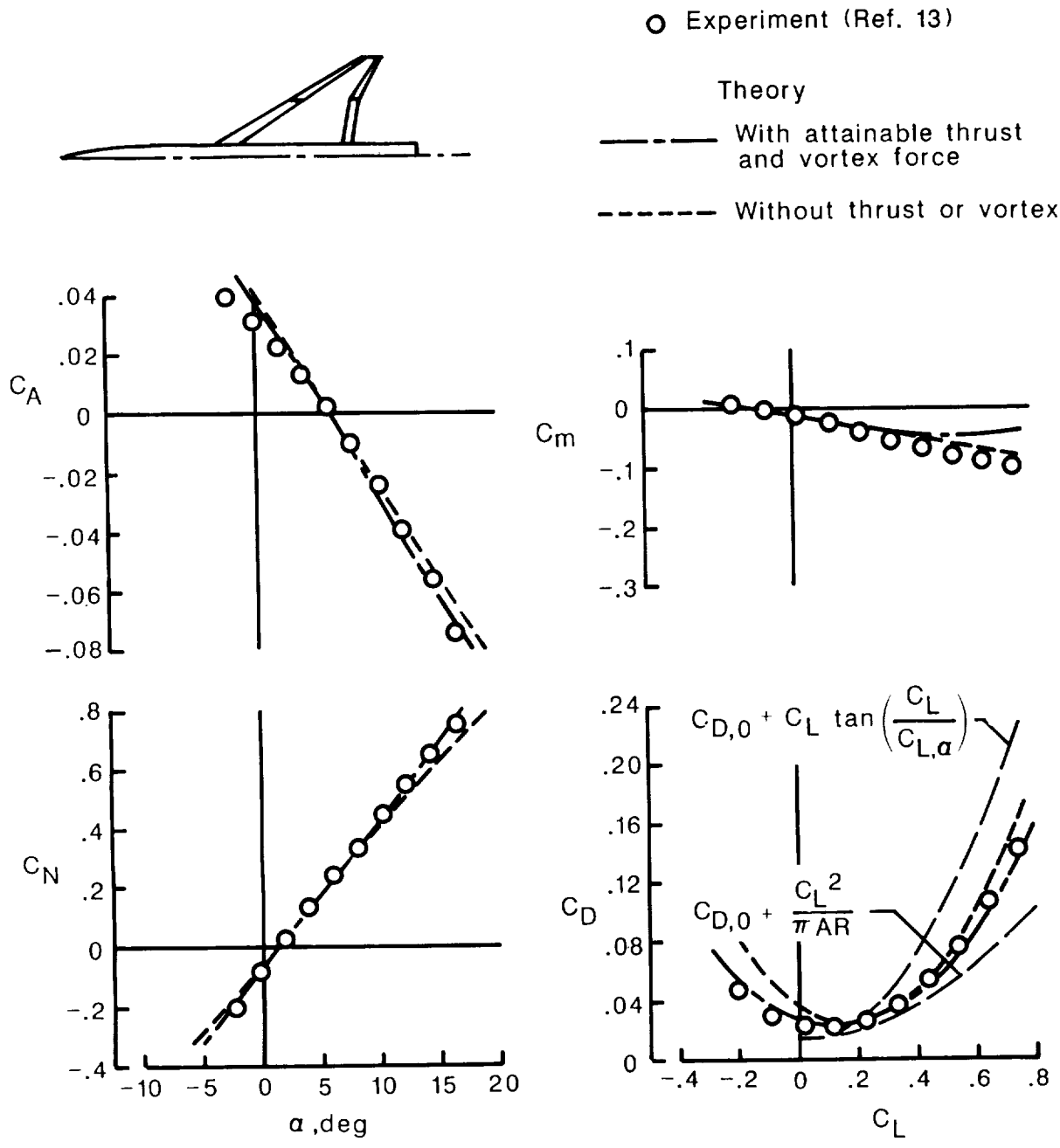

(c) $\delta_{L,s} = 20°/20°$, $\delta_{T,s} = 0°$.

Figure 31. Continued.

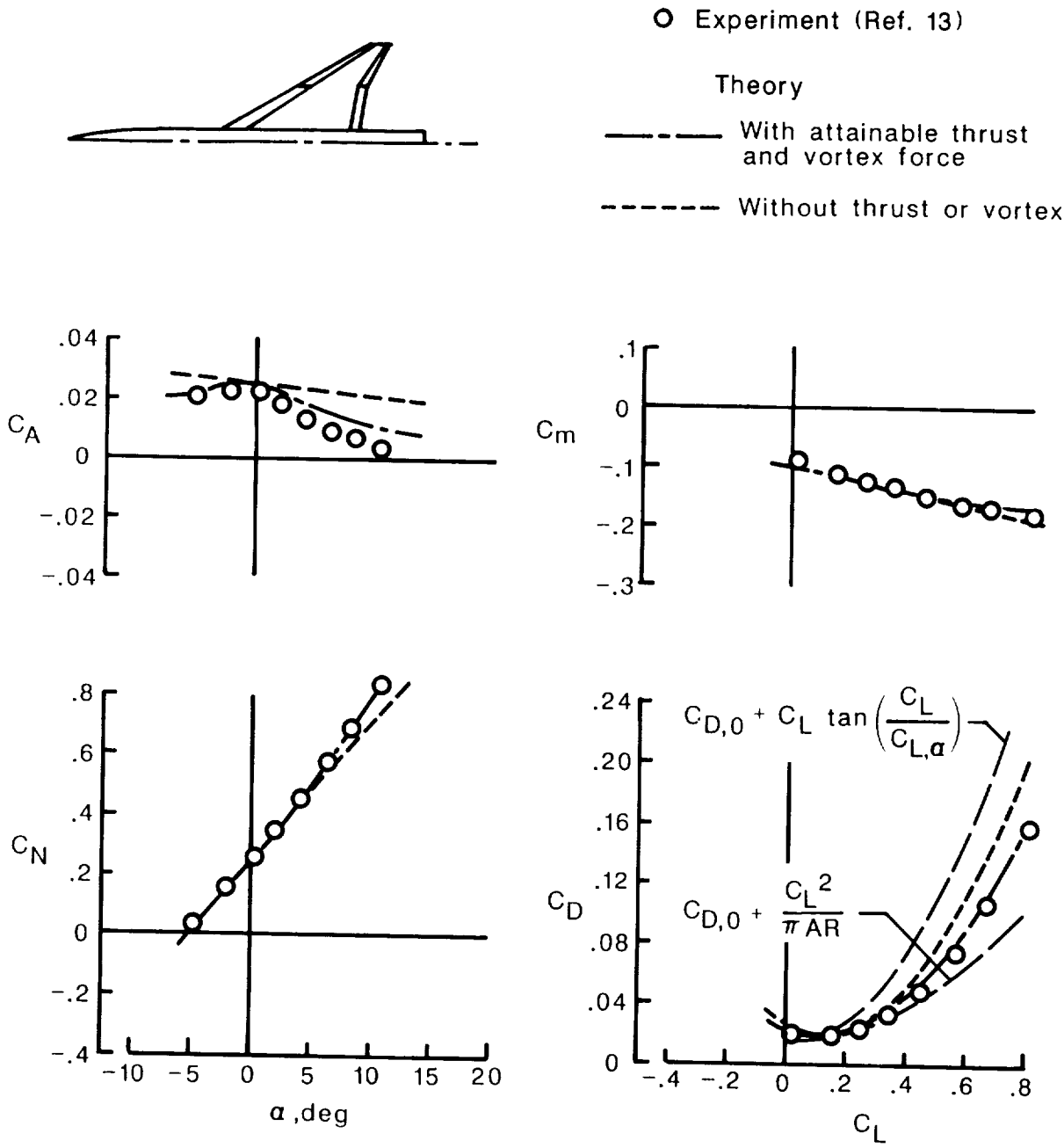

(d) $\delta_{L,s} = 0°$, $\delta_{T,s} = 15°/12°$.

Figure 31. Continued.

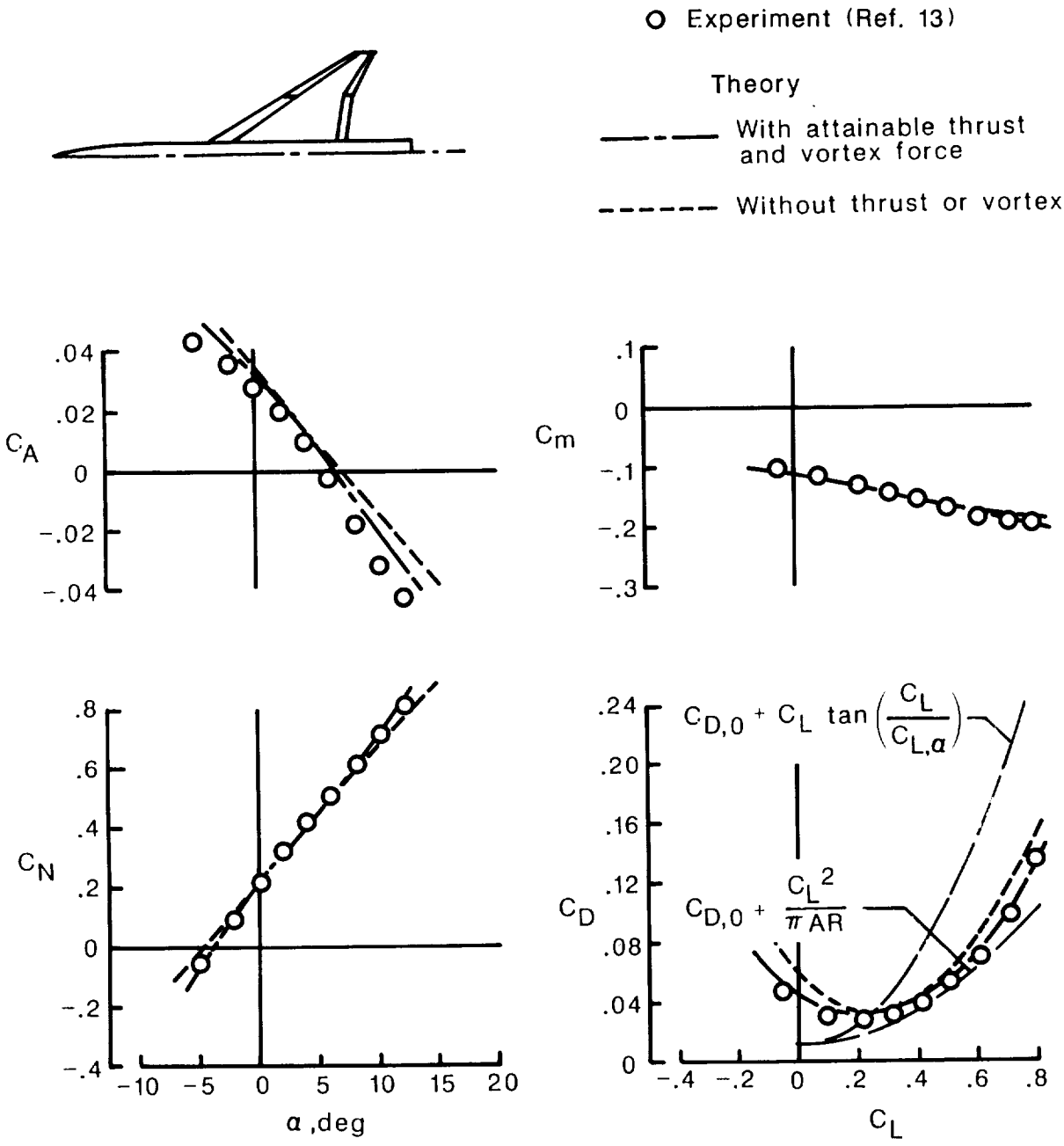

(e) $\delta_{L,s} = 15°/15°$, $\delta_{T,s} = 15°/12°$.

Figure 31. Continued.

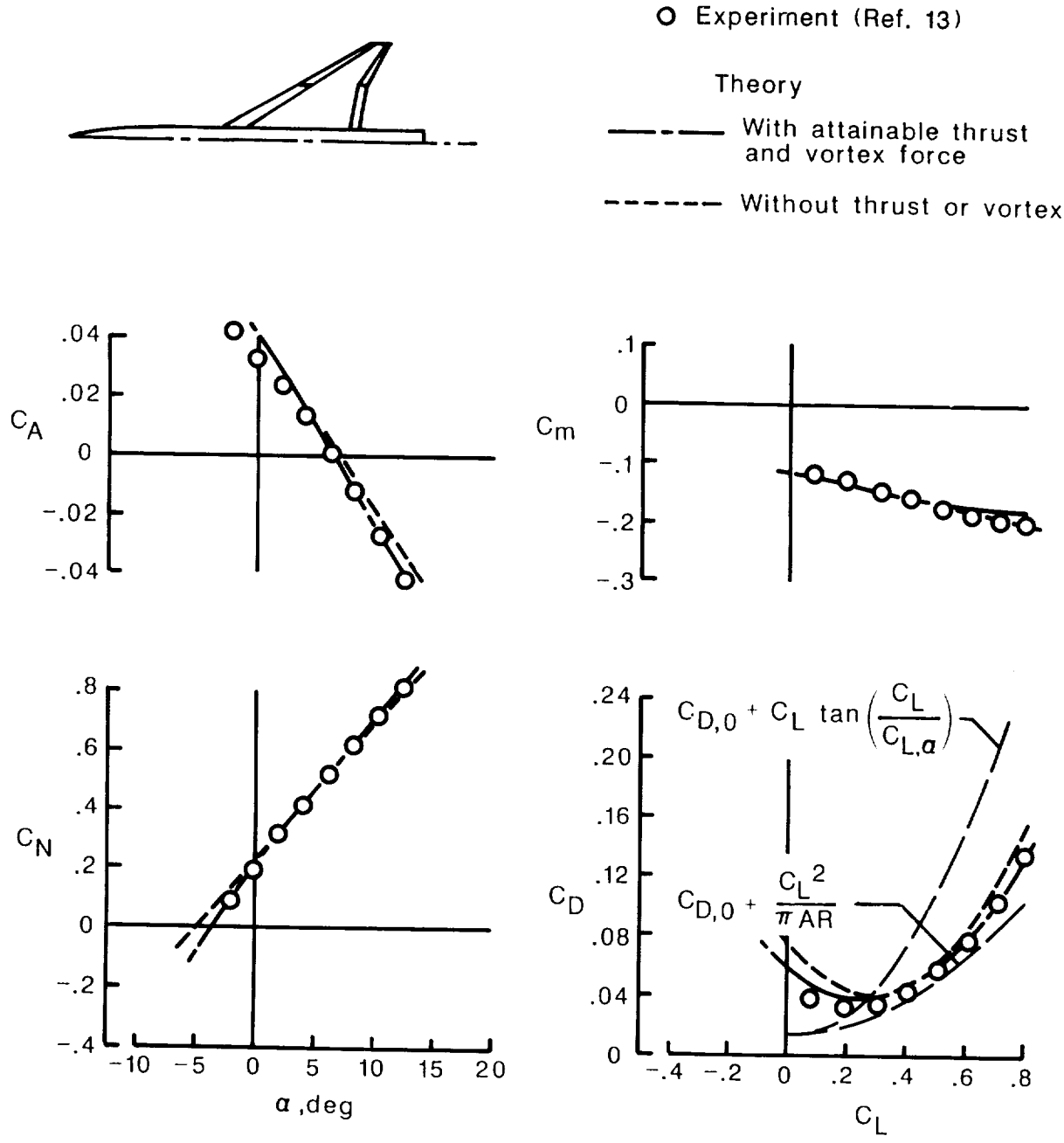

(f) $\delta_{L,s} = 20°/20°$, $\delta_{T,s} = 15°/12°$.

Figure 31. Continued.

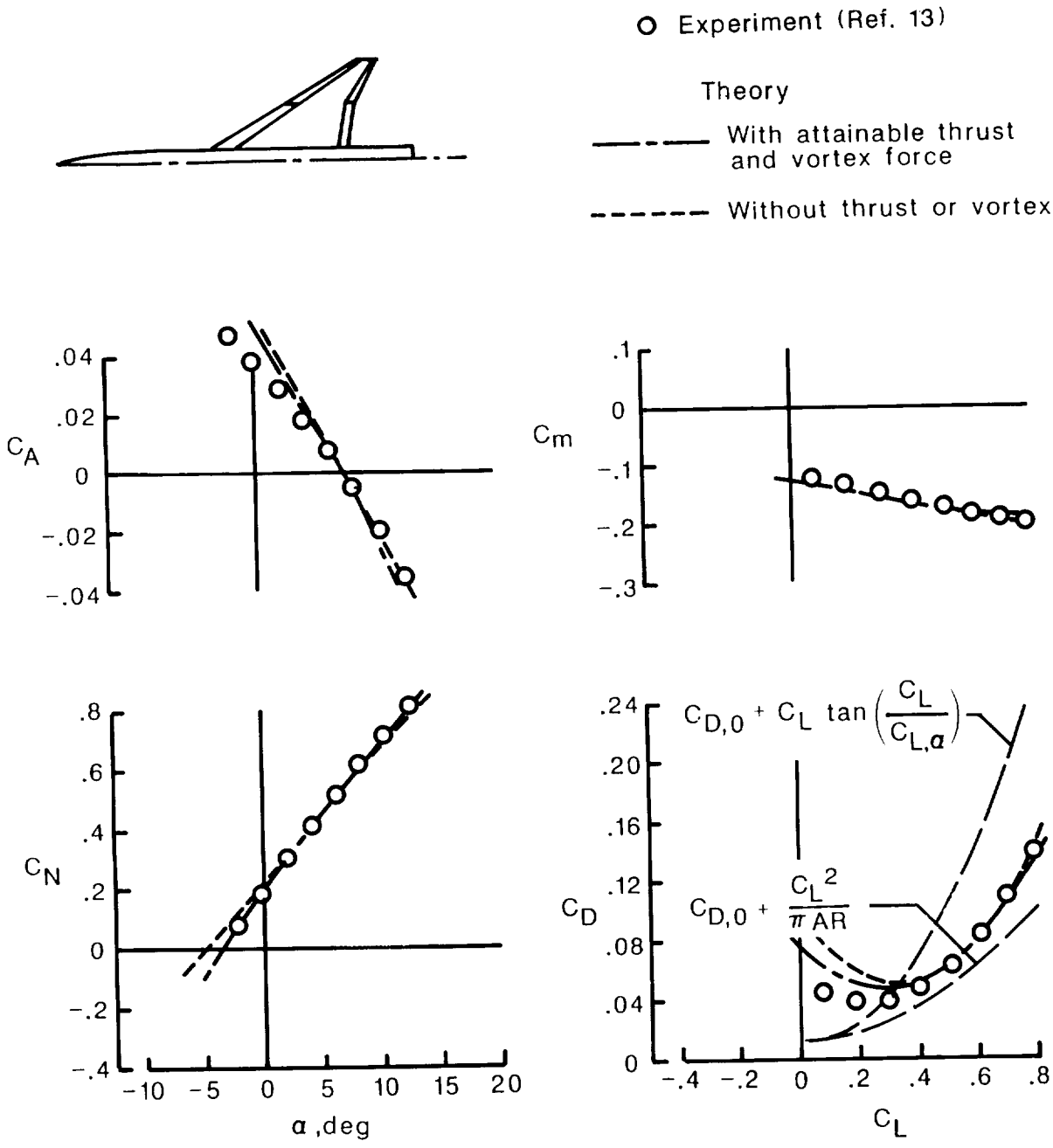

(g) $\delta_{L,s} = 25°/25°$, $\delta_{T,s} = 15°/12°$.

Figure 31. Continued.

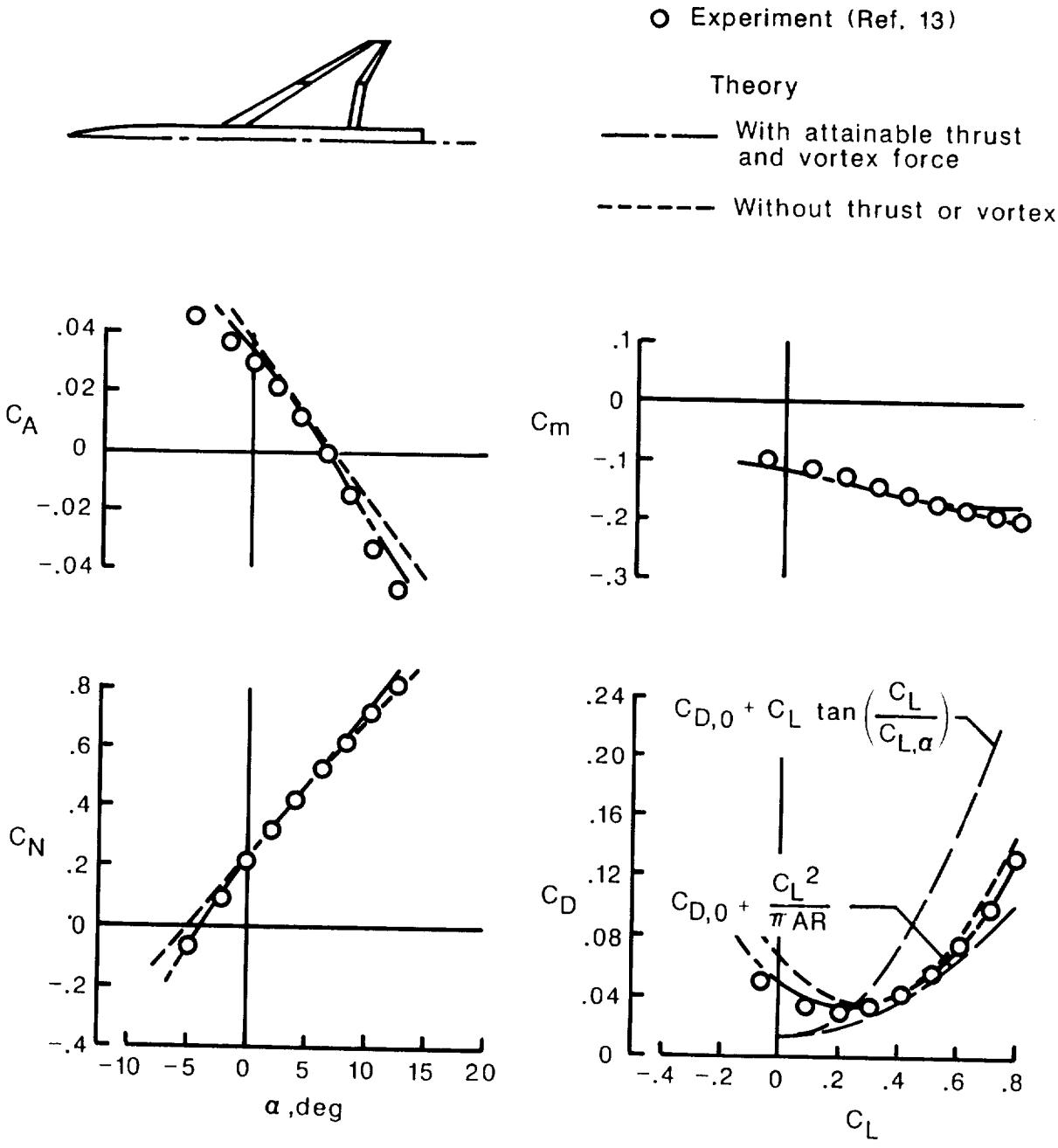

(h) $\delta_{L,s} = 15°/20°$, $\delta_{T,s} = 15°/12°$.

Figure 31. Concluded.

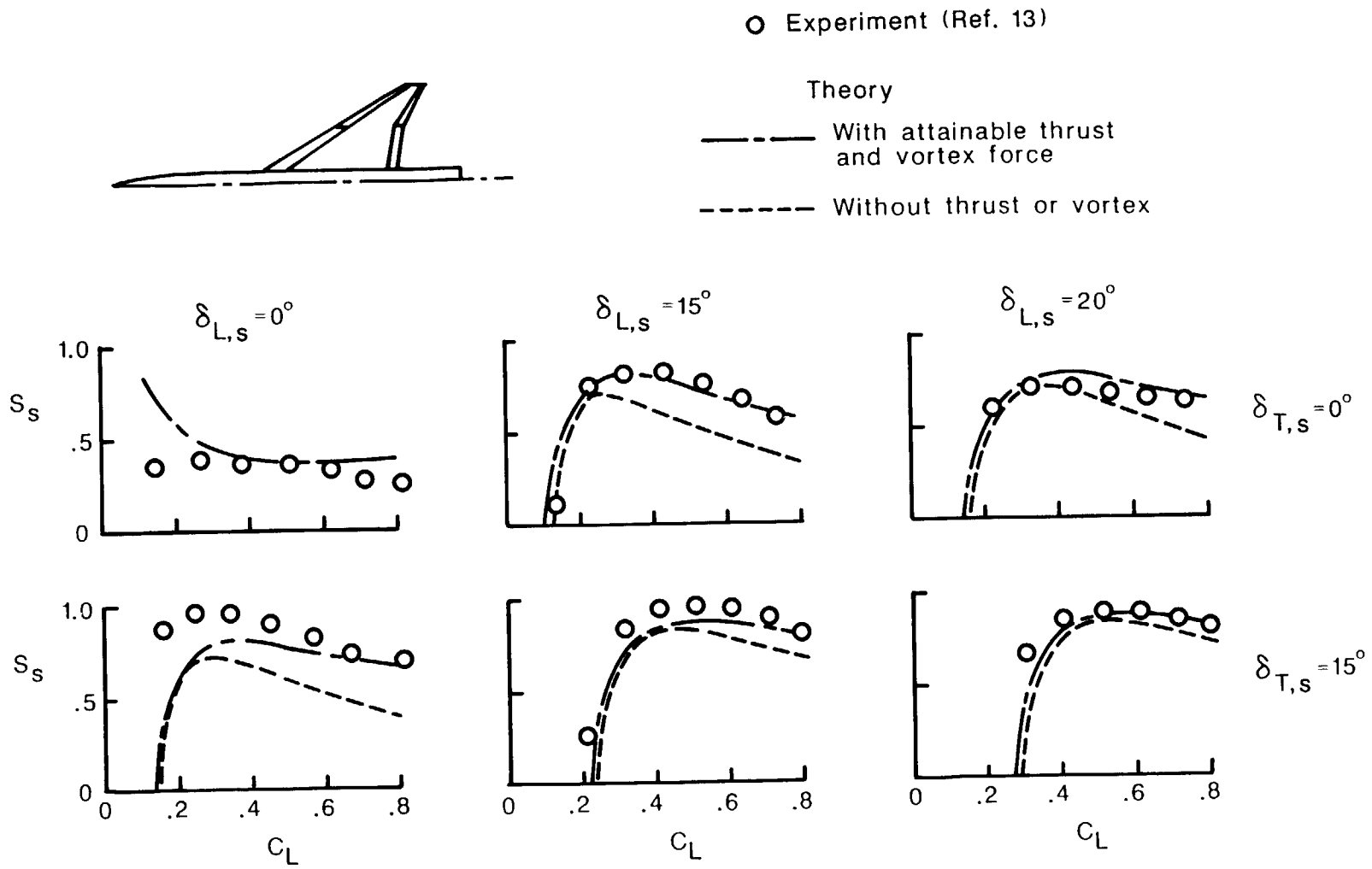

Figure 32. Suction-parameter variation with lift coefficient for various combinations of leading- and trailing-edge flap deflection combinations. 60°-swept trapezoidal-wing fighter; $M = 0.5$; $R = 2.5 \times 10^6$.

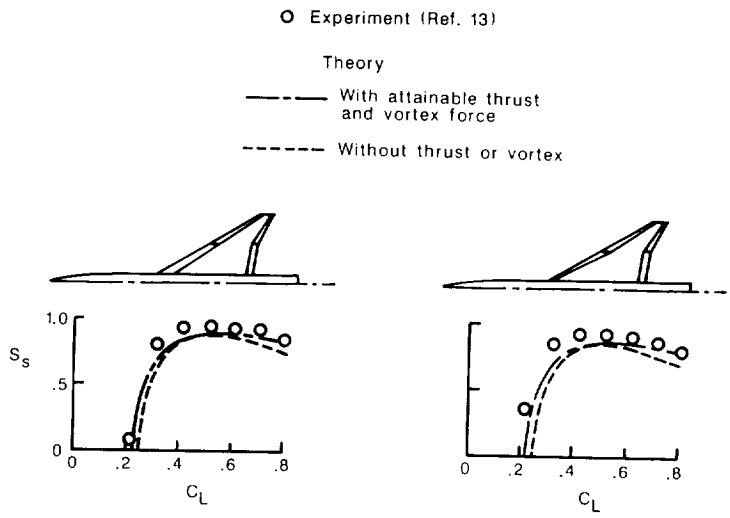

Figure 33. Suction-parameter variation with lift coefficient for two leading-edge flap planforms. 60°-swept trapezoidal-wing fighter. $\delta_{L,s} = 15°/20°$; $\delta_{T,s} = 15°/12°$.

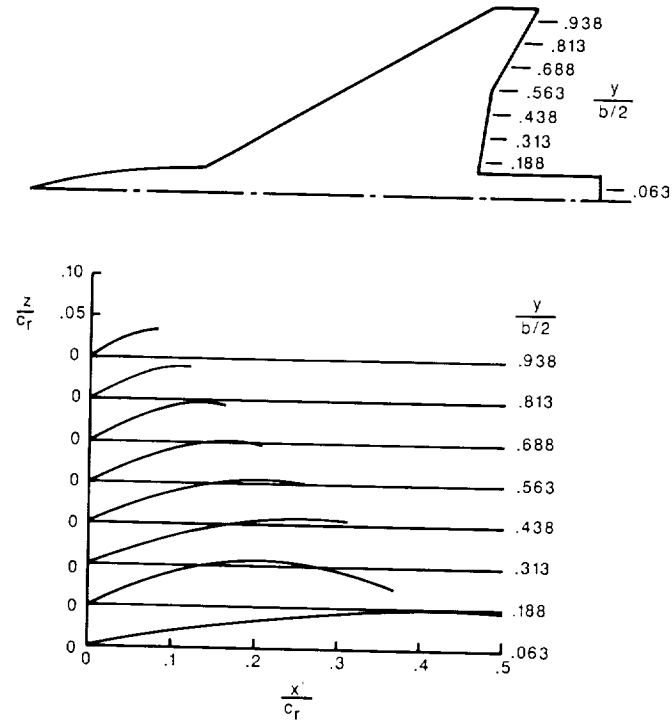

Figure 34. Whole-wing-design camber surface for 60°-swept trapezoidal-wing fighter. $C_{L,\text{des}} = 0.73$; $M = 0.50$; $R = 2.9 \times 10^6$.

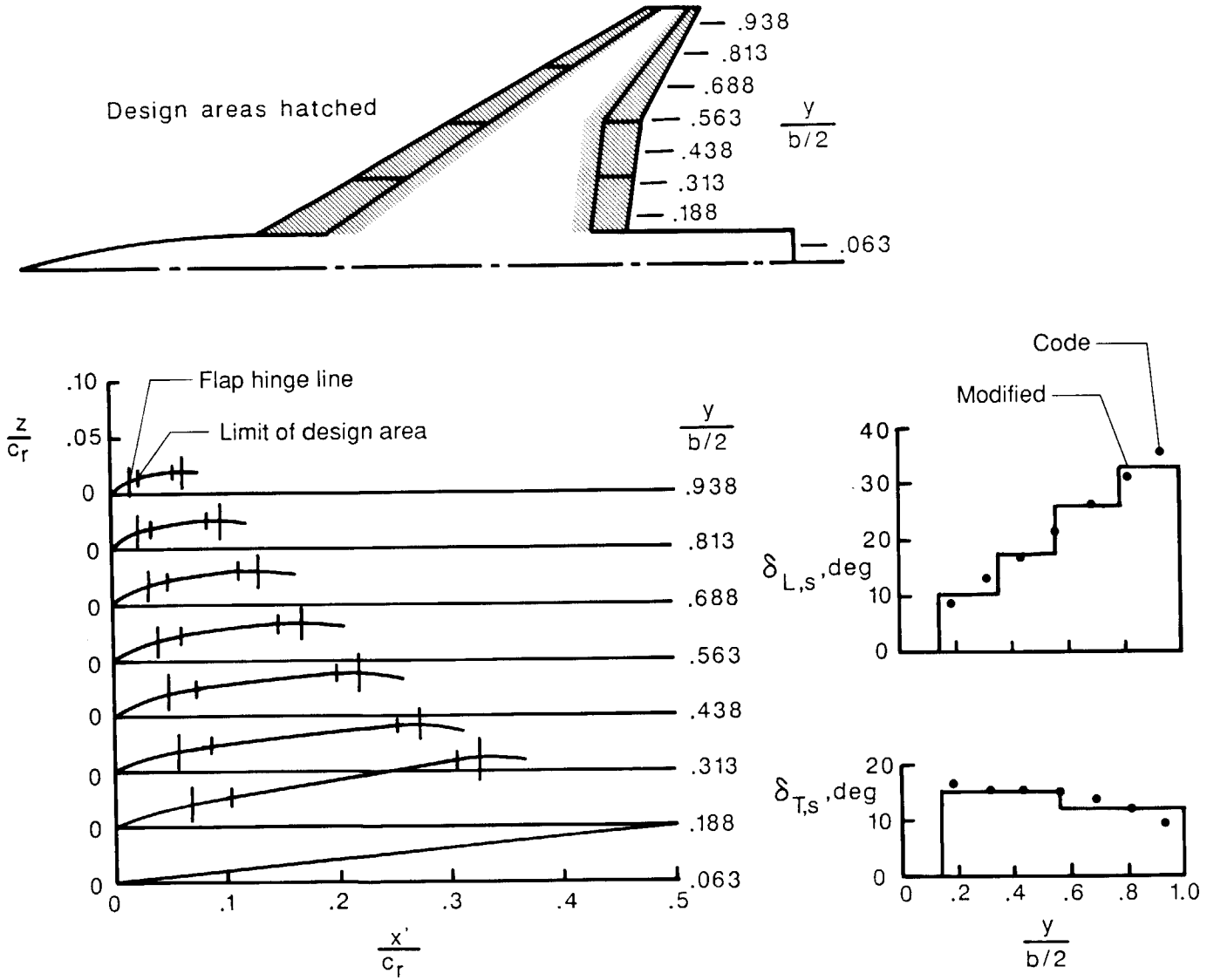

Figure 35. Restricted-area-design camber surface for 60°-swept trapezoidal-wing fighter. $C_{L,\text{des}} = 0.73$; $C_{M,\text{des}} = -0.17$; $M = 0.5$; $R = 2.9 \times 10^6$.

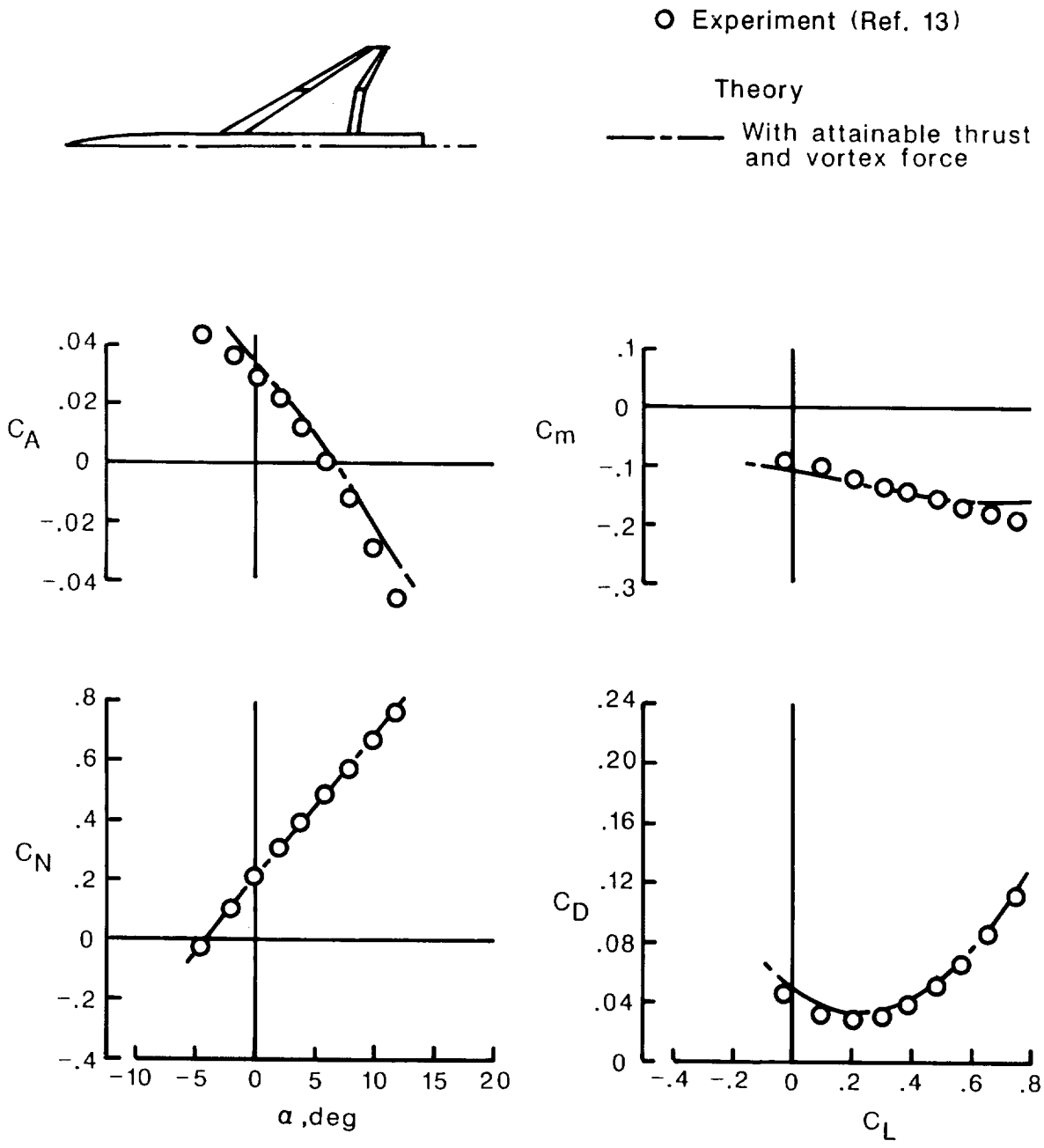

(a) $M = 0.3$, $R = 1.9 \times 10^6$, $\delta_{L,s} = 15°/20°$, $\delta_{T,s} = 15°/12°$.

Figure 36. Theoretical and experimental data for 60°-swept trapezoidal-wing fighter at off-design Mach numbers.

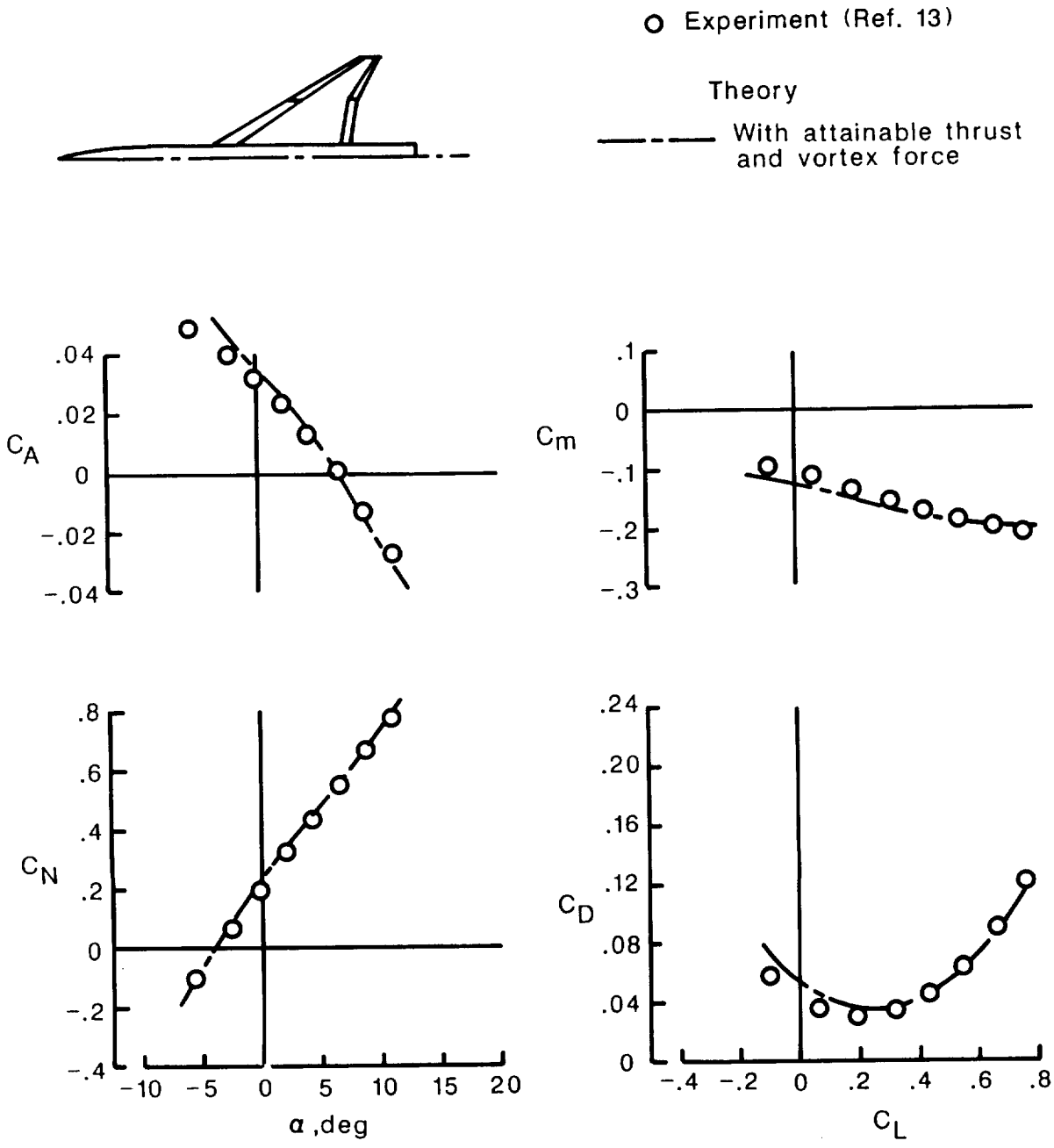

(b) $M = 0.7$, $R = 3.3 \times 10^6$, $\delta_{L,s} = 15°/20°$, $\delta_{T,s} = 15°/12°$.

Figure 36. Concluded.

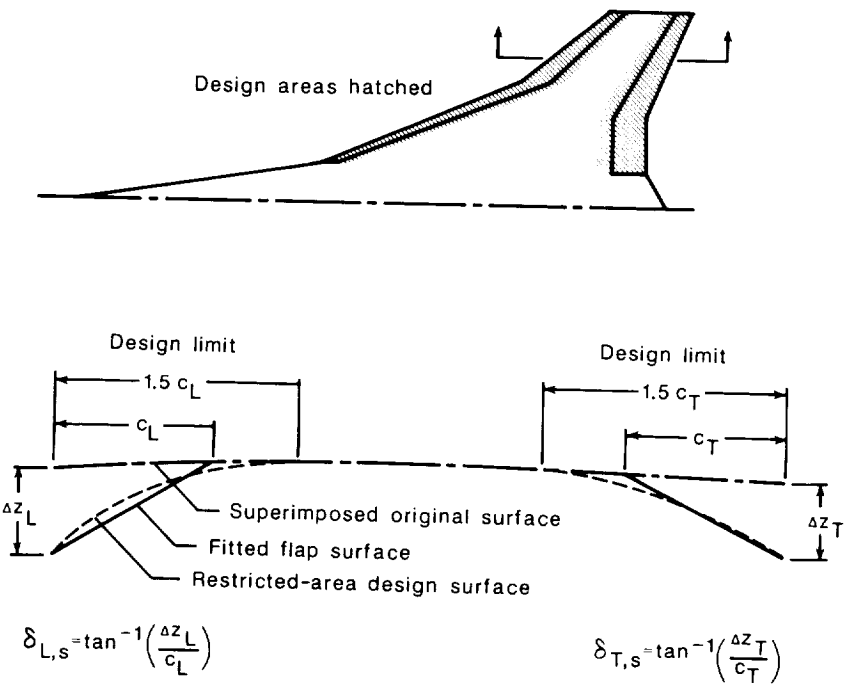

Figure 37. Fitting of flap surfaces to wing-design surface.

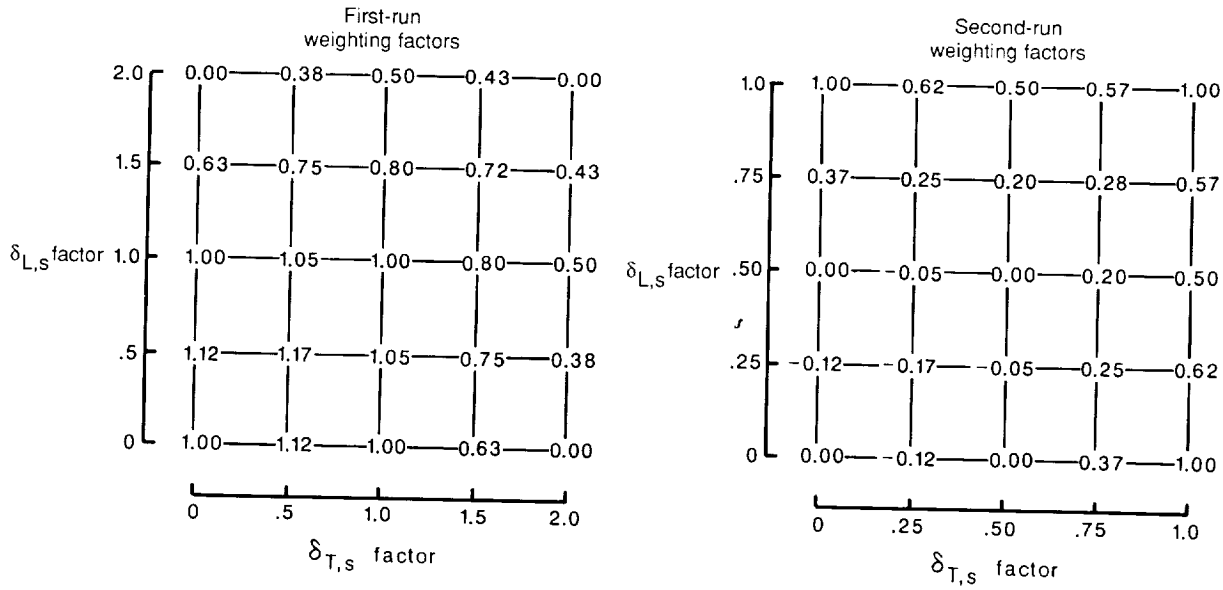

Figure 38. Weighting factors for two-run solution to generate suction-parameter contour maps.

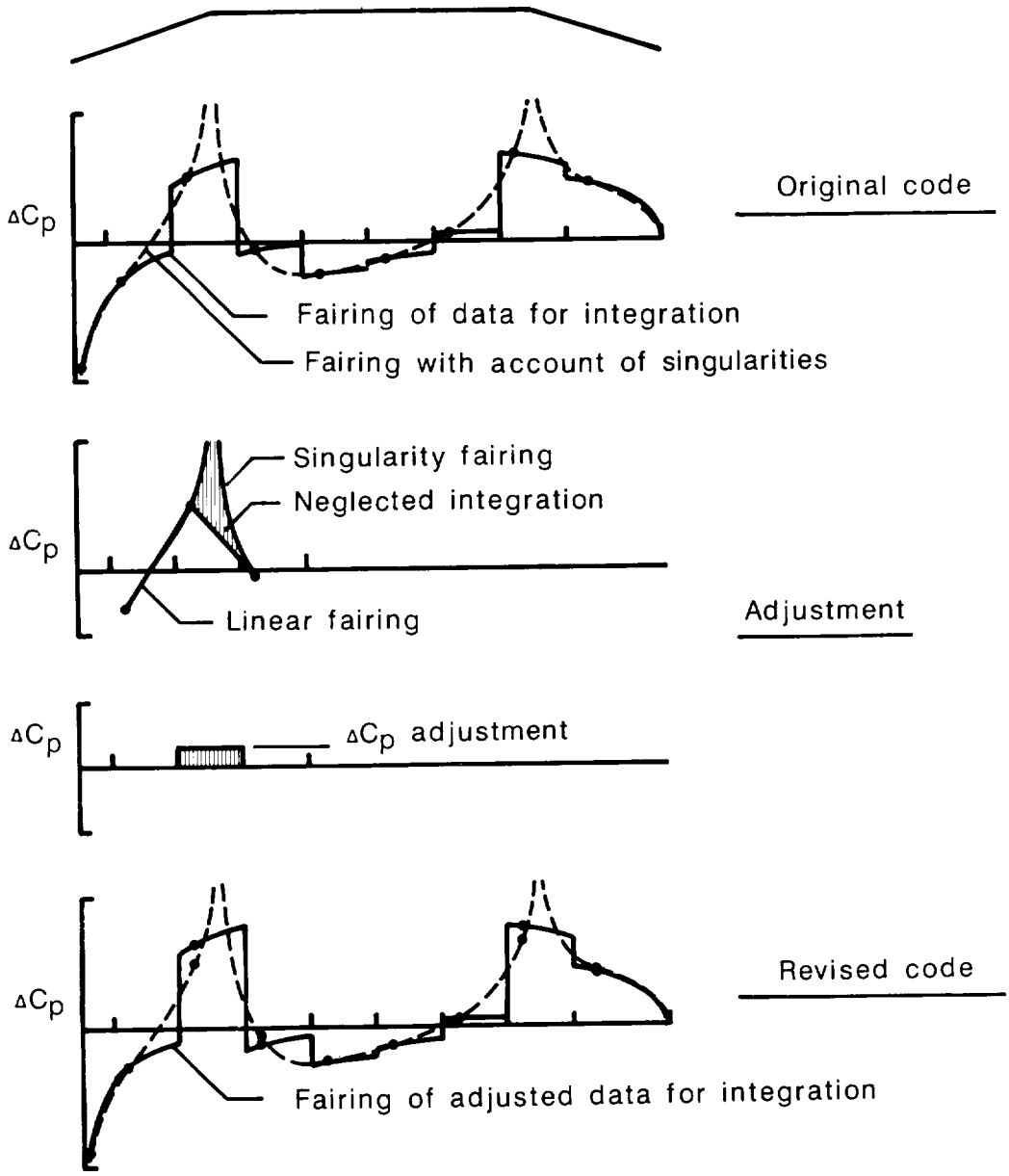

Figure 39. Flap hinge-line singularity adjustment.

NASA National Aeronautics and Space Administration

Report Documentation Page

1. Report No.	2. Government Accession No.	3. Recipient's Catalog No.
NASA TP-2828		

4. Title and Subtitle	5. Report Date
Validation of a Pair of Computer Codes for Estimation and Optimization of Subsonic Aerodynamic Performance of Simple Hinged-Flap Systems for Thin Swept Wings	November 1988
	6. Performing Organization Code
7. Author(s)	8. Performing Organization Report No.
Harry W. Carlson and Christine M. Darden	L-16428
9. Performing Organization Name and Address	10. Work Unit No.
NASA Langley Research Center Hampton, VA 23665-5225	505-61-71-05
	11. Contract or Grant No.
12. Sponsoring Agency Name and Address	13. Type of Report and Period Covered
National Aeronautics and Space Administration Washington, DC 20546-0001	Technical Paper
	14. Sponsoring Agency Code

15. Supplementary Notes

Harry W. Carlson: PRC Systems Services, A Division of Planning Research Corporation, Hampton, Virginia.
Christine M. Darden: Langley Research Center, Hampton, Virginia.

16. Abstract

Extensive correlations of computer-code results with experimental data are employed to illustrate the use of linearized-theory, attached-flow methods for the estimation and optimization of the aerodynamic performance of simple hinged-flap systems. Use of attached-flow methods is based on the premise that high levels of aerodynamic efficiency require a flow that is as nearly attached as circumstances permit. This study covers a variety of swept-wing configurations ranging from fighters to supersonic transports, all with leading- and trailing-edge flaps for enhancement of subsonic aerodynamic efficiency. The results indicate that linearized-theory, attached-flow, computer-code methods (modified to include estimated attainable leading-edge thrust and an approximate representation of vortex forces) provide a rational basis for the estimation and optimization of flap-system aerodynamic performance at subsonic speeds. The analysis also indicates that "vortex-flap" design is not an opposing approach but is closely related to attached-flow design concepts. The successful vortex-flap design actually suppresses the formation of detached vortices to produce a small vortex which is restricted almost entirely to the leading-edge flap itself.

17. Key Words (Suggested by Authors(s))	18. Distribution Statement
Aerodynamics Numerical methods Flap systems Vortex flaps Linearized theory	Unclassified–Unlimited Subject Category 02

19. Security Classif.(of this report)	20. Security Classif.(of this page)	21. No. of Pages	22. Price
Unclassified	Unclassified	116	A06

NASA FORM 1626 OCT 86

NASA-Langley, 1988

For sale by the National Technical Information Service, Springfield, Virginia 22161-2171